JAEA-Conf
2026-001
INDC(JPN)-0213
DOI:10.11484/jaea-conf-2026-001

JAEA-Conf

Proceedings of the 2024 Symposium on Nuclear Data
November 14-15, 2024,
Kumatori Community Center “Smiles Rengakan”,
Kumatori Town, Osaka, Japan

(Eds.) Jun-ichi HORI, Atsushi KIMURA and Kazushi TERADA

Nuclear Science and Engineering Center

June 2026

Japan Atomic Energy Agency

日本原子力研究開発機構

国立研究開発法人日本原子力研究開発機構
原子力科学研究所　プロモーション・オフィス　科学技術情報課
〒 319-1195　茨城県那珂郡東海村大字白方 2 番地 4
E-mail: ird-support@jaea.go.jp

JAEA-Conf 2026-001
INDC(JPN)-0213

Proceedings of the 2024 Symposium on Nuclear Data
November 14-15, 2024,
Kumatori Community Center “Smiles Rengakan”
Kumatori Town, Osaka, Japan

(Eds.) Jun-ichi HORI*[1], Atsushi KIMURA and Kazushi TERADA*[1]

Nuclear Science and Engineering Center
Japan Atomic Energy Agency
Tokai-mura, Naka-gun, Ibaraki-ken
(Received March 23, 2026)

The 2024 Symposium on Nuclear Data was held at Kumatori Town Community Center “Smiles Rengakan” in Kumatori Town on November 14-15, 2024. The symposium was organized by the Nuclear Data Division of the Atomic Energy Society of Japan (AESJ) and the Institute for Integrated Radiation and Nuclear Science, Kyoto University in cooperation with the Investigation Committee on Nuclear Data in AESJ, Nuclear Science and Engineering Center of Japan Atomic Energy Agency, and High Energy Accelerator Research Organization.

The symposium consisted of six oral presentation sessions and a poster session, with 17 talks and 29 posters presented. The total number of participants was 80. Each oral and poster presentation was followed by an active question and answer session. This report consists of a total of 27 papers including 8 oral and 19 poster presentations.

Keywords: Nuclear Data Symposium 2024, Experiments, Nuclear Theory, Nuclear Data Evaluation, Benchmark Test, Nuclear Data Applications

*[1] Institute for Integrated Radiation and Nuclear Science, Kyoto University

JAEA-Conf 2026-001
INDC(JPN)-0213

2024 年度核データ研究会報告集

2024 年 11 月 14 日～15 日

熊取交流センター　すまいるズ　煉瓦館
大阪府熊取町

日本原子力研究開発機構　原子力基礎工学研究センター

（編）堀　順一*[1]、木村　敦、寺田　和司*[1]

(2026 年 3 月 23 日受理)

2024 年度核データ研究会は、2024 年 11 月 14 日～15 日に、大阪府東熊取町にある「熊取交流センター　すまいるズ　煉瓦館」にて開催された。本研究会は、日本原子力学会核データ部会および京都大学複合原子力科学研究所が主催、日本原子力学会「シグマ」調査専門委員会、日本原子力研究開発機構原子力基礎工学研究センター、高エネルギー加速器研究機構が共催した。

研究会では、6 つの口頭発表のセッションとポスターセッションが開催され、17 件の講演と 29 件のポスターが発表された。参加者数は 80 名で、それぞれの口頭発表およびポスター発表では活発な質疑応答が行われた。本報告書は、本研究会における口頭発表 8 件、ポスター発表 19 件の合計 27 件の論文を掲載している。

原子力科学研究所：〒319-1195　茨城県那珂郡東海村大字白方 2-4
*[1] 京都大学

Contents

目次

1. 2024 年度核データ研究会 タイムテーブル

1. Timetable of Symposium on Nuclear Data 2024

開催日 / Date

2024 年 11 月 14 日（木）– 11 月 15 日（金）

Thursday, November 14 – Friday, November 15, 2024

会場 / Venue

熊取交流センター「すまいるズ 煉瓦館」

Kumatori Community Center “Smiles Rengakan”

Web Page

https://conference-indico.kek.jp/event/301/

プログラム / Program

2024 年 11 月 14 日（木） / Thursday, November 14, 2024

施設見学 / Facility Tour

時間 / Time	内容 / Program
10:30 – 12:00	**施設見学 / Facility Tour** 京都大学 複合原子力科学研究所（KURNS） 研究用原子炉（KUR），サイクロトロン Institute for Integrated Radiation and Nuclear Science, Kyoto University Research Reactor (KUR), Cyclotron

開会 / Opening

時間 / Time	題目 / Title	発表者 / Presenter
13:00 – 13:10	開会挨拶・事務連絡 Opening Address and Announcements	堀 順一（京都大学） Jun-ichi HORI (Kyoto University)

核データ部会賞受賞者講演
Presentation by Award of Nuclear Data Division

時間 / Time	題目 / Title	発表者 / Presenter
13:10 – 13:40	中性子放射化分析による中性子捕獲断面積の高精度測定手法の開発 Development of accurate measurement method for neutron capture cross-sections by neutron activation analysis	中村 詔司（原子力機構） Shoji NAKAMURA (JAEA)
13:40 – 14:10	4 次元 Langevin 模型を用いた即発崩壊過程に伴う核分裂観測量の体系的計算のための枠組みの構築 Construction of a framework for the systematic calculation of prompt fission observables using a four-dimensional Langevin model	藤尾 和樹（東京科学大学、現：LANL） Kazuki FUJIO (Institute of Science Tokyo, Present: LANL)

| 14:10 – 14:20 | **休憩 / Break** |

熱中性子散乱則データの現状と課題
Current Status and Issues of the Thermal Neutron Scattering Law

時間 / Time	題目 / Title	発表者 / Presenter
14:20 – 14:50	超小型炉 MoveluX™における CaH_2の温度反応度特性と炉心特性における熱中性子散乱則データの重要性と課題 Importance and Issues of CaH_2 TLS Data for reactivity coefficient and core characteristics of MoveluX™	木村 礼（東芝エネルギーシステムズ株式会社） Rei KIMURA（Toshiba Energy Systems & Solutions Corporation）
14:50 – 15:20	J-PARC における熱中性子散乱則のための微分断面積測定 Differential Cross-section Measurements for Thermal Neutron Scattering Law at J-PARC	木村　敦（原子力機構） Atsushi KIMURA (JAEA)
15:20 – 15:50	原子炉用減速材の熱中性子散乱則評価の現状と課題 Current status and issues of evaluation of thermal neutron scattering law for nuclear reactor moderators	中山　梓介（原子力機構） Shinsuke NAKAYAMA（JAEA）

15:50 – 16:00　**休憩（集合写真） / Break (Group Photo)** |

ポスターセッション（別掲）
Poster Session (Listed Separately)
日時 / Time: **November 14, 16:00 – 18:00**

| 19:30 – 21:30 | **懇親会 / Social Gathering** |

2024 年 11 月 15 日（金） / Friday, November 15, 2024

チュートリアル / Tutorial

時間 / Time	題目 / Title	発表者 / Presenter
09:30 – 10:15	廃止措置のための放射化計算における注意点 Remarks on Activation Analyses for Decommissioning	今野 力（原子力機構） Chikara KONNO (JAEA)

| 10:15 – 10:20 | **休憩 / Break** |

最近のトピックス / Recent Topics

時間 / Time	題目 / Title	発表者 / Presenter
10:20 – 10:50	ベイズ機械学習による核データ評価の新たなアプローチ New Approaches in Nuclear Data Evaluation through Bayesian Machine Learning	岩元 大樹（原子力機構） Hiroki IWAMOTO (JAEA)
10:50 – 11:20	ミュオン核データの進展 Progress in Muon Nuclear Data	河村 成肇（高エネ研/J-PARC） Naritoshi KAWAMURA (KEK/J-PARC)
11:20 – 11:50	三体核力～原子核物理の新しい物質観～ 核データにつなげたいという思い	関口 仁子（東京科学大学） Kimiko SEKIGUCHI (Institute of Science Tokyo)

| 11:50 – 12:50 | **休憩 / Break** |

原子炉施設の現状
Status of Nuclear Reactor Facilities

時間 / Time	題目 / Title	発表者 / Presenter
12:50 – 13:20	臨界集合体 STACY 更新炉の現状と今後の計画 Status and plans for critical facility modified-STACY	荒木 祥平（原子力機構） Shouhei ARAKI (JAEA)
13:20 – 13:50	複合研原子炉施設の現状と今後の計画 Present Status and Future Plans of KURNS	三澤 毅（京都大学） Tsuyoshi MISAWA (Kyoto University)

| 13:50 – 14:00 | **休憩 / Break** |

核データの応用
Applications of Nuclear Data

時間 / Time	題目 / Title	発表者 / Presenter
14:00 – 14:30	核分裂性物質を非破壊分析するための中性子共鳴分析法の技術開発と核データ Development of a neutron resonance analysis technique for nondestructive fissile material assay and nuclear data	李 在洪（原子力機構） Jaehong LEE (JAEA)
14:30 – 15:00	パルス中性子源に同期しない γ 線のスペクトル測定による短寿命 FP 放射能評価 Gamma Ray Spectroscopy for Event Out of Phase of Pulsed Neutron Source for Short Lived Fission Product	名内 泰志（電中研） Yasushi NAUCHI (CRIEPI)
15:00 – 15:30	理研 RI ビームファクトリーにおける医療用ラジオアイソトープの製造 Production of Medical Radioisotopes at RIKEN RI Beam Factory	羽場 宏光（理研） Hiromitsu HABA (RIKEN)
15:30 – 16:00	アクティブ標的 TPC および Si 半導体検出器を用いた残留核の測定 Measurement of residual nuclei with active-target TPCs and Si detectors	川畑 貴裕（大阪大学） Takahiro KAWABATA (Osaka University)

| 16:00 – 16:10 | **休憩 / Break** |

各種報告・閉会挨拶

Various Reports and Closing

時間 / Time	題目 / Title	発表者 / Presenter
16:10 – 16:25	EXFOR ワークショップの報告/ Report on the EXFOR Workshop	須山 賢也（原子力機構） Kenya SUYAMA (JAEA)
16:25 – 16:40	日本原子力学会シグマ調査専門委員会の活動/ Activities of Investigation Committee on Nuclear Data of AESJ	西尾 勝久（原子力機構） Katsuhisa NISHIO (JAEA)
16:40 – 17:00	ポスター賞贈呈式/ Poster Award Ceremony サマリー・総合討論/ Summary and General Discussion 閉会挨拶/ Closing Remarks	片渕　竜也（東京科学大学） 堀 順一（京都大学） 須山 賢也（JAEA） Tatsuya KATABUCHI (Institute of Science Tokyo) Jun-ichi HORI (Kyoto University) Kenya SUYAMA (JAEA)

ポスター発表一覧

List of Poster Presentations

題目 / Title	発表者 / Presenter
Cassini パラメータを用いた核分裂エネルギー曲面でのサドルポイントの探索/ Searching for saddle points on fission energy surfaces using Cassini parameters	荒木 拓斗（関西大学）/ Takuto ARAKI (Kansai University)
リチウムの 14 MeV 中性子大角度散乱断面積ベンチマーク実験における誤差低減のための放射化箔の選定/ Selection of activation foil for error reduction of benchmark experiment on large-angle elastic scattering cross section of Li by 14 MeV neutrons	藤井 大和（大阪大学）/ Yamato FUJII (Osaka University)
多重箔放射化法による京大炉 BNCT 照射場の中性子エネルギースペクトルの再評価/ Re-evaluation of neutron energy spectrum in Kyoto University BNCT irradiation field using multifoil activation method	Jakkrit Prateepkaew （京都大学）/ Jakkrit PRATEEPKAEW (Kyoto University)
6 次元 Langevin 方程式を用いた ^{258}Md 核分裂モードの研究/ Study of fission modes in ^{258}Md with six-dimensional Langevin equation	岡田 和記（原子力機構）/ Kazuki OKADA (JAEA)
多核子移行反応で生成した蒸発残留核の角運動量分布とメカニズムの解明/ Angular momentum distribution and mechanisms of evaporation residues produced in multi-nucleon transfer reactions	中島 滉太（近畿大学）/ Kohta NAKAJIMA (Kindai University)
^{51}V, ^{54}Cr 入射核を用いた新超重元素の合成可能性/ Possibility of synthesizing new superheavy elements using ^{51}V and ^{54}Cr projectiles	川井 幸亮（近畿大学）/ Kosuke KAWAI (Kindai University)
J-PARC MLF ANNRI を用いた ^{99}Tc の中性子捕獲断面積測定/ Measurement of neutron capture cross sections of ^{99}Tc at ANNRI of J-PARC MLF	Maloney Maxwell CLark （東京科学大学）/ Maloney Maxwell CLARK (Science Tokyo)
光核分裂反応を利用した核燃料物質検知技術の開発/ Development of a detection technique for nuclear fuel materials using photonuclear reactions	國友 理紗 （東京科学大学）/ Risa KUNITOMO (Science Tokyo)

題目 / Title	発表者 / Presenter
オージェ電子放出核種の生成法の検討に資する計算システムの開発/ Development of a calculation system contributing to the consideration of production methods for Auger electron emitters	酒井 聖矢（理研）/ Seiya SAKAI (RIKEN)
核分裂過程での中性子放出効果を考慮した動力学模型の改良/ Improvement of a dynamical model considering neutron emission effects during the fission process	原田 壮太（近畿大学）/ Sota HARADA (Kindai University)
定常臨界実験装置 STACY 更新炉の臨界データと核データライブラリの評価結果/ Criticality data of the modified STACY and evaluation results of nuclear data libraries	吉川 智輝（原子力機構）/ Tomoki YOSHIKAWA (JAEA)
融合反応における複雑なダイナミクスの解明/ Understanding the complex dynamics of fusion reactions	上野 雅己（近畿大学）/ Masaki UENO (Kindai University)
高エネルギーガンマ線にのみ感度を持つ検出器の開発/ Development of a gamma-ray detector sensitive only to high-energy gamma rays	有川 雄太 （東京科学大学）/ Yuta ARIKAWA (Science Tokyo)
主成分分析による 4 次元ランジュバン模型の軌道解析/ Trajectory analysis of the four-dimensional Langevin model using principal component analysis	向原 悠太 （東京科学大学）/ Yuta MUKOBARA (Science Tokyo)
紫外線硬化型シンチレータを用いた中性子放射化法の研究/ Development of a neutron activation method using UV-curable resin scintillator	Zefeng Shao （東京科学大学）/ Zefeng SHAO （Science Tokyo）
AMPX-6 を使った熱中性子散乱則データ処理に関する問題/ Problems in processing thermal scattering law data with AMPX-6	今野 力（原子力機構）/ Chikara KONNO (JAEA)
230 MeV/u α 粒子非弾性散乱に関する INC 模型の研究/ Study of an INC model for alpha inelastic scattering at 230 MeV/u	古田 稔将（九州大学）/ Toshimasa FURUTA (Kyushu University)

題目 / Title	発表者 / Presenter
Si フィルターを用いた 129I の keV 中性子捕獲断面積測定/ keV-neutron capture cross section measurement of 129I using a Si-filter neutron beam	Gerard Rovira/ （原子力機構） Gerard ROVIRA (JAEA)
代理反応法測定用測定装置の開発/ Development of a measurement system for the surrogate reaction method	牧井 宏之（原子力機構）/ Hiroyuki MAKII (JAEA)
0 度近傍における陽子入射反応に対する INC 模型の研究/ Study of an INC model for proton-induced reactions near 0 degrees	久富 貴士（九州大学）/ Takashi HISATOMI (Kyushu University)
ENSDF 更新に向けた崩壊データ評価と JENDL-5 Decay Data File の検証/ Evaluation of nuclear decay data for ENSDF revision and verification of JENDL-5 Decay Data File for burnup calculation	飯村 秀紀 （核データ研究所）/ Hideki IIMURA （Nuclear Laboratory LLC）
PHITS による高エネルギー中性子に対する CsI(Tl)と NE213 の応答評価/ Comparison of CsI(Tl) and NE213 responses to high-energy neutrons using PHITS simulation	李 恩智（高エネ研）/ Eunji LEE (KEK)
JENDL-5 共分散ライブラリ作成と RSG GAS 炉への不確かさ評価応用/ Generation of JENDL-5 covariance libraries and application to nuclear data uncertainty evaluation for the Indonesian RSG GAS reactor	Peng Hong Liem （NAIS,東京都市大学）/ Peng Hong LIEM (NAIS, Tokyo City University)
崩壊曲線分析による ^{197m}Hg および ^{195m}Hg の崩壊分岐比決定/ Decay branching ratios of ^{197m}Hg and ^{195m}Hg determined by decay curve analysis	大塚 直彦（IAEA）/ Naohiko OTSUKA (IAEA)
宇宙利用のための J-PARC 3NBT および陽子ビーム施設利用/ Proton beam irradiation for space use at J-PARC 3NBT and proton beam irradiation facility plan	明午 伸一郎 （J-PARC/JAEA）/ Shin-ichiro MEIGO (J-PARC / JAEA)
放射化法を用いた ^{nat}W(p,X)反応断面積測定/ Cross section measurement of ^{nat}W(p,X) reactions by an activation method	杉原 健太（高エネ研）/ Kenta SUGIHARA (KEK)
JAEA 反跳生成核分離装置を用いた多核子移行反応研究/	洲嵜 ふみ（原子力機構）/

題目 / Title	発表者 / Presenter
Experimental study of multinucleon transfer reactions using JAEA-RMS	Fumi SUZAKI (JAEA)
TMI-1 照射 UO_2燃料の Cs 同位体分析から得た ^{133}Cs 断面積知見/	山本 徹（元 原子力規制庁）/
Feedback on neutron capture cross section of ^{133}Cs from isotope analysis of UO_2 fuel irradiated in TMI Unit 1	Toru YAMAMOTO (Former NRA)
多核子移行反応における生成核の角運動量と粒子放出角解析/	前田 裕星（近畿大学）/
Analysis of angular momentum of produced nuclei and particle emission angles in multinucleon transfer reactions	Yusei MAEDA (Kindai University)

2. Construction of a framework for the systematic calculation of prompt fission observables using a four-dimensional Langevin model

Kazuki FUJIO[†*1], Shin OKUMURA[2], Chikako ISHIZUKA[1], Satoshi CHIBA[3], and Tatsuya KATABUCHI[1]

[1]Institute of Science Tokyo, Ookayama 2-12-1, Meguro, Tokyo, 152-8850, Japan
[2]NAPC-Nuclear Data Section, International Atomic Energy Agency, Vienna International Centre, 1400 Vienna, Austria
[3]NAT Research Center, NAT Corporation, 38 Shinko-cho, Hitachinaka, Ibaraki, 312-0005, Japan
[†]Email: kazuki.fujio@lanl.gov

Abstract

We proposed a new framework for the systematic calculation of the prompt fission observables. The mass distribution of fission fragments and the total kinetic energy of the fragments before prompt decay were calculated using a four-dimensional Langevin model in this framework. We calculated accurate mass distributions of fission fragments by superposing two Langevin calculations, taking into account the influence of different magic shells. Then, fission observables after prompt decay were calculated in a consistent manner using the Hauser-Feshbach statistical decay model in TALYS. We compared the calculated fission observables with the previous Langevin results, as well as experimental and evaluated data, and found that our results successfully capture the known trends and reasonably reproduce the data for a series of Pu isotopes.

1 Introduction

Fission observables such as the neutron multiplicity, spectrum, and mass/charge distributions of fission products play an important role in evaluating safety and effectiveness of nuclear applications. Nevertheless, the data evaluation is still insufficient. A lot of research is being conducted with the many difficulties. The difficulties of measurement on these types of data come from the limitation due to the sample availability, high radiation background, and so on. Theoretical calculations for these observables are also challenging since the fission process is rooted in several different physical mechanisms. Currently, models based on Monte Carlo or deterministic approaches are developed to calculate the fission observables in a consistent manner. However, many computational codes usually employ the physical quantities before prompt neutron emission prepared by phenomenological methods or experimental results as inputs. These may lack the capability to cover a wide range of nuclides. To overcome the issue, the inputs should be prepared by theoretical models based on nuclear physics.

[*]Present address: Los Alamos National Laboratory, Los Alamos, New Mexico, 87545, USA

We propose a new framework to calculate the prompt fission observables by using the pre-neutron fission observables calculated by theoretical models. In this research, the nuclear deformation up to scission is simulated by a four-dimensional Langevin model [1]. The de-excitation process by emitting prompt neutrons and γ-rays is calculated by a Hauser-Feshbach statistical decay model implemented in TALYS (ver. 1.96) [2].

2 Models and Calculation Method

2.1 Four-dimensional Langevin model

We employed the four-dimensional Langevin model [1] to simulate the deformation of a compound nucleus up to scission. The time evolution of the deformation is solved in the Langevin equation;

$$\begin{aligned} \frac{dq_\mu}{dt} &= \left(m^{-1}\right)_{\mu\nu} p_\nu, \\ \frac{dp_\mu}{dt} &= -\frac{\partial F(\boldsymbol{q},T)}{\partial q_\mu} - \frac{1}{2}\frac{\partial \left(m^{-1}\right)_{\nu\sigma}}{\partial q_\mu} p_\nu p_\sigma - \gamma_{\mu\nu}\left(m^{-1}\right)_{\nu\sigma} p_\sigma + \sqrt{T_\mu^{\rm eff}}\, g_{\mu\nu} R_\nu(t), \end{aligned} \tag{1}$$

where $F(\boldsymbol{q},T)$ is a temperature-dependent free energy, $m_{\mu\nu}$, $\gamma_{\mu\nu}$ are mass and friction tensors, $R_\nu(t)$ is a stochastic force, and $T_\mu^{\rm eff}$ is an effective temperature. The symbol $\{q_\mu\} = \{\tilde{z}_0, \delta_1, \delta_2, \alpha\}$ is a set of time-dependent collective variables, and $\{p_\mu\}$ is the corresponding conjugate momenta. The first variable $\tilde{z}_0$ corresponds to nuclear elongation normalized by the radius of the compound nucleus. The second and third variables δ_1, δ_2 express the deformations calculated from major and minor axes of each fragment. The fourth variable α represents the mass asymmetry calculated from masses of each fragment. In addition to the variables, we have a parameter ε to describe the neck configuration of a compound nucleus. These variables and parameter are represented in the two-center shell model.

We calculated two fission fragment yields corresponding to the Standard I and II modes $Y_{\rm ST1}(A, {\rm TKE})$, $Y_{\rm ST2}(A, {\rm TKE})$ in Brosa's notation [3] by adjusting ε. These calculated yields are superposed by using a superposing ratio ζ:

$$Y_{\rm ff}(A, {\rm TKE}) = \zeta Y_{\rm ST1}(A, {\rm TKE}) + (1-\zeta) Y_{\rm ST2}(A, {\rm TKE}), \tag{2}$$

where $Y_{\rm ff}(A, {\rm TKE})$ is the fission fragment yield which is comparable with experimental data. The ratio ζ is determined by a least squares method to reproduce the peak positions of experimental fission fragment yields for ^{238,240,242}Pu(sf) and ^{239}Pu(n,f) [4]. More details about the model and method can be found in Ref [5].

2.2 Connection to the Hauser-Feshbach statistical decay model

The excitation energy and spin-parity distributions are necessary as inputs of the Hauser-Feshbach statistical decay calculation for fission fragments. TALYS generates both of the distributions. Here, we explain how we prepare inputs of the excitation energy distribution. The excitation energy distribution $G(E_x)$ is expressed in the form of a Gaussian distribution:

$$G(E_x) = \frac{1}{\sqrt{2\pi}\sigma_{E_{l,h}}} \exp\left\{ -\frac{(E_x - \bar{E}_{l,h})^2}{2\sigma_{E_{l,h}}^2} \right\}, \tag{3}$$

where $\sigma_{E_{l,h}}$ is a standard deviation of the excitation energy for a light or heavy fragment, and $\bar{E}_{l,h}$ is an average excitation energy for a light or heavy fragment. The charge distribution

is necessary to calculate $\sigma_{E_{l,h}}$ and $\bar{E}_{l,h}$. We combine the Wahl's Z_p model with the obtained Langevin results to generate the charge distribution. Then, we convert the TKE obtained from the Langevin calculation into the total excitation energy (TXE) with the Q-value. The average excitation energy $\bar{E}_{l,h}$ is calculated by the obtained TXE with an energy-dependent R_T model [6]. The deviation $\sigma_{E_{l,h}}$ is calculated with the deviation of TKE and $\bar{E}_{l,h}$. More details and related references about the distributions can be found in Ref [7].

3 Results and Discussion

3.1 Fission fragment yields and average TKEs from four-dimensional Langevin model

The upper panels of Figure 1 represent the comparisons of the calculated fission fragment yields with the previous Langevin calculations for ^{238,240,242}Pu(sf) and ^{239}Pu(n_{th},f). Whereas the yields in this research are calculated by superposing two different neck parameters, the previous results are calculated by using one neck parameter. The comparisons indicate that the present approach generally reproduces the experimental results and improves the accuracies of the peak position and width of the yields.

The lower panels of Figure 1 show the comparisons of the average TKEs. It is noted that the adjustment of ε improves not only the accuracy of the yields but also that of TKEs. The accuracy of TKEs is improved for $A \geq 140$ for all systems. Table 1 represents the calculated and experimental average TKEs. The deviation between the present results and experimental data is within approximately 2% for ^{238,240,242}Pu(sf) and within around 1% for ^{239}Pu(n_{th},f).

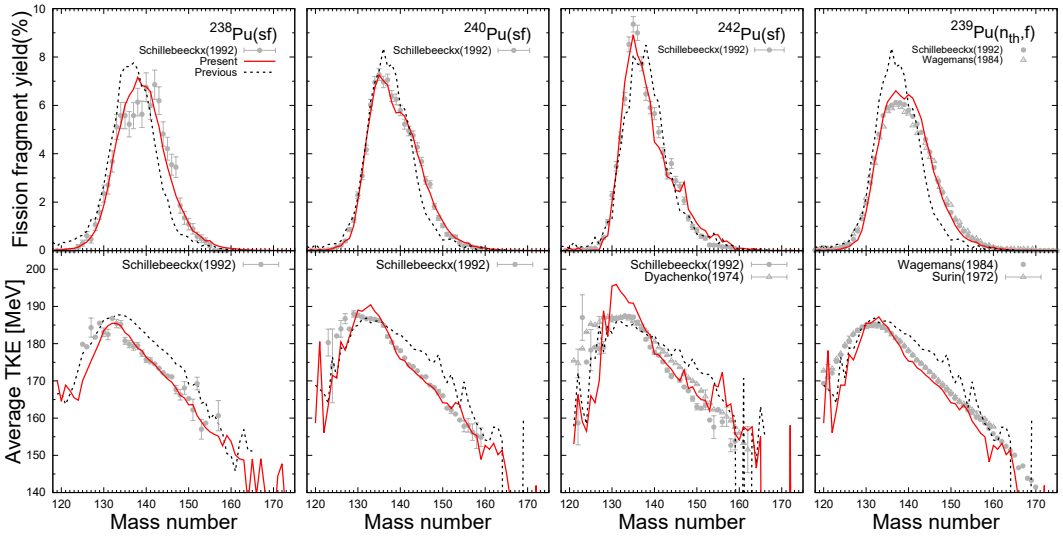

Figure 1: The calculated fission fragment yields (upper) and average TKEs (lower) for ^{238,240,242}Pu(sf) and ^{239}Pu(n_{th},f). The red lines correspond to the present results, and the black dashed lines present the previous results.

Table 1: The calculated and experimental average TKEs for ^{238,240,242}Pu(sf) and ^{239}Pu(n_{th},f) (in MeV unit).

		Standard I	Standard II	Average TKE
^{238}Pu(sf)	Present calc.	195.87	174.36	176.47
	Demattè et al.[8]			176.4±0.3
	Schillebeeckx et al.[4]			177.0±0.3
^{240}Pu(sf)	Present calc.	194.79	173.44	179.23
	Demattè et al.[8]			178.5±0.1
	Schillebeeckx et al.[4]			179.4±0.1
^{242}Pu(sf)	Present calc.	194.22	172.57	183.01
	Demattè et al.[8]			180.5±0.1
	Schillebeeckx et al.[4]			180.7±0.1
^{239}Pu(n_{th},f)	Present calc.	194.78	173.65	176.88
	Schillebeeckx et al.[4]			177.93±0.01
	Surin et al.[9]			177.7±0.1
	Tsuchiya et al.[10]			176.2±1.4

3.2 Prompt fission observables from Hauser-Feshbach statistical decay model

The left panel of Figure 2 shows the prompt neutron multiplicity $\bar{\nu}_n(A)$ of ^{239}Pu(n,f) at incident neutron energies of thermal energy and 5 MeV. The calculation result reproduces a saw-tooth shape where $\bar{\nu}_n(A)$ increases as the mass number of each fragment increases. The result also represents the increase of $\bar{\nu}_n(A)$ from heavy fragments as the incident energy increases. These tendencies are consistent with trends known from experimental results. On the other hand, the calculated $\bar{\nu}_n(A)$ overestimate (underestimate) the experimental data in the light (heavy) fragments. It is considered that these discrepancies are caused by the energy partitioning of the TXE. Several research group employ a mass-dependent R_T model based on the idea that the nuclear deformation at scission is different from each fission fragment pair and report that the mass-dependent R_T model improves the accuracy of $\bar{\nu}_n(A)$. The R_T model employed in this work does not depend on the mass number of the fission fragments. Thus employing the mass-dependent R_T model is considered as a future perspective.

The right panel of Figure 2 represents the prompt neutron multiplicity as a function of the incident energy $\bar{\nu}_n(E)$ of ^{239}Pu(n,f). The calculated result is consistent with the experimental and evaluated data ranging from thermal up to 5 MeV. Particularly, the calculated $\bar{\nu}_n(E)$ at thermal energy could reproduce the evaluated data.

The left panel of Figure 3 shows the prompt fission neutron spectrum (PFNS) in the laboratory frame for ^{239}Pu(n_{th},f), and the inset represents that as a ratio to a Maxwellian spectrum at $T = 1.32$ MeV. The calculated result approximately reproduces the shape of the spectrum in the logarithmic scale. However, the underestimation is seen between 3 to 10 MeV. It is known that the spin-parity distribution of the fission fragments and the fission fragment yield have impacts on the PFNS [11, 12]. Further adjustments and improvements are required to calculate more accurate PFNS.

The right panel of Figure 3 represents the independent fission product yield $Y(A)$ of ^{239}Pu(n_{th},f). Although the calculated $Y(A)$ reproduces the width and fine structure partially, the overestimations are seen in the vicinity of $A = 97$ and 141. It is considered that these overestimations are derived from the overestimations in the fission fragment yield $Y_{ff}(A)$ around $A = 137$ and 140. The accurate fission fragment yield is required to calculate more accurate independent fission product yield.

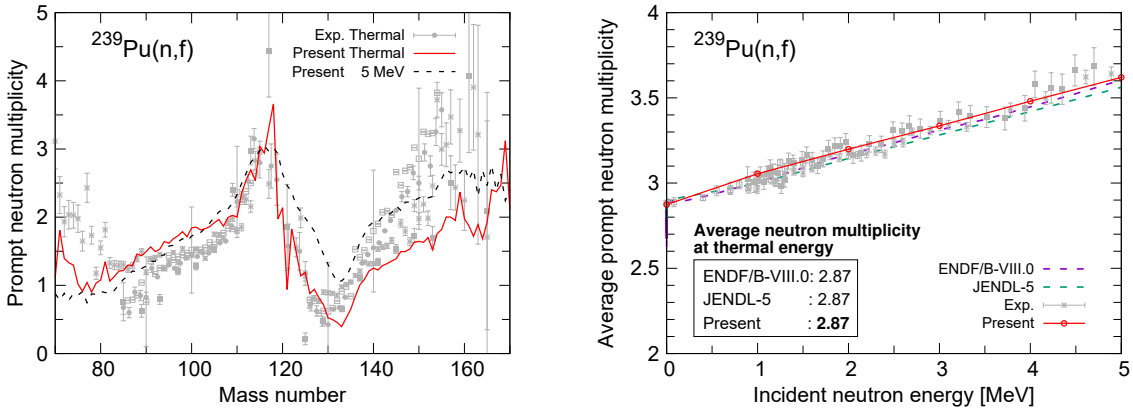

Figure 2: (Left) the prompt neutron multiplicities as a function of the fission fragment mass for ^{239}Pu. The red solid and black dashed lines correspond to the results at thermal and 5 MeV incident neutron energies, respectively. (Right) the prompt neutron multiplicity as a function of the incident neutron energy for ^{239}Pu. The red solid line represents the calculated result, and the dashed lines correspond to the evaluated data.

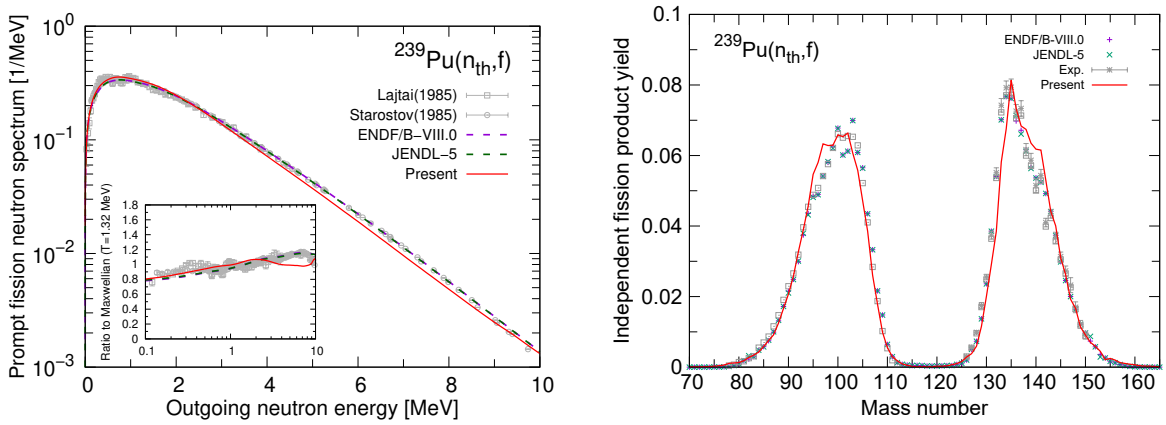

Figure 3: (Left) the prompt fission neutron spectrum (PFNS) in the laboratory frame for ^{239}Pu(n_{th},f). The inset figure represents the PFNS as a ratio to a Maxwellian spectrum at $T = 1.32$ MeV. (Right) the independent fission product yield for ^{239}Pu(n_{th},f). The red solid lines represent the calculated results, and the dashed lines correspond to the evaluated data.

4 Conclusions

We constructed a framework for systematically calculating the fission observables and to investigate its effectiveness with Pu isotopes. In this framework, a novel method is proposed to calculate more accurate fission fragment yield. Two different fission modes are calculated separately in the four-dimensional Langevin model and are superposed to reproduce the peak position of the experimental yields. The improvement of the accuracy is verified for fission fragment yield and TKE by comparing with the previous Langevin result. Furthermore, we calculate the prompt fission observables in the Hauser-Feshbach statistical decay model implemented in TALYS with the obtained Langevin results. The calculated results capture the known trends and reasonably reproduce the experimental and evaluated data. There are still rooms for improvement in the accuracy of fission observables. We plan to improve the accuracy and apply this framework to actinides where direct measurements are difficult in the future.

References

[1] Ishizuka C., Usang M. D., Ivanyuk F. A., Maruhn J. A., Nishio K., Chiba S., Four-dimensional Langevin approach to low-energy nuclear fission of ^{236}U, Phys. Rev. C96, 2017, 064616.

[2] Koning A., Hilaire S., Goriely S., TALYS: modeling of nuclear reactions, Eur. Phys. J. A59, 2023, 131.

[3] Brosa U., Grossmann S., Müller A., Nuclear scission, Phys. Rep. 197, 1990, pp. 167-262.

[4] Schillebeeckx P., Wagemans C., Deruytter A.J., Barthélémy R., Comparative study of the fragments' mass and energy characteristics in the spontaneous fussion of ^{238}Pu, ^{240}Pu and ^{242}Pu and in the thermal-neutron-induced fission of ^{239}Pu, Nucl. Phys. A545, 1992, pp. 623-645.

[5] Fujio K., Okumura S., Ishizuka C., Chiba S., Katabuchi T., Connection of four-dimensional Langevin model and Hauser-Feshbach theory to describe statistical decay of fission frag-ments, J. Nucl. Sci. Technol. 61, 2024, pp. 84-97.

[6] Okumura S., Kawano T., Lovell A. E., Yoshida T., Energy dependent calculations of fission product, prompt, and delayed neutron yields for neutron induced fission on ^{235}U, ^{238}U, and ^{239}Pu, J. Nucl. Sci. Technol, 59, 2022, pp. 96-109.

[7] Fujio K., Construction of a Framework for Systematical Computation of Prompt Fission Observables, Tokyo Institute of Technology, 2024, Ph. D. thesis.

[8] Dematté L., Wagemans C., Barthélémy R., D'hondt P., Deruytter A., Fragments' mass and energy characteristics in the spontaneous fission of ^{236}Pu, ^{238}Pu, ^{240}Pu, ^{242}Pu, and ^{244}Pu, Nucl. Phys. A617, 1997, pp. 331-346.

[9] Surin V. M., Sergachev A. I., Rezchikov N. I., Kuz'minov B. D., Yields and kinetic energies of fragments at the fission of ^{233}U and ^{239}Pu by 5.5 and 15 MeV neutrons (in Russian), Yadern. Fiz. 14, 1971 , pp. 935-938.

[10] Tsuchiya C., Nakagome Y. Yamana H., Moriyama H., Nishio K., Kanno I., Shin K., Kimura I., Simultaneous Measurement of Prompt Neutrons and Fission Fragments for ^{239}Pu(n_{th},f), J. Nucl. Sci. Technol. 37, 2000, pp. 941–948.

[11] Kawano T., Okumura S., Lovell A. E., Stetcu I., Talou P., Influence of nonstatistical prop-erties in nuclear structure on emission of prompt fission neutrons, Phys. Rev. C104, 2021, 014611.

[12] Fujio F., Al-Adili A., Nordström F., Lemaître J.-F., Okumura S., Chiba S.,Koning A., TALYS calculations of prompt fission observables and independent fission product yields for the neutron-induced fission of ^{235}U, Eur. Phys. J. A59, 2023, 178.

Acknowledgments

Authors acknowledge the Grant-in-Aid for Scientific Research (B), MEXT, Japan, and by Japan Society for the Promotion of Science (JSPS) KAKENHI Grant Number [21H01856].

3. Importance and issues of CaH_2 TLS data for reactivity coefficient and core characteristics of MoveluX™

Rei KIMURA[a*]

[a]*Toshiba Energy Systems & Solutions Corporation, 4-1, Ukichima-cho, Kawsaki-ku, Kawasaki, 210-0862, Japan*

Email:rei.kimura@toshiba.co.jp

Toshiba Energy Systems & Solutions has been developing a MoveluX™ reactor system with 10 MWt and 3-4 MWe power output. The MoveluX™ core uses calcium hydride (CaH_2) as the solid-state neutron moderator. The hydrogen in CaH_2 dissociated above 800 ºC; thus, this temperature is the operation limitation temperature of the core. From the viewpoint of the core characteristics, the CaH_2 moderator shows a positive temperature reactivity coefficient from room temperature to near the operation temperature. The MoveluX™ core utilizes this positive temperature reactivity coefficient to assure critical safety during transport. To evaluate this core characteristic, the TSL of CaH2 is very important input data for the core calculation. However, only JEFF published TSL data on the CaH2, and it was based on one experiment's data. On the other hand, the Toshiba Energy Systems & Solutions Corporation measured TSL of CaH_2 in the past research with Tokyo Tech and Kyoto University. Additionally, JAEA also evaluates this TSL based on the simulation. The MoveluX™ core had around 200 pcm between these TLS data, furthermore, more than a 2% difference in temperature reactivity coefficient was confirmed. These differences were not small, thus, improvement of the CaH2 TLS data will be required.

Keywords: MoveluX™; CaH_2; TSL; S(α,β); microreactor; SMR

1. Introduction

To realize a decarbonized society, various organizations are developing small modular reactors and microreactors as shown in Figure 1 [1]. Toshiba Energy Systems & Solutions Corporation has been developing the MoveluX™ reactor system that has 10MWt and 3-4 MWe power output and can provide a high-temperature heat source of around 700 ºC. The MoveluX™ core uses LEU less than 5% of ^{235}U enrichment as the fuel material and does not use HALEU from the viewpoint of procurability.

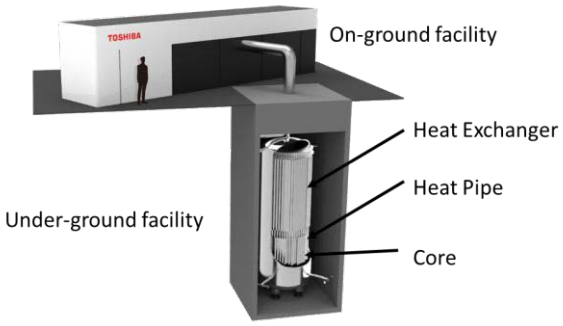

Figure 1. Schematic view of the MoveluX^{TM} reactor system

Therefore, the neutron moderator is required to realize a small core based on the LEU, and this moderator should be used in a high-temperature environment. For this reason, the MoveluX^{TM} core selected the calcium-hydride (CaH_2) as the solid-state neutron moderator. The CaH_2 moderated small core had a unique core characteristic, specifically, it showed a positive temperature reactivity coefficient from room temperature to near the operation temperature [2].

Figure 2 shows this positive temperature reactivity coefficient, and Figure 3 shows the spectrum shift with the temperature. This positive temperature reactivity coefficient originated from this spectrum shift; therefore, this reactivity can be controlled to negative in the operation temperature by adding the poison nuclides.

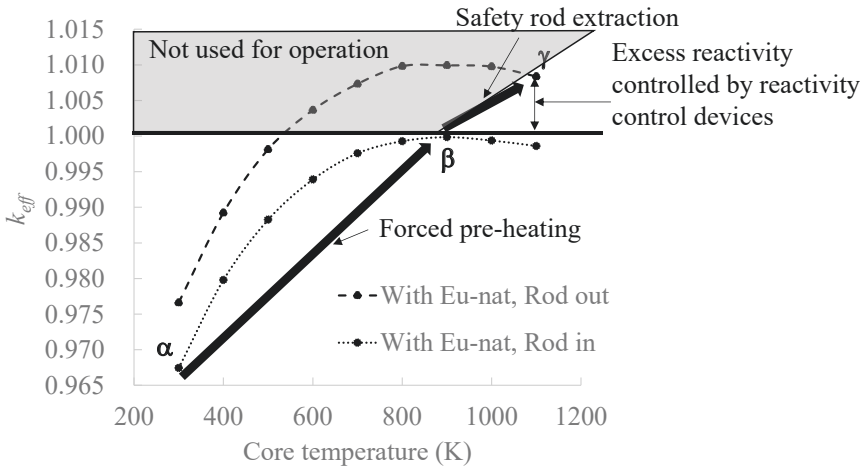

Figure 2. Reactivity characteristics of the MoveluX^{TM} core [2]

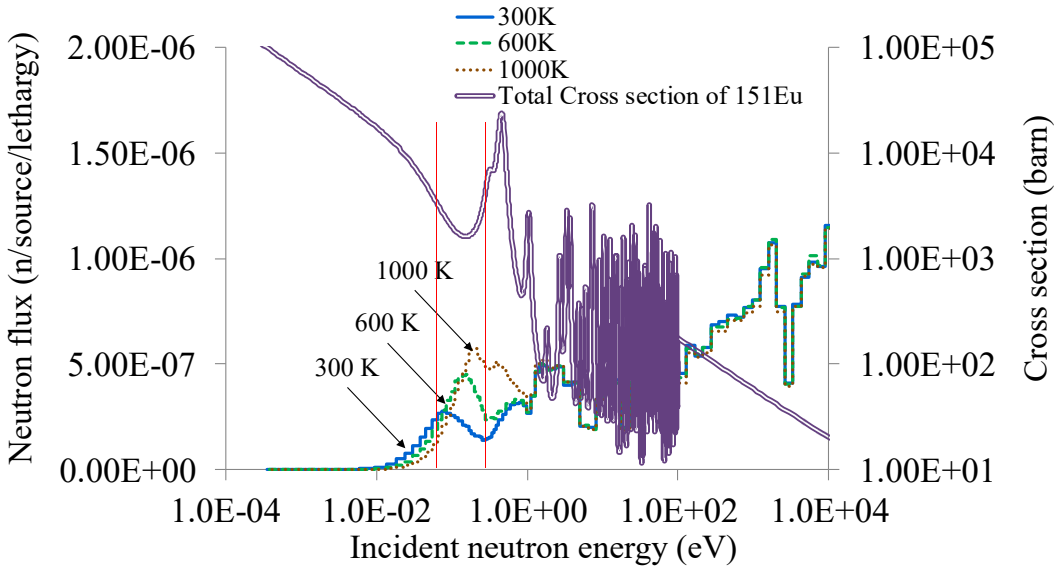

Figure 3. Spectrum shift with the temperature [2]

The Thermal Scattering Law (TSL) data dominated this core characteristic. Hence, the TSL data of the CaH_2 was critically important for the core neutronics design of the MoveluX^{TM}. However, the TSL data of the CaH_2 was only published in the JEFF, and was based on the experiment conducted multiple decades ago.

On the other hand, unpublished TSL data of the CaH_2 was measured by the author, Dr. Nishiyama, and Prof. Hori in 2019, furthermore, calculated TSL data was provided by Dr. Nakayama [3]. This paper realizes the impact of the difference of these TSL data on the core eigenvalue.

2. Calculation Model

Table 1 and Figure 4 show the core specifications and the horizontal cross-section of the MoveluX^{TM} core. The MVP-3.0 code and JENDL-4.0 are the core neutronics code and the nuclear data library [4-5]. However, JEFF-3.2 was used for the reference TSL data of the CaH_2 because JENDL-4.0 does not store TSL data of CaH_2 [6]. Furthermore, the CaH2 TSL data was replaced by other TSL data summarized in Table 2. The neutronics calculation evaluated k_{eff} of the core in different core temperatures from 300 K to 1200 K.

Table 1. Core specifications

Item	Value
Fuel material	U_3Si_2
Moderator material	CaH_2
Neutron breeder material	BeO
Number of the fuel	66
Number of the moderator	72
Number of the neutron breeder	228
Width of the fuel elements	10 cm
Width of moderator elements	8.6 cm
Core diameter/height	180 cm/220 cm
Maximum/Average ^{235}U Enrichment	4.99 wt%

Table 2. Used CaH_2 TSL data and its conditions

Library(ID)	Note
JEFF-3.2	Only published CaH_2 data
JENDL-5	Based on the first-principles calculation evaluated by Dr. Nakayama(JAEA)
Present	Measured by author, Dr. Nishiyama (Tokyo City Univ.), and Dr. Hori (Kyoto Univ.)

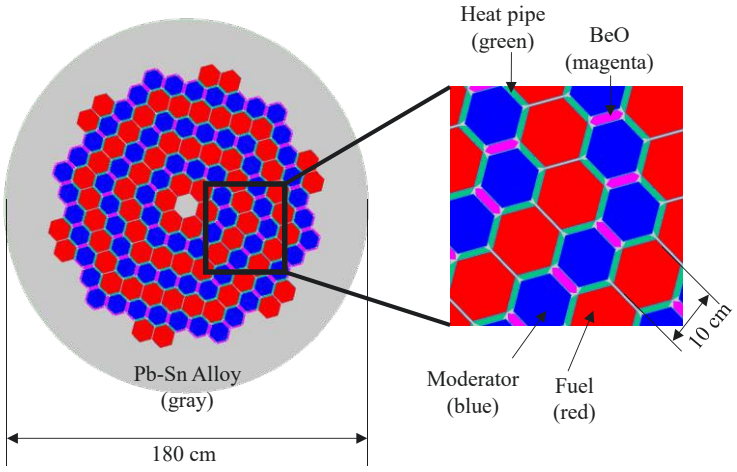

Figure 4. Core horizontal cross section

3. Reactivity difference between TSL data

Figure 5 shows the temperature-dependent k_{eff} of each case. The around 200 pcm difference of k_{eff} between libraries was confirmed. Moreover, the temperature reactivity coefficient dk/dT was 2%. This difference was not small from viewpoint of reactor core design especially for the reactor kinetic behavior.

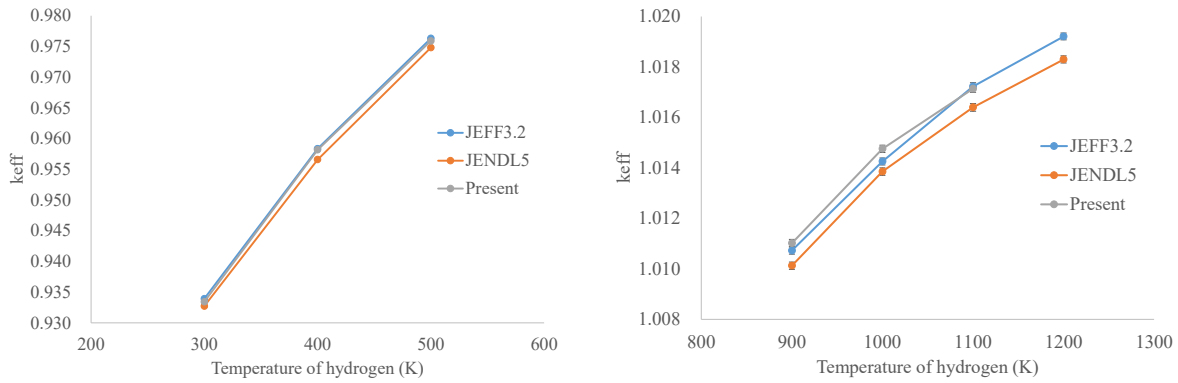

Figure 5. Temperature dependent k_{eff} of each case

4. Conclusion

The impact of CaH_2 TSL difference on the MoveluX^{TM} core neutronics was up to around 200 pcm. Furthermore, a 2% difference in temperature reactivity coefficient existed. This difference was not small for the core design, especially for the reactor kinetic behavior. Therefore, the precision of this TSL data, the new measurement, and integral experiments are required to improve the precision of TSL data and core neutronics evaluation.

Acknowledgements

We would like to thank Dr. Shinsuke Nakayama, Prof. Jun-ichi Hori and Dr. Jun Nishiyama for providing the CaH_2 TSL data.

References

[1] Kimura R, Asano K, Iwaki C, et al., The conceptual design of heat-pipe cooled and calcium hydride moderated vSMR. Proceedings of ICAPP2019; 2019 May 12-15; Juan-les-pins, France.

[2] Kimura R, Asano K., Ensuring criticality safety of vSMR core during transportation based on its temperature reactivity. Nucl Sci Eng. 2019; 194: pp. 213–220.

[3] Nakayama S, Iwamoto O., Development of nuclear data evaluation framework for innovative reactor (II), 5; Development of evaluated nuclear data files Proc. AESJ 2024 Annual Mtg.; 2024 Mar 26-28; Osaka, Japan.

[4] Nagaya Y, Okumura K, Sakurai K, et al., MVP/GMVP version 3: general purpose monte carlo codes for neutron and photon transport calculations based on continuous energy and multigroup methods. Tokai-mura (Japan): Japan Atomic Energy Agency; 2017. JAEA-Data/Code 2016-018.
[5] Shibata K, Iwamoto O, Nakagawa T, et al., JENDL-4.0: a new library for nuclear science and technology. J Nucl Sci Technol. 2011; 48: pp. 1–30.
[6] "JEFF-3.2 evaluated data library—Neutron data", Organisation for Economic Co-operation and Development Nuclear Energy Agency Data Bank (2014); http://www.oecd-nea.org/dbforms/data/eva/evatapes/jeff_32/, (accessed 2025-03-07).

4. Current status and issues of evaluation of thermal neutron scattering law for nuclear reactor moderators

Shinsuke NAKAYAMA

Nuclear Data Center, Japan Atomic Energy Agency
2-4 Shirakata, Tokai, Ibaraki 319-1195, Japan

In this paper, we introduce and discuss the current status and issues of the evaluation of thermal scattering laws (TSL) in the development of the Japanese Evaluated Nuclear Data Library, JENDL. We have recently started to establish a method for evaluating the TSL of crystalline materials with the aim of enhancing the TSL data in JENDL. In addition, further improvements are underway for the TSL of light water. We are developing a method for evaluating TSL using molecular dynamics calculations with potentials based on first-principles calculations. The new TSL evaluation method for light water is also introduced.

1. Introduction

In thermal neutron reactors, the TSL of the moderator has a significant impact on core calculations. In the JENDL series, the latest version, JENDL-5 [1], is the first to include an original evaluation of TSL. In this evaluation, the TSL of water, a typical moderator, and hydrogen-containing organic compounds such as methane, which is used as a moderator in neutron sources, were evaluated based on molecular dynamics simulations. However, data for crystalline materials was obtained from the ENDF/B-VIII.0 library [2]. Crystalline materials are also used as moderators in thermal neutron reactors. Such examples are graphite in high-temperature gas-cooled reactors and molten salt reactors, and calcium hydride (CaH_2) in small modular reactors.

Under these circumstances, we have started to establish a method for evaluating the TSL of crystalline materials with the aim of enhancing the TSL data in JENDL. As a result, by using an evaluation method based on first-principles calculations [3], we have obtained results for graphite that well reproduce the experimental values measured at J-PARC [4]. We then applied this TSL evaluation method to CaH_2. In this paper, we will discuss the results for CaH_2 in particular.

Moreover, further improvements are underway for the TSL of light water. In order to improve reliability under high-temperature and high-pressure conditions such as reactor operation conditions, we are developing a method for evaluating TSL using molecular dynamics simulations with potentials based on first-principles calculations, which are considered to have high predictability for changes in temperature and pressure. This method incorporates ingenuity not only in potential but also in molecular dynamics simulation in itself. Specifically, path integral molecular dynamics simulation is employed to consider the quantum vibrational behavior of hydrogen. We also introduce this new TSL evaluation method for light water.

2. TSL evaluation for crystalline material

2.1. TSL evaluation for graphite

Regarding TSL for graphite, porosity-dependent data is provided in ENDF/B-VIII.0. Note that the evaluation method in the latest version of ENDF/B-VIII.1 is almost the same as that in ENDF/B-VIII.0. However, even graphite with porosity should be considered to have an ideal crystalline structure for the carbon portion that causes inelastic scattering in it, for the following reasons [5]: (i) in graphite with porosity, the vacancies have a larger size (several hundred micrometers) than in crystal structure, (ii) thus, there is a clear separation between the vacancy part and the rest where carbon atoms are present (each part does not coexist at the scale of crystal level).

For these reasons, in Ref. [3], we evaluated the inelastic scattering components in the TSL for graphite assuming ideal crystalline graphite (i.e., 0 % porosity). This assumption was verified through comparison with the experimental neutron scattering data measured at J-PARC [4]. As a result, it was found that the evaluated values assuming crystalline graphite reproduced the experimental values better than the evaluated values of ENDF/B-VIII.0 for 10 % and 30 % porosity. Since the graphite used in the experiment has a porosity of 15 %, it was found that the evaluation of the inelastic scattering component should be performed assuming crystalline graphite, independent of the porosity. See Ref. [3] for more detailed results and discussion.

2.2. TSL evaluation for CaH_2

Next, we describe the TSL evaluation for CaH_2, which is being considered for use as a solid moderator in small modular reactors. Since CaH_2 is a crystalline material, as in the case of graphite in Ref. [3], the inelastic scattering components due to lattice vibrations in the crystal were evaluated based on the phonon density of states obtained from first-principles calculations and lattice vibration calculations.

The first-principles calculations were performed by the Quantum ESPRESSO code [6] and the lattice vibration calculations were performed by the Phonopy code [7], respectively. The first-principles calculations were performed using pseudopotentials and plane-wave basis. Winmostar [8], a simulation interface software, was used to create the input data for the Quantum ESPRESSO code. To account for long-range effects on atomic displacements, calculations were performed for a supercell with several unit crystals, as shown in Figure 1. The phonon density of states obtained from this method was given as input to the LEAPR module of the nuclear data processing code NJOY2016 [9] to derive the TSL for inelastic scattering.

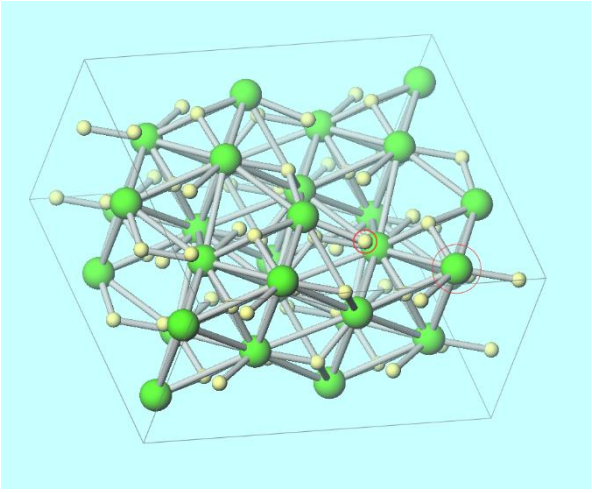

Figure 1. Supercell of CaH_2 crystal

The inelastic scattering cross sections obtained from the evaluated TSL are shown in Figure 2. For the hydrogen component in CaH_2, the present evaluation (solid red line) and the currently available data from JEFF-3.3 [10] (dashed green line) show a similar trend. In JEFF-3.3, the energy spectra of the scattered neutrons for the

CaH_2 target are measured and the phonon density of states is estimated from them. Although the methods used in the present evaluation and JEFF-3.3 differ greatly, the evaluated values are in general agreement with each other. On the other hand, there is a large difference between the present evaluation (solid blue line) and JEFF-3.3 (dashed yellow line) regarding the components of calcium. This is due to the fact that in the evaluation of JEFF-3.3 the phonon density of states estimated for CaH_2 is distributed for the hydrogen and calcium components at the ratio roughly estimated, respectively. This procedure results in a large ambiguity of the component of calcium, which has small cross sections. Therefore, for the component of calcium, the present evaluation based on the first-principles calculations is considered more reliable than JEFF-3.3.

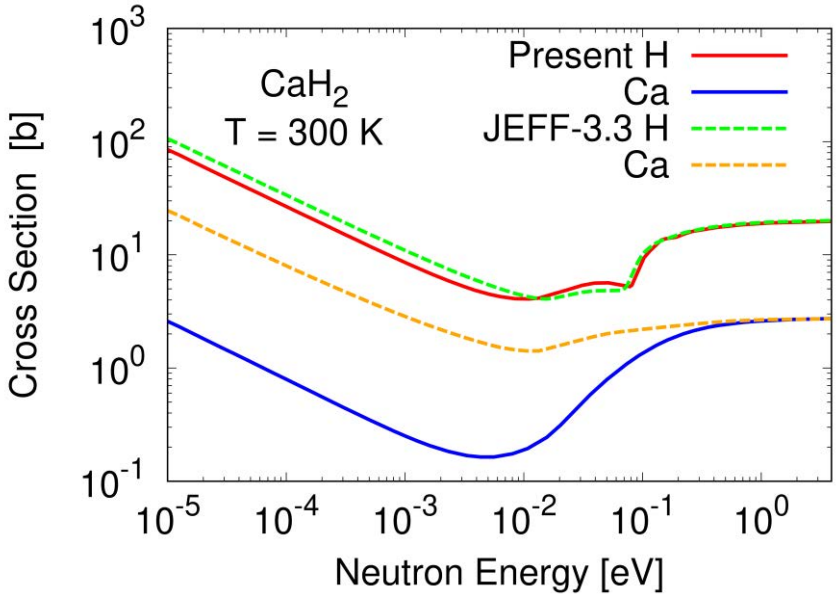

Figure 2. Inelastic scattering cross sections for hydrogen and calcium in CaH_2

Next, the total cross section was obtained by adding the elastic scattering components (i.e., incoherent and Bragg scattering components) to the evaluated inelastic scattering components, and it was compared with the total cross section at 300 K obtained from the neutron transmission experiment at J-PARC [11]. The result is shown in Figure 3. The total cross section of CaH_2 (red solid line), which was obtained by doubling the hydrogen component (blue solid line) and adding it to the calcium component (green solid line), reproduces the experimental value well, and the reliability of the evaluated value in this study was validated. The result of a comparison with the JEFF-3.3 evaluation is shown in Figure 4. As shown in the figure, the evaluated values in this work are almost the same as JEFF-3.3, and both are generally consistent with the experiments. However, according to the integral calculations for the reactor core containing CaH_2, it has been reported that there are non-negligible differences in the reactivity coefficients calculated using these two TSL data [12]. These differences may be attributed to the neutron spectrum of inelastic scattering, which cannot be identified from a comparison in terms of total cross sections. As a future work, it is desirable to perform the double differential cross section measurement to verify which of the two evaluation values is more appropriate in terms of the inelastic scattering spectrum. In addition, it

would be desirable to conduct an integral experiment to determine which of the above integral calculation results is more plausible, as non-negligible differences from the viewpoint of the reactor core design have been observed.

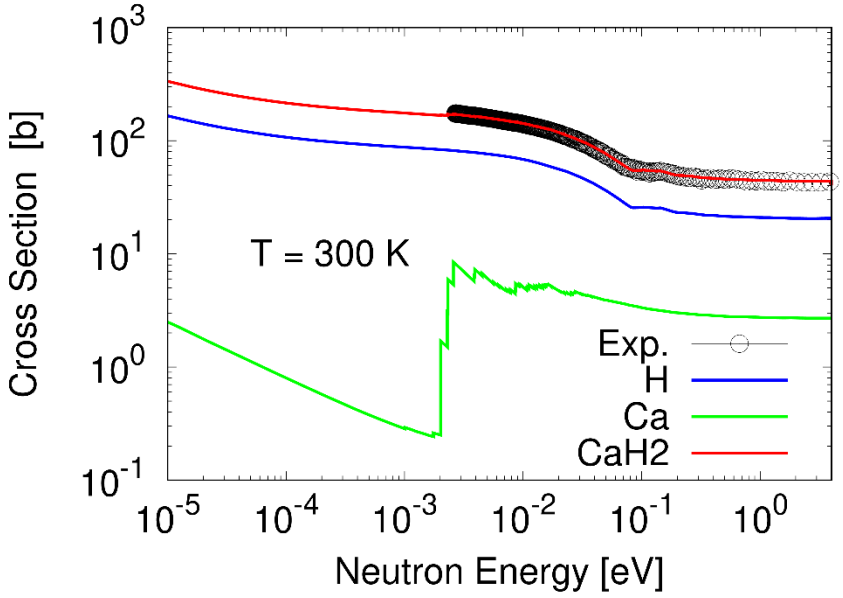

Figure 3. Total cross sections for hydrogen and calcium in CaH_2

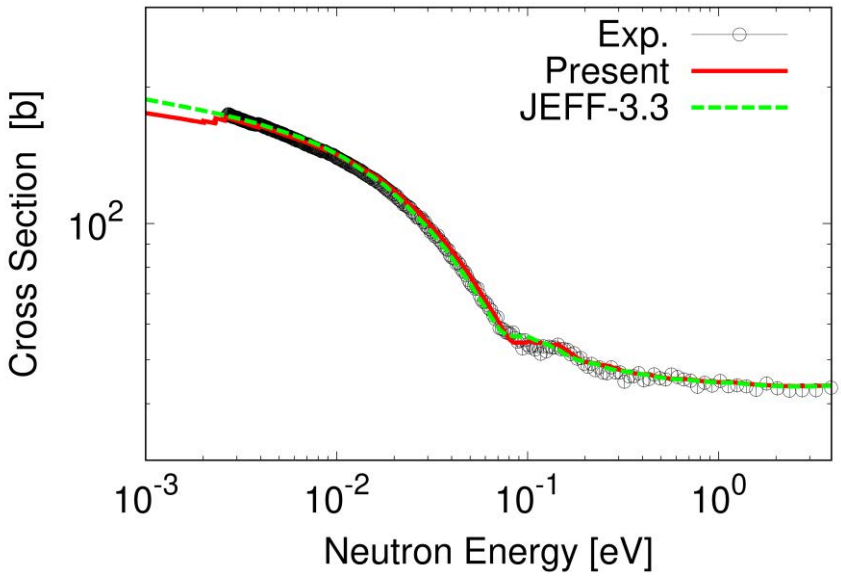

Figure 4. Total cross sections for CaH_2 (comparison with the JEFF-3.3 evaluation)

3. TSL evaluation for high-temperature light water

Since TSL is data describing neutron scattering due to atomic and molecular motion of materials, it varies with material phase, temperature, and pressure. From the viewpoint of core calculations, TSL at high temperatures and pressures such as a reactor operation condition is particularly important.

In recent nuclear data libraries such as JENDL, ENDF/B, and JEFF, TSL data for light water are evaluated based on molecular dynamics simulations using empirical force fields optimized around room temperature [13, 14]. These TSLs for light water have been shown to be accurate around room temperature from various differential neutron scattering experiments and integral benchmark tests in light-water moderated systems. On the other hand, through the comparison with the resent neutron scattering experiments, it is pointed out that evaluated values deviating from experimental ones are stored at high-temperature and high-pressure conditions, which are most important from the viewpoint of reactor applications [15].

To overcome this challenge, we are aiming at a new evaluation of the TSL for light water at high temperatures and pressures by molecular dynamics simulations based on first-principles calculations, which do not use empirical force fields and are considered to be highly extrapolative to temperature and pressure changes. Apart from this, hydrogen, a major neutron scattering source in light water, is known to have pronounced quantum vibration effects. In order to incorporate this effect, the path integral molecular dynamics method is used for molecular dynamics simulations. The PIMD code [16] is used for this calculation. This method has been shown to reproduce experimental results well even under high-temperature and high-pressure conditions [17] and is expected to be a promising new TSL evaluation method for light water. Moreover, in order to reduce the computation time, the interatomic potentials are not obtained by first-principles calculations at each step of molecular dynamics, but by machine learning potentials that are created in advance to reproduce the results of the first-principles calculations. Attempts to evaluate new TSLs for light water using the above methods have just begun and are ongoing. We plan to publish the results in an appropriate place as soon as they are obtained.

4. Summary and outlook

In this paper, we discussed the current status of the TSL evaluation in the development project of JENDL. In particular, we discussed the evaluation of TSLs, which are closely related to nuclear reactor applications.

As for the TSL evaluation for crystalline material, TSL for graphite and CaH_2, which are used as moderators in innovative reactors, were evaluated based on first-principles calculations. The evaluation results were in good agreement with the new experimental values at J-PARC. Through the above, we have established a method for evaluating the TSL of crystalline materials.

As for the TSL evaluation for high-temperature light water, despite its importance in applications, TSL of light water in high temperature and pressure conditions has not been adequately validated. Under these circumstances, new TSL evaluation is going to be performed using a calculation method with high reliability to temperature and pressure changes.

Acknowledgements

This work includes the result of the “Development of Nuclear Data Evaluation Framework for Innovative Reactor” founded by the Ministry of Education, Culture, Sports, Science and Technology of Japan and JSPS KAKENHI Grant Number JP24K01408. A part of this work was conducted with the supercomputer HPE SGI8600 in Japan Atomic Energy Agency.

References

[1] O. Iwamoto, N. Iwamoto, S. Kunieda et al., Japanese evaluated nuclear data library version 5: JENDL-5, *J. Nucl. Sci. Technol.* 60, pp. 1-60, (2023).

[2] D.A. Brown, M.B. Chadwick, R. Capote et al., ENDF/B-VIII.0: The 8th Major Release of the Nuclear Reaction Data Library with CIELO-project Cross Sections, New Standards and Thermal Scattering Data, *Nucl. Data Sheets* 148, pp. 1-142, (2018).

[3] S. Nakayama, O. Iwamoto, and A. Kimura, Evaluation of thermal neutron scattering law of nuclear-grade isotropic graphite, *EPJ Web of Conf.* 294, 07001, (2024).

[4] A. Kimura, S. Endo, and S. Nakamura, Total and Double Differential Scattering Cross-Section Measurements of Isotropic Graphite, *EPJ Web of Conf.* 294, 01002, (2024).

[5] I. Al-Qasir, Y. Cheng, J. Lin et al., Neutron thermalization in nuclear graphite: A modern story of a classic moderator, *Ann. Nucl. Energy* 161, 108437, (2021).

[6] P. Giannozzi, O. Baseggio, P. Bonfa et al., Quantum ESPRESSO toward the exascale, *J. Chem. Phys.* 152, 154105, (2020).

[7] A. Togo and I. Tanaka, First principles phonon calculations in materials science, *Scr. Mater.* 108, pp. 1-5, (2015).

[8] Winmostar V10, X-Ability Co. Ltd., Tokyo, Japan, (2022).

[9] R.E. MacFarlane and A.C. Kahler, Methods for processing ENDF/B-VII with NJOY, *Nucl. Data Sheets* 111, pp. 2739-2890, (2010).

[10] A.J.M. Plompen, O. Cabellos, C. De Saint Jean et al., The joint evaluated fission and fusion nuclear data library, JEFF-3.3, *Eur. Phys. J. A* 56, 181, (2020).

[11] A. Kimura, G. Rovira, S. Nakayama et al., Differential Cross-Section Measurements for Thermal Neutron Scattering Law at J-PARC, presented at this conference, (2024).

[12] R. Kimura, Importance and issues of CaH_2 TLS data for reactivity coefficient and core characteristics of MoveluX^{TM}, presented at this conference, (2024).

[13] Y. Abe, T. Tsuboi, and S. Tasaki, Evaluation of the neutron scattering cross-section for light water by molecular dynamics, *Nucl. Instrum. Methods. Phys. Res. A.* 735 pp. 568-573, (2014).

[14] J.I. Marquez Damian, J.R. Granada, and D.C. Malaspina, CAB models for water: A new evaluation of the thermal neutron scattering laws for light and heavy water in ENDF-6 format, *Ann. Nucl. Energy* 65, pp. 280-289, (2014).

[15] V. Jaiswal, Theoretical and experimental approach towards generation of thermal scattering law for light water, Ph.D. thesis, University of Lille, Lille, (2018).

[16] M. Shiga, M. Tachikawa, and S. Miura, A unified scheme for ab initio molecular orbital theory and path integral molecular dynamics, *J. Chem. Phys.* 115, pp, 9149-9159, (2001).

[17] B. Thomsen and M. Shiga, Ab initio study of nuclear quantum effects on sub- and supercritical water, *J. Chem. Phys.* 155, 194107, (2021).

5. Remarks on Activation Analyses for Decommissioning

Chikara KONNO*
Nuclear Science and Engineering Center, Japan Atomic Energy Agency
2-4 Shirakata, Tokai-mura, Naka-gun, Ibaraki-ken 319-1195, Japan
*Email: konno.chikara@jaea.go.jp

Activation analyses are essential in planning and execution of reactor decommissioning. This presentation points out problems in activation analyses. The ORIGEN2 and ORIGEN-S codes are often used in Japan but they have several limitations. The ORIGEN code, which is bundled in the US nuclear safety analysis code system SCALE6.2 or later, has less limitations and is easier to use than ORIGEN2 and ORIGEN-S. However the bundled ORIGEN libraries are not always consistent. To disseminate JENDL-5, I produced JENDL-5 libraries for ORIGEN adequately. I also introduce remarks on calculations with the two-dimensional Sn code DORT which is often used to calculate neutron spectra for activation calculations.

1. Introduction

I started activation analyses for decommissioning in 2017, when I was involved to a collaboration program on activation analyses for decommissioning. The collaboration program completed in 2019, but I continued the study on activation analyses for decommissioning with the relevant departments in JAEA. In this tutorial, I introduce remarks which I found in the study on activation analyses. It is my pleasure if this tutorial helps researchers and engineers related to activation analyses.

2. Activation analysis for decommissioning and its issue

Activation analyses are essential in planning and execution of reactor decommissioning. Radioactive inventories are calculated with neutron spectra (or neutron flux intensities) at evaluation points,

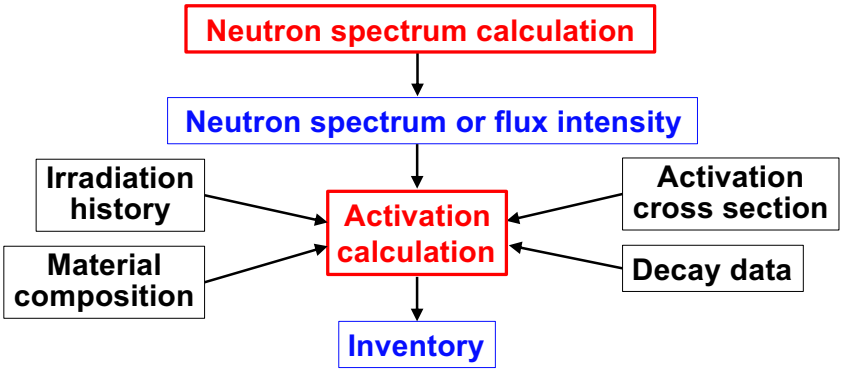

Fig. 1 Activation analysis flow.

irradiation history, material compositions, activation cross section data and decay data as shown in Figure 1.

It is required in decommissioning of Japan to calculate inventories of 274 nuclei (e.g. ^{123}Te [Half-life : 6 × 10^{14} years] and ^{178m2}Hf [Half-life : 31 years]) specified in Nuclear Regulation Authority Ordinance No. 16 of 2020 “Ordinance on confirmation, etc. that the radioactivity concentration of radioactive materials contained in materials and other items used in factories, etc. does not require measures to prevent damage from radiation” [1], which is called “the new clearance regulation” later. The ORIGEN2 [2], ORIGEN-S [3] and ORIGEN [4] codes have been used for activation calculations, but it is noted that they cannot always calculate inventories of all the 276 nuclei in the new clearance regulation.

3. ORIGEN code and ORIGEN library produced from JENDL-5

The ORIGEN2 and ORIGEN-S codes have been often used for activation calculations in Japan, but they have the following defects.

- The number of activation reactions that can be handled is not enough and the activation reaction data are old.
- They use not detailed neutron spectra but neutron flux intensities at evaluation points.

On the contrary, the ORIGEN code uses new cross section data of 12,617 activation reactions for 774 nuclei and detailed neutron spectra (e.g. 200-group neutron spectra) at evaluation points and the calculation time is comparable to that of ORIGEN-S. Input data of ORIGEN are much easier to understand than those of ORIGEN2 and ORIGEN-S. I hope that ORIGEN will be often used in Japan.

The activation cross section, decay and fission yield libraries used in ORIGEN are only from JEFF-3.1 [5], ENDF/B-VII.1 [6] and ENDF/B-VII.1, respectively, and I found that these libraries were not always consistent each other. Then I have produced these libraries for ORIGEN, which are consistent each other, from JENDL-5 [7]. JENDL-5 activation cross section library for ORIGEN produced with the AMPX-6 [8] code were released in 2023 as ActLib-J5 [9, 10]. Figure 2 plots the produced 200-group cross section of the ^{59}Co(n,γ)^{60g}Co reaction of JENDL-5 with that of continuous energy. Recently I also produced JENDL-5 decay and fission yield libraries for ORIGEN with my simple program. In principle, ORIGEN with these libraries can calculate inventories of all the 276 nuclei in the new clearance regulation.

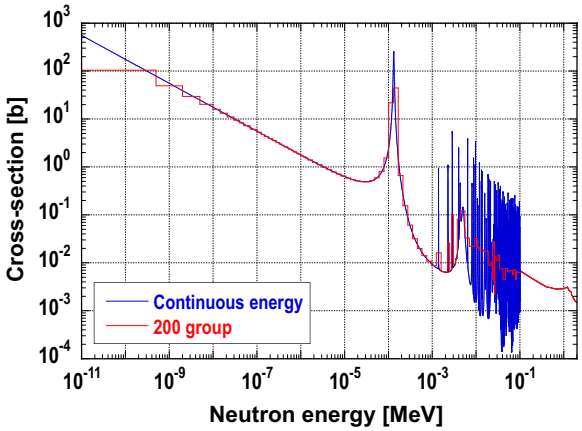

Fig. 2 Cross section of ^{59}Co(n,γ)^{60g}Co.

4. Example of ORIGEN calculation

As the first example of ORIGEN calculations with the JENDL-5 libraries, an activation calculation of bio-shield concrete in JPDR (Japan Power Demonstration Reactor) [9] is introduced here. First, neutron spectra in the concrete were calculated with the two-dimensional Sn code DORT [11] and the multigroup cross section file MATXSLIB-J40 (neutron: 199-group) [12]. Second, ORIGEN calculated inventories

inside the concrete with the calculated neutron spectra, where three library sets in Table 1 were adopted. Note that Case 1 is a set of the bundled libraries in SCALE6.2.4.

Table 1 Library set

	Activation library	Decay library	Fission yield library
Case1	JEFF-3.1	ENDF/B-VII.1	ENDF/B-VII.1
Case2	JENDL-5	ENDF/B-VII.1	ENDF/B-VII.1
Case3	JENDL-5	JENDL-5	JENDL-5

Figure 3 shows Case 3 result with the measured data. The calculated inventory disagrees with the measured one because unknown reinforcing steel bars in the bio-shield concrete were not included in the calculation model. The difference between Case 1 and Case 2 reflects that between activation libraries, which is around 10 % as shown in Fig. 4, and that between Case 2 and Case 3 reflects that between decay and fission yield libraries, which is very small as shown in Fig. 5. The calculation results for the key nuclei such as ^{60}Co are similar among the libraries.

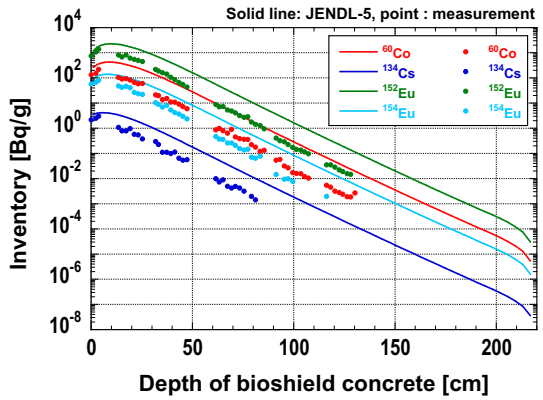

Fig. 3 Inventory distribution in concrete.

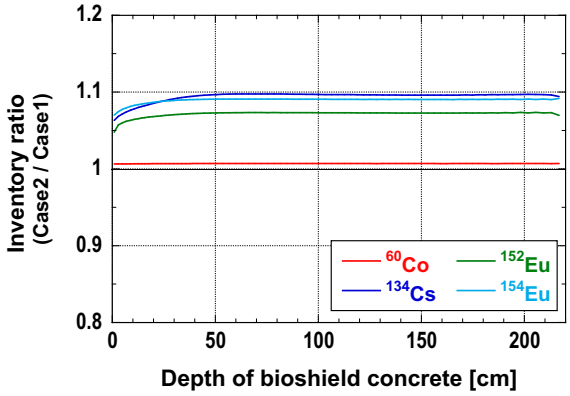

Fig. 4 Inventory ratio of Case 2 to Case 1.

As the second example of ORIGEN calculations with the JENDL-5 libraries, it was examined whether ORIGEN with the JENDL-5 libraries could calculate all the 274 nuclei in the new clearance regulation. The neutron spectrum at the depth of 50 cm in the concrete of JPDR and the library sets (Case 1 and Case 3) in Table 1 were adopted. The inventories were calculated after cooling for one year assuming that there were all natural elements of 0.001 g. Table 2 demonstrates that Case 3 (JENDL-5 library set) can calculate inventories of nuclei which cannot be calculated with Case 1 (the bundled library set). It is confirmed that all the 274 nuclei in the new clearance regulation are calculated except for ^{203}Po and ^{211}At, which seem never to be produced

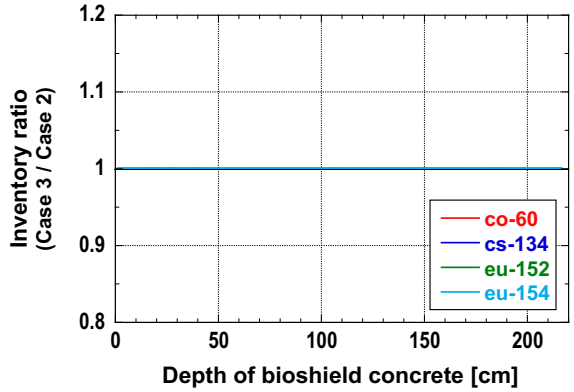

Fig. 5 Inventory ratio of Case 3 to Case 2.

from natural element.

Table 2 Calculated inventories for special nuclei.

Nucleus	Case 1	Case 3
^{178m}Hf	0.0	4.72E-05
^{194m}Ir	0.0	1.05E-01
^{123}Te	(stable nucleus)	1.00E-08

5. Remarks on neutron spectrum calculation with Sn codes

ORIGEN requires detailed neutron spectra at evaluation points. It is no problem if neutron spectra are calculated with Monte Carlo codes, e.g. MCNP [13] and PHITS [14]. However Sn codes, e.g. DORT, are often used to calculate neutron spectra for decommissioning activation calculations. Then if the following items are not considered adequately, calculated neutron spectra change drastically and calculated inventories are also far from correct ones.

- Self-shielding correction in multigroup libraries
- Up-scattering
- Group structure of multigroup libraries

5.1. Self-shielding correction

A lot of nuclei have resonances, and the self-shielding correction is essential in multigroup libraries. The Bondarenko method [15] is often adopted for the self-shielding correction, where the following weighting function should be used.

$$W_\ell = \frac{C(E)}{[\sigma_0+\sigma_t(E)]^{\ell+1}} , \qquad (1)$$

where $C(E)$ is the smooth part, $\sigma_t(E)$ is the total cross section, σ_0 is the background cross section, and ℓ is the Legendre order. However, the weighting function without ℓ is used in many multigroup libraries, which causes insufficient self-shielding correction. It is recommended to use multigroup libraries produced from MATXS files, which use the weighting function of Eq. (1) and the smallest σ_0 of which is below 0.1 b, with the TRANSX [15] code. Figure 6 shows neutron spectra calculated with the one-dimensional Sn code ANISN [11] at 60 cm from the center of an iron sphere of 1 m in diameter with a neutron source of 17.33 – 19.64 MeV, where JENDL-4.0 [16] was used. If the weighting function without ℓ is used, the calculated neutron spectrum is very different from that with the weighting function

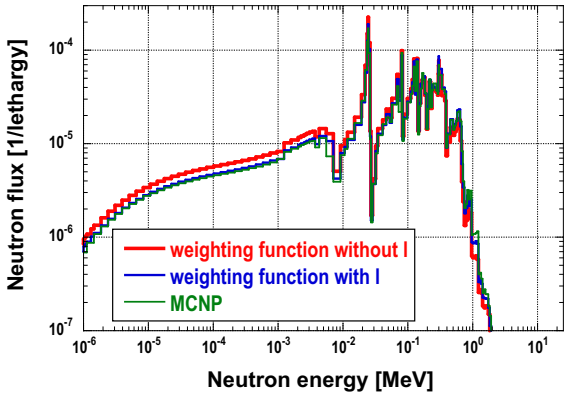

Fig. 6 Calculated neutron spectra at 60 cm from iron sphere center.

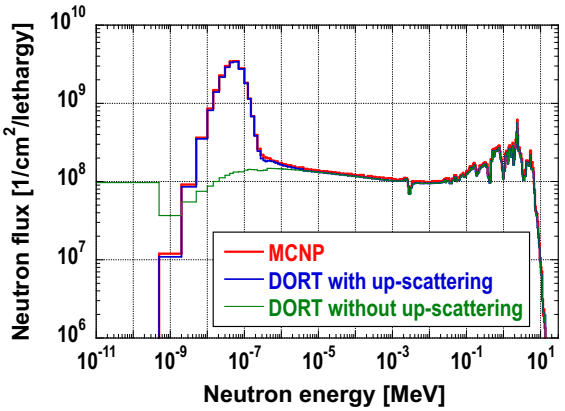

Fig. 7 Calculated neutron spectra at 33.7 cm from concrete front surface in JPDR.

depending on ℓ, which is almost the same as that with MCNP.

5.2. Up-scattering

Up-scattering produces the thermal neutron peak. The thermal neutron peak mainly contributes to inventories of nuclei produced through the capture reaction. To consider up-scattering in Sn calculations, users must use multigroup libraries with enough group number in the thermal energy region and up-scattering data and to perform the outer iteration in Sn calculations. MATXSLIB-J40 is recommended because it has 26 groups below 1 eV and up-scattering data. Figure 7 demonstrates the up-scattering effect, where neutron spectra in the concrete of JPDR described in Sec. 4 were calculated. Note that the calculated neutron spectrum without up-scattering has no thermal peak.

5.3. Group structure

There are various multigroup libraries, but depending on the energy boundary settings of the groups, the self-shielding correction may not be performed sufficiently, and appropriate calculation results may not be obtained. In my experience, the best group is the 199-group of the US multi-group shielding library VITAMIN-B6 or the 200-group (which adds a group of 19.64-20 MeV to the 199-group) adopted in the activation cross section libraries of ORIGEN. ORIGEN bundles activation cross section libraries not only for the 200-group but also for the 56, 44 and 47-groups. Using DORT and ORIGEN calculations for JPDR, it was investigated which group was better. In this calculation I added the 48-group which was used in the previous JPDR calculation [17]. Figure 8 plots the ratio of thermal neutron flux of each group to that of the 200-group and Figure 9 does the ratio of ^{152}Eu inventory of each group to that of the 200-group. Clearly the thermal neutron flux and ^{152}Eu inventory change depending on the group structure. It is considered that the 48-group is better, though it is rougher.

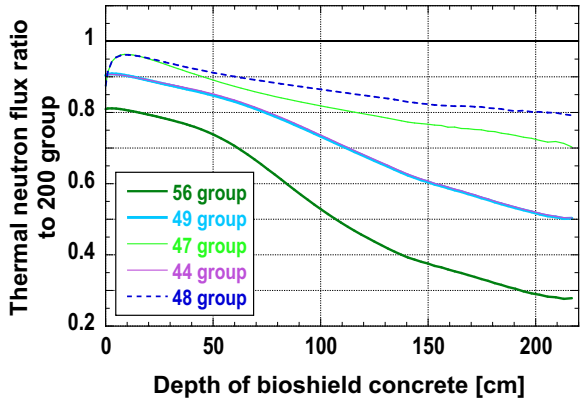

Fig. 8 Thermal neutron flux ratio to 200 group.

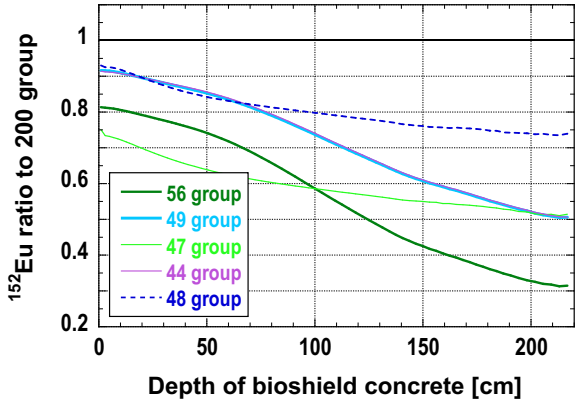

Fig. 9 ^{152}Eu inventory ratio to 200 group.

6. Summary

This tutorial introduces remarks on activation analyses for decommissioning. It is recommended to use the ORIGEN code in SCALE6.2 or later and ORIGEN libraries from JENDL-5, which will be released soon. If neutron spectra used in ORIGEN calculations are calculated with Sn codes, the following items should be considered adequately.

- Self-shielding correction in multigroup libraries
- Up-scattering

- Group structure of multigroup libraries ⇒ the 200-group is recommended and the 48-group is the next.

I hope that my findings help researchers and engineers perform activation analyses.

References

[1] e-gov 法令検索, “工場等において用いた資材その他の物に含まれる放射性物質の放射能濃度が放射線による障害の防止のための措置を必要としないものであることの確認等に関する規則”, https://laws.e-gov.go.jp/law/502M60080000016, (accessed 2025-03-07) [in Japanese].

[2] Croff, A.G., ORIGEN2 - A Revised and Updated Version of the Oak Ridge Isotope Generation and Depletion Code, ORNL-5621, 1980.

[3] ORNL, SCALE: A Modular Code System for Performing Standardized Computer Analyses for Licensing Evaluation, ORNL/TM-2005/39 Version 6, 2009.

[4] (Ed.) Wieselquist, W.A., Lefebvre, R.A., SCALE6.3.1 User Manual, ORNL/TM-SCALE6.3.1, 2023.

[5] Plompen, A.J.M, et al., The joint evaluated fission and fusion nuclear data library, JEFF-3.3, The European Physics J. A, Vol.56, 2020, p. 181.

[6] Chadwick, M.B. et al., ENDF/B-VII.1 Nuclear Data for Science and Technology: Cross Sections, Covariances, Fission Product Yields and Decay Data, Nuclear Data Sheets, vol.112, 2011, pp.2887-2996.

[7] Iwamoto, O., Iwamoto, N., Kunieda, S., et al., Japanese Evaluated Nuclear Data Library version 5 : JENDL-5, J. Nucl. Sci. Technol. vol.60, 2023, pp.1-60.

[8] Wiarda, D., Dunn, M.E., Greene, N.M., Williams, M.L., Celik, C., Petrie, L.M., AMPX-6: A Modular Code System for Processing ENDF/B, ORNL/TM-2016/43, 2016.

[9] Konno, C., Kochiyama, M., Hayashi, H., Generation and verification of ORIGEN and ORIGEN-S activation cross-section libraries of JENDL-5 and JENDL/AD-2017, Mechanical Engineering Journal, Vol.11, 2024, 23-00386.

[10] Japan Atomic Energy Agency, Nuclear Science and Engineering Center, Research Group for Reactor Physics and Thermal Hydraulics Technology, https://rpg.jaea.go.jp/main/en/act-lib, (accessed 2025-07).

[11] ORNL RSICC, DOORS3.2a: One, two- and three-dimensional discrete ordinates neutron/photon transport code system, CODE PACKAGE CCC-650, 2007.

[12] Japan Atomic Energy Agency, Nuclear Science and Engineering Center, Research Group for Reactor Physics and Thermal Hydraulics Technology, https://rpg.jaea.go.jp/main/ja/library_matxslibj40 (accessed 2025-03-07) [in Japanese].

[13] Werner, C.J. (Ed.), MCNP® USER’S MANUAL Code Version 6.2, LA-UR-17-29981, 2017.

[14] Sato, T., et al., Features of Particle and Heavy Ion Transport code System (PHITS) version 3.02, Nucl. Sci. Technol., Vol.55, 2018, pp.684-690.

[15] MacFarlane, R.E., TRANSX 2: a code for interfacing MATXS cross-section libraries to nuclear transport codes, LA-12312-MS, 1993.

[16] Shibata, K., Iwamoto, O., Nakagawa, T., et al. JENDL-4.0: a new library for nuclear science and engineering, J. Nucl. Sci. Technol. 48, 2011, pp. 1-30.

[17] Sukegawa, T., Sasamoto, N., Fujiki, K., Accuracy verification for calculation of inventory in JPDR due to neutron activation, INDC(JPN)-164, 1993.

6. New approach in nuclear data evaluation through Bayesian machine learning

Hiroki IWAMOTO[†1]

[1]Nuclear Science and Engineering Center, Japan Atomic Energy Agency

[†]Email: iwamoto.hiroki@jaea.go.jp

Abstract

Nuclear data are critical for various applications, but their evaluation faces challenges such as resource shortages, lengthy revision cycles, and reliance on specialized expertise. This study proposes a Bayesian machine learning (ML) method using Gaussian process regression to address these issues. While still under development, the method could offer a promising path toward automated, efficient, and timely nuclear data evaluation.

1 Introduction

Nuclear data play an essential role in nuclear and radiation applications. These data are evaluated through a complex process involving experimentation, experimental data collection, theoretical modeling, and validation. Figure 1 presents a schematic representation of nuclear data evaluation, which consists of four components: Experiment, Theory, Evaluation, and Application. However, various challenges within each component pose significant difficulties for the long-term sustainability of the evaluation process.

As a potential solution to this issue, this paper presents an evaluation method for nuclear data utilizing Bayesian machine learning (ML), based on our previous work [1, 2, 3, 4].

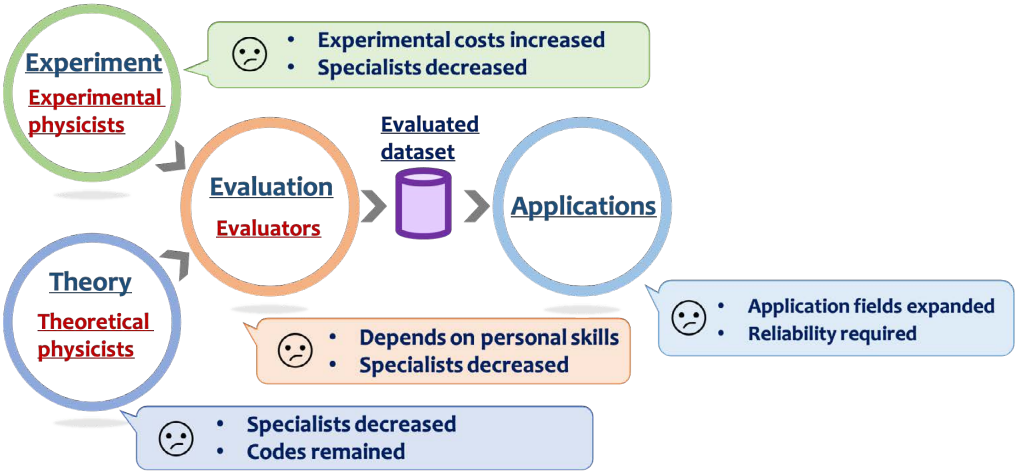

Figure 1: Schematic of typical nuclear data evaluation and its issues.

2 Proposed method

As illustrated in Fig. 1, a fundamental challenge of conventional nuclear data evaluation methods is the shortage of human resources in the respective components. To address this challenge, it is desirable for nuclear data evaluation to be conducted by machines rather than humans, with the evaluation process being systematized and automated as much as possible.

Figure 2 illustrates a schematic of the proposed method for nuclear data evaluation utilizing Bayesian ML. In this evaluation process, Bayesian ML functions as the evaluator. The ML model is trained on experimental data sets and subsequently evaluates the nuclear data of interest. Among the various ML models, Gaussian process regression appears to be the most suitable Bayesian ML model because it can account for experimental uncertainties and does not require large amounts of data. If theoretical information about the nuclear data is available, it can be incorporated into the ML model as prior knowledge. If this process can be successfully applied, nuclear data evaluation can be achieved based on both experimental evidence from measurements and theoretical understanding derived from physics models.

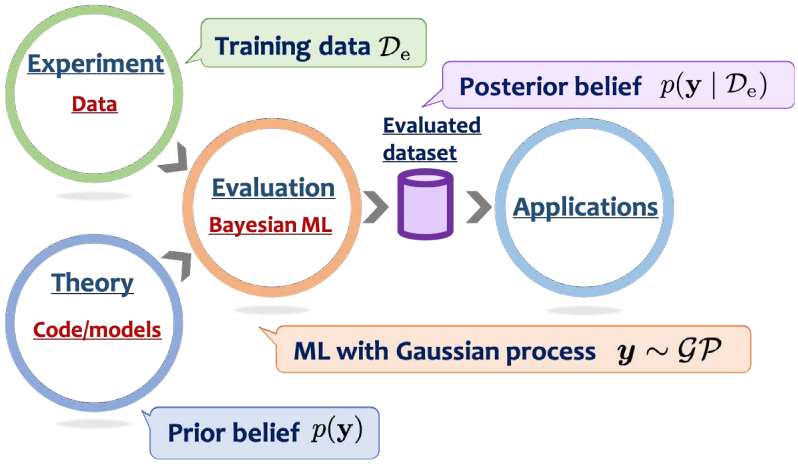

Figure 2: Schematic of proposed nuclear data evaluation.

This evaluation process was effectively applied to proton-induced nuclide production cross sections in Ref. [3]. In the previous study, the ML model was trained using experimental data obtained from the experimental nuclear reaction database EXFOR [5]. To demonstrate that the cross sections can be evaluated (or estimated) without relying on a theoretical physics model, the evaluation was conducted without incorporating any prior knowledge. As detailed in Ref [3], the proposed ML method enabled the evaluation of ^{3}H ($T_{1/2} = 12.32$ y) and ^{7}Be ($T_{1/2} = 53.22$ d) production cross sections over a wide incident energy range, spanning from MeV to GeV for target nuclei with $Z = 6$ to $Z = 83$, using limited experimental data.

The proposed evaluation method was successfully applied to the evaluation of the total nuclear capture rate of a negative muon, as detailed in Ref. [4]. In this work, the Goulard-Primakoff formula [6], which describes the total nuclear capture rate theoretically, was provided to the ML model as prior knowledge, and literature values were used to train the model for a comprehensive evaluation of the total nuclear capture rate. The developed ML model was shown to outperform theoretical physics models in both accuracy and comprehensiveness. The data evaluated using the proposed method will be published as part of 'muon nuclear data [7]'.

Another challenge in nuclear data evaluation is the prolonged time required to revise evaluated nuclear data during which evaluation expertise and skills may be lost before the next

edition is released. Moreover, it often takes several years for new experimental results obtained after an evaluation to be incorporated into the evaluated nuclear data. This challenge could be addressed by further enhancing the proposed Bayesian ML model. Figure 3 presents a conceptual diagram, where an improved Gaussian process regression model is arranged sequentially in a row, enabling the model to learn data iteratively. This could provide evaluated nuclear data in a more timely manner without the need for specialized skills in nuclear data evaluation.

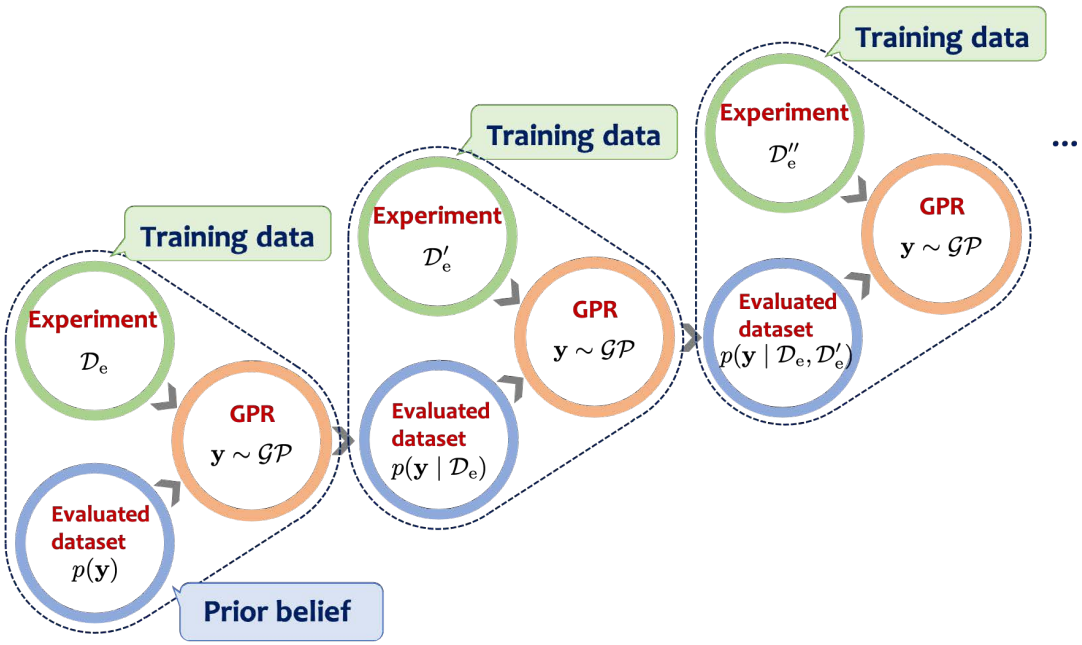

Figure 3: Schematic of iterative evaluation using an improved Gaussian process model.

3 Conclusion

We have introduced a nuclear data evaluation method utilizing Bayesian ML as an approach to address the challenges associated with conventional nuclear data evaluation. While the proposed method is still under development and offers room for improvement and further study, its application is expected to significantly advance nuclear data evaluation methods beyond the limitation of traditional approaches.

References

[1] Iwamoto, H., Generation of nuclear data using Gaussian process regression, J. Nucl. Sci. Technol., vol. 57, no. 8, 2020, pp.932–938.

[2] Iwamoto, H., Iwamoto, O., S, Kunieda, G-HyND: a hybrid nuclear data estimator with Gaussian processes, J. Nucl. Sci. Technol., vol. 59, no. 3, 2022, pp.334–344.

[3] Iwamoto, H., Meigo, S., Sugihara, K., Comprehensive estimation of nuclide production cross sections using a phenomenological approach, Phys. Rev. C, vol. 109, 2024, pp.054610.

[4] Iwamoto, H., Niikura, M., Mizuno, R., Comprehensive Bayesian machine learning approach to estimating the total nuclear capture rate of a negative muon, Phys. Rev. C, (submitted).

[5] Otuka, N., Dupont, E., Semkova, V., Towards a more complete and accurate experimental nuclear reaction data library (EXFOR): International collaboration between Nuclear Reaction Data Centres (NRDC), Nucl. Data. Sheets, vol. 120, 2014, pp.272–276.

[6] Goulard, B., Primakoff, H., Nuclear muon-capture sum and mean nuclear excitation energies, Phys. Rev. C, vol. 10, 1974, p.2034.

[7] Niikura, M., Abe, S., Kawase, S., et al. Muon nuclear data, JAEA-Conf 2014-002, 2024, pp.29–34.

7. Status and plans for critical facility modified STACY

Shouhei ARAKI[1*],Yu ARAKAKI[1], Tomoyuki MAEKAWA[1], Takahiko MURAKAMI[1],
Kenta HASEGAWA[1], Tomoki YOSHIKAWA[1], Yutaka KAMIKAWA[1], Masato SUMIYA[1],
Masakazu SEKI[1], Eiju AIZAWA[1], Junichi ISHII[1], Kazuhiko IZAWA[1], Daiki IWAHASHI[2],
Shigeki SHIBA[2], and Satoshi GUNJI[1]
[1]Japan Atomic Energy Agency
2-4 Shirane, Shirakata, Tokai-mura, Naka-gun, Ibaraki-ken 319-1195, Japan
[2]Nuclear Regulation Authority
1-9-9 Roppongi Minato-ku, Tokyo, Japan
[*]Email: araki.shohei@jaea.go.jp

The Static Experimental Critical Facility (STACY) was renovated from a homogeneous system using solution fuel to a heterogenous system using fuel rods and light water moderator, with the construction completed in December 2023 to contribute to the study of criticality characteristics of fuel debris in the Tokyo Electric Power Company's Fukushima Nuclear Power Plant accident. The modified STACY's core is assembled in the open-top core tank with the fuel rods containing UO_2 pellets and light water. Experimental apparatus can be loaded inside the core within the scope of the license. The first criticality of the modified STACY was achieved on 22nd April 2024. After a series of performance inspections, an experimental campaign for investigation of characteristics of the fuel debris was started in August 2024, and the experiments are currently being conducted in the core consisting only of the fuel rods and light water moderators. The experiments on the core containing the experimental apparatus will be conducted in January 2025.

1. Introduction

The criticality control of the fuel debris generated in the Tokyo Electric Power Company's Fukushima Nuclear Power Plant accident, is one of the key challenges in ensuring the safety of its decommissioning process. The fuel debris was formed through various processes such as molten core interaction, and fuel is mixed with the reactor structural materials such as iron and concrete. To understand the criticality characteristics of the fuel debris, the Japan Atomic Energy Agency (JAEA) has conducted a comprehensive numerical analysis assuming the composition of fuel debris containing iron and concrete [1-3]. However, the validation of these analytical results has not been thoroughly investigated, because integral experiment data including such materials are scarce.

Under the circumstances, the JAEA decided to modify the Static Experiment Critical Facility (STACY) in the Nuclear Fuel Cycle Safety Engineering Research Facility (NUCEF). The original STACY, which was a homogeneous system using solution fuel ($UO_2(NO_3)_2$), played a key role in obtaining the criticality benchmark data for fuel reprocessing plants [4,5] from 1995 to 2011. The original

STACY was converted to the modified STACY, a heterogeneous thermal system, with the modification completed by December 2023. This report provides an overview of the current status of the modified STACY.

2. Modified STACY

The modified STACY was designed as a general-purpose criticality facility for a thermal neutron system. The modification was applied in 2015, and it took about five and a half years from the application to the approval of the modified STACY. The construction work was carried out from 2018 to December 2023.

Figure 1 shows the overview of the modified STACY and a photo of the core tank. The modified STACY comprises a reactor shutdown system, an open-top core tank, and a sample loading system. The reactor shutdown system is located above the core tank and holds cadmium safety plates during operation. The sample loading system, used to insert irradiation samples to the center of the core, is installed below the core tank. The modified STACY's core is assembled in the open-top core tank.

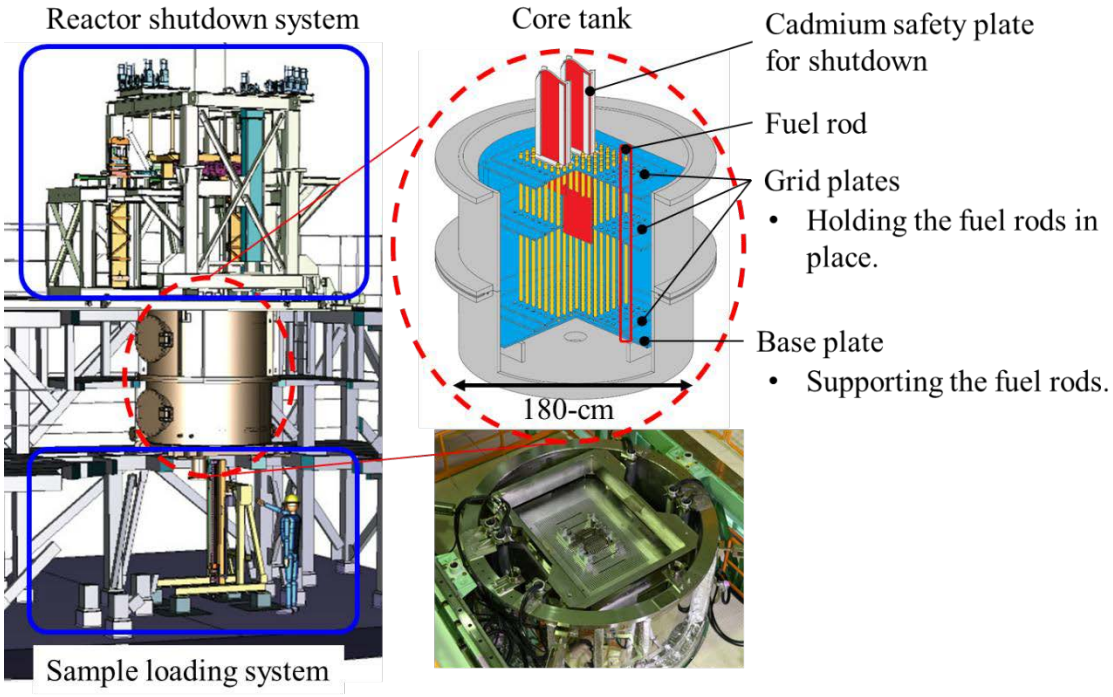

Figure 1. Overview of the modified STACY and photograph of its core tank.

A base plate and three grid plates are installed in the core tank to load fuel rods or experimental apparatus. Guide pins made of zirconium alloy were also loaded in the gride plates to insert the safety plates. Two types of grid plates with 1.27-cm and 1.50-cm lattice intervals are currently available. Each fuel rod consisted of a zirconium alloy clad tube (9.5-mm outer diameter) and UO2 pellets (8.2-mm diameter) with 5wt.% ^{235}U enrichment. The length of each fuel rod was approximately 1500-mm. The diameter and length of the guide pin were 10.8-mm and approximately 1540-mm, respectively. Additionally, sample materials to simulate the fuel debris compositions can be loaded in the core tank by using debris simulant devices. A schematic diagram of the devices under preparation is shown in Figure 2. These devices are almost the same size as the fuel rods and can be loaded on the grid plates like the fuel

rods. The concrete rod consists of pseudo-concrete pellets and an aluminum alloy tube. The iron rod is made of stainless steel. The refillable rod is a zirconium alloy clad tube, and the outer diameter of the encapsulated sample is less than 7.5-mm and the linear density is less than 263 g/m.

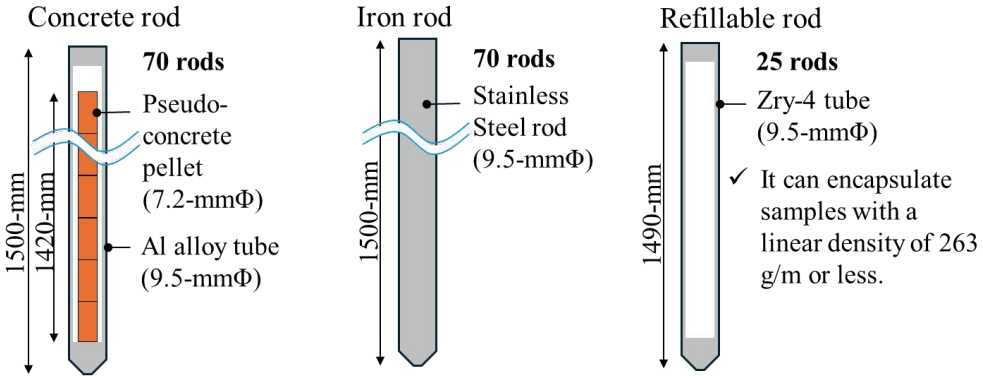

Figure 2. Schematic diagram of debris simulant devices.

The license restricted the operation conditions of the modified STACY. Significant restrictions are shown in Table 1. The maximum thermal power is only 200-W, thus fuel burn-up is negligible and cooling water is unnecessary. Although the use of 900 fuel rods with an enrichment of up to 10wt.% is permitted, current experiments use 400 fuel rods with an enrichment of 5wt.%. The reactivity is controlled by adjusting the water level in the core tank by feed and drain, and no control rods are used to adjust criticality.

Table 1. Specifications of the modified STACY core

Item	Limitation
Thermal power	≤ 200-W
Critical water level	40-cm – 140-cm
Number of fuel rods	≤ 400 (900)
Enrichment of ^{235}U	≤ 10 wt.%
Volume ratio of moderator to fuel	0.9 – 11
Excess reactivity	≤ 0.8$
Excess reactivity (normal operation)	≤ 0.3$
Reactivity addition rate	≤ 3 cents/s
Shutdown margin	≤ 0.985 (keff)
One-rod stuck margin	≤ 0.995 (keff)

The experiments of several types of neutron fields will be conducted using the two grid plate types. Figure 3 shows the neutron spectra calculated by MVP code [6] with JENDL-4.0 [7] in the core of the modified STACY. By increasing the lattice intervals of the fuel rods, neutrons can be moderated to form a softer neutron spectrum.

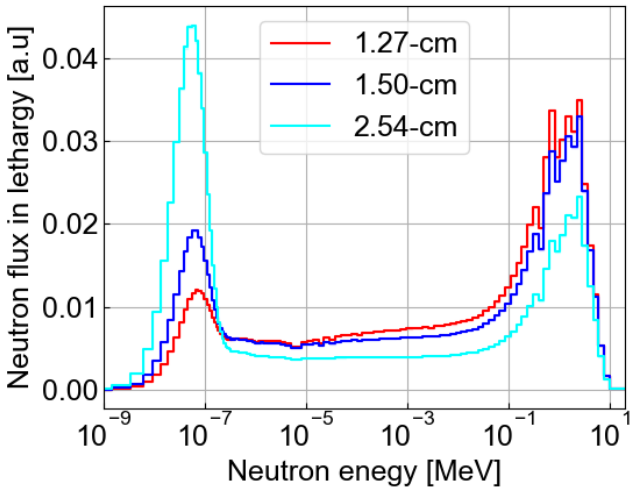

Figure 3. Neutron spectra in the core of the modified STACY.

3. Status of Experiments

3.1. Inspection cores

Performance inspections have been conducted to confirm that the core has become critical using each of the two grid plates and satisfied the licensing requirements since April 2024. The loading patterns of the inspections are shown in Figure 4. It was confirmed that each of these four cores became the critical and satisfied the limitations shown in Table 1. The results of the analysis using these experimental results are described in Yoshikawa et al [8].

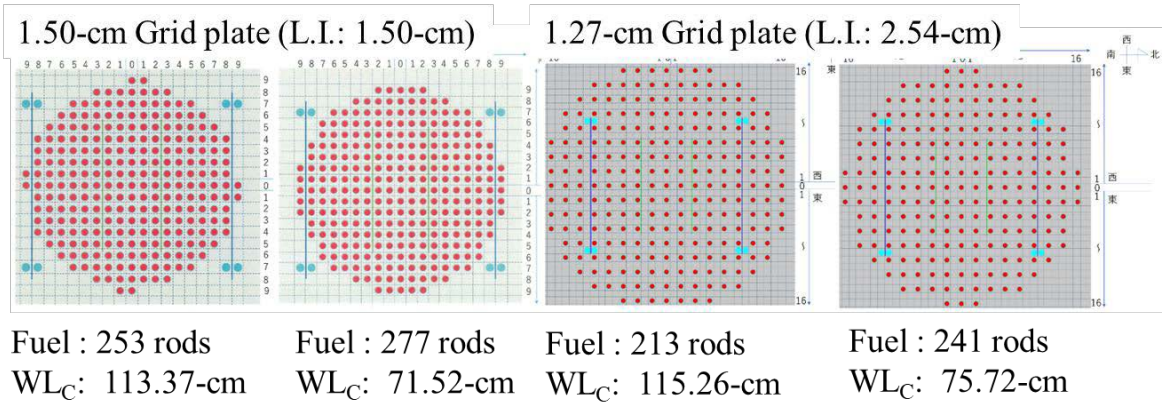

Figure 4. The loading patterns of the inspection core. Red and blue circles represent fuel rods and guide pins, respectively.

3.2. Experimental core

Various experiments are being planned [9] at the modified STACY, an example of which is shown here. The experiments commenced in August 2024 after the performance inspections. The first experimental campaign aimed to investigate the core characteristics of the modified STACY. Examples of experimental cores are shown in Figure 5. The core consisted of light water and the fuel rods arranged in a rectangular pattern. Experiments were conducted in each lattice plate with different core configurations at different critical water levels. Water level reactivity coefficients and basic criticality

data were obtained and will be used to analyze later experimental results.

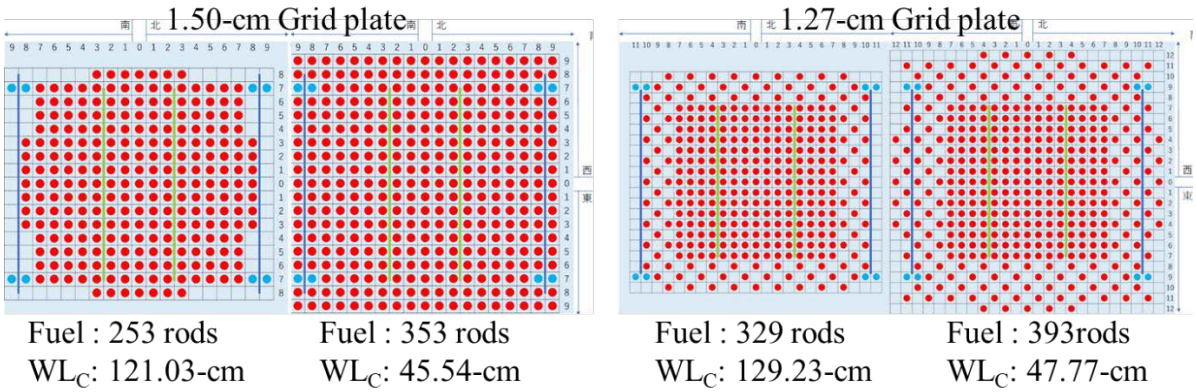

Figure 5. The loading patterns of the first experimental campaign. Red and blue circles represent fuel rods and guide pins, respectively.

The experimental cores for reactivity worth measurement are shown in Figure 6. The core consists of the fuel rods, light water, and debris simulant devices. The reactivity worth of the sample materials such as concrete simulant or stainless steel will be obtained.

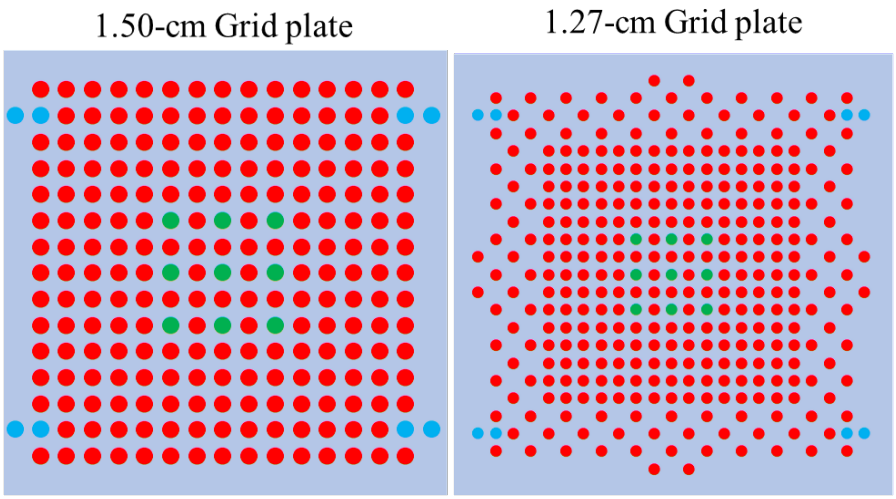

Figure 6. The loading patterns of the worth measurement experiments. Red , blue, and green circles represent the fuel rods and the guide pins and the debris simulant devices, respectively.

4. Summary

The JAEA modified the STACY to obtain integral experimental data for the critical control of fuel debris at the Fukushima Daiichi Nuclear Power Plant. The modification of the STACY was completed in December 2023. In the modified STACY, several neutron energy fields can be generated by changing the lattice intervals of fuel rods, and sample materials can be inserted into the core using the debris simulant devices. Inspection operations were initiated in April 2024. The experiments commenced in August 2024, acquiring fundamental data regarding the core configuration, which consists of fuel rods and light water. Beginning in February 2025, additional experimental data will be obtained by using the debris simulant devices in the core.

References

[1] Izawa, K. et al., Infinite multiplication factor of low-enriched UO_2–concrete system: Fukushima NPP Accident Related. *Journal of Nuclear Science and Technology, 49(11), 2012, pp.1043–1047*. https://doi.org/10.1080/00223131.2012.730893

[2] Tonoike, et al., Progress of criticality control study on fuel debris by Japan Atomic Energy Agency to support Secretariat of Nuclear Regulation Authority. *In Proceedings of the International Conference on Nuclear Criticality Safety (ICNC2019)(p.9). Paris, France.*

[3] Watanabe, T. et al., Criticality characteristics of fuel debris mixed by fuels with different burnups based on fuel loading pattern. *In Proceedings of the International Conference on Nuclear Criticality Safety (ICNC2019) (p.8). Paris, France*.

[4] Tonoike K. et al., "Kinetic Parameter βeff/ℓ Measurement on Low Enriched Uranyl Nitrate Solution with Single Unit Cores (600ℓ, 280T, 800ℓ) of STACY," *Journal of Nuclear Science and Technology*, 39:11, 2002, pp. 1227-1236.

[5] Miyoshi Y. et al., "Critical experiments on STACY homogeneous core containing 10% enriched uranyl nitrate solution," *Proceedings of International Conference on Nuclear Criticality Safety (ICNC2003)*, 2003, pp. 154-159.

[6] Nagaya, Y. et al., MVP/GMVP Version 3: General purpose Monte Carlo codes for neutron and photon transport calculations based on continuous energy and multigroup methods. JAEA-Data/Code 2016-018, 2017, 421p.

[7] Shibata, K. et al., (2011). *JENDL-4.0: A new library for nuclear science and engineering*. *Journal of Nuclear Science and Technology*, 48(1).

[8] Yoshikawa, T. et. al., Criticality data of the modified STACY and evaluation results of nuclear data libraries., Proceedings of Symposium on Nuclear Data 2024 (P-11), Kumatori, 2024.

[9] Gunji, S. et al., Study of experimental core configuration of the modified STACY for measurement of criticality characteristics of fuel debris. *Progress in Nuclear Energy, 101*(C), 2017, pp.321-328. https://doi.org/10.1016/j.pnucene.2017.03.002

Acknowledgments

This report includes results of the contract work funded by the Nuclear Regulation Authority (NRA)/ the Secretariat of NRA of Japan. I would like to express my sincere gratitude to Dr. Suyama for his constructive feedback, which greatly enhanced the quality of this paper.

8. Development of a neutron resonance analysis technique for nondestructive fissile material assay and nuclear data

Jaehong LEE[1*], Fabiana ROSSI[1], Kota Hironaka[1], Mitsuo KOIZUMI[1] and Tomooki SHIBA[1]
[1] Integrated Support Center for Nuclear Nonproliferation and Nuclear Security,
Japan Atomic Energy Agency
2-4 Shirane, Shirakata, Tokai-mura, Naka-gun, Ibaraki-ken 319-1195, Japan
[*]Email: lee.jaehong@jaea.go.jp

The Japan Atomic Energy Agency (JAEA) has been developing various non-destructive assay (NDA) techniques to verify nuclear materials. However, one major challenge in NDA is measuring highly radioactive materials. To address this, neutron resonance analysis (NRA) has been proposed as a promising active neutron NDA technique. NRA combines neutron resonance transmission analysis (NRTA) with neutron resonance capture analysis (NRCA) and the newly introduced neutron resonance fission neutron analysis (NRFNA). In an NRA system, a pulsed neutron beam, in conjunction with the neutron time-of-flight (TOF) method, is used to measure transmitted neutrons, capture gamma-rays, and fission neutrons from a fissile material sample. The system employs a GS20 glass scintillator for detecting transmitted neutrons, while a pulse shape discrimination (PSD) plastic scintillator is used to detect and discriminate between capture gamma-rays and fission neutrons. The positions and depths of resonance peaks or dips in the TOF spectra are determined by the neutron cross sections of nuclides and their amount in the sample. Therefore, to accurately identify and quantify fissile materials based on these spectra, the use of the evaluated nuclear data library is essential. This paper will provide a detailed overview of the NRA project and discuss the critical role of accurate nuclear data in its success.

1. Introduction

Passive neutron and gamma-ray detections of nuclear materials are widely used for nuclear safeguards and security. However, using these techniques to measure high-radioactive nuclear materials or shielded nuclear materials is particularly challenging. To overcome these difficulties, the Integrated Support Center for Nuclear Nonproliferation and Nuclear Security (ISCN) of the Japan Atomic Energy Agency (JAEA) is developing neutron resonance analysis (NRA) as an active neutron non-destructive assay (NDA) technique [1].

NRA combines three active neutron NDA techniques: neutron resonance transmission analysis (NRTA) [2, 3], neutron resonance capture analysis (NRCA) [3, 4], and the newly introduced neutron resonance fission neutron analysis (NRFNA) [5]. In the proposed NRA, resonance dips or peaks are observed using the neutron time-of-flight (TOF) method at pulsed neutron facilities. The positions and heights of these are determined by the nuclides and their amounts, allowing us to identify and quantify

nuclear materials in a fissile material sample by analyzing the TOF spectra. NRTA, NRCA, and NRFNA utilize resonances in neutron total, capture, and fission cross sections. By leveraging different neutron reaction cross sections, these methods provide various types of information about the nuclides in the sample, enhancing the analytical capabilities for nuclear materials.

In an NRA measurement system, EJ-276D plastic scintillators [6] served as neutron/gamma pulse shape discrimination (PSD) detectors to distinguish between capture gamma-rays and fission neutrons emitted from the sample. Additionally, a GS20 glass scintillator [7] was used to detect the transmitted thermal and epithermal neutrons through the sample.

In the present study, we conducted an NRFNA experiment using natural uranium (^{nat}U) samples at the Kyoto University, Institute for Integrated Radiation and Nuclear Science - Linear Accelerator (KURNS-LINAC) [8] to evaluate the system's ability to identify and quantify fissile nuclear material. Based on the experimental data, we assessed and discussed the performance of the NRFNA system.

2. Experiment and analysis

The NRFNA experiment was performed using a 12-meter neutron flight path at the KURNS-LINAC with the TOF method. The KURNS-LINAC operated with a pulse width of 2 μsec, a repetition rate of 50 Hz, an average current of about 42 μA, and an acceleration energy of about 30 MeV. Accelerated electrons bombarded a water-cooled Tantalum (Ta) target [9], generating fast neutrons through the Ta(γ, xn) reaction. The fast neutrons were moderated in a water tank (20 cm in diameter and 30 cm in height) to produce thermal and epithermal neutrons. The moderated neutrons were collimated into a 3 × 3 cm beam using lead (Pb) and 20% boron-loaded polyethylene (B-Poly) bricks. The collimated pulse neutron beam was directed at the ^{nat}U sample, causing prompt fission neutrons to be emitted from the sample via the ^{235}U(n, f) reaction.

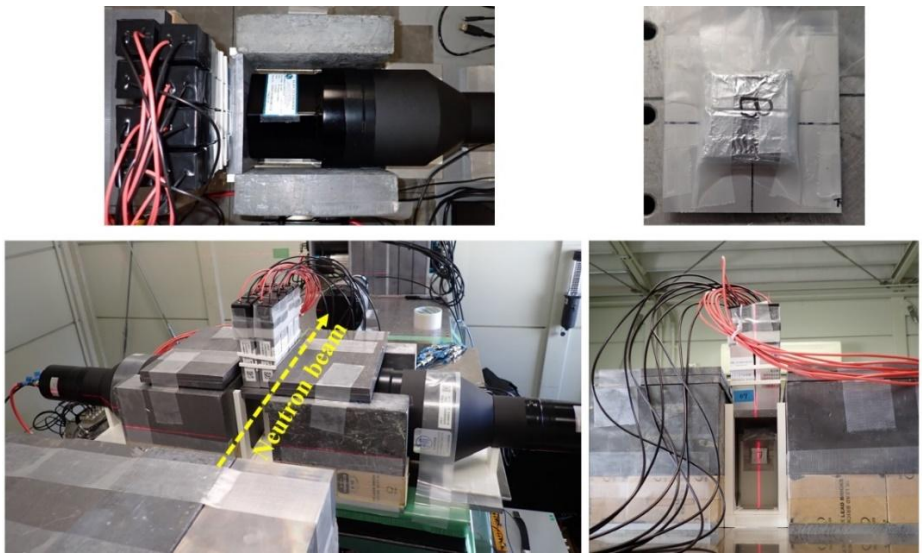

Figure 1. Experimental setup in a 12-meter measurement room.

Figure 1 shows the experimental setup in a 12-meter measurement room. In this experiment, three ^{nat}U samples (2 × 2 cm in size) with different thicknesses (1 sheet: 0.15 cm, 2 sheets: 0.3 cm, 4 sheets: 0.6 cm) were assembled and wrapped in aluminum foil. To detect the fission neutrons emitted from the sample, a detector assembly consisting of two hexagonal EJ-276D scintillators (6.4 cm per side, 10 cm

thick) and eight square EJ-276DH scintillators (2.5 × 2.5 × 10 cm) was used. The scintillators were shielded with 1–5-thick lead to suppress the gamma-ray background radiation.

Data from the detectors were sent to a CAEN V1730D digitizer [10] (14 bit, 500 MSample/s, 16 ch) and recorded on personal computer's hard disk for off-line analysis. The recorded data included Q_S, Q_L, and t, where Q_S and Q_L are the charges measured within short and long gate, respectively, and t represents the neutron TOF. In this experiment, the short gate and long gates for all detectors were set to 40 ns and 500 ns, respectively. To discriminate between gamma-ray and neutron signals, the PSD parameter was calculated as [11]:

$$\mathrm{PSD} = \frac{Q_L - Q_S}{Q_L} \tag{1}$$

Figure 2 shows the two-dimensional scatter plot of the PSD versus Q_L for one of the EJ-275D scintillator. As seen in **Figure 2**, two distinct peaks were observed using the PSD technique: one for gamma-ray events, centered at ~0.22, and another for neutron events, centered at ~0.36. In this study, Gate 1 and Gate 2 were defined for gamma-ray and neutron events, and were used to obtain the neutron TOF spectra of ^{nat}U for both gamma-rays and fission neutrons. Using the TOF method, the incident neutron energy was calculated with the following equation [2]:

$$E_n = \left(\frac{72.3 \times L}{t}\right)^2 \tag{2}$$

where, E_n is the incident neutron energy and L is the neutron flight path length.

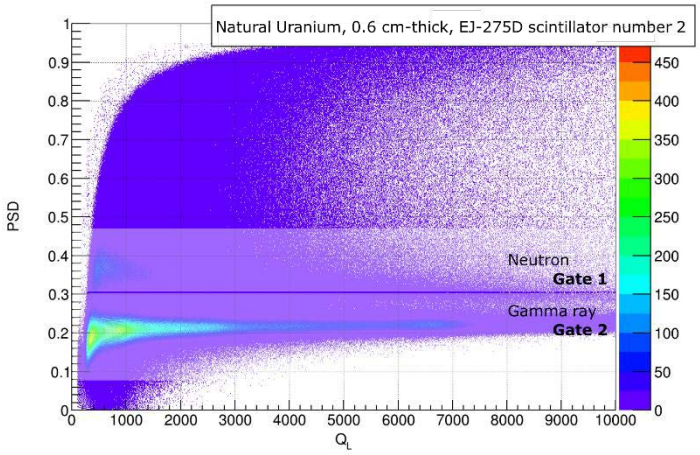

Figure 2. PSD vs Q_L spectrum as obtained by one of the hexagonal EJ-275D scintillator.

3. Results and discussion

Figure 3(a) shows the neutron energy spectra of the three ^{nat}U samples at Gate 2 for neutron events within the incident neutron energy range of 0.01 to 100 eV. Numerous resonance peaks were observed in the energy range from 1 to 40 eV. These resonance peaks were compared with the evaluated nuclear reaction data library for ^{235}U. The resonance energies and shapes obtained in this study showed good agreement with the evaluated ^{235}U(n, f) cross section data. From these results, we confirmed that it is possible to identify fissile material in the sample using the NRFNA technique, combined with the evaluated (n, f) cross section data library, can be used to identify fissile material in a sample. Additionally, we observed that increasing the sample thickness (or material quantity) resulted in a proportional increase in the counting rate of the resonance peaks. This demonstrates that the NRFNA technique, when used

with a reference sample of known properties, can also quantify the amount of fissile material in a sample.

To evaluate the background level in the NRFNA system, we measured the 0.6-cm thick ^{nat}U sample with resonance filters, Co, In, Ag, Mn, and Cd, as well as with no sample. **Figure 3(b)** shows the measured neutron energy spectra at Gate 2 for the energy range of 0.005 to 200 eV, along with the neutron energy spectrum of the 0.6-cm thick ^{nat}U sample. From the spectrum measured with no sample, we confirmed that the room background was very low. Additionally, from the spectrum of the 0.6-cm thick ^{nat}U sample with the resonance filters, we determined that the sample-dependent background was below 1% at the resonance peaks. These findings indicate that the NRFNA system, with the use of PSD discrimination, achieves a low background level, ensuring reliable measurements.

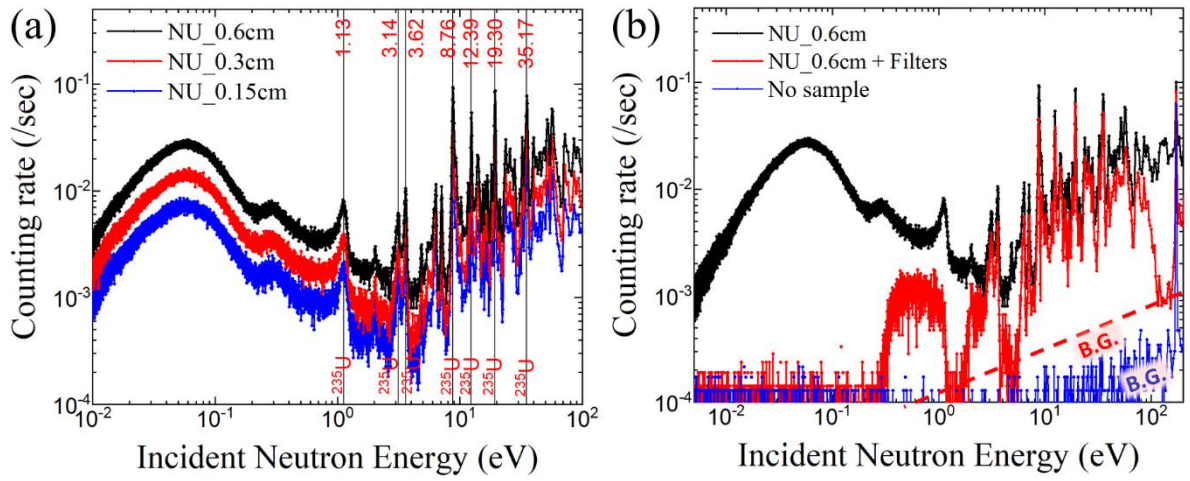

Figure 3. (a) Neutron energy spectra of the ^{nat}U samples with three different thicknesses at Gate 2 for neutron events. (b) Neutron energy spectra for different cases: 6-mm thick ^{nat}U sample, 6-mm thick ^{nat}U sample with resonance filters, and no sample.

4. Summary and future plan

The JAEA/ISCN has been developing a combined NRA system, integrating NRTA, NRCA, and NRFNA, as an active neutron NDA technique. In this study, an NRFNA experiment was conducted using three ^{nat}U samples of different thicknesses. The neutron TOF method was employed at the KURNS-LINAC to assess the system's capability for identifying and quantifying fissile nuclear material.

The experiment successfully observed the resonance peaks of the ^{235}U(n, f) reaction in the neutron energy spectra for the three ^{nat}U samples, each exhibiting different counting rates. These results confirmed that NRFNA is effective for identifying and quantifying fissile nuclear materials in samples. Additionally, background measurements demonstrated that the use of PSD discrimination significantly reduces background levels, enhancing the reliability of NRFNA measurements.

Moving forward, we plan to further enhance the NRA system. Key developments include: designing a detector assembly comprising ten EJ-276D detectors; optimizing PSD parameters (e.g., Q_S and Q_L) for improved signal discrimination; developing a neutron collimator system tailored for NRTA and NRFNA applications; testing a new NRTA detector (EJ-270). In addition, Monte Carlo simulations with evaluated nuclear data libraries will be employed to calculate self-shielding factors for samples, thereby improving the quantification of fissile nuclear material. These advancements aim to strengthen NRA's analytical capabilities and broaden its applications in nuclear material analysis and nuclear data refinement.

References

[1] F. Rossi, J. Lee, Y. Kodama et al., Development of a combined neutron resonance analysis technique as a nondestructive assay for fissile material quantification, In Proceedings of the 2024 IMMM & ESARDA Joint Annual Meeting (Portland, USA, 2024).

[2] P. Schillebeeckx, B. Becker, H. Harada, and S. Kopecky, Neutron Resonance Spectroscopy for the Characterisation of Materials and Objects, JRC Science and Policy Reports, JRC 91818, EUR 26848 EN (2012).

[3] H. Postma and P. Schillebeeckx, Neutron resonance capture and transmission analysis, Encyclopedia of Analytical Chemistry (New York: John Wiley & Sons Ltd.), (2009).

[4] H. Postma, M. Blaauw, P. Bode, P. Mutti, F. Corvi, and P. Siegler, Neutron-resonance capture analysis of materials, J. Radio. Nucl. Chem. 248, (2001), pp. 115–120.

[5] K. Hironaka, J. Lee, M. Koizumi, F. Ito, J. Hori, K. Terada, and T. Sano, Neutron resonance fission neutron analysis for nondestructive fissile material assay, Nucl. Instr. Methods Phys. Res. A. 1054, (2023), 168467.

[6] P. Pant, K. Banerjee, P. Roy, R. Shil, and A.K. Saha, Characterization of EJ-276D plastic scintillator and its comparison with EJ-299-33A and BC-501A, Journal of Instrumentation. 19, (2024), P10036

[7] F. Ito, J. Lee, K. Hironaka, T. Takahashi, S. Suzuki, T. Mochimaru, J. Hori, K. Terada, M. Ko izumi, Li-glass detector to gamma rays by a coincidence method, Nucl. Instr. Methods Phys. Res. A. 1064, (2024), 169465.

[8] J. Hori, Nuclear Data Measurement at KURRI-LINAC. International Atomic Energy Agency. Report No. IAEA-TECDOC-1743, 2014, pp. 286–294.

[9] T. Sano, J. Hori, Y. Takahashi, H. Yashima, J. Lee, H. Harada, Analysis of energy resolution in the KURRI-LINAC pulsed neutron facility. EPJ Web Conf. 146, (2016), 03031.

[10] CAEN, V1730 / V1730S, Available from: https://www.caen.it/products/v1730/, (accessed 2025-03-07).

[11] CAEN, User Manual UM5960 CoMPASS, Available from: https://www.caen.it/?downloadfile=11299, (accessed 2025-03-07).

Acknowledgements

The authors would like to thank the LINAC staff of the Institute for Integrated Radiation and Nuclear Science, Kyoto University, for their support in the continuous operation of the accelerator. This research was implemented under a subsidy for “promotion of strengthening nuclear security and the like” of the Ministry of Education, Culture, Sports, Science, and Technology, Japan.

9. Gamma Ray Spectroscopy for Event Out of Phase of Pulsed Neutron Source for Short Lived Fission Product

Yasushi NAUCHI[1*], Jun-ichi HORI[1] Kazushi TERADA[2] and Tadafumi SANO[3]
[1]Energy Transformation Research Laboratory, Central Research Institute of Electric Power Industry
2-6-1 Nagasaka, Yokosuka-shi, Kanagawai-ken 240-0101, Japan
[2]Institute for Integrated Radiation and Nuclear Science, Kyoto University
2 Asashiro-Nishi, Kumatori-cho, Sen-nan-gun, Osaka-fu 590-0494, Japan
[3]Atomic Energy Research Institute, Kindai University
3-4-1 Kowakae, Higashi-Osaka-shi, Osaka-fu 577-0818, Japan

[*]Email: nauchi@criepi.denken.or.jp

γ rays from short lived fission products (FPs) are measured for ^{235}U using pulsed neutron source in the KURNS-LINAC facility. For that, out of phase event spectroscopy (OOPS) have been developed, where γ rays are measured in time region after thermal neutrons decay away. Discrete energy γ rays are measured with larger peak to noise ratio. FPs with half-lives from 0.5 s to 3.0 h are identified based on the peak energies.

1. Introduction

In the primary containment vessel (PCV) of units 1, 2, and 3 of Fukushima Dai-ichi nuclear power station, fuel debris has been formed and accumulated. In 2024, trial removal of the fuel debris had successfully completed from the PCV of unit 2 [1] and uranium was detected in the retrieved fuel debris by destructive measurement [2]. TECO plans to continue such trial retrieval and examination for a while to establish a safer and more efficient scheme of the retrieval. After the establishment, the scale of the retrieval will be enhanced. The retrieved fuel debris will be stored in a facility intermediately [3].

We must take care to prevent criticality accidents in the storage facility for fuel debris. The reactivity of fuel debris is mainly determined by its isotopic composition. When we pick up a chunk of fuel debris, the isotopic and atomic composition of it varies so much since pellets of several kinds of initial ^{235}U enrichment with different irradiation conditions had been mixed heterogeneously and non-uniformly with non-actinide materials. In traditional criticality management scheme, we should assume conservative isotopic composition for such fuel debris to prevent criticality accidents. By taking such assumption, we have to construct a facility with larger scale. To mitigate the situation, the isotopic composition should be estimated based on non-destructive measurements.

Nauchi et al. have claimed reaction rate ratio of radiative capture to fission can be estimated by neutron induced gamma ray spectroscopy (NIGS) [4]. The ratios are useful to certify negative reactivity brought by the capture reaction of non-nuclear material and burn-up depletion of fissile [5, 6]. In NIGS, the fission rate is estimated by count rate of fission prompt γ ray. However, the γ ray emission spectra of fissions of $^{235, 238}$U and $^{239, 241}$Pu are similar and the ratio of γ ray to neutron emission varies with fissile [7]. Thus, some techniques to determine ratio of fission of them are desirable. The delayed gamma ray assay (DGA) is preferable for the purpose since the fission product (FP) yield varies with fissile [8]. In the conventional DGA, a fuel sample once irradiated by neutron is transferred to the front of the γ ray spectrometer to avoid neutron radiation of the spectrometer. Due to the time duration for the transferring, γ rays from FPs with half-lives shorter than 10 s are difficult to detect. For that, Nauchi et al. have succeeded in measuring FP rays from nuclear material surrounded by massive polyethylene during neutron irradiation of the material since neutron is well shielded by the polyethylene [5]. On the irradiation condition, γ rays from FPs with half-life shorter than 10 s can be measured. Accordingly, DGA becomes even promising.

The accuracy of DGA relies on that of the fission product yield and decay (FPY&FPD) data. FPY&FPD have been evaluated for years [9,10] To validate such evaluation, discrete energy γ ray measurements in differential manner have been conducted at LINAC neutron source facility in Institute for Integrated Radiation and Nuclear Science, Kyoto University (KURNS) [11, 12]. In this manuscript, the experimental procedures are outlined, and the preliminary results are presented for ^{235}U.

2. Out of Phase Event Spectroscopy

Measurement of the short-lived FP γ rays are generally suffered from background γ rays which consist of fission prompt and radiative capture components. For the evaluation of FPY&FPD data, such background components should be discriminated from the decay component. For that purpose, the time-of-flight technique was applied. In Figure 1, a schematic view of the measurement is presented.

Pulsed electron beam accelerated to 30 MeV in LINAC was periodically injected onto a target of a tantalum target and the Bremsstrahlung rays were emitted. Photo-nuclear reactions were induced by the rays and neutrons were emitted. The neutrons were moderated in the light water tank surrounding the target. The moderated neutrons were introduced to a sample located 11.4 m distant from the target through a neutron collimator. In the sample, triuranium octoxide (U_3O_8) particles are distributed randomly in the matrix of aluminum. Uranium content was 1.102 g and its ^{235}U enrichment of U is 93% so that the ratio of fast neutron induced fission of ^{238}U might be negligibly low. Prompt γ rays form fission and capture reactions in the samples as well as delayed γ rays from decay of FPs and activated materials were measured with a HPGe detector with the relative efficiency of 35% compared to a sodium iodine scintillator of 3 inch in radius and 3 inch in thickness. The detector was well shielded from neutrons by the collimator so that we can measure γ rays from FPs without transferring either the sample or the detector. The induced electric charge in the HPGe detector was integrated to make a pulse signal in the pre-amplifier. The signal was amplified and shaped in the linear amplifier. The pulse height of the amplified signal was acquired together with the time length from the electron injection onto the target to the γ ray detection in the HPGe.

The time-of-flight spectrum measured for the U_3O_8 sample and a boron sample (^{10}B) are shown in Figure 2. From the boron sample, 478 keV γ rays were promptly radiated from the ^{10}B(n, α_1) reaction. The reaction was mainly induced by the thermal neutrons indicated by the time peak around 3 ms (1500

ch) in the figure. The thermal neutron component decays until 16 ms (8000 ch). After the component decays away, there is a time region without neutron. γ ray emissions in this region are considered from radioactive decay of nuclides which are generated by number of pulsed neutrons until the detection of the γ rays. The time region is **O**ut **O**f **P**hase (OOP) of last pulsed neutron. We decided to focus on the OOP time region since the region is free from the prompt component.

For the **O**ut **O**f **P**hase event **S**pectroscopy (OOPS), determination of the beam frequency F is essential. In LINAC, the beam current integrated over a unit time is proportional to F. Using the waiting time d for decay out of the thermal neutron, the measuring time per second is 1 - dF. The counting rate of γ rays, C, in the OOP region is roughly proportional to

$$C(t) \propto F \times F \times \left(\frac{1}{F} - d\right) \quad (1)$$

Considering the eq. (1) and the measured decay time for the ^{10}B sample, we decided F = 30 Hz and d = 20 ms in this work. The decay time measured for the U_3O_8 sample is longer than that for the ^{10}B sample. That is due to the short lived FPds of which half-lives are shorter than several ms.

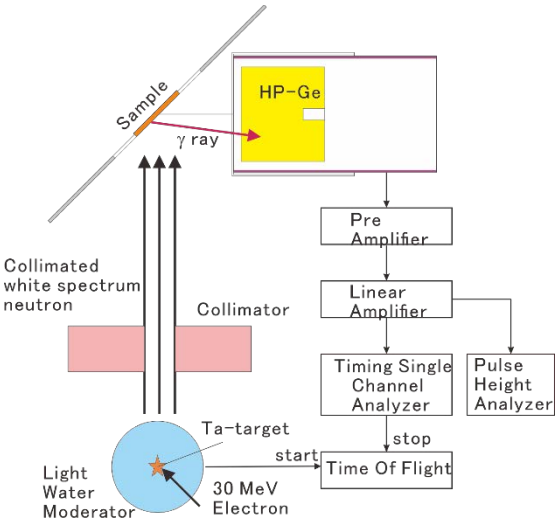

Figure 1. Schematic view of measurement.

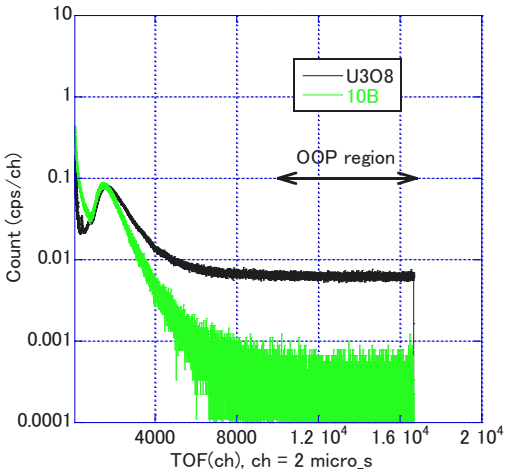

Figure 2. Time of flight spectrum.

γ ray pulse height spectra in the HPGe detrector for the U_3O_8 sample are shown for time regions in Figure 3. The spectra were acquired by measurement for 17 hours with the electron beam current of 62 μA from LINAC. OOP region ranges from 20 to 33 ms. In the time region where thermal neutrons exist, 7724 keV γ rays from ^{27}Al(n, γ) reactions are prominent as well as 2223 keV γ rays from H(n, γ) reactions. Al was used in the sample. Hydrogen existed in the collimator, additional neutron shields not shown in Fig. 1, and floor of the room. The measured pulse height spectrum ranges from 800 keV to 9000 keV. In the pulse height from 1000 to 4000 keV, continuum component exists. That would be the fission prompt component [7]. As time-of-flight increases, the total count rate decreases and capture γ rays from hydrogen and aluminum become to vanish and decay γ ray of 1778 keV from decay of ^{28}Al with half-life of 2.245 minutes come to be identified after 6 ms. In the time range from 6 to 8 ms, the prompt fission component decays away so that the 1778 keV γ ray becomes to be identified. In the time region after 14

ms, prompt capture γ rays decay away and discrete peaks with larger peak to base ratio are found as we expected.

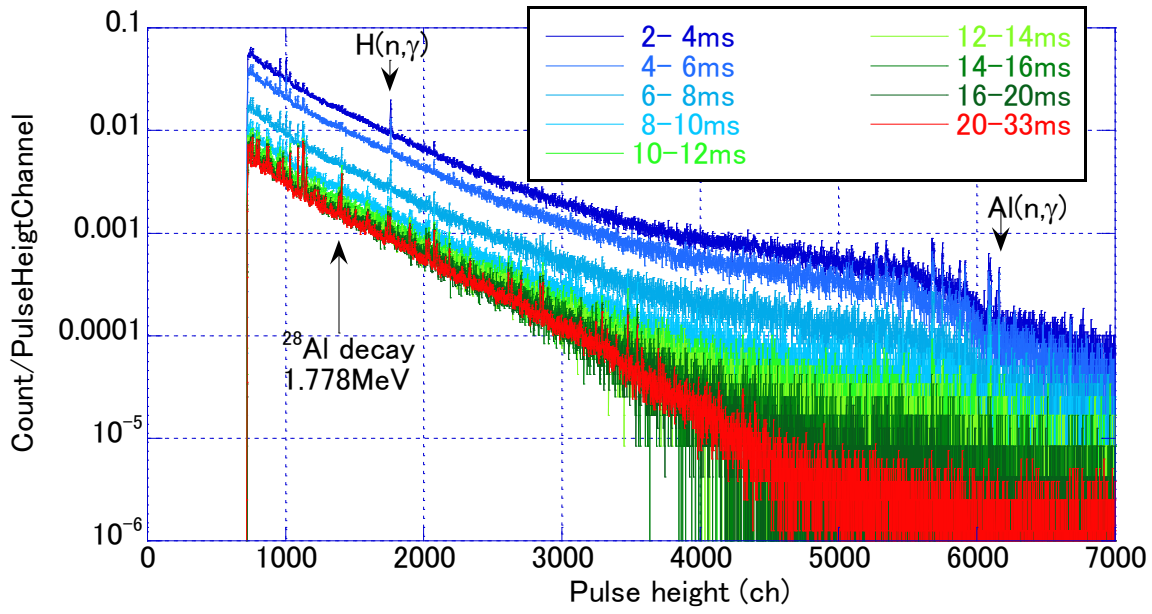

Figure 3. Pulse height spectrum measured for U_3O_8 sample for time regions.

3. Nuclide Identification

The pulse height spectrum measured for the OOP time region is shown in Figure 4. Peaks are found from 800 to 5500 keV with larger peak to base ratio. To identify the peaks, γ ray emission rate was calculated based on JENDL/FPY&FPD-2011 data [9] In the calculation, FP yield data for fission of ^{235}U induced by the thermal neutron were used. From the nuclides directly generated in the fission, production and decay of them and their descendant nuclides were calculated by solving the Bateman's equation. The calculated time dependent radio-activities of the nuclides after a fission of ^{235}U were integrated over 17 hours of measurement time assuming stable and continuous reaction rate and γ ray detection. Here, the time spectrum of fission indicated by that of ^{10}B(n,α_1) reaction in Figure 2 was neglected as well as the decay time d = 20 ms acting as the dead time for OOPS. The integrated activity corresponds to the number of decay of each nuclide during the period of 17 h. By multiplying the number by the γ ray emission per decay, we can quantify the number of γ ray emission. We compared the number to the measured data and identified FP nuclides with half-life from 0.5 s to 3.0 h, such as ^{95,96,97,98}Y, ^{89,90,90m,91}Rb, ^{86}Br, ^{95}Sr, etc. One of the advanced points of OOPS is radio-activities of FPs with wider dynamic range of half-lives are measurable simultaneously.

For the application of FPY & FPD data for the DGA of fuel debris, γ rays of energy from 3 to 5 MeV are significant. Then the quantitative comparison of the measured and calculated number of γ ray emission listed in Table 1 would be significant. For that, the errors in calculation by the assumption described above should be quantified.

Table 1. Identified γ rays useful for delayed gamma ray assay

Nuclide	Half-life	Energy(keV)
^{90}Rb	2.63 m	4136
		4366
^{90m}Rb	4.3 m	3317
^{91}Rb	58.4 s	3600
^{95}Y	10.3 m	3576
^{97}Y	3.75s	3288
		3401
^{98}Y	0.55s	4450

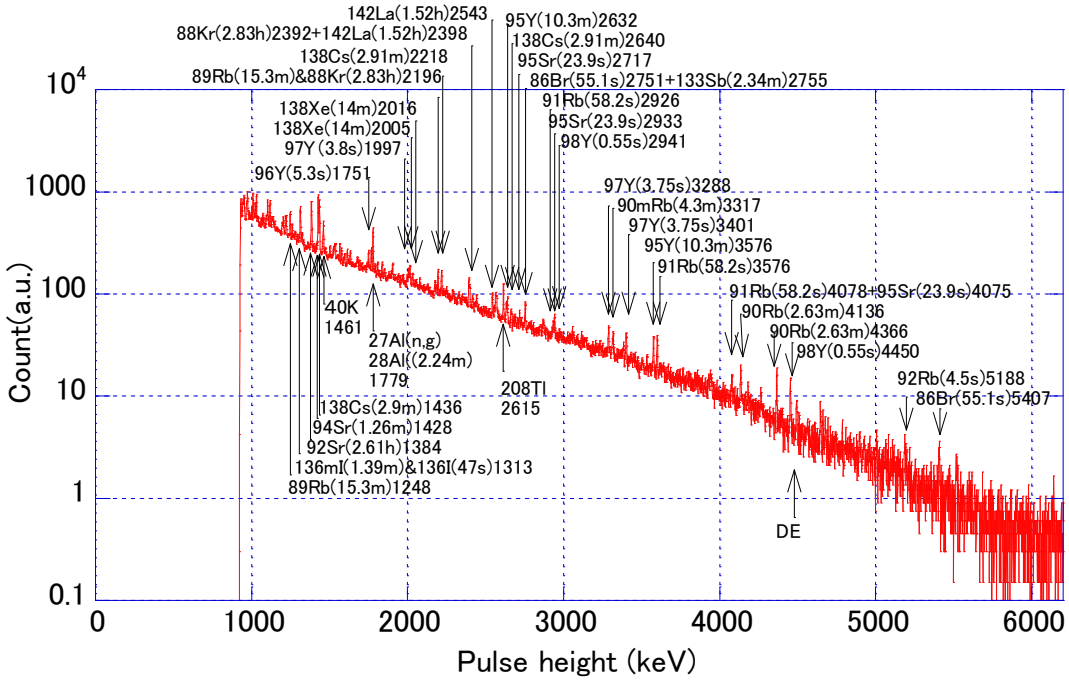

Figure 4. Identification of discrete gamma ray peaks measured in OOP time region.

4. Summary and Future work

In order to give experimental radioactivity data to validate FPY & FPD data, OOPS has been established using the pulsed neutron source facility at KURNS-LINAC. By OOPS, γ rays with energy from 800 to 5600 keV from FPs with half-lives from 0.5 s to 3.0 h were successfully measured. The advanced points of OOPS are 1) FP with half-life shorter than 10 s is measurable since samples need not to be transferred, 2) the discrete γ ray spectra are obtained with larger peak to base ratio by discriminating prompt γ ray emission.

As the future work, we have planned to make the detection threshold energy of γ rays down to 200 keV. By the extension, validation of FPY & FPD data for decay heat calculation in the time range from 100 ms to several hours would be promoted. A measurement to determine the detection efficiency

is also planned. Contrarily, calculation of the γ ray emission rate based on latest version of FPY & FPD data [10] is also mandatory. The time structure of fission and dead time effect shall be considered for the calculation for the validation.

Acknowledgements

This work was partially supported by the Joint Usage/Research of the Institute for Integrated Radiation and Nuclear Science, Kyoto University (KURNS) (No.PR8-4. PR6-4).

References

[1] World Nuclear News, Fuel debris sample extracted from Fukushima Daiichi reactor, https://www.world-nuclear-news.org/articles/Fuel-debris-sample-extracted-from-damaged-Japanese-reactor, (accessed 2025-01-25).

[2] NHK world, Uranium found in fuel debris retrieved from Fukushima Daiichi reactor, https://www3.nhk.or.jp/nhkworld/en/news/20241223_17/, (accessed 2025-01-25).

[3] Tokyo Electric Power Company Holdings, The Status of Fuel Debris Retrieval, https://www.tepco.co.jp/en/hd/decommission/progress/retrieval/index-e.html, (accessed 2025-01-25)

[4] Nauchi Y. et al., Concept of capture credit based on neutron-induced gamma ray spectroscopy. J. Nucl. Sci. Technol., vol 52, no. 7-8, 2015, pp. 1074-1083.

[5] Nauchi Y. et al., Proceedings of the 11th International Conference on Nuclear Criticality Safety (ICNC2019), Paris, France, 2019, track-2.

[6] Suyama K. et al., Proceedings of the 12th International Conference on Nuclear Criticality Safety (ICNC2023), October 1-6, 2023, Sendai International Center, Sendai, Miyagi, Japan, JAEA-Conf 2024-001, 2024, 40p.

[7] Verbeke J.M. et al., Simulation of neutron and gamma ray emission from fission and photo fission. LLNL Fission Library 2.0.2, UCRL-AR-228518-REV-1, 2016.

[8] Rodriguez D.C., Development and testing of a delayed gamma-ray spectroscopy instrument utilizing Cf-252 neutrons evaluated for nuclear safeguards applications, Nucl. Instrum. Methods Phys. Res. A, 1014, 2021, 165685.

[9] Katakura J., JENDL FP decay data file 2011 and fission yields data file 2011, JAEA-Data/Code 2011-025, 2012, 73p.

[10] Iwamoto O. et al., Japanese evaluated nuclear data library version 5: JENDL-5, J. Nucl. Sci. Technol., vol 60, no. 1, 2023, pp. 1-60.

[11] Nauchi Y. et al., Identification of nuclear material in spent nuclear fuel (1), KURNS progress report 2022, 2023, p. 74.

[12] Nauchi Y. et al., Identification of nuclear material in spent nuclear fuel (2), KURNS progress report 2023, 2024, p. 47.

10. Searching for saddle points on fission energy surfaces using Cassini parameters

Takuto ARAKI[†1], Takahiro WADA[1], and Kazuki OKADA[2]

[1]Department of Pure and Applied Physics, Kansai University,
3-3-35 Yamatecho, Suita, 564-8680, Japan
[2]Nuclear Data Center, Japan Atomic Energy Agency, Tokai, 319-1195, Japan

[†]Email: k289736@kansai-u.ac.jp

Abstract

To analyze the fission modes in nuclear fission, we focus on the structure of the multidimensional deformation potential. The structure of the multidimensional deformation potential is characterized by the position and height of the minima and the saddle points connecting the minima. We searched the position and height of the saddle points using the immersion method and the dam method. The deformation of the nucleus was described using Cassini parametrization. We considered the four-dimensional cases (α, α_1, α_3, α_4) or (α, α_1, α_4, α_6) and the five-dimensional case (α, α_1, α_3, α_4, α_6). The deformation potential was calculated with the macroscopic-microscopic model. In the spontaneous fission of Fm isotopes, it is known that as the neutron number increases, the mass distribution of the fission fragments changes from a shape with peaks in asymmetric fission to a shape with a peak in symmetric fission. For ^{254}Fm, ^{256}Fm, ^{258}Fm, and ^{260}Fm, we studied how the minima and saddle points change, and found that for A =254 and 256, the third fission barrier is mass-asymmetric, while for A =258 and 260, the third fission barrier is mass-symmetric and lower than the second barrier. It is found that the α_6 parameter plays an important role in this change.

1 Introduction

The mass and total kinetic energy (TKE) distribution of fission fragments brings essential infor-mation on fission dynamics. The fission dynamics have been investigated theoretically with the multi-dimensional Langevin approach, in particular, for actinide nuclei [1]. In this approach, the deformation potential plays a key role in determining the fragment distribution. In order to understand the results of multi-dimensional Langevin calculations, a specific analysis of the structure of the deformation potential is essential. In general, double-humped barrier struc-tures are known for actinide nuclei, but triple-humped barriers are predicted for some nuclides. Identification of the positions and heights of saddle points corresponding to second and third bar-riers in the multi-dimensional potential space will explain the mass-TKE distributions obtained by Langevin calculations and contribute to the understanding of the origin of various fission modes. In this study, to investigate the structure of the energy surface in a multi-dimensional deformation space, we focus on the positions and heights of minima and saddle points. The deformation space is described by the Cassini parameter, which is composed of an overall elon-gation α and deformation parameters α_n, and can flexibly describe various nuclear shapes [2]. We used (α, α_1, α_3, α_4, α_6) and investigated the structure of the energy surface in a 5-dimensional deformation space. The deformation potential was calculated by adding the microscopic shell correction

energy to the macroscopic droplet energy. The saddle points are searched for using the water immersion method. In a multi-dimensional space, there may be many saddle points, and the dam method is used to find them [3]. The 5-dimensional energy surface described by the Cassini parameter is complex, with many saddle points. This is the first attempt to analyze their distribution and height.

2 Method

2.1 Cassini parameterization

In this study, the Cassini parameter is used as a model to describe the shape of nuclei. Cassini ellipse is an ellipse represented by a set of points in the Cartesian curve coordinate system (R, x) where the product of the distances from the two foci are constant [2]. The R = const lines correspond to the surface of Cassini ovals which represent the division of a spherical shape into separated objects by varying the elongation parameter α. When α is 0, the Cassini ellipse represents a sphere, and as the value of α increases, the shape is elongated to form an ellipse. As α is further increased, a neck is formed. When α = 1, it splits completely. To describe various shapes that appear during fission process, we introduce Legendre expansion of the Cassini elliptic surface R as a function of x as in the equation below, where R_0 is the radius of the nucleus and P_m is the Legendre polynomial of order m.

$$R(x) = R_0 \left[1 + \sum \alpha_m P_m(x)\right] \tag{1}$$

The expansion coefficient corresponding to P_m, α_m, can be regarded as a deformation parameter in this model because a set of α_m corresponds to a specific shape. Besides α, among the many deformation parameters α_n, Among many deformation parameter α_n is important to select the parameters that are effective in describing the nuclear shape. The α_n represents asymmetric deformation when n is odd and symmetric deformation when n is even. α_1 denotes the mass asymmetry of the fission fragments. Since asymmetric fission, in which fission fragments with different mass numbers are produced, is important for fission, consideration of α_1 is essential. In addition, α_4 corresponds to the quadrupole deformation of the fission fragments and is considered to be an effective parameter for describing the overall deformation of the fission fragments as well as the ground state of nuclei. The three dimensions of α, α_1, α_4 are the basic parameter set for fission of any nuclide. In addition, α_3 and α_6 are used as additional parameters. α_3 corresponds to the asymmetry of the shape of the splitting fragments, and in combination with α_1 is expected to improve the reproducibility of asymmetric splitting. The α_6 affects the distance between the centers of gravity of the split fragments.

2.2 potential energy

The deformation potential is calculated by the macroscopic microscopic model [4]. In this approach, the deformation potential is expressed as

$$V_{\mathrm{def}}(\mathrm{shape}) = V_{\mathrm{FRLDM}}(\mathrm{shape}) + V_{\mathrm{micro}}(\mathrm{shape}) \tag{2}$$

and is obtained by adding the microscopic correction term V_{micro} to the macroscopic energy V_{FRLDM}. In this study, the macroscopic energy V_{FRLDM} uses the finite-range liquid drop model [5].
The microscopic correction term is calculated as

$$V_{\mathrm{micro}} = \sum_{v=n,p} \left(V^v_{\mathrm{shell}} + V^v_{\mathrm{pair}}\right), \tag{3}$$

where V_{shell} is the shell correction energy and V_{pair} is the pairing correction energy. As a way to obtain the shell correction energy, it is evaluated by the difference between the total energy E_{shell} obtained from the single particle energy and the total energy obtained from the level density smoothed by the Strutinsky method [6]. V_{pair} is calculated in the BCS approximation [7].

2.3 Immersion method

The Immersion method [3] is a method that can unambiguously identify the lowest saddle point between two minima of a fission energy surface. The two minima are called the entry point (A) and the exit point (B), respectively. The potential energy is defined on a mesh in the coordinate space. Local minima can be determined from the condition that they have energy values lower than the energy values of all nearest neighbors on the mesh. Physically strange minima or low depth minima are not considered. Fill the inlet point (A) with water and define (A) as WET and the other points as dry. Next, the energy (E') above the energy of the entrance point (A) is selected and the entire coordinate grid is scanned, changing from dry to wet when both of the following conditions are met at each point.

(1) If the scanned point is below a certain energy (E').
(2) If the point has a WET point in the nearest neighborhood of that point.
Repeat the above procedure until the new point no longer switches to WET. Now raise the water level (E') further and repeat the process. When the water level is high enough, the outlet (B) gets wet and the point of energy at that point is the saddle point. This is illustrated in the following Fig. 1.

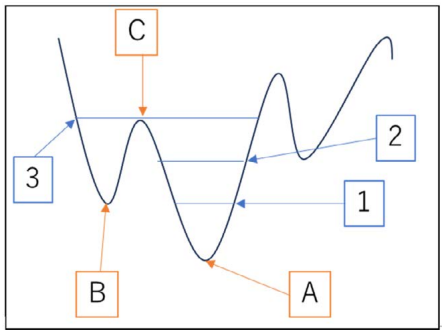

Figure 1: Diagram of Immersion method. A is the entry point, B is the exit point, C is the saddle point, and the numbers represent water levels (E').

2.4 Dam method

Although the above methods can search the lowest saddle point, the energy surface may have multiple saddle points, and the lowest saddle point may not be the correct saddle to fission. The dam method [7] exists as a method to search for a saddle other than the lowest saddle. To find an even higher energy saddle point between the entry point (A) and the exit point (B), "dam" the lowest saddle point. First, identify the lowest saddle point and raise the energy at that location to a very large value, say 1000 MeV. Again find the lowest saddle point with the Immersion method. If the new saddle point is adjacent to a very high energy value, again that point also raises the energy since the water is only flowing around a partial dam in the lowest pass. This is repeated until finally the next saddle point is detached from the dam.

3 Result

The minima and saddle points for ^{254}Fm, ^{256}Fm, ^{258}Fm and ^{260}Fm in 5D{3D(α, α_1, α_4)+α_3+α_6} space were shown in Figs. 2 to 3.

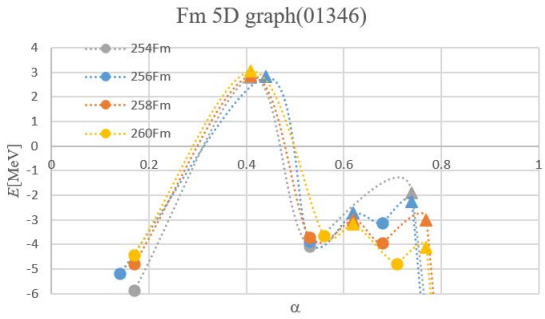

Figure 2: Energy of the minima and saddle points along fission path in 5D space. Circles represent minima and triangles represent the saddles. The dotted lines represent the approx-imate curves connecting the saddles and min-ima.

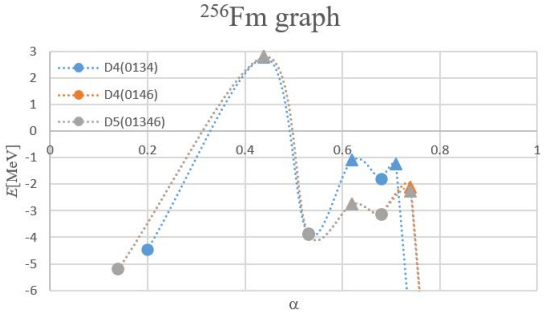

Figure 3: Energy of the minima and saddle points along fission in ^{256}Fm.
Blue represents 4D(α, α_1, α_3, α_4).
Orange represents 4D(α, α_1, α_4, α_6).
Gray represents 5D (α, α_1, α_3, α_4, α_6).

For ^{254}Fm and ^{256}Fm, an asymmetric 3rd saddle point arises which induces asymmetric fission. In contrast, in ^{258}Fm and ^{260}Fm, we obtain the symmetric shape at the 3rd saddle point. The mass of the fission fragment for ^{256}Fm is A =138, which is similar to the experimental data [8]. The nuclear shapes of each Fm isotope are shown in Figs. 4 to 7. ^{254}Fm has a minimum around α=0.68, but at a depth shallower than 0.2 MeV, thereby reducing the number of saddle points to two. All Fm isotopes have the same energy at the second minimum, but asymmetric fission results when the energy of the third saddle is higher than the energy of the second saddle, and symmetric fission when it is lower. Figure 2 also shows that the inclusion of α_6 makes this change near fission more pronounced. Similar results were obtained for Fm isotopes other than ^{256}Fm. The saddle point toward asymmetric fission in isotopes with mainly symmetric fission was confirmed to be about 0.5 MeV higher than symmetric fission in ^{258}Fm and about 1.5 MeV higher than symmetric fission in ^{260}Fm. The saddle point toward symmetric fission

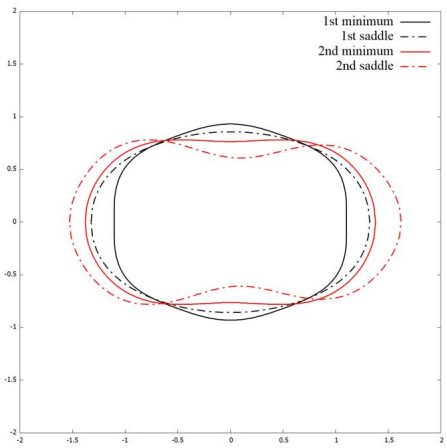

Figure 4: Fission shape in ^{254}Fm.

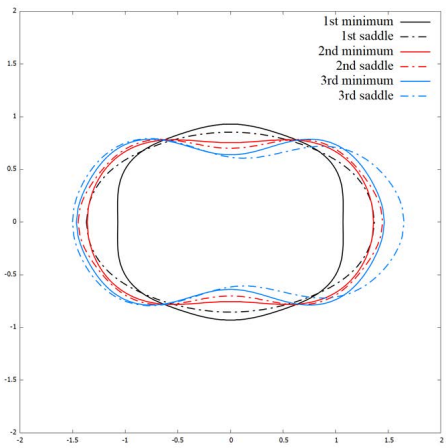

Figure 5: Fission shape in ^{256}Fm.

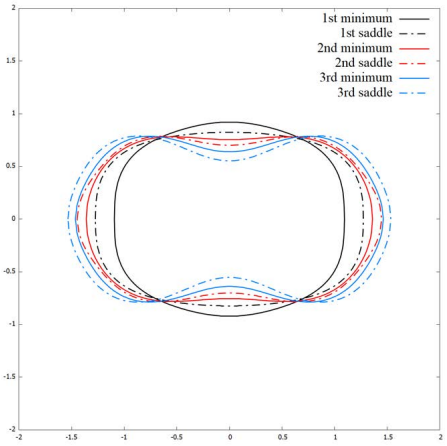

Figure 6: Fission shape in ^{258}Fm.

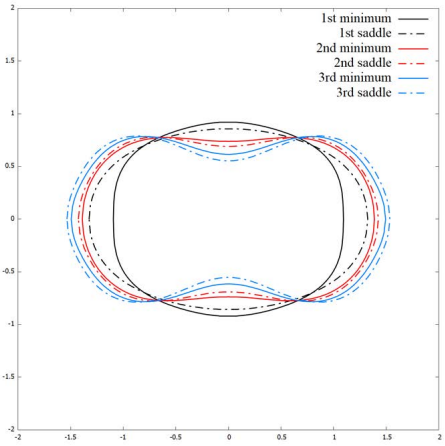

Figure 7: Fission shape in ^{260}Fm.

in isotopes with mainly asymmetric fission was confirmed to be about 0.8 MeV higher than asymmetric fission in ^{254}Fm and about 0.3 MeV higher than asymmetric fission in ^{256}Fm. Around ^{256}Fm and ^{258}Fm, where the transition from symmetric to asymmetric splitting occurs, the energies of both symmetric and asymmetric splitting are close, but the difference increases as they move apart, such as ^{254}Fm and ^{260}Fm. The changes in the barrier structure in response to the neutron number are thought to lead to changes in the mass distribution.

4 Summary

We examined the structure of the deformation energy surface in 5D deformation space de-scribed with Cassini parameters. For Fm isotopes, we showed the splitting changes from asymmetric (^{254}Fm,^{256}Fm) to symmetric (^{258}Fm,^{260}Fm), depending on the height of the sec-ond and third saddles. The changes in the barrier structure in response to the neutron number lead to changes in the mass distribution. In this study, α_6 was shown to be an important pa-rameter for fission. It has recently been suggested that α_2 may be an important parameter and should be studied in the future when α_2 is introduced. Our next plan is to investigate the 6D deformation potential with (α, α_1, α_2, α_3, α_4, α_6).

References

[1] K. Okada, T. Wada, and N. Carjan,EPJ Web of Conferences 284, 04018 (2023).

[2] V. V. Pashkevich, Nucl. Phys. A 169, 2 (1971).

[3] P. Moller, A. J. Sierk, T. Ichikawa, A. Iwamoto, R. Bengtsson, H. Uhrenholt, and S. Aberg, Phys. Rev. C 79, 064304 (2009).

[4] P. Moller, J. R. Nix, W. D. Myers, W. J. Swiatecki, Atomic Data and Nuclear data Tables 7, 185 (1995).

[5] P. Moller, A. J. Sierk, T. Ichikawa H. Sagawa, Atomic Data and Nuclear data Tables 109, 1 (2016).

[6] V. M. Strutinsky, Nucl. Phys. A 95, 420 (1967).

[7] V. M. Strutinsky, Nucl. Phys. A 122, 1 (1968).

[8] D. C. Hoffman, J. B. Wilhelmy, J. Weber, W. R. Daniels, E. K. Hulet, R. W.Lougheed, J. Landrum, J. F. Wild and R. J. Dupzyk, Phys. Rev. C 21, 972, (1980).

11. Selection of activation foil for error reduction of benchmark experiment on large angle elastic scattering reaction cross section of Li by 14 MeV neutron

Yamato FUJII[1*], Indah Rosidah MAEMUNAH[1, 2], Yuya ONISHI[3], Shingo TAMAKI[1],
Sachie KUSAKA[1], Isao MURATA[1]
[1]Graduate School of Engineering, Osaka University
2-1 Yamada-oka, Suita, Osaka 565-0871, Japan
[2] Research Organization for Nuclear Energy, National Research and Innovation Agency
Building No. 80, BJ Habibie Integrated Science Area, South Tangerang 15310, Indonesia
[3]School of Engineering, Osaka University
2-1 Yamada-oka, Suita, Osaka 565-0871, Japan
[*]Email: fujii24@qr.see.eng.osaka-u.ac.jp

Accuracy improvement in benchmark experiment on large angle scattering cross section has a large contribution on precision of neutron transport calculation in fusion reactor design. This cross section is smaller than the forward scattering cross section. However, it must not be disregarded, considering a gap streaming by blanket. In the previous study, a benchmark experiment for lithium target was carried out with hafnium as the activation foil. However, the amount of activation of the hafnium foil was small, resulting in a large statistical error. It was difficult to detect enough scattered neutrons in the conventional experimental system. In this study, we examined candidates of the new activation foil based on factors such isotope abundance, reaction cross section, threshold value, and half-life. As a result, 13 candidates for the activation foil were successfully selected.

1. Introduction

In high-energy and high-intensity neutron environments, such as the fusion reactor blanket, large angle scattering reaction cross sections significantly affect neutron transport calculation results. Konno has identified discrepancies between experimental and calculated values in the blanket benchmark experiments in Japan Atomic Energy Agency (JAEA) [1]. Therefore, benchmarking studies for large angle scattering cross sections are indispensable. The authors' group has previously developed a benchmark experimental technique for large angle scattering reaction cross sections and performed benchmark experiments for several elements, such as iron, tungsten, and silicon [2-5]. Four experiments for a certain sample were conducted using two shadow bars composed of conical irons with and without the sample to extract large angle scattering neutrons.

In this paper, we focus on lithium, which is used as a blanket material for fusion reactors. **Figure 1** shows the neutron elastic scattering cross section of ^{7}Li by 14 MeV [6-8]. As shown in **Figure 1**, there are large discrepancies among nuclear data libraries for ^{7}Li. Benchmark experiments require the detection of neutrons scattered at large angles by the target material. The objective of this study is to select a new activation foil capable of reducing statistical error in the benchmark experiment for ^{7}Li.

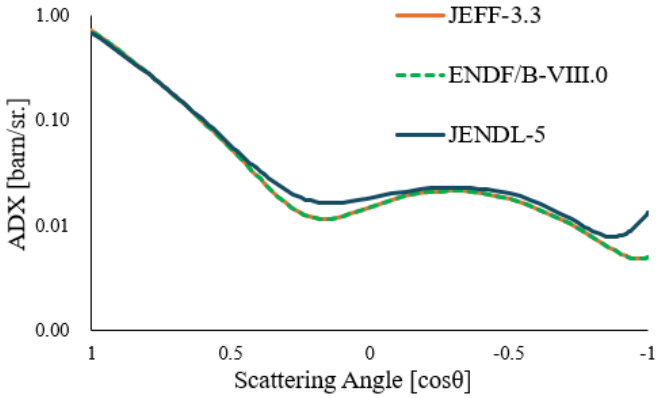

Figure 1 Angular differential elastic scattering cross section of ^{7}Li at 14 MeV [6-8].

2. Experimental Method

In the previous study, we developed a benchmark experimental system to validate the large angle scattering reaction cross sections of targets with a container using the foil activation method [9]. **Figure 2** shows the schematic experimental arrangement of the benchmark experiment at OKTAVIAN facility at Osaka University. The system consists of deuterium-tritium (D-T) neutron source, activation foil, iron shadow bar, target sample, stainless container, and it is surrounded by concrete wall of about 1 m thickness. The shadow bar is an iron trapezoidal conical bar and set up to prevent incident neutrons from entering directly to the activation foil. In the benchmark technique, two types of shadow bars, S1 (thin shadow bar) and S2 (thick shadow bar), were used in the experiments, as shown in **Figure 3**. For each shadow bar, two experiments were conducted with and without the target sample, as shown in **Figure 4**. These four systems are named as follows: S1TC and S1C are systems using S1 with and without a target sample, S2TC and S2C are systems using S2 with and without a target sample, respectively. In each experiment out of four experiments in total, the reaction rates of the activation foil were measured.

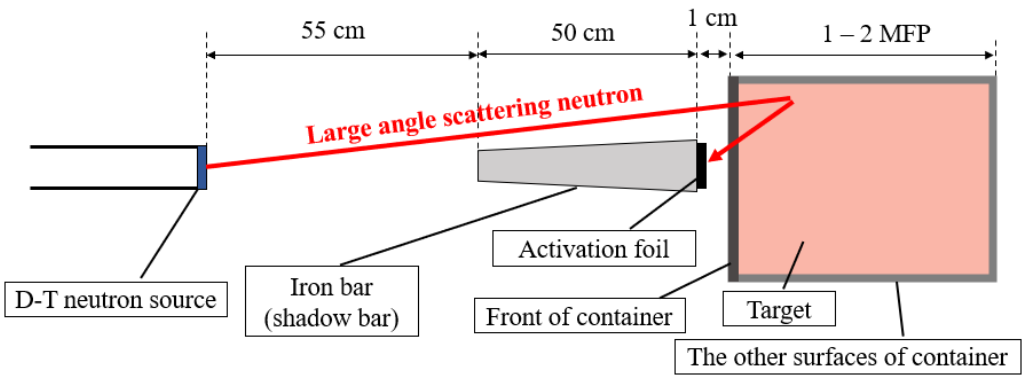

Figure 2 Schematic arrangement of the benchmark experimental system.

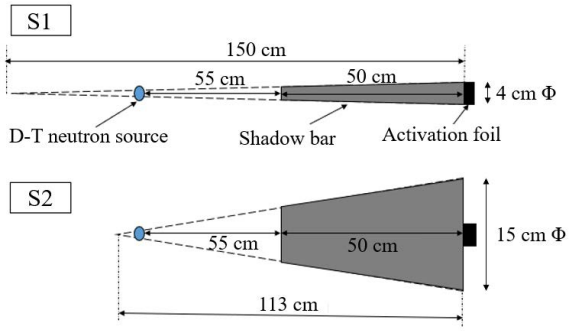

Figure 3 Two types of shadow bars in the benchmark experimental systems.

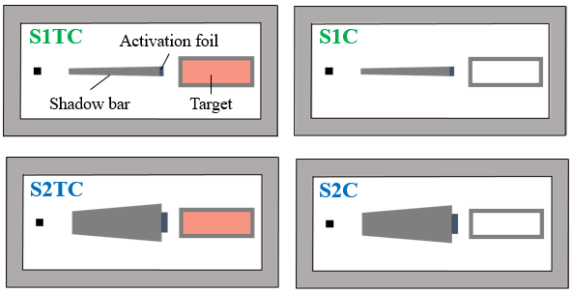

Figure 4 Four benchmark experimental systems.

In the benchmark experimental room, there are five elements which neutrons can pass through, i.e., the shadow bar, target sample, front of stainless container, other surfaces of the container, and wall. Therefore, 31 paths (${}_5C_1 + {}_5C_2 + {}_5C_3 + {}_5C_4 + {}_5C_5$) can exist in total as the neutron transport path. Excluding pathways that do not physically exist, 19 pathways remain as shown in **Figure 5**. Path ⑥ is the path of neutrons large angle scattered by the target sample. This path ⑥ only exists in the S1TC system because the target sample does not exist in the S1C and S2C systems, and neutrons cannot enter the target sample without passing through the thick shadow bar in S2TC system. Subsequently, the contribution of large angle scattered neutrons was deduced from the four reaction rates of gold foils using Equation (1), where R_{net} represents the reaction rate due to only large angle scattered neutrons, and R_{S1TC}, R_{S2TC}, R_{S1C}, and R_{S2C} denote the reaction rates in each experiment. This is because the contributions of neutrons passing through other paths are cancelled out with each other or very small to be ignored as shown in **Table 1**.

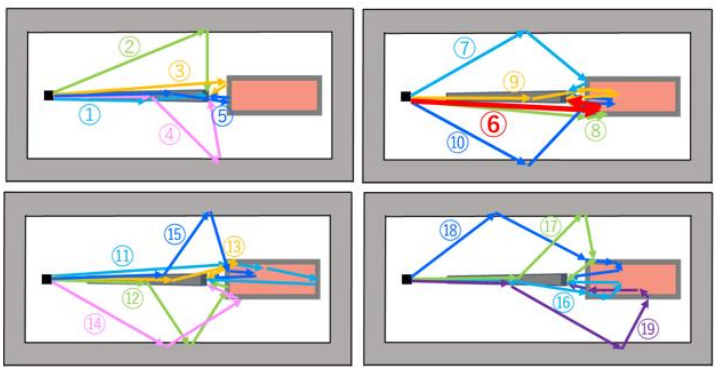

Figure 5 Nineteen pathways of neutrons entering the activation foil.

$$R_{net} = R_{S1TC} - R_{S2TC} - (R_{S1C} - R_{S2C}) \quad (1)$$

Table1 Calculated reaction rates of hafnium foils induced by neutrons passing through each pathway in case of lithium target. [10^{-9} reaction/source neutron/cm^3]

Path	R_{S1TC}	R_{S2TC}	R_{S1C}	R_{S2C}	R_{net}
①	0.000	0.001	0.000	0.001	0.000
②	0.041	0.017	0.041	0.017	0.000
③	0.008	0.000	0.008	0.000	0.000
④	0.072	0.041	0.072	0.041	0.000
⑤	0.000	0.000	0.000	0.000	0.000
⑥	**0.084**	0.000	0.003	0.000	0.081
⑦	0.003	0.002	0.003	0.002	0.000
⑧	0.000	0.000	0.000	0.000	0.000
⑨	0.003	0.000	0.000	0.000	0.003
⑩	0.002	0.000	0.000	0.000	0.002
⑪	0.005	0.000	0.006	0.000	-0.001
⑫	0.000	0.001	0.000	0.001	0.000
⑬	0.000	0.000	0.000	0.000	0.000
⑭	0.000	0.000	0.000	0.000	0.000
⑮	0.000	0.001	0.000	0.000	-0.001
⑯	0.000	0.000	0.000	0.000	0.000
⑰	0.000	0.001	0.000	0.001	0.000
⑱	0.098	0.097	0.127	0.125	-0.001
⑲	0.003	0.006	0.003	0.007	0.000
Total	0.320	0.168	0.264	0.196	**0.083**

3. Previous Study

In the previous study, the author's group calculated the counts obtained with the Ge detector and the associated statistical errors were calculated when various elements were used as the activation foil, concluding that hafnium was the best activation foil for benchmark experiment for lithium. However, the statistical error estimation did not account for background contributions of Ge detector, a significant factor in the experiment. Furthermore, the cooling and measurement times required further optimization. The author's group conducted a benchmark experiment for lithium as the target sample using hafnium as the activation foil. However, due to the low mass of lithium, the detection of large angle scattering neutrons posed a significant challenge, resulting in substantial experimental errors attributable to neutrons scattered from walls and surrounding materials. Therefore, more accurate estimation of statistical errors is needed.

4. Method

Candidate activation foils were selected to reduce statistical error by considering the following factors. In this study, the data from JENDL-5 was used for the selection [8].

(i) The material is in a solid or liquid state at room temperature.

(ii) Isotope abundance is more than 10%.

(iii) The reaction cross section at 14 MeV neutrons is more than 100 mb.

(iv) The threshold value is less than approximately 7.85 MeV.

(v) Half-life is more than 1 minute and less than 1 year.

(vi) The nuclear data of the activation reaction thoroughly validated.

The value of 7.85 MeV in (iv) is calculated by Equation (2) as the energy of neutrons when scattered 180° by lithium. In this equation, E, E_n, and E_M represent the energy of the scattered neutron, that of incident neutron, and that of the recoil nucleus (lithium), respectively. M and m represent the mass of the neutron and that of the recoil nucleus, respectively. θ represents the scattering angle. Since the energy of incident D-T neutrons is approximately 14.1 MeV, the energy of those elastically scattered at 180° in lithium is 7.85 MeV.

$$E = E_n - E_M = E_n - \frac{2Mm}{(M+m)^2}(1 - cos\ \theta)E_n \quad (2)$$

5. Result

Thirteen candidate activation foils were selected from the methods in chapter 4. **Table 2** shows these candidate isotopes, each reaction, isotope abundance, energy and intensity of emitted γ-ray, and half-life. The results indicate that one of these thirteen candidates should be used as the activation foil for benchmark experiments on large angle scattering of lithium with high accuracy.

Table 2 Thirteen candidate activation foils

Reaction	Isotope abundance	γ ray (Energy, Intensity)	Half-life
^{180}Hf(n,n')^{180m}Hf	35.08%	215.43 keV, 81.32% 332.27 keV, 94.12% 443.16 keV, 81.88%	5.47 h
^{24}Mg(n,p)^{24}Na	78.99%	1368.63 keV, 99.99%	14.997 h
^{27}Al(n,α)^{24}Na	100%	1368.63 keV, 99.99%	14.997 h
^{28}Si(n,p)^{28}Al	92.223%	1778.85 keV, 100%	2.245 m
^{31}P(n,α)^{28}Al	100%	1778.85 keV, 100%	2.245 m
^{56}Fe(n,p)^{56}Mn	91.754%	846.75 keV, 98.87% 1810.72 keV, 27.19% 2113.05 keV, 14.34%	2.5789 h
^{58}Ni(n,p)^{58}Co	68.007%	810.76 keV, 99.45%	70.86 d
^{64}Zn(n,p)^{64}Cu	49.17%	1345.77 keV, 0.48%	12.701 h
^{92}Mo(n,np)^{91}Nb	14.53%	1204.67 keV, 2.02%	60.86 d
^{160}Gd(n,2n)^{159}Gd	21.86%	58.00 keV, 2.49% 348.28 keV, 0.24% 363.54keV, 11.78%	18.479 h
^{169}Tm(n,2n)^{168}Tm	100%	198.25 keV, 54.49% 447.51 keV, 23.98% 815.99 keV, 50.95%	93.1 d
^{170}Er(n,2n)^{169}Er	14.91%	8.41 keV, 0.17%	9.392 d
^{176}Yb(n,2n)^{175}Yb	12.996%	113.81 keV, 3.87% 282.52 keV, 6.13% 396.33 keV, 13.15%	4.185 d

6. Conclusion

In this study, thirteen candidate activation foils were selected by considering the material's state at room temperature, the isotope abundance, the reaction cross section, the threshold value, half-life, and thorough validation of the nuclear data of the activation reaction for accuracy improvement in benchmark experiments on large angle scattering cross section of lithium by 14 MeV neutrons.

In the future, we will determine the optimal activation foil by calculating the activation response rate of the experiment using each of these candidates with MCNP5 and estimating the statistical error. In addition, we will develop an experimental system that further minimizes statistical errors by optimizing the materials and configurations of surrounding components and carry out benchmark experiments for Li by using the optimal activation foil.

References

[1] Ohnishi S., Kondo K., Azuma T., et al., New integral experiments for large angle scattering cross section data benchmarking with DT neutron beam at JAEA/FNS. Fusion Eng Des. 2012;87(5-6):695-699, doi: 10.1016/j.fusengdes.2012.02.002.

[2] Hayashi N., Ohnishi S., Fujiwara Y., et al., Optimization of Experimental System Design for Benchmarking of Large Angle Scattering Reaction Cross Section at 14 MeV Using Two Shadow Bars. Plasma Fusion Res. 2018;13(0):2405002, doi: 10.1585/pfr.13.2405002.

[3] Yamaguchi A., Fukui K., Fujiwara Y., et al., Benchmark experiment of large-angle scattering reaction cross section of iron at 14 MeV using two shadow bars – Comparison of experimental results with ENDF/B-VIII–, J. Nucl. Sci. Technol. 2020;58(1):80-86. doi:10.1080/00223131.2020.1804475.

[4] Maemunah I. R., Araki S., Miyazawa R., et al., A benchmark study of large-angle neutron scattering cross section of tungsten using two shadow bars technique at 14 MeV. EPJ Web Conf. 2023;284:07002, doi: 10.1051/epjconf/202328407002.

[5] Araki S., Fukui K., Maemunah I. R., et al., Design study of benchmark experiment for large-angle scattering cross section for non-solid target with 14 MeV neutron. EPJ Web Conf. 2023;284:07003, doi: 10.1051/epjconf/202328407003.

[6] Plompen A. J. M., Cabellos O., De Saint Jean C., et al., The joint evaluated fission and fusion nuclear data library, JEFF-3.3., Eur. Phys. J. A., 2020;56(7), doi: 10.1140/epja/s10050-020-00141-9.

[7] Brown D. A., Chadwick M. B., Capote R., et al., ENDF/B-VIII.0: The 8 th Major Release of the Nuclear Reaction Data Library with CIELO-project Cross Sections, New Standards and Thermal Scattering Data, Nucl Data Sheets, 2018;148:1–142, doi: 10.1016/j.nds.2018.02.001.

[8] Iwamoto O., Iwamoto N., Kunieda S., et al., Japanese evaluated nuclear data library version 5: JENDL-5, J. Nucl. Sci. Technol., 2023;60(1):1–60, doi: 10.1080/00223131.2022.2141903.

[9] Fukui K., Yamaguchi A., Fujiwara Y., et al., Detailed examination of benchmark method for large angle scattering reaction cross section at 14MeV for a flake target, Proceedings of the 2019 Symposium on Nuclear Data; November 28-30, 2019, Kyushu University, Chikushi Campus, Fukuoka, Japan: JAEA-Conf-2020-001, 2020, pp.153–158.

12. Re-evaluation of Neutron Energy Spectrum in Kyoto University BNCT Irradiation Field Using Multifoil Activation Method

Jakkrit PRATEEPKAEW[1*], Yoshinori SAKURAI[2]
[1]Graduate School of Engineering, Kyoto University,
Kyoto Daigaku-katsura, Nishikyo-ku, Kyoto, 615-8530, Japan
[2]Institute for Integrated Radiation and Nuclear Science, Kyoto University,
2 Asashiro-nishi, Kumatori-cho, Sennan-gun, Osaka 590-0494, Japan
[*]Email: prateepkaew.jakkrit.36d@st.kyoto-u.ac.kp

The Heavy-Water Thermal Neutron Facility of Kyoto University Research Reactor (KUR) began operation for boron neutron capture therapy (BNCT) in May 1974. After undergoing a facility upgrade for epithermal neutron irradiation in 1996, it was renamed as Heavy-Water Neutron Irradiation Facility (HWNIF), and neutron energy spectra were evaluated using multifoil activation method. In May 2010, KUR shifted its operation from high-enrichment to low-enrichment fuel. Despite this transition, a precise reevaluation of the neutron energy spectrum at KUR-HWNIF has not been conducted. This study presents reevaluation result of the neutron energy spectrum for the standard epithermal-neutron irradiation mode, using multifoil activation method with some adjustment from previous evaluation. Two difference unfolding codes, MAXED and GRAVEL, were used to achieve this reevaluation. The future plan to confirm neutron energy spectrum evaluation accuracy of two different unfolding code is described in this paper.

1. Introduction

Boron neutron capture therapy (BNCT) is a cancer treatment that involves the use of a drug agent containing ^{10}B, which has high neutron absorption cross-section property. The drug agent is delivered to tumor tissue, upon reacting with neutrons, ^{10}B produces heavy charged particles, including ^{7}Li and alpha particles, which are highly effective in destroying cancer cells. These particles exhibit a high linear energy transfer and have a very short range within biological tissues, enabling them to selectively target and destroy cancer cells while causing minimal damage to surrounding healthy tissues. This short range, approximately equivalent to the size of a cell, ensures precise targeting at the cellular level. Due to its ability to selectively target cancer cells, BNCT holds great promise as a therapeutic approach for enhancing patient's quality of life [1, 2].

The Heavy-Water Thermal Neutron Facility at the Kyoto University Research Reactor (KUR) has been utilized for clinical research in boron neutron capture therapy (BNCT) since May 1974 [3]. Following an upgrade to the facility in 1996, its name was changed to the Heavy-Water Neutron Irradiation Facility (HWNIF), and the neutron energy spectrum was evaluated using the multifoil

activation method [4]. In May 2010, KUR transitioned from high-enrichment to low-enrichment fuel [5]; however, the neutron energy spectrum at the KUR-HWNIF had not been reevaluated with high accuracy since the transition. In this study, the neutron energy spectrum at the KUR-HWNIF was reevaluated using multifoil activation method after the change in fuel enrichment.

In the previous neutron energy spectrum evaluation of KUR-HWNIF [4], NEUPAC unfolding code [6], which utilized energy-dependent group cross-section libraries for neutron dosimetry reactions based on ENDF/B-V [7], was employed for unfolding procedure. However, NEUPAC unfolding code is no longer available, and more advanced nuclear data and unfolding codes have since been developed, providing significant improvements for neutron energy spectrum evaluation. In this study, we utilized the MAXED and GRAVEL unfolding codes, both widely recognized for their reliability in neutron energy spectrum unfolding procedure [8].

In the earlier evaluation, activation foils were irradiated during full-power KUR operations at 5 MW for 10 hours. Currently, KUR normally operates in a weekly schedule consisting of a 1 MW operation for 45~47 hours and a 5 MW operation for 6 hours [9]. Due to the limited irradiation time at 5 MW, the activation foils were irradiated during the 1 MW operation. The reduced neutron intensity resulted in lower counts for some foils that had been used in the prior evaluation. To address this, adjustments were made in this study to the types of foils, irradiation time, and experimental setup to ensure measurable results from the irradiated foils.

2. Method

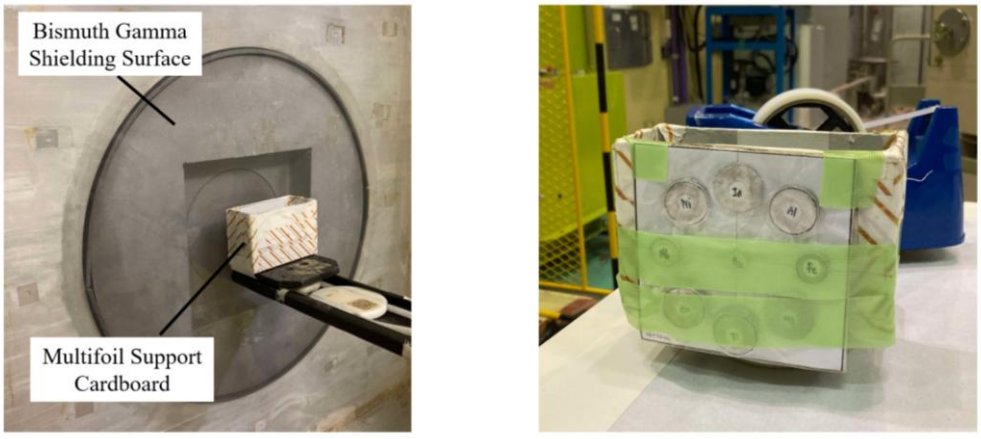

Figure 1: Multifoil irradiation

(a) Irradiation setup, (b) Multifoil arrangement

Figure 1(a) shows the irradiation setup for activation foils positioned in neutron irradiation direction, near the bismuth gamma shielding surface of KUR-HWNIF. In this study, the standard epithermal-neutron irradiation mode, commonly used for the treatment of deep-seated tumors, was employed. All of activation foils were covered with 0.5-mm-thick cadmium during irradiation to cut the effects of thermal neutrons. The foils used in the measurements were positioned radially, with equal spacing between each foil as shown in Figure 1(b).

Two different sets of activation foils, low fluence irradiation set and high fluence irradiation set, were used depending on the irradiation time. During irradiation, the neutron flux could fluctuate due to

factors such as adjustments to the control rods in the reactor core; therefore, a gold foil was placed at the center for neutron flux monitoring. Tables 1 and 2 list the types of activation foils used in each set. The low fluence irradiation set was designed for spectrum evaluation in the epithermal neutron region (0.5 eV~10 keV). Considering the higher expected count rates from the epithermal neutron flux in the KUR-HWNIF, the irradiation time was set to 15 minutes. On the other hand, the high fluence irradiation set was intended for spectrum evaluation in the fast neutron region (above 10 keV), where lower count rates are received. As a result, the irradiation time was set to 15 hours.

3. Results and discussion

In unfolding method, it requires several pieces of information, including "saturated activity per unit mass," "response function," and "initial guess spectrum," to estimate the neutron energy spectrum.

The count rates of irradiated foils were measured with a high-purity germanium (HPGe) semiconductor detector (ORTEC, GEM20P4-70). The saturated activity per unit mass for each irradiated foil was then calculated [10], and results shown in Tables 1 and 2.

Table 1: Measured saturated activities of low fluence irradiation foils

Foil	Reaction	Saturated activity per unit mass [Bq g^{-1}]	Measurement uncertainty [%]
Au	$^{197}Au(n,\gamma)^{198}Au$	4.48×10^{7}	0.92
NaCl	$^{23}Na(n,\gamma)^{24}Na$	1.82×10^{5}	0.92
Manganin (11.5%Mn-Cu)	$^{55}Mn(n,\gamma)^{56}Mn$	3.56×10^{6}	0.96
Sc	$^{45}Sc(n,\gamma)^{46}Sc$	4.46×10^{6}	1.02
Ta	$^{181}Ta(n,\gamma)^{182}Ta$	1.73×10^{7}	3.43
W	$^{186}W(n,\gamma)^{187}W$	1.81×10^{7}	1.89

Table 2: Measured saturated activities of high fluence irradiation foils

Foil	Reaction	Saturated activity per unit mass [Bq g^{-1}]	Measurement uncertainty [%]
Au	$^{197}Au(n,\gamma)^{198}Au$	4.43×10^{7}	0.32
In	$^{115}In(n,n')^{115m}In$	2.01×10^{3}	4.00
Al	$^{27}Al(n,p)^{27}Mg$	1.84×10^{2}	10.08
	$^{27}Al(n,a)^{24}Na$	5.71×10^{1}	6.01
Mg	$^{27}Mg(n,p)^{24}Na$	1.42×10^{2}	7.48
Ti	$^{47}Ti(n,p)^{47}Sc$	3.85×10^{2}	2.17
	$^{48}Ti(n,p)^{48}Sc$	1.16×10^{1}	7.71
Zr	$^{90}Zr(n,2n)^{89}Zr$	2.87×10^{1}	15.13
Ni	$^{58}Ni(n,p)^{58}Co$	1.43×10^{3}	5.56

For the response function, JENDL-5.0 Nuclear Data Library [11] was utilized, except for the $^{115}In(n,n')^{115m}In$ reaction, for which the 532DOS2 [12] library was used due to the absence of relevant data in JENDL-5.0.

In this study, initial guess spectrum was based on a previous neutron energy spectrum evaluation of KUR-HWNIF [4].

Once all required information was determined, neutron energy spectrum of the irradiation field was estimated using unfolding method. The UMG package, which includes MAXED and GRAVEL codes, was used for this spectrum unfolding procedure [8].

Figure 2(a) shows the unfolding results obtained using the MAXED and GRAVEL codes, with the total neutron flux normalized to 1, which was previously reported [13]. In MAXED unfolding results, irregularities were found in neutron energy spectrum around 10 MeV. A possible for these irregularities is the significant measurement uncertainty of high-fluence irradiation foils, which are used to analyze the neutron energy spectrum in the fast neutron region.

In this paper, we solved the problem of irregularity above 10 MeV neutron energy spectrum by eliminating $^{90}Zr(n,2n)^{89}Zr$ information which contain high measurement uncertainty of 15.13%. Figure 2 (b) shows the unfolding results obtained using the MAXED and GRAVEL codes, without $^{90}Zr(n,2n)^{89}Zr$ information. The irregularity above 10 MeV neutron energy spectrum was disappeared. Furthermore, the shape of the neutron energy spectrum obtained using the MAXED and GRAVEL codes becomes more similar when the $^{90}Zr(n,2n)^{89}Zr$ reaction information is excluded, compared to when it is included.

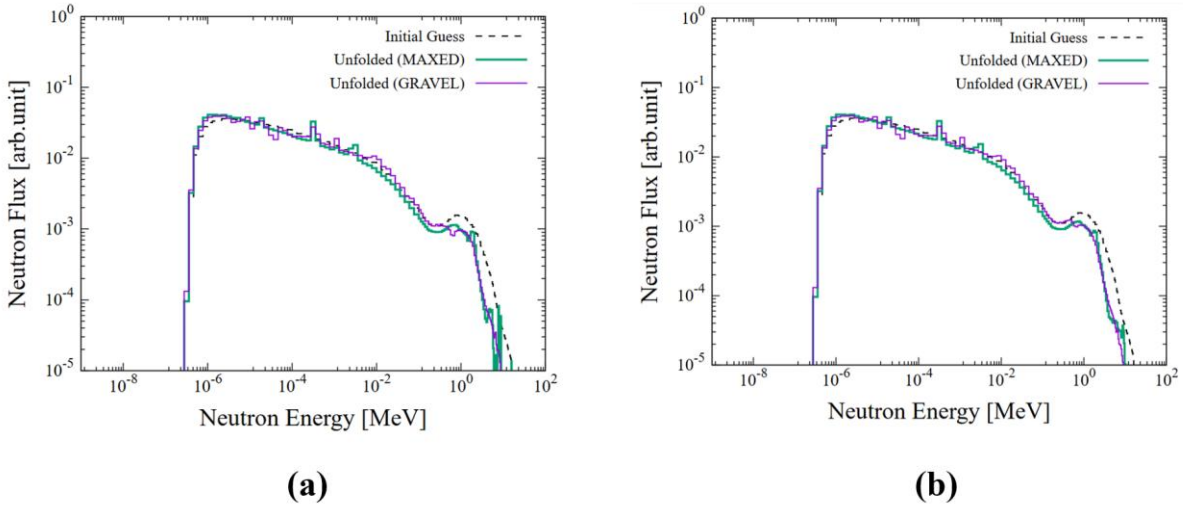

Figure 2: Unfolding neutron energy spectrum result
(a) with $^{90}Zr(n,2n)^{89}Zr$ information, (b) without $^{90}Zr(n,2n)^{89}Zr$ information

To evaluate initial guess and unfolded neutron energy spectra against experimental results, the "folding" method was employed for both the initial guess and the unfolding spectra. The unfolded neutron energy spectra obtained from the MAXED and GRAVEL codes, as well as the initial guess, were separately folded to generate corresponding results. For each foil, the comparison between the measured saturated activity per unit mass and the folded results (from the initial guess, MAXED, and GRAVEL spectra) is expressed as the E/C ratio. By normalizing $^{197}Au(n,\gamma)^{198}Au$ as 1, E/C is shown in Figure 3.

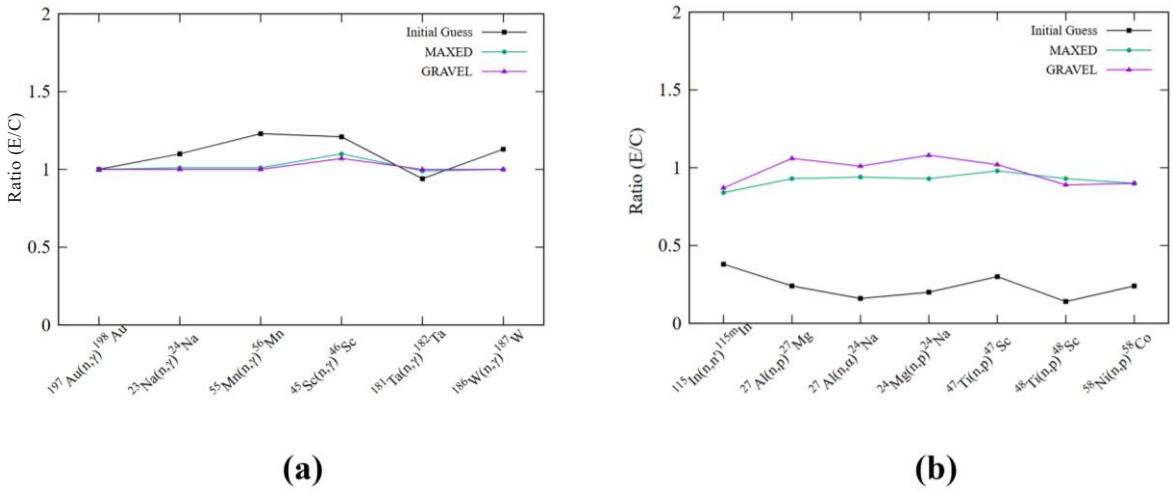

Figure 3: Ratio between experimental and calculated results for the specific activity
(a) low fluence irradiation; (b) high fluence irradiation.

For foils subjected to low-fluence irradiation, the E/C ratio for the initial guess results ranged from 0.94 to 1.23. As shown in Figure 3(a), these foils mostly exhibited a high response in the epithermal neutron region, indicating that the epithermal neutron flux exceeded the initial guess spectrum. Conversely, in Figure 3(b), foils subjected to high-fluence irradiation, the E/C ratio for the initial guess results ranged from 0.14 to 0.38, these foils showed a significant lower response in the neutron energy range above 1 MeV, highlighting the contribution of the fast neutron region. In both cases, the E/C ratios of the unfolding results were close to 1.0, demonstrating that unfolding process effectively adjusted the neutron energy spectrum to better match the experimental results.

In Figure 2(b), there is a noticeable difference between the initial guess spectrum and the unfolding results obtained from the two different unfolding codes. This variation can be attributed to the replacement of high-enrichment fuel with low-enrichment fuel.

To confirm the evaluation accuracy of two unfolding codes, we plan to conduct water phantom irradiation experiment which placed downstream of irradiation field. Various foils, such as In, Ni, and Au, will be positioned along the central axis of water phantom, and their saturated activity per unit mass will be measured. By comparing the measurement results with simulation results based on neutron energy spectra derived from the different unfolding codes, the evaluation accuracy can be verified.

4. Conclusion

The neutron energy spectrum in standard epithermal-neutron irradiation mode at the evaluation position of the KUR-HWNIF was reevaluated using the multifoil activation method. This represents the first neutron spectrum reevaluation with higher accuracy after KUR operation transitioned from high-enrichment to low-enrichment fuel. To confirm neutron energy spectrum evaluation accuracy of two different unfolding code, MAXED and GRAVEL, water phantom irradiation experiment which placed downstream of irradiation field will be conduct in the future.

References

[1] Locher G.L., Biological effects and therapeutic possibilities of neutron. American journal of roentgenology, radium therapy and nuclear medicine. vol.36, 1936, pp.1-36.

[2] Barth R.F., et al. Boron Neutron Capture Therapy of Cancer: Current Status and Future Prospects. Clinical Cancer Research, vol.11, no.11, 2005 pp. 3987-4002.

[3] Kanda K. et al., Thermal neutron standard field with a Maxwellian distribution using the KUR heavy water facility. Nuclear Instruments and Methods, vol.148, no.3, 1978, pp. 535-541.

[4] Sakurai Y. et al., Spectrum evaluation at the filter-modified neutron irradiation field for neutron capture therapy in Kyoto University Research Reactor, Nucl Instrum Methods Phys Res A, vol.531, no.3, 2004, pp. 585-595.

[5] Unesaki H. et al., Operational Experience of Kyoto University Research Reactor (KUR) with LEU Fuel, Proceeding of 33rd International Meeting on Reduced Enrichment for Research and Test Reactors, Santiago, 2011.

[6] Taniguchi T. et al., Neutron Unfolding Package Code NEUPAC-83, NEUT Research Report 83-10, 1983.

[7] Kinsey R. et al., ENDF/B Summary Documentation, BNL-NCS-17541, 1979.

[8] Reginatto M., The 'Few-Channel' Unfolding Programs in the UMG Package: MXD FC33 and GRV FC33 and IQU FC33, 215 Technical Report, 2004.

[9] KUR, KUR operation plan, https://www.rri.kyoto-u.ac.jp/KURdiv/operation.php (Access: 2025-01-12). [in Japanese]

[10] Misawa T. et al., Nuclear Reactor Physics Experiments, Kyoto University Press, Kyoto, 2010.

[11] Iwamoto O. et al., Japanese evaluated nuclear data library version 5: JENDL-5., J Nucl Sci Technol., vol.60, no.1, 2023, pp. 1-60.

[12] Little R.C. et al., Dosimetry/Activation Cross Sections for MCNP, 1984.

[13] Prateepkaew J. et al., Spectrum evaluation at the filter-modified neutron irradiation field for neutron capture therapy in Kyoto University Research Reactor, Nucl Instrum Methods Phys Res B, vol.557, 2024.

13. Angular momentum distribution and mechanisms of evaporation residue produced in multi-nucleon transfer reaction

Kohta NAKAJIMA[†1] and Yoshihiro ARITOMO [*1]

[1]Kindai University 3-4-7 Kowakae, Higashiosaka, Osaka 577-8502, Japan
[†]Email: kohta.nakajima@kindai.ac.jp

Abstract

Recently, multi-nucleon transfer (MNT) reactions have attracted attention as a method for producing neutron-rich nuclei. However, the reaction mechanism is not yet well un-derstood due to its novelty and complexity. Therefore, we aim to clarify the mechanism by investigating the angular momentum of compound nuclei (CN) produced by the MNT reaction. The angular momentum has been found to be an important physical quantity that determines whether the CN produced by the MNT reaction survives as an evaporation residue (ER) or fission and decay. In this study, we describe the reaction using a dynam-ical model and discuss the reaction mechanism from the angular momentum, the number of nucleon transfer, and the projectile-like nucleus scattering angle based on the calculation results.

1 Introduction

Up to date, elements up to $Z = 118$ have been identified. If we succeed in synthesizing the next superheavy element (SHE) from $Z = 119$, we will reach the 8th period of the periodic table. To determine how many elements can exist, it is necessary to study the production and nuclear structure of nuclei on "Islands of Stability" [1]. Theoretical calculations predict an "Islands of Stability" of 114-120 protons and 184 neutrons in the center of the SHE region. In addition, "r-process", the elemental synthesis process of the universe, is still not fully understood. This requires the production of unknown neutron-rich nuclei in the heavy-element region and the analysis of nuclear data. However, there is a limit to bringing in enough neutrons to synthesize Islands of Stability and neutron-rich nuclei in conventional fusion reactions. To solve this problem, the MNT reaction, which was frequently used in the 1970s and 1980s, is attracting renewed attention.

The utility of MNT reactions for research in unexplored areas (unknown neutron-rich heavy nuclei and superheavy nuclei) has been discussed to reach islands of stability [2]. However, the mechanism is not well understood because MNT reactions in the heavy and SHE region are novel and complex. Optimal conditions are being studied for producing the target nuclei using the MNT reaction. Here we focus on the angular momentum of CN produced in the MNT reaction. Angular momentum is known to be an important physical quantity that determines whether CN survives as ER or fission and decay [3]. In this regard, theoretical methods that can predict the angular momentum with high accuracy are highly desired.

[*]Present address: Kindai University 3-4-7 Kowakae, Higashiosaka, Osaka 577-8502, Japan

In this study, we investigated the relationship between angular momentum of CN, the projectile-like scattering angle, and the number of nucleons transferred to the target nucleus using a dynamical model. The results deal with the reaction system ^{86}Kr $+^{166}$ Er, for which experimental data are available. The objective is to calibrate the various parameters used in the theoretical model. We would like to clarify the mechanism by using the knowledge obtained in this study. In the future, we plan to discuss the synthesis of superheavy elements and the production of unknown neutron-rich nuclei from the MNT reaction with heavy nuclei.

2 Theoretical Model

2.1 Transition from the diabatic to the adiabatic state

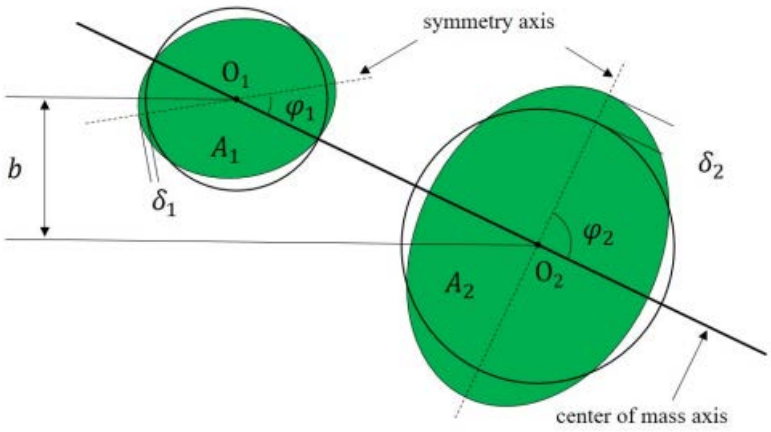

Figure 1: Geometrical diagram when both the deformed incident nucleus and the target nucleus collide with each other in the different initial orientation angles.

We adopt the dynamical model based on the multidimensional Langevin equations to calculate the time evolution of nuclear shape [4]. Potential energy changes gradually from diabatic potential to adiabatic potential [5]. Therefore, we treat the transition of two reaction stages with a time-dependent weighting function:

$$V = V_{\mathrm{diab}}(q)f(t) + V_{\mathrm{adiab}}(q)[1 - f(t)], \tag{1}$$

$$f(t) = \frac{1}{1 + \exp\left(-\frac{t}{\tau_{\mathrm{relax}}}\right)}. \tag{2}$$

Here, q denotes a set of collective coordinates representing nuclear shape. The diabatic potential $V_{\mathrm{diab}}(q)$ is calculated within the double-folding method with Migdal nucleon-nucleon forces [4]. The adiabatic potential energy $V_{\mathrm{adiab}}(q)$ of the system is calculated using an extended two-center shell model [6]. The interaction time t used here is the time starting with the contact time between the projectile and target nuclei as zero. $f(t)$ is the weighting function included the relaxation time τ_{relax}. We use the relaxation time $\tau_{\mathrm{relax}} = 10^{-21}$ s proposed in [5]. With the two-center parameterizations [7], the nuclear shape is represents by three deformation parameter is defined as follows: z_0 (distance between the centers of two potentials), δ (deformation of fragment), and α (mass asymmetry of colliding nuclei); $\alpha = \frac{A_2 - A_1}{A_2 + A_1}$, where A_1 and A_2 not only stand for the mass numbers of the projectile and target respectively [5, 8] but also are then used to indicate mass numbers of the two fission (light and heavy) fragments. The parameter

δ is defined as $\delta = \frac{3(a-b)}{2a+b}$, where a and b represent the half length of the ellipse axes in the z_0 and ρ directions, respectively [7]. In addition, we use scaling to save computation time and use the coordinate z defined as $z = \frac{z_0}{R_{\rm CN}B}$, where $R_{\rm CN}$ denotes the radius of the spherical compound nucleus and the parameter B is defined as $B = \frac{3+\delta}{3-2\delta}$. We solve the dynamical equation numerically. Therefore, we restricted the number of degrees of freedom as three deformation parameters to avoid the huge calculation time.

2.2 Consideration of the nuclear orientation

When we use the deformed nucleus, in order to consider the orientation effects we apply the axially-symmetric potential $V_{\rm ax}^{\rm sym}$ the axially-asymmetric one $V_{\rm ax}^{\rm asym}$ in the stage of the diabatic potential. When two deformed nuclei collide with each other, mainly there are four colliding patterns: the so-called tip-to-tip ($\varphi_1^0 = \varphi_2^0 = 0$), side-to-side ($\varphi_1^0 = \pi/2$, $\varphi_2^0 = \pi/2$), tip-to-side ($\varphi_1^0 = 0$, $\varphi_2^0 = \pi/2$). φ_1^0 and φ_2^0 denote the initial orientation angle of the projectile and target nuclei corresponding to φ_1 φ_2 shown in Fig. 1. Here, we investigae the reaction system of ^{86}Kr +^{166} Er. We select the various φ_2^0 of the deformed ^{166}Er nucleus fixing φ_1^0 of the spherical ^{86}Kr nucleus. In the treatment of the spherical nucleus ^{86}Kr, it makes sense to define angles even for spherical nuclei, since the model used now is treated as a classical system. In the case of the tip collision ($\varphi_2^0 = 0$), we use the diabatic potential of axially-symmetric states $V_{\rm diab} = V_{\rm ax}^{\rm sym}$. If calculations for the side collision ($\varphi_2^0 = \pi/2$) or colliding patterns of the others ($0 < \varphi_2^0 < \pi/2$) are performed, we use the diabatic potential of axially-asymmetric states $V_{\rm diab} = V_{\rm ax}^{\rm sym}$. Here, note that $V_{\rm ax}^{\rm asym}$ depends on the nuclear orientation angle. Besides, while Vdiab of the axially-asymmetric states transits to $V_{\rm adiab}$ which is the axially-symmetric states, the ellipsoid deformations are adjusted with restores of the systems using the time-dependent form, and the final ellipsoid deformations $\delta_i^{\rm in}$ [9] finished the restoration of the axially-symmetry is obtained as

$$\tilde{\delta} = \delta_i f_{\rm res}(t) + \delta_i^{\rm fin}[1 - f_{\rm res}(t)], \tag{3}$$

$$f_{\rm res}(t) = \exp\left(-\frac{t}{\tau_{\rm res}}\right), \tag{4}$$

$$\delta_i^{\rm fin} = (1+\delta_i)[\delta_i(2+\delta_i)\sin\varphi_2^0 + 1]^{-\frac{3}{4}} - 1. \tag{5}$$

$f_{\rm res}$ is the weighting function including the relaxation time $\tau_{\rm res}$, which performs the restoration from the axially-asymmetric system to the axially-symmetric one. We use $\tau_{\rm res} = 10^{-21}$ s in this paper. This value involved in the restoration of the system is also has been used in Ref. [9]. In the collision system using the deformed ^{166}Er nucleus, we treat as $\delta_i \sim 0.246$ with $\delta_i = 3\beta_2/(\beta_2 + \sqrt{16\pi/5})$ [10]. The quadrupole deformation β_2 for for the deformed nucleus^{166}Er is 0.245 [11]. The details of the calculation method are described in the Ref. [12].

2.3 Dynamical equations

The trajectory calculations [4, 5] are performed on the time-dependent unified potential energy using the multidimensional Langevin equations [5, 8] as follows:

$$\frac{dq_i}{dt} = (m^{-1})_{ij} p_j, \tag{6}$$

$$\frac{dp_i}{dt} = -\frac{\partial V}{\partial q_i} - \frac{1}{2}\frac{\partial}{\partial q_i}(m^{-1})_{jk} p_j p_k - \gamma_{ij}(m^{-1})_{jk} p_k + g_{ij} R_j(t), \tag{7}$$

$$\frac{d\vartheta}{dt} = \frac{\ell}{\mu_R R^2}, \tag{8}$$

$$\frac{d\varphi_1}{dt} = \frac{L_1}{\Im_1}, \tag{9}$$

$$\frac{d\varphi_2}{dt} = \frac{L_2}{\Im_2}, \tag{10}$$

$$\frac{d\ell}{dt} = -\frac{\partial V}{\partial \vartheta} - \gamma_{tan}\left(\frac{\ell}{\mu_R R} - \frac{L_1}{\Im_1}a_1 - \frac{L_2}{\Im_2}a_2\right) R + R g_{tan} R_{tan}(t), \tag{11}$$

$$\frac{dL_1}{dt} = -\frac{\partial V}{\partial \varphi_1} + \gamma_{tan}\left(\frac{\ell}{\mu_R R} - \frac{L_1}{\Im_1}a_1 - \frac{L_2}{\Im_2}a_2\right) a_1 - a_1 g_{tan} R_{tan}(t), \tag{12}$$

$$\frac{dL_2}{dt} = -\frac{\partial V}{\partial \varphi_2} + \gamma_{tan}\left(\frac{\ell}{\mu_R R} - \frac{L_1}{\Im_1}a_1 - \frac{L_2}{\Im_2}a_2\right) a_2 - a_2 g_{tan} R_{tan}(t). \tag{13}$$

The collective coordinates q_i represent z, δ and α, the symbol p_i denotes the momentum conjugated to q_i, and V is the multidimensional potential energy. m_{ij} and γ_{ij} are the shape-dependent collective inertia and friction tensors. We adopted the hydrodynamical inertia tensor m_{ij} in the Werner-Wheeler approximation [13]. The one-body friction tensors γ_{ij} j are evaluated within the wall-and-window formula [14, 15]. The normalized random force tensor $R_i(t)$ is assumed to be white noise, $\langle R_i(t)\rangle = 0$ and $\langle R_i(t_1)R_j(t_2)\rangle = 2\delta_{ij}\delta(t_1 - t_2)$. According to the Einstein relation [16], the strength of the random force g_{ij} is given as $\gamma_{ij}T = \sum_k g_{ik}g_{jk}$. ϑ and μ_R indicate the relative orientation of the nuclei and the reduced mass. R is the distance between the nuclear centers $\mathrm{A}_1, \mathrm{A}_2$ as shown in Fig. 1. φ_1 and φ_2 represent the orientation angles of each nucleus (see Fig. 1). $a_{1,2} = \frac{R}{2} \pm \frac{R_1 - R_2}{2}$ is the distance from the center of the fragment to the middle point between the nuclear surfaces, and $R_{1,2}$ are the nuclear radii. The total angular momentum $L_{tot} = \ell + L_1 + L_2$ is preserved. The phenomenological nuclear friction forces for separated nuclei are expressed in terms of the tangential friction γ_{tan} and the radial friction γ_R using the Woods-Saxon radial form factor suggested in Ref. [5].

3 Results and Discussion

In this study, the reaction system ^{86}Kr +^{166} Er, for which experimental data [17] are available, was chosen to calibrate the free parameters of the model in order to clarify the mechanism of the MNT reaction. The calculation results are an analysis of target-like compound nuclei (CN), and here we discuss the reaction that gain nucleons from the projectile ^{86}Kr nucleus to the target ^{166}Er nucleus. The calculation results can also analyze the reaction in which the target nucleus gives nucleons to the projectile nucleus.

The results of the mass distribution obtained from this calculation are shown in Fig. 2. The incident energy $E_{\mathrm{c.m.}}$ was determined from Ref. [17] as the calculation condition, and the Bass barrier V_{B} was obtained by calculation in the ^{86}Kr +^{166} Er from Ref. [18]. This result indicates that this calculation captures the change in mass number due to the MNT reaction.

The distribution shown in Fig. 3 is the sum of all collision angles. θ is 180 degrees is the maximum back-scattering angle and 0 degrees is the maximum forward-scattering. In this reaction system, the reaction cross section after around 23 transitional nucleons is small. Fig. 3

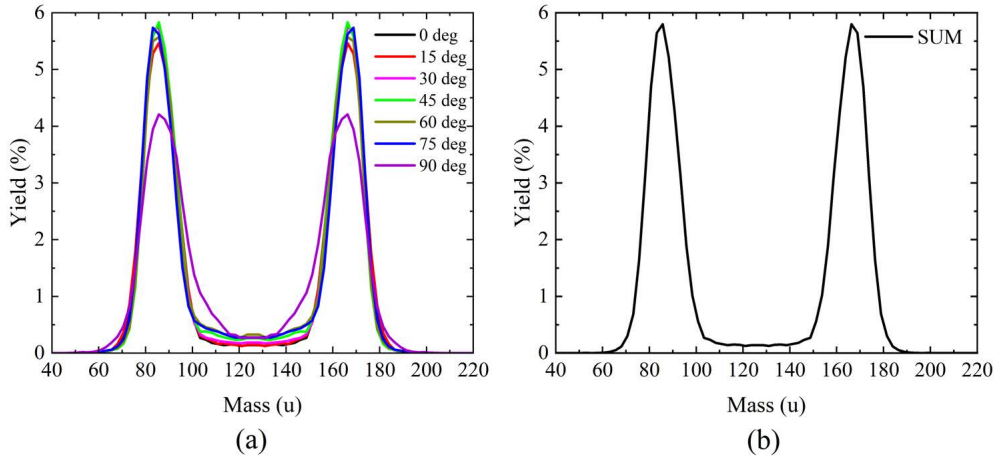

Figure 2: (a) Mass distribution per collision angle and (b) Mass distribution for all collision angles added together, calculated for the reaction system ^{86}Kr +^{166} Er with $E_{\mathrm{c.m.}} = 464$ MeV and $V_{\mathrm{B}} = 259$ MeV. The collision angle is the orientation angle at the collision due to the use of the deformed-target ^{166}Er nucleus.

(a) shows that as n_{tra} increases, the mean θ changes from 113 degrees to around 80 degrees. The change in θ from the back-scattering region to the forward-scattering region can be thought of as an increase in contact time. This indicates that the n_{tra} increases with contact time. Fig. 3 (b) shows that theta has a larger mean L_2 and saturates after 110 degrees. This means that the angular momentum brought into the CN increases as the contact time increases, but there is a limit to the angular momentum that can be brought in. Fig. 3 (c) shows the dependence of n_{tra} and mean L_2. The more intense the exchange of nucleons, the greater the angular momentum brought into the CN. These three physical quantities n_{tra}, θ, and L_2 are interrelated and may be useful in analyzing the mechanism of the MNT reaction. Our calculations also provide results for each collision angle, which we think will contribute to a detailed analysis of important factors in the mechanism that cannot be observed experimentally.

4 Summary

In this study, we analyzed the MNT reaction using a dynamical model. As a first step to clarify the mechanism, we focused on the angular momentum of CN, the scattering angle of projectile-like nucleus and the number of nucleons transferred to the target and performed calculations. It also suggests that our model may be able to contribute to future analyses of the MNT reaction. In the future, we would like to study the neutron-rich nuclei in the heavy and SHE regions for MNT reactions with heavy nuclei, leading to the understanding of "Islands of Stability" and "r-process".

References

[1] Y. T. Oganessian and K. P. Rykaczewski, Phys. Today 68(8), 32 (2015).

[2] V. I. Zagrebaev, Yu. Ts. Oganessian, M. G. Itkis, and W. Greiner, Phys. Rev. C 73, 031602(R) (2006).

[3] S. Tanaka, *et al.*, Phys. Rev. C 105, (2022) L021602.

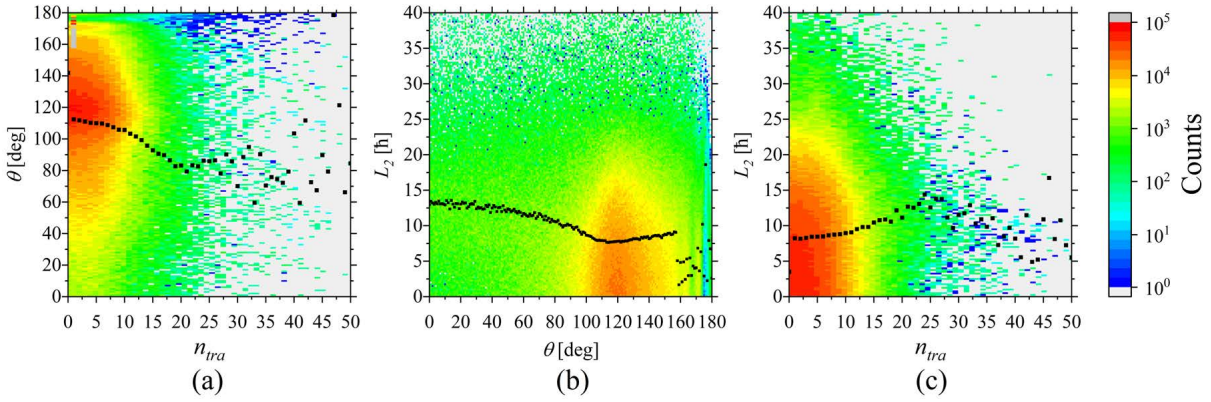

Figure 3: (a) the distribution of the relationship between n_{tra} and θ, (b) the distribution of the relationship between θ and L_2, and (c) the distribution of the relationship between n_{tra} and L_2. n_{tra} is the number of nucleons transferred to ^{166}Er. θ is the scattering angle of the projectile-like nucleus. L_2 is the angular momentum of target-like CN. The dots represent (a), (b), and (c) mean θ, L_2, and L_2, respectively.

[4] V. Zagrebaev and W. Greiner, J. Phys. G: Nucl. Part. Phys. 34, 2265 (2007).

[5] V. Zagrebaev and W. Greiner, J. Phys. G: Nucl. Part. Phys. 31, 825 (2005).

[6] V. Zagrebaev, A. Karpov, Y. Aritomo, M. Naumenko, and W. Greiner, Phys. Part. Nucl. 38, 469 (2007).

[7] J. Maruhn and W. Greiner, Zeitschrift für Physik 251, 431 (1972).

[8] Y. Aritomo and M. Ohta, Nucl. Phys. A 744, 3 (2004).

[9] V. V. Saiko and A. V. Karpov, Phys. Rev. C 99, 014613 (2019).

[10] Y. Aritomo, K. Hagino, K. Nishio, and S. Chiba, Phys. Rev. C 85, 044614 (2012).

[11] P. Moller, J. Nix, W. Myers, and W. Swiatecki, At. Data Nucl. Data Tables 59, 185 (1995).

[12] Y. Aritomo, Phys. Rev. C 80, 064604 (2009).

[13] K. T. R. Davies, A. J. Sierk, and J. R. Nix, Phys. Rev. C. 13, 2385 (1976).

[14] J. Randrup and W. Swiatecki, Nucl. Phys. A 429, 105 (1984).

[15] A. J. Sierk and J. R. Nix, Phys. Rev. C 21, 982 (1980).

[16] H. Hofmann and D. Kiderlen, Int. J. Mod. Phys. E 07, 243 (1998).

[17] Gobbi A, Lynen U, Olmi A, Rudolf G and Sann H 1981 *Proc. Int. School of Phys. 'Enrico Fermi', Course LXXVII (Varenna, 1979)* (Amsterdam: North-Holland), p. 1

[18] R. Bass, *Nuclear Reactions with Heavy Ions* (Springer, 1980).

Acknowledgments

The Langevin calculation were performed using the cluster computer system (Kindai-VOSTOK) which is supported by JSPS KAKENHI Grant Number 20K04003 and Research funds for External Fund Introduction 2021 by Kindai University.

14. Possibility of Synthesizing New Superheavy Element using ^{51}V, ^{54}Cr Projectiles

Kosuke KAWAI† and Yoshihiro ARITOMO

Kindai University, Higashi-osaka, Osaka 577-8502, Japan
†Email: kawai.kosuke@kindai.ac.jp

Abstract

Hot fusions using ^{48}Ca beam and actinides as targets were successful for many superheavy elements up to Og (Z=118). When synthesizing element 119 using ^{48}Ca, the target would be Es (Z=99). However, actinides after Es have so short half-lives. It is not practical to use Es as a target. Therefore, it is necessary to use heavier projectiles than ^{48}Ca such as V and Cr. This allows the target to be determined relatively stable nuclide in actinides. The synthesis of superheavy elements can be divided into three stages depending on the reaction times. They are the touching process, the formation process, and the decay process. The evaporation residue cross sections can be calculated by combining three probabilities of these processes. We calculated the evaporation residue cross sections using ^{51}V and ^{54}Cr as projectiles and actinides as targets. We also analyzed the effects of different combinations of projectile and target. We mainly discussed the effect of the relationship between the reaction Q-value and the Coulomb barrier height.

1 Introduction

In recent years, research on new superheavy elements has been conducted around the world. Superheavy elements were discovered mainly by the heavy-ion fusion reaction, and from Fl (Z=114) to Og (Z=118) were discovered by hot fusion using ^{48}Ca beam and actinides as targets [1]. The advantage of using ^{48}Ca is the large ratio of neutrons over protons.

Hot fusion is one of the methods for synthesizing superheavy elements. Actinides are used as target in this method. The reason why this is called hot fusion is that the formed compound nucleus is relatively excited.

When synthesizing element 119 with ^{48}Ca beam, the target would be Es (Z=99). However, actinides after Es have so short half-lives. It is not practical to use Es as a target. Therefore, it is necessary to use heavier projectile than ^{48}Ca such as V and Cr. This allows the target to be determined relatively stable nuclide in actinide.

In 2023, a Russian group reported the successful synthesis of ^{54}Cr+^{238}U→$^{292-x}$Lv [2]. In 2024, an American group reported the successful synthesis of ^{50}Ti+^{244}Pu→$^{294-x}$Lv [3]. Successful cases of hot fusion using heavier projectiles than ^{48}Ca are extremely rare, and it is expected that new superheavy elements will be synthesized with heavier projectiles.

In this work, we compared the ^{51}V and ^{54}Cr projectiles. We calculated the evaporation residue cross sections of ^{51}V+^{238}U→$^{289-x}$Mc, ^{54}Cr+^{238}U→$^{292-x}$Lv, ^{51}V+^{248}Cm→$^{299-x}$119 and ^{54}Cr+^{243}Am→$^{297-x}$119. We also analyzed the effects of different combinations of projectile and target.

2 Model

2.1 Evaporation residue cross section

The synthesis of superheavy elements includes three stages. The first is the projectile-target contact process. This determines the touching probability. The second is the competition process between compound nucleus formation and quasi-fission. This determines the formation probability. The third is the decay process. This determines the survival probability of the excited compound nucleus. The evaporation residue cross section σ_{ER} is calculated by combining these three probabilities, following

$$\sigma_{ER} = \frac{\pi\hbar^2}{2\mu_0 E_{c.m.}} \sum_{\ell=0}^{\infty} (2\ell+1) T_\ell(E_{c.m.}, \ell) P_{CN}(E^*, \ell) W_{sur}(E^*, \ell), \tag{1}$$

where μ_0 denotes the reduced mass in the entrance channel. $E_{c.m.}$ and E^* denote the incident energy in the center-of-mass frame and the excitation energy of the composite system, respectively. T_ℓ is the barrier penetration coefficient of the ℓth partial wave through the potential barrier. P_{CN} is the probability of forming a compound nucleus in the competition with quasi-fission. W_{sur} is the survival probability of the excited compound nucleus.

We use incident and excitation energies depending on the reaction stages, reaction Q-value is used for these energies conversion, following

$$E^* = E_{c.m.} + Q, \tag{2}$$

$$Q = \{M_{CN} - (M_P + M_T)\}c^2, \tag{3}$$

where M_{CN}, M_P, and M_T denote the mass of the compound nucleus, the projectile nucleus, and the target nucleus, respectively. We calculate the reaction Q-value using the mass excesses of the mass table [4]. M_{CN} is the uncertain parameter because the mass of a superheavy element cannot be measured. Therefore, we often correct the reaction Q-value to match the calculated results to the experimental cross sections. This is because the reaction Q-value fluctuates depending on the uncertainty of the compound nucleus mass.

2.2 Dynamical model

We use the multidimensional Langevin equation to describe the time evolution of the shape of the nucleus. The nuclear shape is defined by two-center parametrization [5, 6], which has three deformation parameters, z, δ, and α. z is the parameter related to the distance between two potential centers, δ is the deformation of the fragments, and $\alpha = (A_1 - A_2)/(A_1 + A_2)$ is the mass asymmetry of the two fragments, where A_1 and A_2 are the mass numbers of heavy and light fragments [7].

For given value of a temperature of a system T, the adiabatic potential energy is defined as

$$V(q, \ell, T) = V_{LD}(q) + \frac{\hbar\ell(\ell+1)}{2I(q)} + V_{SH}(q, T), \tag{4}$$

$$V_{LD} = E_S(q) + E_C(q), \tag{5}$$

$$V_{SH}(q, T) = E^0_{\text{shell}}(q)\Phi(T), \tag{6}$$

$$\Phi(T) = \exp\Big(-\frac{aT^2}{E_d}\Big), \tag{7}$$

where $q = \{z, \delta, \alpha\}$ is the deformation coordinate. V_{LD} is the potential energy calculated with the finite-range liquid drop model, given as the sum of the surface energy E_S [8] and the Coulomb

energy E_C. V_{SH} is the shell correction energy evaluated for each temperature using the factor $\Phi(T)$, in which E_d is the shell damping energy chosen to be 20 MeV [9] and a is the level density parameter. At zero temperature ($T = 0$), the shell correction energy reduces to E^0_{shell}. The second term on the right hand side of Eq.(4) is the rotational energy for an angular momentum ℓ [7], with a moment of inertia $I(q)$.

The multidimensional Langevin equations [7, 10] are given as

$$\frac{dq_i}{dt} = (m^{-1})_{ij} p_j, \tag{8}$$

$$\frac{dp_i}{dt} = -\frac{\partial V}{\partial q_i} - \frac{1}{2}\frac{\partial}{\partial q_i}(m^{-1})_{jk} p_j p_k - \gamma_{ij}(m^{-1})_{jk} p_k + g_{ij} R_j(t), \tag{9}$$

where $q_i = \{z, \delta, \alpha\}$ is the deformation coordinate, and $p_i = m_{ij} dq_i/dt$ is a momentum conjugate to coordinate q_i. In the Langevin equation, m_{ij} and γ_{ij} are the shape-dependent collective inertia parameter and the friction tensor, respectively. The wall-and-window one-body dissipation [11] is adopted for the friction tensor. A hydrodynamical inertia tensor is adopted with the Werner-Wheeler approximation for the velocity field [12].

The normalized random force $R_i(t)$ is assumed to be that of white noise, that is,

$$\langle R_i(t) = 0 \rangle, \quad \langle R_i(t_1) R_j(t_2) \rangle = 2\delta_{ij}\delta(t_1 - t_2). \tag{10}$$

The strength of the random force g_{ij} is related to the friction tensor γ_{ij} by the classical Einstein relation,

$$\sum_k g_{ik} g_{jk} = \gamma_{ij} T. \tag{11}$$

We calculate the fusion probability using the dynamical model.

2.3 Statistical model

We use the statistical model [13, 14] to estimate the survival probability of excited compound nucleus. The survival probability is calculated, following

$$W_{sur} = \prod_{i=1}^{N} \frac{\Gamma_n^{(i)}}{\Gamma_n^{(i)} + \Gamma_f^{(i)}}, \tag{12}$$

where Γ_n and Γ_f are neutron emission width and fission width, respectively. And i means the each step of neutron emission, and N is the neutron number emitted before the nucleus reaches below the particle threshold and the fission barrier.

In the equation (4), Γ_n/Γ_f is calculated as follows [14],

$$\frac{\Gamma_n}{\Gamma_f} = \frac{k_{coll}(gr.st.)}{k_{coll}(saddle) \cdot k_{kramers}} A_0 \exp\Big\{2\sqrt{a_n(E_{int} - B_n)} - 2\sqrt{a_f(E_{int} - B_f)}\Big\}, \tag{13}$$

where $k_{coll}(gr.st.)$ and $k_{coll}(saddle)$ are collective enhancements of the ground state and the saddle point [14], and $k_{kramers}$ is the Kramers factor [14, 15]. The factors in front of the exponential function are combined into A_0, and a_n and a_f are the level density parameters of the ground state and the saddle point, respectively. E_{int} is the intrinsic excitation energy of the compound nucleus. B_n is the neutron separation energy and B_f is the fission barrier height.

The statistical model contains many uncertain parameters. One of them is the fission barrier height. We use the shell correction energy of the mass table [4] as the fission barrier height. In the superheavy region, the shell correction energy can be approximated as the fission barrier height because superheavy elements have almost no fission barrier of liquid drop energy.

3 Results and discussion

3.1 Calibration to experimental value

As discussed in 2.1, the reaction Q-value should be corrected to match the calculated results to the experimental values. In addition, the regions without experimental values are calculated after calibrating the parameters in a system with experimental values. This allows for relative comparisons even if there are no experimental values. In this study, ^{48}Ca+^{245}Cm and ^{48}Ca+^{249}Cf were chosen for the calibration of the ^{238}U target and element 119 calculations, respectively. This is because these atomic and mass numbers of compound nuclei are close.

3.2 Reactions of ^{51}V+^{238}U and ^{54}Cr+^{238}U

Figure 1 shows the evaporation residue cross sections of ^{51}V+^{238}U and ^{54}Cr+^{238}U reactions for the excitation energy. ^{51}V+^{238}U is about 3 fb and ^{54}Cr+^{238}U is about 0.1 pb. The evaporation residue cross sections using ^{54}Cr are larger than using ^{51}V. We realized that this is an effect of the relationship between reaction Q-value and Coulomb barrier height. Figure 2 shows the capture cross sections of ^{51}V+^{238}U and ^{54}Cr+^{238}U reactions. Figure 2 (a) is for the incident energies and (b) is for the excitation energies. Focusing on (a), the capture cross sections using ^{51}V are larger than using ^{54}Cr at the same incident energy. This is the effect of the Coulomb barrier height. Adding the reaction Q-value to (a), this is converted to the excitation energy (b). Then, the capture cross sections using ^{54}Cr are larger than using ^{51}V at the same excitation energy. This is because the reaction Q-value of using ^{51}V is relatively small. Small capture cross sections have negative effects to the evaporation residue cross sections at the same excitation energy.

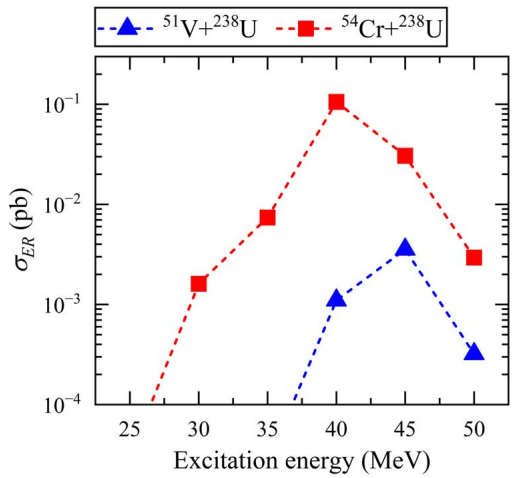

Figure 1: Excitation functions for ^{51}V+^{238}U (blue triangles) and ^{54}Cr+^{238}U reactions (red squares) for the summation of all evaporation channels. The dashed lines through the plot are drawn to guide the eye.

3.3 Reactions of ^{51}V+^{248}Cm and ^{54}Cr+^{243}Am

Figure 3 shows the evaporation residue cross sections of ^{51}V+^{248}Cm and ^{54}Cr+^{243}Am reactions for the excitation energy. ^{51}V+^{248}Cm is about 0.04pb and ^{54}Cr+^{243}Am is about 0.2pb. The evaporation residue cross sections using ^{54}Cr are larger than using ^{51}V. We realized that this is an effect of the relationship between reaction Q-value and Coulomb barrier height. Figure

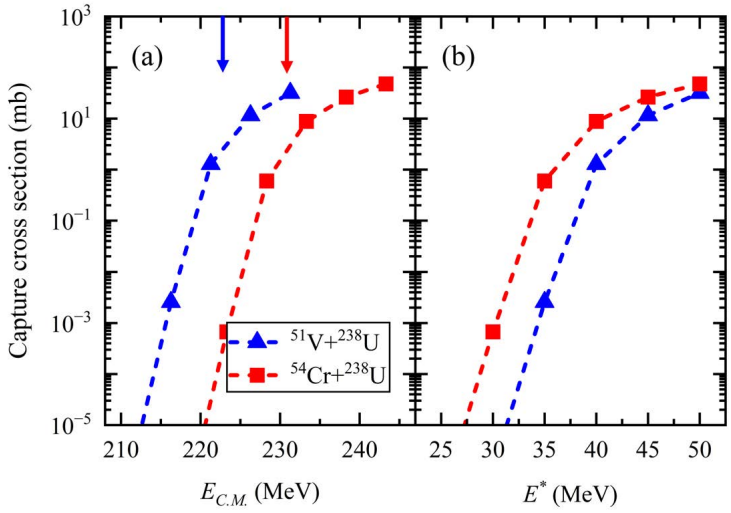

Figure 2: Capture cross sections of ^{51}V+^{238}U and ^{54}Cr+^{238}U reactions. The dashed lines through the plot are drawn to guide the eye. (a) Incident energy functions. Colored arrows denote Bass barriers. (b) Excitation functions.

4 shows the capture cross sections of ^{51}V+^{248}Cm and ^{54}Cr+^{243}Am reactions. Since the same thing happens as described in 3.1, the explanation is omitted.

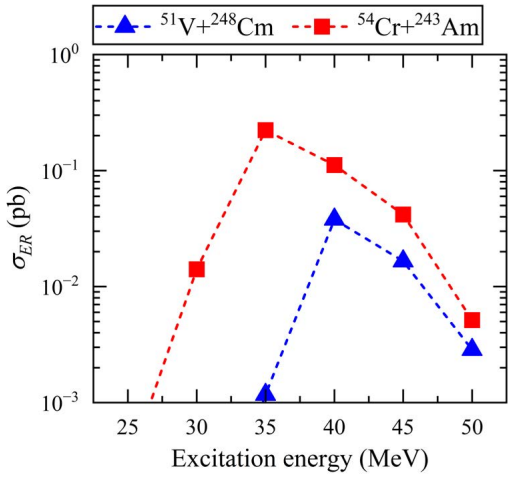

Figure 3: Excitation functions for ^{51}V+^{248}Cm (blue triangles) and ^{54}Cr+^{243}Am reactions (red squares) for the summation of all evaporation channels. The dashed lines through the plot are drawn to guide the eye.

4 Summary

We realized that the relationship between the reaction Q-value and the Coulomb barrier height is important in the synthesis of superheavy elements. In the comparison between ^{51}V+^{238}U and ^{54}Cr+^{238}U, the latter has larger evaporation residue cross sections. Furthermore, in the comparison between ^{51}V+^{248}Cm and ^{54}Cr+^{243}Am, the latter has larger evaporation residue cross sections. These results can be explained by the effect of the relatively small reaction

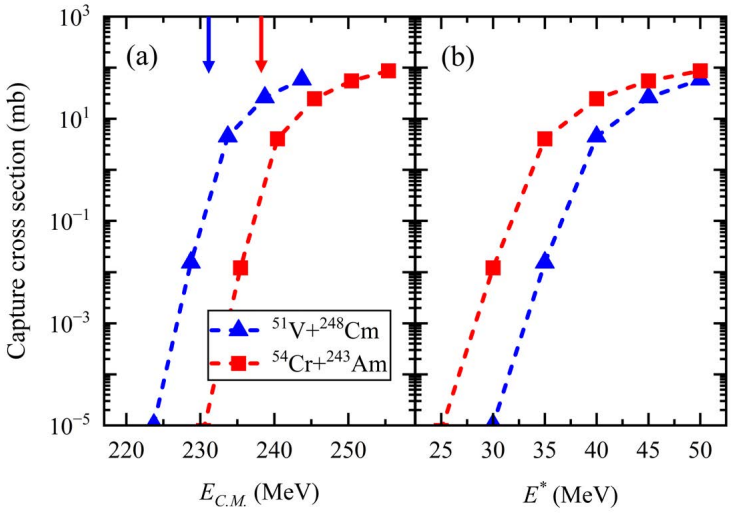

Figure 4: Capture cross sections of ^{51}V+^{248}Cm and ^{54}Cr+^{243}Am reactions. The dashed lines through the plot are drawn to guide the eye. (a) Incident energy functions. Colored arrows denote Bass barriers. (b) Excitation functions.

Q-value using ^{51}V projectile. In the same target or compound nucleus case, using ^{51}V has an advantage over using ^{54}Cr in terms of the Coulomb barrier height, but has a greater disadvantage in terms of the reaction Q-value. Due to the above factors, we thought ^{54}Cr+^{243}Am is better combination than ^{51}V+^{248}Cm in the synthesis of element 119. According to our calculations and analysis, the reaction Q-value might be a more important factor than previously thought.

References

[1] Yu. Ts. Oganessian, *et al.*, Rhys. Rev. C 70, 064609 (2004).
[2] Joint Institute for Nuclear Research, https://www.jinr.ru/posts/v-lyar-oiyai-vpervye-v-mire-sintezirovan-livermorij-288/, (accessed 2025-03-07).
[3] J. M. Gates, *et al.*, Phys. Rev. Lett. 133, 172502 (2024).
[4] P. Möller, J. R. Nix, W. D. Myers and W. J. Swiatecki, Atomic Data and Nuclear Data Tables 59, 185-381 (1995).
[5] J. Maruhn and W. Greiner, Z. Phys. 251, 431 (1972).
[6] K. Sato, A. Iwamoto, K. Harada, S. Yamaji, and S. Yoshida, Z. Phys. A 288, 383 (1978).
[7] Y. Aritomo and M. Ohta, Nucl. Phys. A 744, 3 (2004).
[8] H. J. Krappe, J. R. Nix, and A. J. Sierk, Phys. Rev. C 20, 992 (1979).
[9] A. N. Ignatyuk, G. N. Smirenkin, and A. S. Tishin, Sov. J. Nucl. Phys. 21, 255 (1975).
[10] V. Zagrebaev and W. Greiner, J. Phys. G 31, 825 (2005).
[11] H. Feldmeier, Rep. Prog. Phys. 50, 915 (1987).
[12] K. T. R. Davies, A. J. Sierk, and J. R. Nix, Phys. Rev. C 13, 2385 (1976).
[13] N. Bohr and J. A. Wheeler, Phys. Rev. 56, 426 (1939).
[14] M. Ohta, Proceedings of Fusion Dynamics at the Extremes, Dubna, 25-27 May 2000, World Scientific, Singapore, 2001, pp. 110-122.
[15] H. A. Kramers, Physica(Utrecht) 7, 284 (1940).

15. Development of a calculation system contributing to the consideration of production methods for Auger electron emitters

Seiya SAKAI[†1], Hideaki OTSU[1], Osamu IWAMOTO[2], Nobuyuki IWAMOTO[2], Shinsuke NAKAYAMA[2], Hidetoshi KIKUNAGA[3], and Tokio FUKAHORI[2]

[1]RIKEN Nishina Center, 2-1, Hirosawa, Wako-shi, Saitama-ken, 351-0198, Japan
[2]Japan Atomic Energy Agency, 2-4, Shirakata, Tokai-mura, Naka-gun, Ibaraki-ken, 319-1195, Japan
[3]Research Center for Electron Photon Science, Tohoku University, 1-2-1, Mikamine, Taihaku-ku, Sendai-shi, Miyagi-ken, 982-0826, Japan
[†]Email: seiya.sakai@riken.jp

Abstract

The SEKIGUCHI Three-Nucleon Force Project is developing a CCONE-based calculation system contributing to the consideration of production methods for nuclides useful in applied science field. Using this system, the optimal production method for Auger electron emitters, which are medical RIs, from light particle (up to α particle) injection reactions was considered.

1 Introduction

Recently nuclear medicine therapy using nuclides emitting α rays and Auger electrons is gathering attention [1]. α rays and Auger electrons have a higher linear energy transfer than β rays and are expected to enable the therapy with little damage to normal cells surrounding the tumor. Especially Auger electron emitters have an advantage that their daughter nuclei are less likely to decay compared to α ray emitters. Since there are many Auger electron emitters, and their production reactions and paths are diverse, the best nuclide for practical use and its production method have not been established at present. We are also working for improving the accuracy of nuclear data considering three-nucleon forces in the SEKIGUCHI Three-Nucleon Force Project [2]. Based on the above situation, we have developed a system to calculate and illustrate nuclide production cross sections and Thick Target Yield (TTY) from various nuclear reactions. In this article, an overview of the developed calculation system and a consideration of the optimal production method for Auger electron emitters using this system are described.

2 Development of a calcualtion system

An overview of the developed calculation system is summarized below.

- Projectile (n, p, d, t, ^{3}He, α, γ), kinetic energy of projectile (E_{proj}), target (including natural compositions), and produced nuclide can be selected.

- The nuclear reaction model calculation code CCONE [3] (default calculation) is used to calculate nuclide production cross sections.
- The CCONE calculated values are converted to ENDF-6 format [4] to compare with existing nuclear data libraries.
- The sum of multiple nuclide production cross sections (e.g., ^{77}Br+^{77}Kr (decays to ^{77}Br with a half-life of 1.24 hours [5])) can also be output.

3 Consideration of production methods for Auger electron emitters

3.1 Input

Using the developed calculation system, we considered the optimal production method for Auger electron emitters. The conditions in this consideration are as follows.

- Projectile: n, p, d, α, γ
- E_{proj}: 1 - 50 MeV
- Target: natural element target
- Produced nuclide:
  ^{77}Br, ^{77}Br+^{77}Kr, ^{71}Ge, ^{97}Ru, ^{97}Ru+^{97}Rh, ^{67}Ga, ^{67}Ga+^{67}Ge, ^{64}Cu, ^{99}Mo, ^{119}Sb

Since t and ^{3}He are practically difficult to use for projectile, they were excluded from this consideration. Moreover, in the CCONE, ions larger than α cannot be injected.

3.2 Nuclide production cross section

Here the result for ^{77}Br is described as an example. First, at the projectiles and E_{proj} shown in Section 3.1, we focus on natural element targets with reactions that ^{77}Br production cross section is greater than 1 mb. As a result, ^{75}As, $^{\mathrm{nat}}$Se, $^{\mathrm{nat}}$Br, and $^{\mathrm{nat}}$Kr remain as natural element targets. ^{77}Br production cross section when targeting ^{75}As, $^{\mathrm{nat}}$Se, $^{\mathrm{nat}}$Br, and $^{\mathrm{nat}}$Kr are shown in Figure 1. Moreover, top 5 reactions with the largest ^{77}Br production cross section is shown in Table 1. From Figure 1 and Table 1, the reaction that maximizes the ^{77}Br production cross section is found to be α+^{75}As ($E_{\mathrm{proj}} = 25$ MeV).

3.3 Thick Target Yield

The yield depends not only on the nuclide production cross section, but also on the stopping power and the target thickness. Therefore, we calculated the stopping power for p, d, and α using SRIM [6](Stopping and Range of Ions in Matter), and calculated Thick Target Yield [7](TTY, yield for a target with infinite thickness) when the projectiles are p, d, and α. TTY is obtained by

$$\mathrm{TTY} = \int_0^{E_{\mathrm{proj}}} \frac{\sigma(E)}{S(E)} dE, \tag{1}$$

where $\sigma(E)$ and $S(E)$ are the nuclide production cross section and the stopping power, respectively. ^{77}Br TTY when targeting ^{75}As, $^{\mathrm{nat}}$Se, $^{\mathrm{nat}}$Br, and $^{\mathrm{nat}}$Kr are shown in Figure 2. Moreover, top 5 reactions with the largest ^{77}Br TTY is shown in Table 2. Note that here we compare TTYs at E_{proj} of 50 MeV. From Figure 2 and Table 2, the reaction that maximizes the ^{77}Br TTY is found to be p+$^{\mathrm{nat}}$Se (except when the projectiles are n and γ).

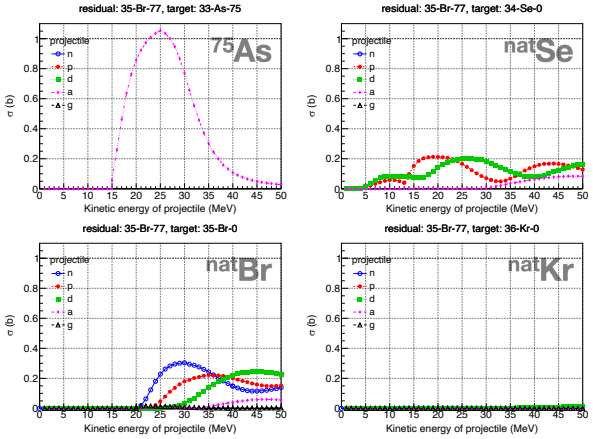

Figure 1: ^{77}Br production cross section when targeting ^{75}As (top left), $^{\mathrm{nat}}$Se (top right), $^{\mathrm{nat}}$Br (bottom left), and $^{\mathrm{nat}}$Kr (bottom right).

Table 1: Top 5 reactions with the largest ^{77}Br production cross section. E_{proj} when the ^{77}Br production cross section is at its maximum is shown in parentheses.

rank	reaction	^{77}Br production cross section
1	α+^{75}As	1.054 b (25 MeV)
2	n+$^{\mathrm{nat}}$Br	0.304 b (30 MeV)
3	d+$^{\mathrm{nat}}$Br	0.247 b (45 MeV)
4	p+$^{\mathrm{nat}}$Br	0.221 b (35 MeV)
5	p+$^{\mathrm{nat}}$Se	0.213 b (19 MeV)

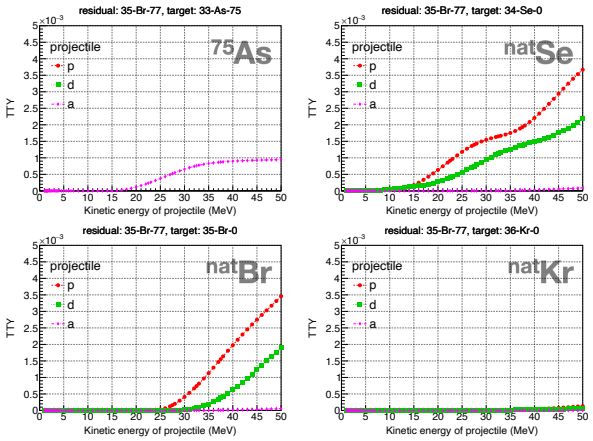

Figure 2: ^{77}Br TTY when targeting ^{75}As (top left), $^{\mathrm{nat}}$Se (top right), $^{\mathrm{nat}}$Br (bottom left), and $^{\mathrm{nat}}$Kr (bottom right).

Table 2: Top 5 reactions with the largest ^{77}Br TTY.

rank	reaction	^{77}Br TTY (except n and γ)
1	p+$^{\mathrm{nat}}$Se	3.669×10^{-3}
2	p+$^{\mathrm{nat}}$Br	3.460×10^{-3}
3	d+$^{\mathrm{nat}}$Se	2.177×10^{-3}
4	d+$^{\mathrm{nat}}$Br	1.900×10^{-3}
5	α+^{75}As	0.945×10^{-3}

3.4 Results for other Auger electron emitters

Table 3 shows the reactions that maximize the production cross section and TTY for ^{77}Br and other Auger electron emitters. The reason why there is no α injection reaction among the reactions that maximize the TTY is thought to be because the stopping power for α is large and the TTY becomes small.

4 Evaluation of unwanted nuclides that may be produced

It is important to know how many unwanted nuclides (impurities) other than Auger electron emitters can be produced when Auger electron emitters are produced via the reactions summarized in Table 3. Therefore, we illustrated the production cross sections of all residual nuclei that can be produced when the following conditions are satisfied.

Table 3: Reactions that maximize the production cross section and TTY for ^{77}Br and other Auger electron emitters. E_{proj} when the nuclide production cross section is at its maximum is shown in parentheses.

nuclide	nuclide production cross section	TTY (except n and γ)
^{77}Br	α+^{75}As (25 MeV)	p+$^{\mathrm{nat}}$Se
^{77}Br+^{77}Kr	α+^{75}As (25 MeV)	p+$^{\mathrm{nat}}$Se
^{71}Ge	d+$^{\mathrm{nat}}$Ga (13 MeV)	d+$^{\mathrm{nat}}$Ga
^{97}Ru	α+$^{\mathrm{nat}}$Mo (38 MeV)	p+^{103}Rh
^{97}Ru+^{97}Rh	α+$^{\mathrm{nat}}$Mo (38 MeV)	p+^{103}Rh
^{67}Ga	α+$^{\mathrm{nat}}$Cu (24 MeV)	p+$^{\mathrm{nat}}$Zn
^{67}Ga+^{67}Ge	α+$^{\mathrm{nat}}$Zn (18 MeV)	p+$^{\mathrm{nat}}$Zn
^{64}Cu	n+$^{\mathrm{nat}}$Zn (11 MeV)	d+$^{\mathrm{nat}}$Zn
^{99}Mo	n+$^{\mathrm{nat}}$Mo (15 MeV)	p+$^{\mathrm{nat}}$Mo
^{119}Sb	d+$^{\mathrm{nat}}$Sn (25 MeV)	p+$^{\mathrm{nat}}$Sn

- If the maximum nuclide production cross section exceeds 1 mb in the CCONE calculation.
- If experimental values exist in EXFOR [8].

When using natural element targets, the reaction that maximizes the ^{77}Br TTY was p+$^{\mathrm{nat}}$Se. On the other hand, when using enriched targets, the reaction that maximizes the ^{77}Br TTY becomes p+^{78}Se. Therefore, we confirmed all residual nuclei that can be produced by p+^{78}Se and found that ^{69,70}Ga, $^{72\text{-}74}$Ge, $^{72\text{-}77}$As, $^{74\text{-}77}$Se, and ^{75,76,78,79}Br can be produced in addition to ^{77}Br. Assuming that ^{69,70}Ga, $^{72\text{-}74}$Ge, $^{72\text{-}77}$As, and $^{74\text{-}78}$Se with different atomic number from ^{77}Br can be chemically separated, the production yields of ^{75,76,78,79}Br become an issue. $^{75\text{-}79}$Br production cross sections by p+^{78}Se are shown in Figure 3.

According to the CCONE calculation, the ^{77}Br production cross section by p+^{78}Se is maximum at E_{proj} of 20 MeV. Therefore, if E_{proj} is 20 MeV, only ^{78,79}Br become an issue, since the ^{75,76}Br production cross sections are zero below E_{proj} of 20 MeV. To estimate how many ^{78,79}Br are produced, we confirmed the time variation of nuclide production yield $N(t)$ [7]. $N(t)$ is defined as

$$N(t) = \begin{cases} \frac{I_0 y T_h}{\ln 2}\left\{1 - \exp\left(-\frac{\ln 2}{T_h}t\right)\right\} & (\text{for unstable nuclide}) \\ I_0 y t & (\text{for stable nuclide}) \end{cases}, \tag{2}$$

where I_0 $[1/h]$ is the beam intensity (this time we set $I_0 = 1$), y is the TTY at a given E_{proj}, T_h $[h]$ is the half-life, and t $[h]$ is the beam irradiation time. Time variation of $^{77\text{-}79}$Br production yields by p+^{78}Se (E_{proj} = 20 MeV) is shown in Figure 4. Moreover, Table 4 shows the $^{77\text{-}79}$Br TTYs by p+^{78}Se (E_{proj} = 20 MeV), half-life of $^{77\text{-}79}$Br [5], and $^{77\text{-}79}$Br production yields after irradiating 24 hours. From Figure 4 and Table 4, it is found that ^{78,79}Br production yields are less than 1% of ^{77}Br production yield after irradiating 24 hours.

5 Summary

We have developed a CCONE-based calculation system contributing to the consideration of production methods for nuclides useful in applied science field, such as Auger electron emitters. By using this system, the reactions that maximize nuclide production cross sections and TTYs, unwanted nuclides that can be produced, and the time variation of nuclide production yield

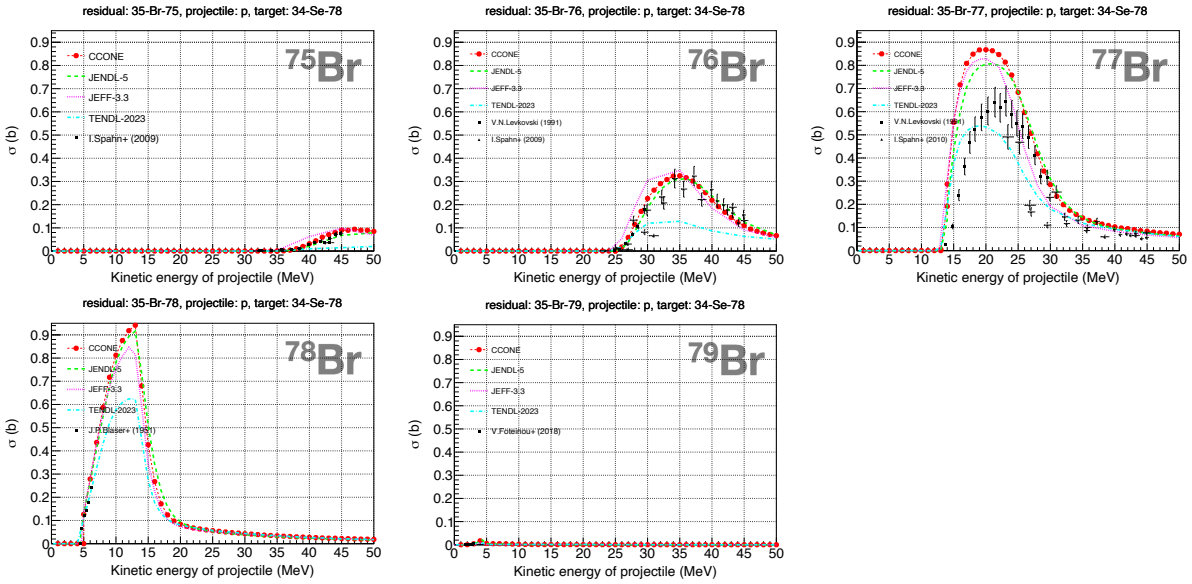

Figure 3: $^{75\text{-}79}$Br production cross sections by p+^{78}Se. As a reference, nuclear data library values [9–11] and experimental values [12–16] are also shown.

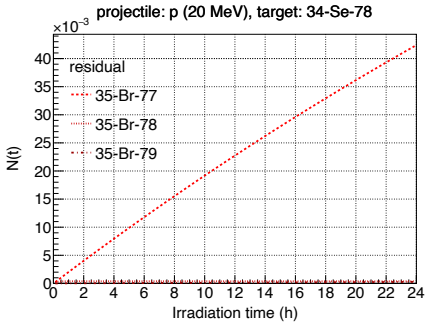

Figure 4: Time variation of $^{77\text{-}79}$Br production yields by p+^{78}Se ($E_{\mathrm{proj}} = 20$ MeV).

Table 4: $^{77\text{-}79}$Br TTYs by p+^{78}Se ($E_{\mathrm{proj}} = 20$ MeV) (y), half-life of $^{77\text{-}79}$Br [5] (T_h), and $^{77\text{-}79}$Br production yields after irradiating 24 hours ($N(t = 24\ h)$).

nuclide	y	T_h	$N(t = 24\ h)$
^{77}Br	2.036×10^{-3}	2.38 d	4.239×10^{-2}
^{78}Br	2.494×10^{-3}	6.45 m	3.868×10^{-4}
^{79}Br	1.117×10^{-5}	-	2.640×10^{-4}

can be understood. In addition, the CCONE calculated values and nuclear data library values can be easily compared with experimental values. In the future, we will apply this system to nuclides other than Auger electron emitters to improve the accuracy of nuclear data. We will also compare with experimental values in quantities other than nuclide production cross sections and TTYs, and confirm how the consistency with the experimental values changes by adjusting the CCONE parameters.

References

[1] Filosofov, D. et al., Potent candidates for Targeted Auger Therapy: Production and radiochemical considerations, Nucl. Med. Biol., vol.94-95, 2021, pp.1-19.

[2] TOMOE, JST ERATO Three-Nucleon Force Project, https://www.jst.go.jp/erato/sekiguchi/ (ac-cessed 2024-11-14).

[3] Iwamoto, O. et al., The CCONE Code System and its Application to Nuclear Data Evaluation for Fission and Other Reactions, Nucl. Data Sheets, vol.131, 2016, pp.259-288.

[4] Brown, D.A., ENDF-6 Formats Manual - Data Formats and Procedures for the Evaluated Nuclear Data Files ENDF/B-VI, ENDF/B-VII and ENDF/B-VIII, Report BNL-224854-2023-INRE, 2023.

[5] NuDat 3.0, https://www.nndc.bnl.gov/nudat3/ (accessed 2024-11-14).

[6] Ziegler, J.F. et al., SRIM - The stopping and range of ions in matter (2010), Nucl. Instrum. Methods Phys. Res., Sect. B, vol.268, no.11, 2010, pp.1818-1823.

[7] Otuka, N. and Takács, S., Definitions of radioisotope thick target yields, Radiochim. Acta, vol.103, no.1, 2015, pp.1-6.

[8] Experimental Nuclear Reaction Data (EXFOR), https://www-nds.iaea.org/exfor/ (accessed 2024-11-14).

[9] Iwamoto, O. et al., Japanese evaluated nuclear data library version 5: JENDL-5, J. Nucl. Sci. Technol., vol.60, no.1, 2023, pp.1–60.

[10] Plompen, A.J.M. et al., The joint evaluated fission and fusion nuclear data library, JEFF-3.3, Eur. Phys. J. A, vol.56, no.181, 2020, pp.1-108.

[11] Koning, A.J. et al., TENDL: Complete Nuclear Data Library for Innovative Nuclear Science and Technology, Nucl. Data Sheets, vol.155, 2019, pp.1-55.

[12] Spahn, I. et al., New cross section measurements for production of the positron emitters ^{75}Br and ^{76}Br via intermediate energy proton induced reactions, Radiochim. Acta, vol.97, no.10, 2009, pp.535-541.

[13] Levkovski, V.N., Activation cross sections for the nuclides of medium mass region (A = 40-100) with medium energy (E = 10-50 MeV) protons and α-particles (Experiment and Systematics), Inter-Vesti, Moscow, Russia, 1991.

[14] Spahn, I. et al., New cross section measurements for the production of the Auger electron emitters ^{77}Br and ^{80m}Br, Radiochim. Acta, vol.98, no.12, 2010, pp.749-755.

[15] Blaser, J.P. et al., Anregungsfunktionen und Wirkungsquerschnitte der (p,n)-Reaktion (II), Helv. Phys. Acta, vol.24, 1951, pp.441-464.

[16] Foteinou, V. et al., Cross section measurements of proton capture reactions on Se isotopes relevant to the astrophysical p process, Phys. Rev. C, vol.97, no.035806, 2018, pp.1-21.

Acknowledgments

This work is supported by JST ERATO Grant No. JPMJER2304, Japan.

16. Improvement of dynamical model considering neutron emission effect during fission process

Sota HARADA[1], Shinya TAKAGI[1,2], Yoshihiro ARITOMO[1], Kentaro HIROSE[2] and Katsuhisa NISHIO[2]
[1]Graduate of Science and Engineering, Kindai University, Higashiosaka, Osaka, Japan
[2]Advanced Science Research Center, Japan Atomic Energy Agency Tokai, Ibaraki-ken 319-1195, Japan
*Email: 2433340418f@kindai.ac.jp

Abstract

Joint research conducted by the Japan Atomic Energy Agency and Kindai University has demonstrated that the yield distribution of fission products (fission fragments) changes significantly depending on the neutrons emitted from the compound nucleus. This phenomenon is explained by the concept of multi-chance fission (MCF). In this study, we improved the treatment of neutron evaporation during the fission process in the Langevin model, aiming to describe the entire reaction process in a unified framework. The calculated results successfully reproduced the experimental data for the fission-fragment mass distribution.

1. Introduction

The Japan Atomic Energy Agency (JAEA) has successfully produced a wide range of nuclei and various excited states through multi-nucleon transfer (MNT) reactions, enabling detailed observations of their fission behavior. The fission fragment mass distributions (FFMDs) obtained from MNT experiments exhibit a distinctive double-humped structure, characteristic of actinide nuclear fission, even at high excitation energies. This phenomenon can only be explained by incorporating the concept of multi-chance fission (MCF).In a previous study [1], the effect of MCF was modeled using statistical approaches, such as the GEF code (Version 2016/1.2) [2], to simulate neutron-fission competition, and Langevin calculations to describe the fission dynamics. These methods accurately reproduced the experimentally measured FFMDs with high precision. However, neutron emission

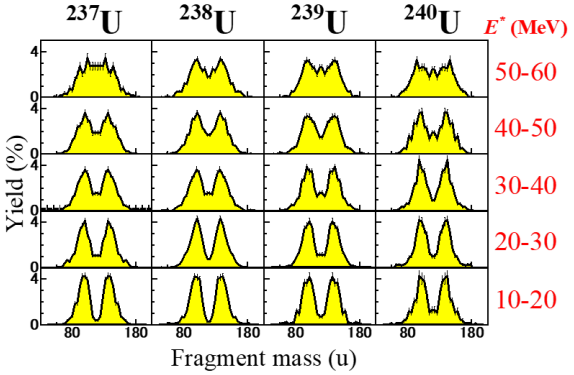

Figure 1. Experimental FFMDs of the U isotopes and their dependence on excitation energy in the range of E^*=10-60 MeV.

during the fission process was not explicitly considered in this approach. To address this, our group has been developing a model that incorporates the neutron evaporation process into the dynamical model to describe neutron emission during the fission process [3]. The previous model accounted for the effects of neutron emission by considering the reduction in excitation energy and the associated changes in shell correction energy. In this study, we further refined the model to include changes in the liquid-drop model potential caused by neutron emission, aiming for a more realistic depiction of the fission process in the highly excited energy region.

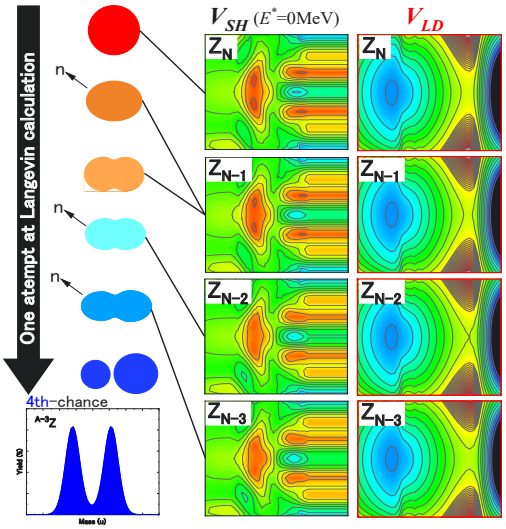

Figure 2. Schematic diagram of multi-chance fission calculation

2. Theory and Method

A simple neutron decay width based on detailed balance is adopted, and the Gilbert and Cameron equation is used for the level density ρ [4-6]. The Γ_n and ρ are given as

$$\Gamma_n^J = \frac{1}{2\pi\rho(E_{CN}^*,J)}\int_0^{E_f}\sum_{l'}\sum_{s'}T_l(\varepsilon)\rho\left(E_f-\varepsilon,I'\right)d\varepsilon \tag{1}$$

$$\rho(U^*,J) = \frac{\sqrt{\pi}}{12a^{1/4}U^{*1/4}}\exp\left(2\sqrt{aU^*}\right)\times\frac{2J+1}{2\sqrt{\pi}\sigma^3}\exp\left[-\frac{(J+1/2)^2}{2\sigma^2}\right] \tag{2}$$

Where E_{CN}^* and U^* are the excitation energy of the compound nucleus and the effective excitation energy of the compound nucleus, respectively. The effective excitation energy of the intermediate nucleus E_f can be expressed by $E_f = E_{CN}^* - B_n - E_k$ (B_n: neutron binding energy, E_k: emitted neutron kinetic energy). σ is the spin cut-off parameter. The level density parameter a is given as

$$a = \tilde{a}_n\left\{1+\frac{\delta_{shell}}{E_{CN}^*}\left(1-\exp\left(-\frac{E_{CN}^*}{E_d}\right)\right)\right\} \tag{3}$$

where δ_{shell} is the shell correction energy at temperature of the compound nucleus $T=0$. The shell damping energy E_d of 20 MeV was used in this work. In the Langevin model adopted in this study, random number determines the ratio of the Langevin's time step to the neutron decay width.

The level density parameter $\tilde{a}_n$ is givens as

$$\tilde{a}_n = \frac{A}{14.61}\left(1+3.114A^{-1/3}X_{22}+5.626A^{-2/3}X_{33}\right) \tag{4}$$

$$X_{22} = 2\pi\left(\alpha\beta\frac{\sin^{-1}\Phi}{\Phi}\beta^2\right)/4\pi R^2 \tag{5}$$

$$X_{33} = \frac{2\pi}{\alpha\Phi}\left(\frac{\beta^2}{2}\log\frac{1+\Phi}{1-\Phi}\right)/8\pi R \tag{6}$$

$$\Phi = \sqrt{1 - \frac{1}{\eta^2}}, \qquad \eta = \alpha/\beta \tag{7}$$

where α and β are the lengths of the major and minor axes of the deformed nucleus, respectively [7].

In this work, the three-dimensional two-center parametrization was adopted to describe nuclear shape. z is the distance between two potential centers, δ is the deformation of the fragment, α is the mass asymmetry of the two fragments. The advantage of this model is that it can represent both fusion and the fission with a relatively small number of parameters. The two-center parametrization is described using two harmonic oscillators. z_1 and z_2 are the distances from the origin of contact of the harmonic oscillator to the center of each harmonic oscillator. The z_0, δ and α are given as

$$z_0 = |z_1| + |z_2| \tag{8}$$

$$\delta = \frac{3(a-b)}{2a-b} \tag{9}$$

$$\alpha = \frac{A_1 - A_2}{A_1 + A_2} \tag{10}$$

where A_1 and A_2 is the mass number of heavy and light fragments, and a and b are the half length of the axes of an ellipse in the z_0 and ρ directions of the cylindrical coordinate, respectively. In order to shorten the calculation time of the computer when solving the equation of motion, we introduce z as

$$z = \frac{z_0}{R_{CN}B}, B = \frac{3+\delta}{3-2\delta} \tag{11}$$

where R_{CN} is the radius of the compound nucleus.

In the two-center parametrization, the size of the connecting cross section (neck size) of each fragment is described by the neck parameter ε. The ε is givens as

$$\varepsilon(A_c) = 0.01007A_c - 1.94 \tag{12}$$

where A_c is the mass number of the compound nucleus [8].

In the fission process, the nuclear potential is described by the adiabatic potential $V_{adiab}(q)$. In this case, the density of a nucleus is constant. The adiabatic potential is described by the sum of the potential of the liquid drop model and the shell correction energy as

$$V_{adiab}(q, L, T) = V_{LD}(q) + V_{SH}(q, T) \tag{13}$$

$$V_{LD}(q) = E_S(q) + E_C(q) \tag{14}$$

$$V_{SH}(q, T) = E_{shell}(q)\Phi(T) \tag{15}$$

$$\Phi(T) = \exp\left(-\frac{aT^2}{E_d}\right) \tag{16}$$

where V_{LD} is the potential of the liquid drop model. The excitation energy can be expressed by $E^* = aT^*$(a: level density parameter). V_{SH} is shell correction energy considering temperature dependence. E_S and E_C are the surface and coulomb energy, respectively. At the high energy, the shell correction energy becomes extremely small, and the internal structure of the nucleus disappears, resulting in mass symmetric fission. In this work, the time evolution of nuclear shape is described by the Langevin equation. The Langevin equation is given as

$$\frac{dq_i}{dt} = (m^{-1})_{ij}p_j \tag{17}$$

$$\frac{dp_i}{dt} = -\frac{\partial V}{\partial q_i} - \frac{1}{2}\frac{\partial}{\partial q_i}(m^{-1})_{ik}p_j p_k - \gamma_{ij}(m^{-1})_{jk}p_k + g_{ij}R_j(t) \tag{18}$$

where $q_i = \{z, \delta, \alpha\}$ and $p_i = m_{ij} dq_i/dt$ is a momentum conjugate to coordinate q_i. In the Langevin equation, m_{ij} and γ_{ij} are the sharp-dependent collective inertia and the friction tensors, respectively.

3. Result and Discussion

In this work, the FFMDs of $^{234-240}$U were calculated in an initial excitation energy range of $E^* = 15 - 55$ MeV. Figure 3 shows a comparison between the calculated results and the experimental data obtained using JAEA's tandem accelerator. From Figure 3, it can be observed that the calculation results based on the improved model demonstrate that the mass-asymmetric shape of the FFMDs is preserved even at high excitation energies, with only minor changes in most FFMDs. However, some FFMDs exhibit dramatic differences when compared to the results obtained using the pre-improved model.

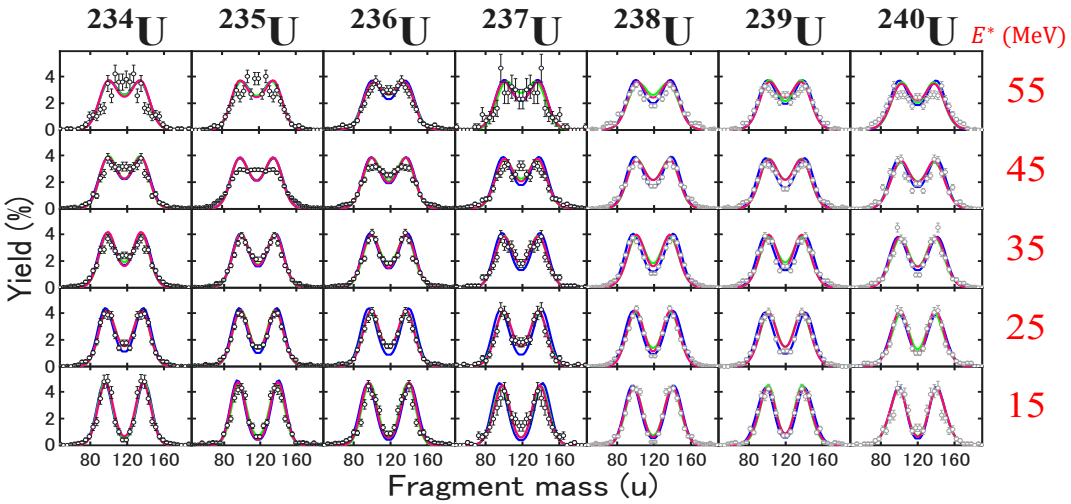

Figure 3. Experimental FFMDs (points with error bars) of the U isotopes and their dependence on excitation energy in the range of E^* = 10-60 MeV [9-11]. The experimental FFMDs are compared with Langevin calculations, respectively, with GEF code (blue curves), using the pre-improved model [3] (green curves), and using the improved model (pink curves).

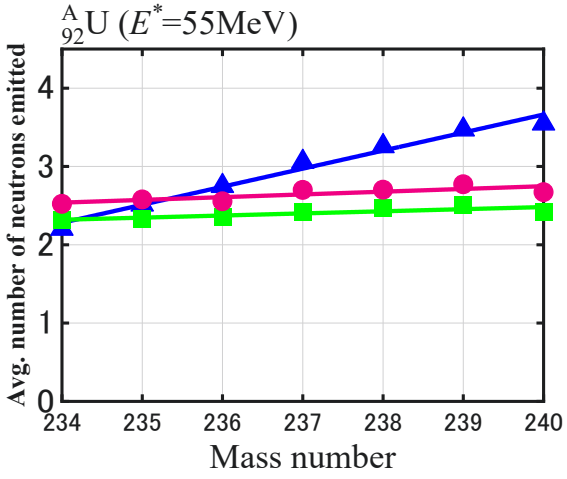

Figure 4. Average number of neutrons emitted from the compound nucleus: $^{234-240}$U with the excitation energy E^*=55 MeV calculated by GEF code (blue dot), pre-improved model (green dot), and improved model (pink dot).

The average number of neutrons emissions of $^{234-240}$U was calculated at the excitation energy of $E^* = 55$ MeV. The results were compared with those from the GEF code, as well as with the pre-improved and improved models under identical conditions. As shown in Figure 4, the average number of neutrons emitted, as calculated by the improved model, is higher than that of the pre-improved model. Additionally, the results from the GEF code exhibit an isotope-dependent trend. In contrast, neither the pre-improved model nor the improved model shows an isotope-dependent trend.

Therefore, based on trajectory analysis, we investigated the cause of the dramatic changes in FFMDs, despite the unresolved issue of neutron emission numbers. The trajectory analysis results shown in Figure 5 reveal differences in the fission process. We attributed these differences to changes in the liquid-drop potential caused by neutron emission, which increased the potential barrier. Furthermore, as the potential barrier becomes higher, the fission reaction time is prolonged, increasing the probability of neutron emission and resulting in a slight rise in the number of emitted neutrons.

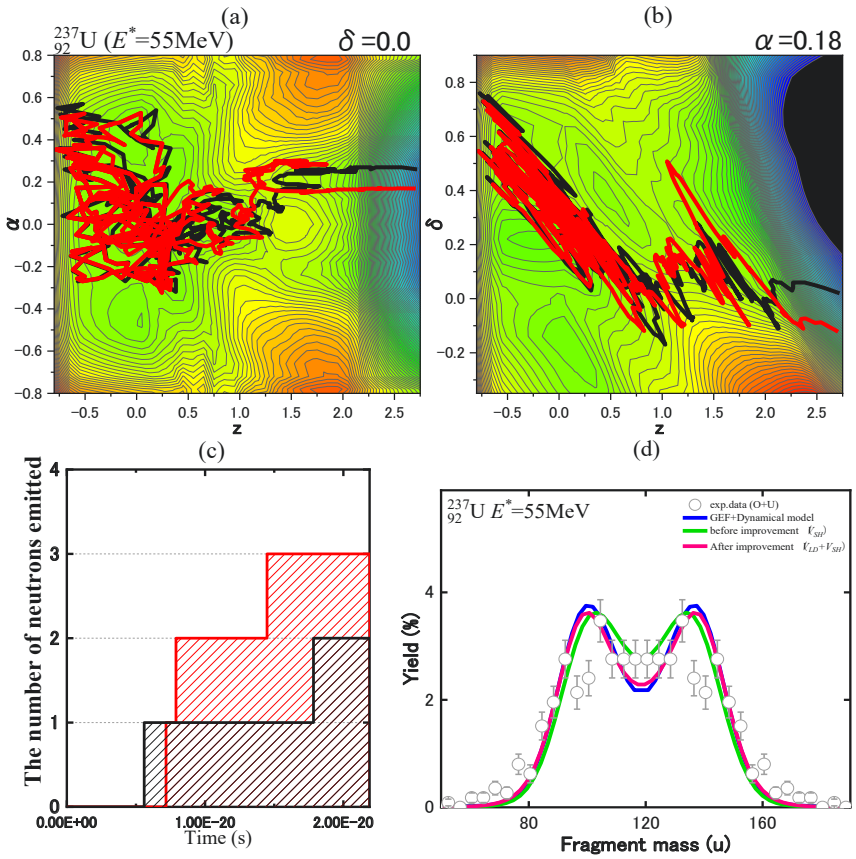

Figure 5. Sample trajectories for ^{237}U, respectively, calculated by pre-modified model (black curves) and modified model (red curves) projected onto the $z-\alpha$ plane at $\delta = 0.0$ (a) and $z-\delta$ plane at $\alpha = 0.18$ (b) The trajectory starts $z = 0.01$, $\delta = 0.20$, and $\alpha = 0.01$, at E^*=55 MeV. Neutron emission time and number of neutrons emitted during the fission process represented by each sample trajectories (c). The experimental FFMDs (points with error bars) of the ^{237}U in the $E^* = 55$ MeV are compared with Langevin calculations, respectively, with GEF code (blue curves), using the pre-improved model (green curves), and the improved model (pink

4. Summary and Perspectives

In this study, we further improved the model to consider changes in the liquid-drop model potential due to neutron emission. Due to changes in the liquid-drop model potential, the potential becomes higher, affecting the fission process and causing dramatic changes in FFMDs.

In this study, the level density is not properly described as the dynamical model that tracks the time evolution of nuclear reactions has not been adopted. Therefore, to consider neutron emission, it is necessary to use a level density that accounts for changes in the surface area and potential of the nucleus associated with its deformation toward fission. Moreover, the GEF code employs a calculation method different from that of the dynamical model, potentially calculating the competition between neutron emission and fission from a spherical nucleus. This difference suggests that the GEF code estimates higher internal energy for the nucleus compared to the dynamical model dealing with the deformation process, which could explain the increase in neutron emission.

References

[1] S. Tanaka, et al., Phys. Rev. C 100 064605 (2019).
[2] K.-H. Schmidt, B. Jurado, C. Amouroux, and C. Schmitt, Nucl. Data Sheets 131, 107 (2016).
[3] R. Yamasaki, et al., proceedings of the 2020 Symposium on Nuclear Data.
[4] A. Gilbert and A.G.W. Cameron, Can.J.Phys. 43, 269 (1965).
[5] V. Weisskopf, Phys. Rev. 52, 295 (1937).
[6] N. Bohr and J.A. Wheeler, Phys. Rev. 56, 426 (1939).
[7] J. Toke and W. J. Swiatecki, Nucl. Phys, A 372, 141 (1981).
[8] Y. Miyamoto, Y. Aritomo, S. Tanaka, et al., Phys. Rev. C 99, 051601 (2019).
[9] R. Leguillon, K. Nishio, K. Hirose, et al., Phys. Lett. B 761, 125 (2016).
[10] K. Hirose, K. Nishio et al., Phys. Rev. Lett. 119, 222501 (2017).
[11] M. Vermeulen, K. Nishio, K. Hirose, et al., Phys. Rev. C 102, 054610 (2020).

17. Criticality data of the modified STACY and evaluation results of nuclear data libraries

Tomoki YOSHIKAWA[1*], Kazuhiko IZAWA[1], Shouhei ARAKI[1], Tomoaki WATANABE[1], Daiki IWAHASHI[2], Shigeki SHIBA[2], and Satoshi GUNJI[1]
[1]Japan Atomic Energy Agency
2-4 Shirane, Shirakata, Tokai-mura, Naka-gun, Ibaraki-ken 319-1195, Japan
[2]Nuclear Regulation Authority
1-9-9 Roppongi Minato-ku, Tokyo, Japan
[*]Email: yoshikawa.tomoki@jaea.go.jp

Abstract

To develop technologies for criticality safety management during the fuel debris retrieval at the Fukushima Daiichi Nuclear Power Plant, JAEA modified the Static Experiment Critical Facility (STACY) from a solution fuel system to a light-water moderated heterogeneous system for critical experiments to study the criticality characteristics of fuel debris. After the modification, STACY was operated to inspect its designed performance on reactor operation, and the first criticality was achieved on April 22, 2024. In this study, we performed criticality calculations of STACY's first critical core and performance test cores using several nuclear data libraries and compared their results. We calculated the neutron effective multiplication factors (keff) of each core using MVP2 with JENDL-4.0, JENDL-5, and ENDF/B-VII.1. The calculations of the keff value for performance test cores at measured critical water levels show similar results between JENDL-4.0 and ENDF/B-VII.1, but overestimated in JENDL-5. To analyze the differences in the keff value between JENDL-4.0 and JENDL-5, a comparison was made for representative nuclides by replacing the nuclear data of each nuclide with JENDL-5 in the calculations using JENDL-4.0. Results of sensitivity analysis showed that ^{235}U, ^{238}U, ^{1}H, and ^{16}O were the main sources of the keff value difference.

1. Introduction

In the severe accident at the Fukushima Daiichi Nuclear Power Plant, the melting of the core generated fuel debris in various compositions, such as concrete and iron. Consequently, a comprehensive analysis is required to understand the criticality characteristics of fuel debris with diverse properties. To evaluate the validity of the analysis results, it is necessary to obtain criticality experiment data of fuel debris, but such criticality experiment equipment did not exist, and the shortage of criticality experiment data was excessive.

Accordingly, the Japan Atomic Energy Agency (JAEA) implemented a project to modify the Static Experiment Critical Facility (STACY) from a solution reactor into a light-water reactor, to obtain various criticality data including fuel debris. The modification work on STACY was completed in December 2023, and various performance inspections were conducted in preparation for the start of

experimental operation in April 2024.

In STACY, 1.27 cm and 1.50 cm grid plates are available for loading fuel rods into the core, and the performance tests were conducted using these two grid plates. For thermal power calibration, another core was also configured with a loaded irradiation sample in the center of the core. Criticality control of STACY in normal operation is performed by adjusting the water level in the core tanks. In this report, the results of the critical water levels measured in the performance test and the neutron effective multiplication factor (keff) at that critical water levels were calculated with MVP2[1] using JENDL-4.0[2], JENDL-5[3], and ENDF/B-VII.1[4]. In addition, to analyze the differences in effective multiplication factors between JENDL-4.0 and JENDL-5, the nuclear data of each nuclide were replaced by JENDL-5 in the calculation using JENDL-4.0, and comparisons were made for all nuclides in the calculation. The nuclides with significant effects were extracted.

2. Experiment

2.1. Core configurations

The performance test cores consisted of five types of cores: (1) 277 fuel rods with a water level of about 70 cm, (2) 253 fuel rods with a water level of about 110 cm, (3) 253 fuel rods with a water level of about 120 cm and irradiation samples for thermal power calibration loaded at the center of the core, (4) 241 fuel rods with a water level of about 70 cm, and (5) 213 fuel rods with a water level of about 110 cm. Fuel rods are cylindrically loaded on grid plates with grid intervals of 1.50 cm for cores (1), (2), and (3), and of 1.27 cm with skipping one by one to achieve fuel intervals of 2.54 cm for cores (4) and (5). The reason for loading fuel rods with grid intervals of 2.54 cm is that the number of fuel rods held in STACY has been analyzed to show that it is not possible to achieve criticality with 1.27 cm grid intervals. The core configurations of (1), (2), and (3), which have grid intervals of 1.50 cm, are shown in Figure 1, and that of (4) and (5), which have grid intervals of 2.54 cm, is shown in Figure 2.

The fuel rod consists of a UO_2 pellet (8.2 mm in diameter) with an enrichment of about 5 wt% and a zirconium alloy cladding tube (9.5 mm outer diameter). The length of the fuel rod was approximately 1500 mm. To accurately insert the cadmium safety plate for shutdown, the guide pin (10.8 mm in diameter and about 1500 mm length) is made of zirconium alloy and loaded into the core. The core of (3) is loaded with an aluminum alloy guide tube (27.2 mm in diameter) in the center that encloses an irradiation sample (gold foils) for thermal power calibration. The irradiation sample is loaded in the guide tube at half of the critical water levels.

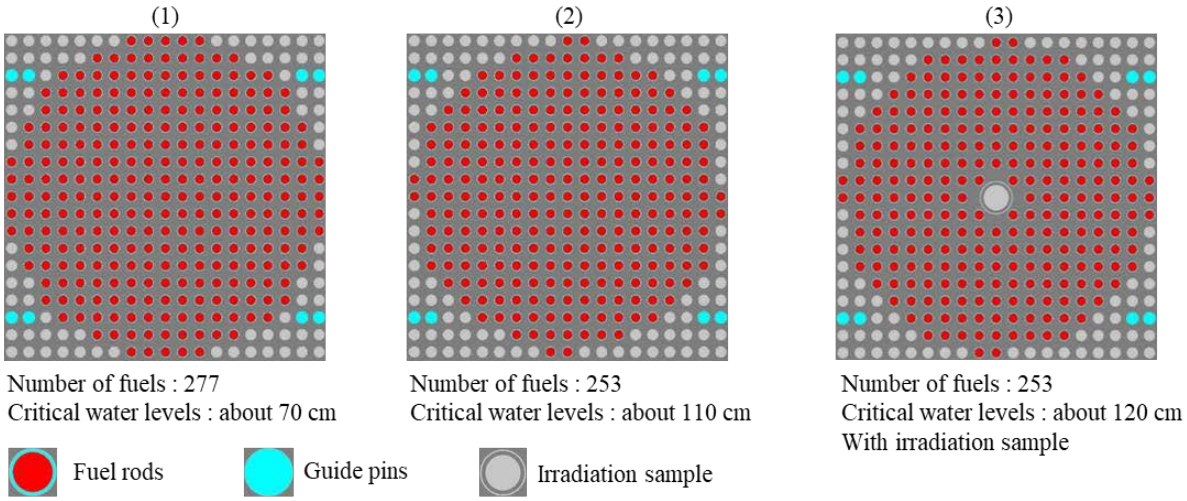

Figure 1: Core configuration with 1.50 cm grid intervals

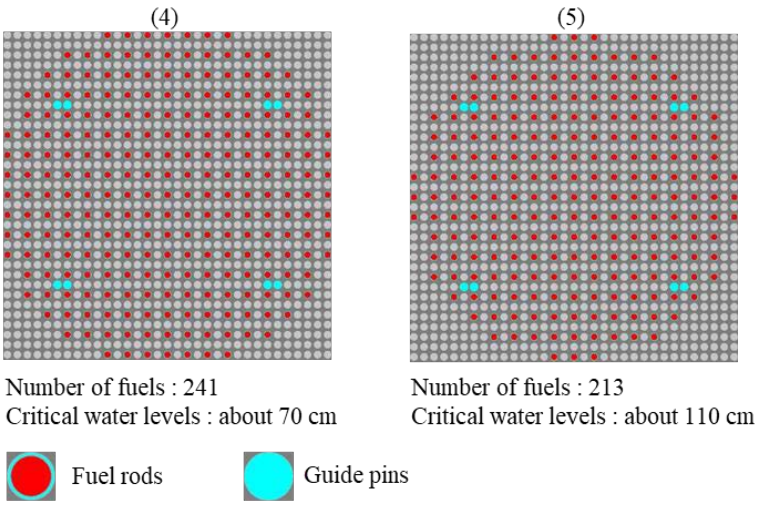

Figure 2: Core configuration with 2.54 cm grid intervals

2.2. Measured critical water levels

Table 1 shows the measured critical water levels for the five cores. The calculations in section 3 used the measured critical water levels in Table 1.

Table 1: Measured critical water levels of each core

Core numbers	Grid intervals (cm)	Number of fuel rods	Irradiation sample	Critical water levels (cm)
(1)	1.50	277	Without	71.519
(2)	1.50	253	Without	113.367
(3)	1.50	253	With	126.573
(4)	2.54	241	Without	75.724
(5)	2.54	213	Without	115.255

3. Evaluation results

3.1. Comparison of the keff value based on different nuclear data libraries

3.1.1. Analysis method

In five types of performance test cores, the neutron effective multiplication factor (keff) was calculated at the measured critical water levels using MVP2 with JENDL-4.0, JENDL-5, and ENDF/B-VII.1. For JENDL-4.0, we used the file JENDL-4.0u that was modified after its release. The calculations were conducted with 1.0×10^{8} histories (one standard deviation of the keff value to be less than 0.0001). Thermal scattering data for only ^{1}H is used in the moderator with JENDL-4.0 and ENDF/B-VII.1, while thermal scattering data for both ^{1}H and ^{16}O are used in the moderator with JENDL-5.

3.1.2. Results

The results of the keff value for each core for each of the nuclear data libraries mentioned above are shown in Figure 3. Gi is the grid intervals (cm), Wl is the measured critical water levels (cm), and Nf is the number of fuel rods in Figure 3. The results with JENDL-4.0 correspond to the experimental data within three standard deviations (about 27 pcm) for the cores with 1.50 cm grid intervals, and they overestimate the keff value by about 33 to 69 pcm for grid intervals of 2.54 cm. The results with JENDL-5 overestimate the keff value in each core by up to 195 pcm, but the keff bias between the two different grid intervals is smaller than the results from the other two nuclear data libraries. The results of the keff value for JENDL-4.0 and ENDF/B-VII.1 correspond within one standard deviation.

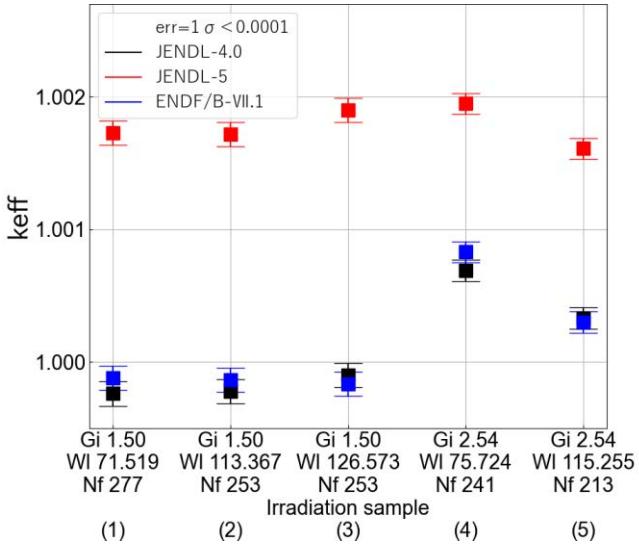

Figure 3: Calculation results of the keff value for each core using MVP2 with JENDL-4.0, JENDL-5, and ENDF/B-VII.1.

3.2. Nuclear data replacement for each nuclide

3.2.1. Analysis method

In (1) and (4) of the core with different grid intervals, we performed calculations based on JENDL-4.0, replacing nuclear data for each nuclide one by one with JENDL-5. The number of histories was set the same as in section 3.1. The treatment of thermal scattering data was the same as in section 3.1. The reactivity was calculated by replacing one nuclide each with JENDL-5 based on the results using only JENDL-4.0:

$$\frac{\Delta k}{k} = \frac{1}{\mathrm{keff}_{\mathrm{JENDL-4.0}}} - \frac{1}{\mathrm{keff}_{\mathrm{JENDL-5}}} \quad (1)$$

where $keff_{\mathrm{JENDL-5}}$ represents the keff value with the nuclear data of one nuclide replaced JENDL-5 and $keff_{\mathrm{JENDL-4.0}}$ represents the result of JENDL-4.0 calculated in section 3.1.

3.2.2. Results

Figure 4 shows the Δk/k value of significantly affected nuclides according to equation (1) in the sensitivity analysis. In both Figures 4(a) and 4(b), only ^{16}O has a negative reactivity effect with replacement to JENDL-5. Figure 4(a) (grid intervals of 1.50 cm) shows ^{1}H has the largest positive reactivity , while Figure 4(b) (grid intervals of 2.54 cm) shows ^{235}U the largest positive reactivity. As a result, the effect of nuclides can be inferred to vary with grid intervals.

In both results (a) and (b) for different grid intervals, the effect of H_2O is roughly consistent with the reactivity of ^{1}H and ^{16}O added together. Furthermore the sum of the Δk/k values of ^{235}U, ^{238}U, ^{1}H, and ^{16}O in both (a) and (b) is almost consistent with the difference between the Δk/k values of JENDL-4.0 and JENDL-5. Thus the overestimation of JENDL-5 in section 3.1 is probably mainly due to these nuclides.

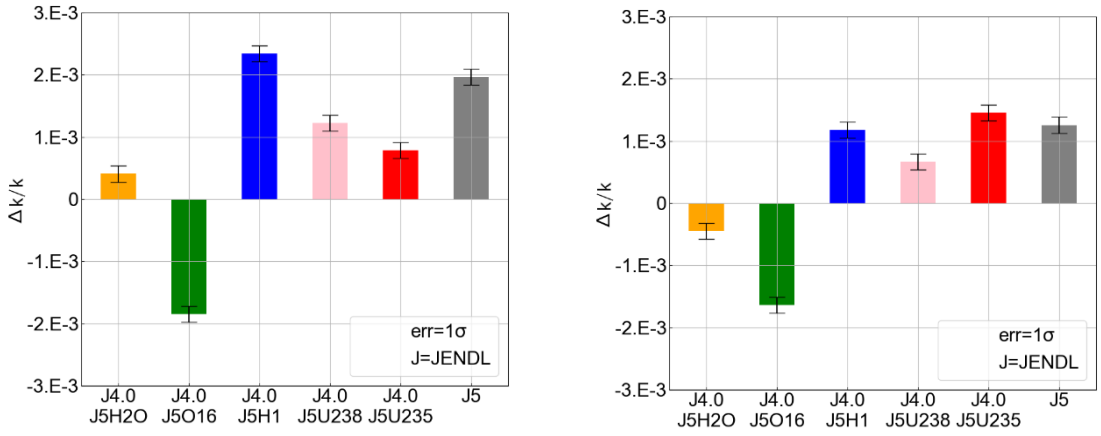

(a) Grid intervals of 1.50 cm and 277 fuel rods (b) Grid intervals of 2.54 cm and 241 fuel rods

Figure 4: The Δk/k values for cores (1) and (4) for each nuclide changed from JENDL-4.0 to JENDL-5.

4. Summary

JAEA modified the STACY from a solution fuel system to a light-water moderated heterogeneous system and performance tests were conducted on five core configurations with two types of grid intervals. In the performance test, the five cores were configured under different conditions (grid intervals, critical water levels, and with or without the irradiation sample) and critical water levels were measured.

The calculation of the keff value using MVP2 for the five cores at measured critical water levels shows similar results between JENDL-4.0 and ENDF/B-VII.1. JENDL-5 overestimate by up to 195 pcm, but keff bias is smaller than the other two nuclear data libraries. For comparison between libraries, the analysis was performed by replacing JENDL-4.0 to JENDL-5 for each nuclide. Although there are different tendencies in the grid intervals, ^{235}U, ^{238}U, and ^{1}H have a larger the keff value, while only ^{16}O has a smaller the keff value. The difference in the keff value between JENDL-4.0 and JENDL-5 is probably due to ^{235}U, ^{238}U, ^{1}H, and ^{16}O.

References

[1] Nagaya, Y. et al., MVP/GMVP II: General Purpose Monte Carlo Codes for Neutron and Photon Transport Calculations based on Continues Energy and Multigroup Methods; JAERI 1348; 2005.

[2] Shibata, K. et al., (2011). JENDL-4.0: A new library for nuclear science and engineering. Journal of Nuclear Science and Technology, 48(1).

[3] Iwamoto, O. et al., Japanese evaluated nuclear data library version 5: JENDL-5 , J. Nucl. Sci. Technol., 60(1), (2023), pp. 1–60.

[4] Chadwick, M.B. et al., ENDF/B-VII.1 Nuclear Data for Science and Technology: Cross Sections, Covariances, Fission Product Yields and Decay Data, Nucl. Data Sheets, vol.112, 2011, pp.2887–2996.

Acknowledgements

This report includes the results of the contract work funded by the Nuclear Regulation Authority (NRA)/ the Secretariat of NRA of Japan.

18. Understanding the complex dynamics of fusion reactions

Masaki UENO[1*], Kohta NAKAJIMA[1], Nobuaki IMAI[2] and Yoshihiro Aritomo[1]
[1]Kindai University
3-4-1, Kowakae, Higashiosaka, Osaka 577-8502, Japan
[2]Center for Nuclear Study, The University of Tokyo
7-3-1, Hongo, Bunkyo, Tokyo 113-0033, Japan
[*]Email: 2433340470y@kindai.ac.jp

Abstract

At present, using the fusion reaction between the projectile and target nuclei, up to Og has been successfully synthesized and projects to synthesis of new superheavy elements (SHEs) are underway at several facilities around the world. However, the mechanism of quasi-fission, which accounts for more than 99% of fusion reactions in the super-heavy element region, is still not fully understood.

To understand the dynamics of the fusion process, we focused on the correlation between fragment mass and its emitting angle of quasi-fission [1]. Our group has succeeded in reproducing the mass angular distribution (MAD) of the emitted nuclei by using a dynamical model, considering the deformation of the target nuclei . This study was calculated using a dynamical model. When using this to predict reactions, it is necessary to determine indeterminate parameters from experimental data.

In this study, we calculated the 42 systems experimented in Ref. [1] under identical conditions except for the number of nucleons and summarized the MAD. Among these, we correct the uncertain parameters and systematically evaluate ^{64}Ni+^{170}Er, ^{48}Ti+^{186}W, and ^{32}S+^{202}Hg, which form the compound nucleus of ^{234}Cm.

1. Introduction

At present, experiments to synthesize element 119 are being conducted in Japan and around the world. In addition, research on the unknown neutron-rich region is also being actively conducted.

Two experimental methods are available for the synthesis of new elements and production of neutron-rich nuclei. Heavy ion fusion reaction is effective for production of new super heavy elements and multi nucleon transfer reaction is effective for production of neutron rich nuclei. These experiments are necessary to explore the limits of elements that can exist in the universe and to understand the r-process caused by supernova explosion. Both reactions are via contact between the target nucleus and the incident nucleus.

When two nucleus contact, they undergo various reactions such as deep inelastic scattering, quasi-fission, and fusion reactions. The probability of these reactions depending on the reaction systems. In the present study, we focused on the correlation between the mass number of fission fragments in quasi-fission and their emission angles [1].

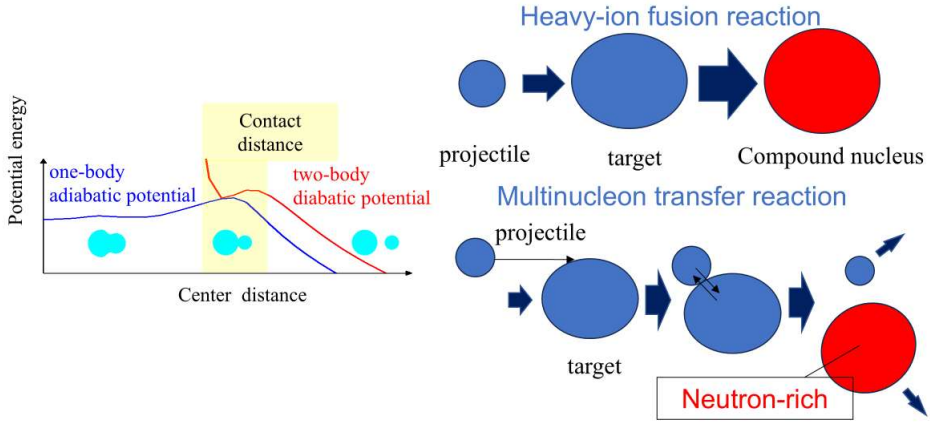

Figure 1. Schematic diagram of MNT and heavy ion fusion reaction and examples of potential transitions associated with the progress of the reaction

2. Model

We use a dynamical model that trace the time evolution of the nucleus shape. The items need for a model are the potential and the equation of motion that solve for it.

2.1. Nucleus shape

The nucleus shape is defined by two-center shall model[2]. It is possible to determine the shape of the nucleus q by the two-center distance z_0, deformation of nucleus $\delta = (3a - b)/(2a - b)$ and the mass asymmetry $\alpha = (A_1 - A_2)/(A_1 + A_2)$. z_0 is normalized by $z = z_0/(R_{CN}B)$. R_{CN} is the radius when the compound nucleus is spherical, A_1 and A_2 are the mass numbers of projectile like fragment and target like fragment, a and b are the short and long diameters of the deformed nucleus, and B is a parameter that corrects the two centers distance by the deformation of nucleus.

2.2. Potential energy

The potentials before and after the contact of the nuclei are divided into two-body (fusion process) and one-body (fission process) potentials. The two potentials are switched by reaction time [3].

$$V = V_{diab}(q)f(t) + V_{adiab}(q, l, T)[1 - f(t)] \quad (1)$$

$$f(t) = \frac{1}{1 + \exp\left(-\frac{t}{\tau}\right)} \tag{2}$$

$V_{diab}(q)$ is the diabatic potential energy (two body) and $V_{adiab}(q, l, T)$ is the adiabatic potential energy (one body). $f(t)$ is a function of time, t is reaction time and τ is the relaxation time. For the present calculations, τ is unified to 0.1zs regardless of the system.

$V_{diabatic}(q)$ is calculated within the double-folding method with Migdal nucleon-nucleon forces [4–7]. $V_{adiabatic}(q, l, T)$ is described by liquid drop potential $V_{LDM}(q)$, shell correction energy $V_{shell}(q, T)$, and rotational energy $V_{rot}(q, l)$.

$$V_{LDM}(q) = E_S(q) + E_C(q) \tag{3}$$

$$V_{shell}(q, T) = E^0_{shell}(q)\,\Phi(T) \tag{4}$$

$$\Phi(T) = \exp\left(-\frac{E^*}{E_d}\right) \tag{5}$$

$$V_{rot}(q, l) = \frac{h^2 \ell(\ell+1)}{2I(q)} \tag{6}$$

$V_{LDM}(q)$ is the potential energy calculated with the finite-range liquid drop model, given as a sum of the surface energy $E_S(q)$ [8] and the Coulomb energy $E_C(q)$. $V_{shell}(q, T)$ is the shell correction energy. $E^0_{shell}(q)$ is evaluated by Strutinsky method [9,10] from the single-particle levels of the two-center shell model. The temperature dependence factor $\Phi(T)$, where E^* indicates the excitation energy of the compound nucleus. E^* is given as $E^* = aT^2$, where a is the level density parameter. E_d is The shell damping energy that is selected as 20 MeV [11]. ℓ is relative angular momentum and $I(q)$ is the rigid body moment of inertia.

2.3. Multidimensional Langevin equation

The trajectory calculations are performed on the time dependent unified using the multidimensional Langevin equations [3].

$$\frac{dq_i}{dt} = (m^{-1})_{ij} p_j \tag{7}$$

$$\frac{d\theta}{dt} = -\frac{l}{\mu_R R^2} \tag{8}$$

$$\frac{d\varphi_1}{dt} = \frac{L_1}{I_1} \tag{9}$$

$$\frac{d\varphi_2}{dt} = \frac{L_2}{I_2} \tag{10}$$

$$\frac{dp_i}{dt} = -\frac{\partial V}{\partial q_i} - \frac{1}{2}\frac{\partial}{\partial q_i}(m^{-1})_{jk} p_j p_k - \gamma_{ij}(m^{-1})_{jk} p_k + g_{ij} R_j(t) \tag{11}$$

$$\gamma_{ij} T = \sum_k g_{ij} g_{jk} \tag{12}$$

$$\langle R(t) \rangle = 0 \tag{13}$$

$$\langle R(t) R(t') \rangle = 2\delta(t - t') \tag{14}$$

$$\frac{dl}{dt} = -\frac{\partial V}{\partial \theta} - \gamma_{tang}\left(\frac{l}{\mu_R R} - \frac{L_1}{I_1} a_1 - \frac{L_2}{I_2} a_2\right) R + R g_{tang} R_{tang}(t) \tag{15}$$

$$\frac{dL_1}{dt} = -\frac{\partial V}{\partial \varphi_1} + \gamma_{tang}\left(\frac{l}{\mu_R R} - \frac{L_1}{I_1}a_1 - \frac{L_2}{I_2}a_2\right)a_1 - a_1 g_{tang} R_{tang}(t) \quad (16)$$

$$\frac{dL_2}{dt} = -\frac{\partial V}{\partial \varphi_2} + \gamma_{tang}\left(\frac{l}{\mu_R R} - \frac{L_1}{I_1}a_1 - \frac{L_2}{I_2}a_2\right)a_2 - a_2 g_{tang} R_{tang}(t) \quad (17)$$

See Ref. [3] for each parameter.

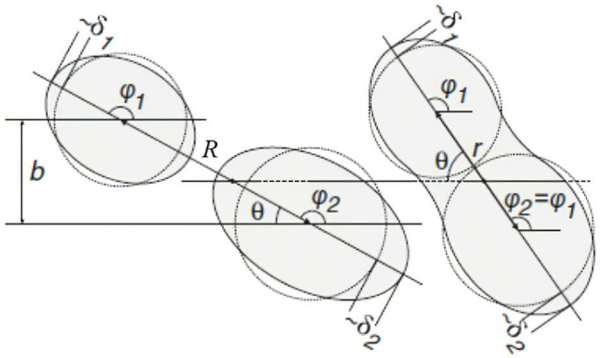

Figure 2. Schematic view of the nuclear degrees of freedom.

3. Results

An overview of the fission fragment mass ration and emission angle distribution (MAD) is shown in Figs. 3 and 4. It shows which reactions are predominant depending on the mapping position. Note that while some reactions are dominant, others are mixed. Figure 5 shows the results of this calculation (left side) and the experimental data (right side) used as reference.

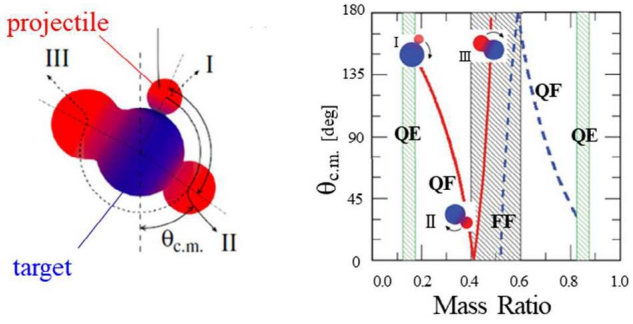

Figure 3. Schematic view of mass angular distribution (MAD) [1]. Region of I is dominated by quasi-elastic (QE) and deep inelastic scattering (DI), II by QF, and III by fusion-fission (FF) reactions.

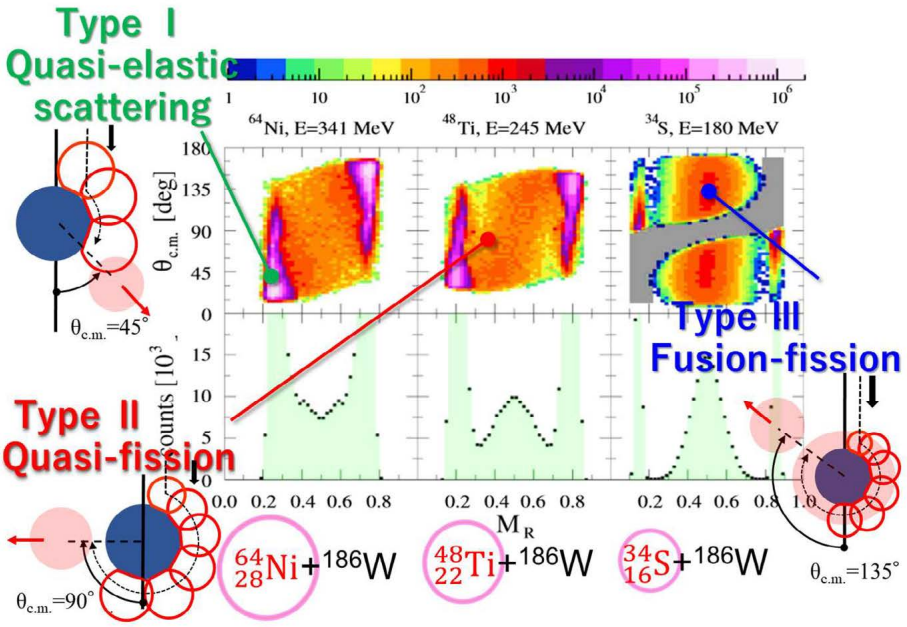

Figure 4. Characteristics of MAD in which each type predominates.

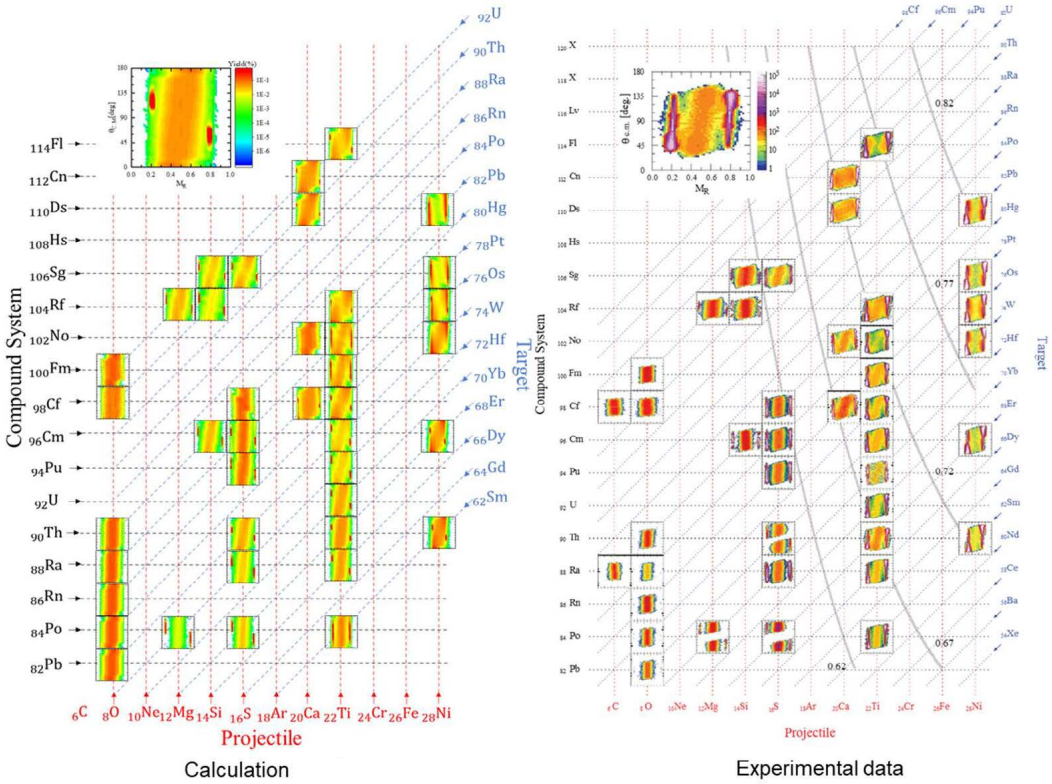

Figure 5. The results of this calculation (left side) and the experimental data (right side) [1] .
The scale is adapted to ^{48}Ti + ^{170}Er. See Ref. [1] for the mass number and incident energy of reaction systems.

Although not quantitative, the larger the mass asymmetry of the reaction system and the smaller mass number of the compound nucleus, the better MAD reproduces the experimental characteristics. Our calculations show that as the reaction transitions from two-body to one-body, the dissipation of internal

energy from kinetic energy, the transition from diabatic to adiabatic potential, and the ease of nucleon transfer change. In calculations, these changes must be fitted from experimental data as the reaction time evolves and is indefinite for each reaction systems. The present calculation is the result of unifying all these indeterminate parameters to 0.1 zs. This was determined from the reaction time to contact when the two nuclei are spherical.

4. Conclusion

The MADs of 41 systems with experimental data were calculated and systematically evaluated. Many systems were able to reproduce the experimental trends. However, quantitative comparisons could not be made. When the difference in mass asymmetry of the reacting systems was small and the mass number of the compound nuclei was large, many systems failed to reproduce the experimental trends. Although we have calculated the indeterminate parameters for the transitions in the system in a unified manner, we believe that these parameters need to be corrected in areas where they are not reproduced well.

References

[1] R. du Rietz et al., Phys. Rev. C 88, 054618 (2013).
[2] Joachim Maruhn and Walter Greiner, The asymmetrie two center shell model, Z. Phys. 251, 431 (1978).
[3] A. V. Karpov and V. V. Saiko, Phys. Rev. C 96, 024618 (2017).
[4] V. Zagrebaev and W. Greiner, J. Phys. G: Nucl. Part. Phys. 34, 2265 (2007).
[5] V. Zagrebaev and W. Greiner, J. Phys. G: Nucl. Part. Phys. 31, 825 (2005).
[6] V. Zagrebaev, A. Karpov, Y. Aritomo, M. Naumenko, and W. Greiner, Phys. Part. Nuclei 38, 469 (2007).
[7] A. B. Migdal, Theory of Finite Fermi Systems and Applications to Atornic Nuclei (Interscience, New York, 1967).
[8] H. J. Krappe, J. R. Nix, and A. J. Sierk, Phys. Rev. C 20, 992 (1979).
[9] V. Strutinsky, Nucl. Phys. A 122, 1 (1968).
[10] M. Brack, J. Damgaard, A. S. Jensen, H. C. Pauli, V. M. Strutinsky, and C. Y. Wong, Rev. Mod. Phys. 44, 320 (1972).
[11] A. V. Ignatyuk, G. N. Smirenkin, and A. S. Tishin, Yad. Fiz. 21, 485 (1975).

Acknowledgements

I would like to express my great appreciation to prof. Aritomo and Mr. Nakajima for their many advices on the calculations, to Associate Prof. Imai who inspired this research, and to the organizers for the opportunity to present my research.

19. Trajectory analysis of the 4-D Langevin model using principal component analysis

Yuta MUKOBARA[†*1], Satoshi CHIBA[2], Tatsuya KATABUCHI[1], and Chikako ISHIZUKA[1]

[1]Institute of Science Tokyo, 2-12-1 Ookayama, Meguro-ku, Tokyo, 152-8550, Japan
[2]NAT Research Center, NAT Corporation, 38 Naka, Ibaraki, 312-0005, Japan
[†]Email: mukobara.y.636f@m.isct.ac.jp

Abstract

Nuclear fission, as a large-amplitude collective motion of a finite group of nucleons, remains fundamentally enigmatic. While it is well established that, in nuclear fission, nuclei ultimately divide into several modes characterized by distinct mass and kinetic energy distributions, the precise timing and underlying mechanisms triggering this bifurcation remain poorly understood. To elucidate this aspect of nuclear fission, trajectory analysis within models treating fission as the time evolution of collective coordinates is considered a suitable approach. In this study, we utilized a four-dimensional Langevin model, which we have previously developed and successfully applied, to analyze fission trajectories. By applying Principal Component Analysis (PCA) to the accumulated trajectories, we investigated which collective coordinates predominantly influence the fate of fission pathways. Our findings revealed that, in the fission of ^{258}Fm, the contribution of the lighter fission fragment is more significant than that of the heavier fragment associated with double magic numbers. This result suggests the potential importance of contributions from components other than those generally assumed to dominate.

1 Introduction

Nuclear fission, a reaction in which an atomic nucleus splits into two or more fragments, releases approximately 200 MeV of binding energy in the form of the kinetic energy of the fission fragments and emitted particles. Nuclear fission holds a critical position in both applied and fundamental sciences. In nuclear engineering, it underpins nuclear power generation, a primary method of power production in many countries. Accurate understanding of nuclear fission is essential for the safe operation of nuclear reactors. In fundamental physics, nuclear fission plays a pivotal role in the rapid process (r-process) of nucleosynthesis in nuclear astrophysics, which is crucial for determining the elemental abundance ratios in the universe [1–4]. Intensive research in this area highlights the importance of elucidating the mechanisms of nuclear fission to bridge gaps in our understanding of both astrophysical phenomena and engineering applications. Thus, unraveling the mechanisms of nuclear fission remains a key challenge and is indispensable for advancing both theoretical insights and practical technologies. Despite its long history of study and its importance, fundamental mechanisms of nuclear fission remain a significant challenge to be fully understood, necessitating extensive research based on nuclear dynamical approaches [5–7].

*Present address: Institute of Science Tokyo, 2-12-1 Ookayama, Meguro-ku, Tokyo, 152-8550, Japan

In this study, we analyze nuclear fission data using Principal Component Analysis (PCA) [8]. The PCA is a statistical method used to extract significant structures from multidimensional data and quantify the contribution of each variable to the principal components. In the fission phenomenon, variables exhibiting significant changes in principal component loadings are likely to represent critical factors influencing the fission process. Particularly, abrupt changes or sign reversals in loadings indicate that these variables play a dominant role in determining the dynamics of nuclear fission. Such analyses enable the identification of key variables essential for predicting the outcomes of fission processes.

The aim of this study is to identify the conditions under which various fission modes occur and the key physical quantities leading fission trajectories to these modes. In this study, we focus our analysis on ^{258}Fm, since ^{258}Fm exhibits a well-balanced mixture of symmetric and asymmetric components (super-short mode and standard mode). To achieve this, the PCA is applied to the trajectory data of ^{258}Fm obtained from the four-dimensional Langevin model [9–12], aiming to elucidate the critical features and factors governing the fission process.

2 Methodology

In this study, fission trajectory data for ^{258}Fm were collected using the four-dimensional Langevin model. Simulations were performed until we obtained 1,000 events for each mode. Figure 1 describes the trajectories obtained from the four-dimensional Langevin model, where 100 events from each mode are plotted.

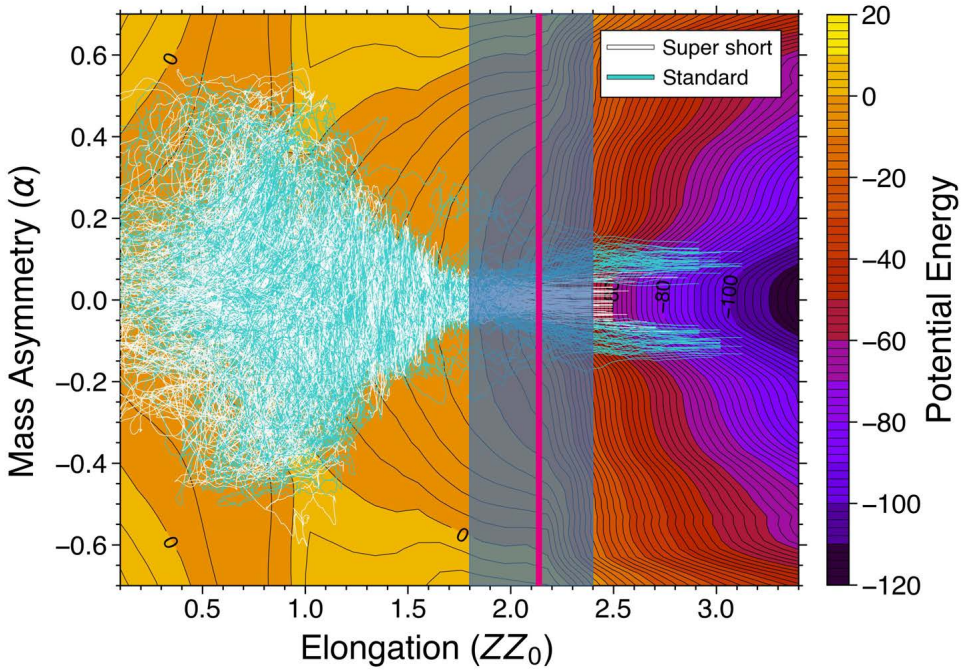

Figure 1: Langevin trajectories of ^{258}Fm are shown, with 100 events plotted for each of the super-short mode and standard mode. The trajectories are projected onto a plane where the energy is minimized with respect to ZZ_0 (x-axis) and α (y-axis). The blue area represents the range analyzed in this study using Principal Component Analysis (PCA), while the magenta lines indicate the step size of 0.025 used for PCA.

The elongation of the compound nucleus ZZ_0 was varied incrementally from 1.800 to 2.400 in steps of 0.025, and the corresponding values for each variable were obtained by the langevin

calculations. The blue area in Figure 1 represents the range of ZZ_0 values (1.800 to 2.400) analyzed in this study, while the magenta lines indicate the step size of 0.025. In the blue area, the differences in the behavior of the two modes in the region leading up to $ZZ_0 = 2.0$ are not visually distinguishable. The analyzed variables include:

- The elongation of the compound nucleus (ZZ_0),
- Mass asymmetry (α),
- Deformation of the heavy fragment (δ_{heavy}),
- Deformation of the light fragment (δ_{light}),
- The momentum associated with each of the above variables (ZZ_0 mom, α mom, δ_{heavy} mom, δ_{heavy} mom).

As a result, we have eight variables as input to the PCA. All data were standardized to a mean of 0 and a standard deviation of 1 to ensure consistency across the dataset.

The PCA was then performed on the standardized data. The target variable is binary, indicating whether the trajectory corresponds to the super-short mode or the standard mode. For details on PCA, refer to [8]. The implementation of PCA was conducted using the Scikit-learn library [13].

3 Results and Discussions

First, Figure 2 shows the variation in the explained variance ratio of the first principal component as a function of ZZ_0. The Explained Variance Ratio is a metric used in Principal Component Analysis (PCA) to indicate the extent to which each principal component accounts for the variance in the dataset. From Figure 2, it can be observed that the explained variance ratio increases significantly around $ZZ_0 \approx 2.0$ and reaches its maximum near $ZZ_0 \approx 2.3$. Furthermore, it is noted that the explained variance ratio slightly decreases when ZZ_0 exceeds 2.3.

In the analyzed range, even the lowest explained variance ratio was found to be nearly 25%, while the first principal component contributed more than 50% at its maximum. Despite using eight variables, the fact that the first principal component contributes approximately 25% or more suggests that it is important to examine the loadings of the first principal component in detail.

Figure 3 shows the loadings of each variable in the first principal component (a) and their absolute values (b). Principal value loadings with signs allow us to examine the correlation and contribution changes of each variable. From Figure 3(a), it can be observed that the momentum of ZZ_0, δ_{heavy}, and δ_{light} shows a positive correlation with the first principal component up to a certain point. Thus, the first principal component is interpreted as representing the relationship between δ_{heavy}, δ_{light} and ZZ_0. However, at $ZZ_0 = 2.1$, δ_{heavy} and δ_{light} takes a negative value, indicating from the sign that the contribution of δ_{heavy} and δ_{light} to the principal component decreases sharply.

This sharply changing region can be regarded as a point where significant variation occurs in the trajectory, suggesting that δ_{light}, the variable with the largest contribution at this point, may have a substantial impact on the fission process.

Next, in the case of absolute values shown in Figure 3(b), attention can be focused solely on the degree of contribution to the principal component. When Figure 3(a) is viewed without signs, it is evident that, except for the region where $ZZ_0 \geq 2.38$, δ_{light} exhibits a slightly greater influence than δ_{heavy}. Therefore, within the range analyzed in this study, it can be concluded that the influence of δ_{light} is consistently greater than that of δ_{heavy}.

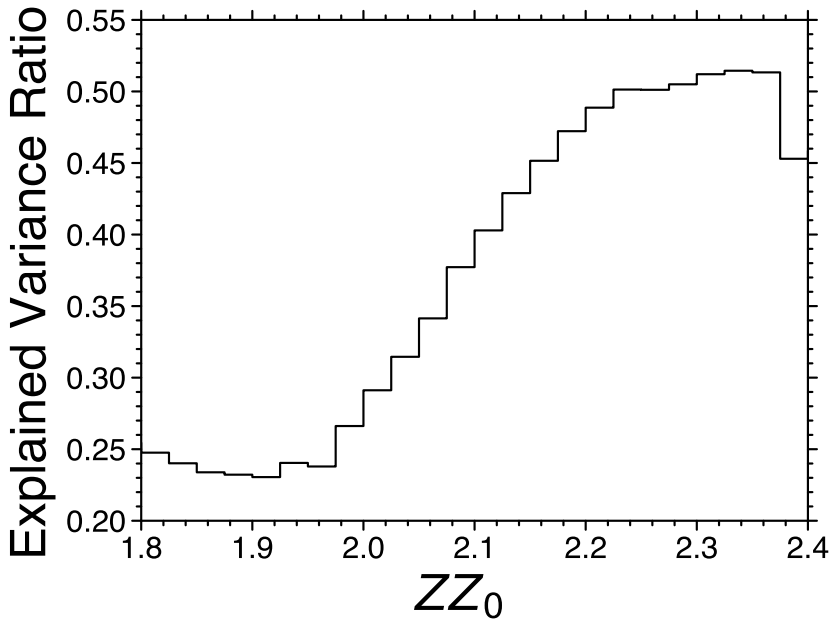

Figure 2: Explained variance ratio of the first principal component.

4 Conclusion

Nuclear fission is an important topic from both nuclear engineering and fundamental physics perspectives. In this study, principal component analysis (PCA) was applied to the trajectories obtained from a four-dimensional Langevin model to identify the conditions under which fission modes occur and the key physical quantities contributing to these modes.

Analysis of the loadings of the first principal component revealed that, in the case of ^{258}Fm, the lighter fragment exhibited a greater contribution than the heavier fragment. This result suggests that contributions from components different from those commonly assumed have become more prominent.

References

[1] Arnould M, Goriely S, Takahashi K. The r-process of stellar nucleosynthesis: Astrophysics and nuclear physics achievements and mysteries. Phys Rep. 2007;450(4):97–213.

[2] Goriely S, Pinedo GM. The production of transuranium elements by the r-process nucleosynthesis. Nucl Phys A. 2015;944:158–176. Special Issue on Superheavy Elements;

[3] Mumpower M, Surman R, McLaughlin G, et al. The impact of individual nuclear properties on r-process nucleosynthesis. Prog Part Nucl Phys. 2016;86:86–126.

[4] Kajino T, Aoki W, Balantekin A, et al. Current status of r-process nucleosynthesis. Prog Part Nucl Phys. 2019;107:109–166.

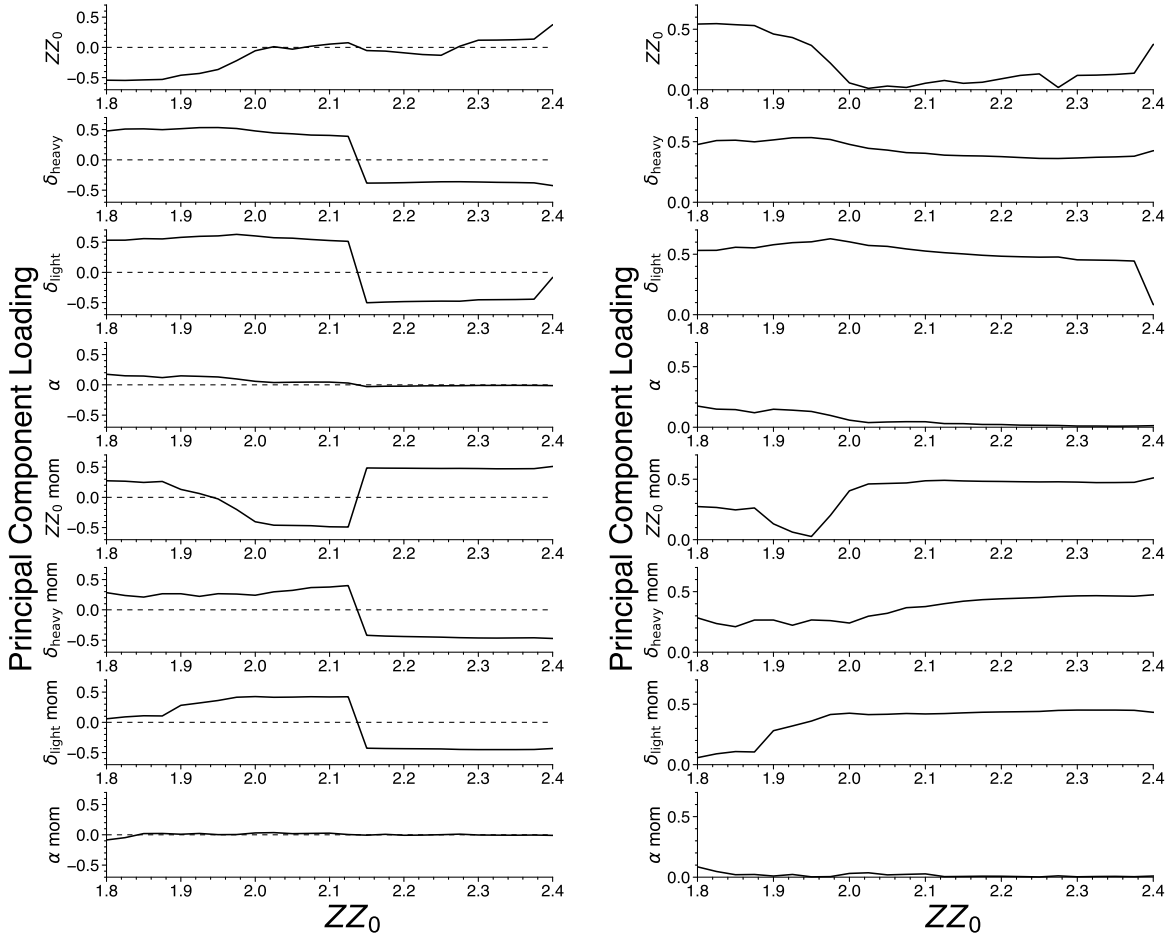

(a) Loadings of each variable on the first principal component.

(b) Absolute value of the loadings of each variable on the first principal component.

Figure 3: Variation in the loadings of each variable for the first principal component with respect to ZZ_0.

[5] Schunck N, Robledo LM. Microscopic theory of nuclear fission: a review. Rep Prog Phys. 2016 Oct;79(11):116301.

[6] Bender M, Bernard R, Bertsch G, et al. Future of nuclear fission theory. J Phys G. 2020 Oct;47(11):113002.

[7] Wilson JN, Thisse D, Lebois M, et al. Angular momentum generation in nuclear fission. Nature. 2021;590(7847):566–570.

[8] Bishop CM. Pattern Recognition and Machine Learning. New York (NY): Springer; 2006.

[9] Ishizuka C, Usang MD, Ivanyuk FA, et al. Four-dimensional Langevin approach to low-energy nuclear fission of ^{236}U. Phys Rev C. 2017 Dec;96:064616.

[10] Usang MD, Ivanyuk FA, Ishizuka C, et al. Correlated transitions in TKE and mass distributions of fission fragments described by 4-D Langevin equation. Sci Rep. 2019 Feb;9(1):1525.

[11] Ishizuka C, Zhang X, Usang MD, et al. Effect of the doubly magic shell closures in ^{132}Sn and ^{208}Pb on the mass distributions of fission fragments of superheavy nuclei. Phys Rev C. 2020 Jan;101:011601.

[12] Fujio K, Okumura S, Ishizuka C, et al. Connection of four-dimensional Langevin model and Hauser-Feshbach theory to describe statistical decay of fission fragments. J Nucl Sci Technol. 2024;61(1):84–97.

[13] Pedregosa F, Varoquaux G, Gramfort A, et al. Scikit-learn: Machine learning in Python. J Mach Learn Res. 2011 Oct;12:2825–2830.

Acknowledgments

This work was partially supported by the Ministry of Education, Science, Sports and Culture, Grant-in Aid for Scientific Research(B), 2021-2024(21H01856, Chikako Ishizuka). This work was supported by JST SPRING, Japan Grant Number JPMJSP2106 and JPMJSP2180.

20. Problems on Processing of Thermal Scattering Law Data with AMPX-6

Chikara KONNO*
Nuclear Science and Engineering Center, Japan Atomic Energy Agency
2-4 Shirakata, Tokai-mura, Naka-gun, Ibaraki-ken 319-1195, Japan
*Email: konno.chikara@jaea.go.jp

The AMPX continuous energy libraries bundled in the US nuclear safety analysis code system SCALE6.2 are produced only from the US nuclear data library ENDF/B. Thus, I address to produce an AMPX continuous energy library of JENDL-5 with the AMPX-6 code. In this nuclear data processing, I encountered an issue that several produced AMPX continuous energy files of the thermal scattering law data in JENDL-5 had unusual cross section data. I examined reasons why the unusual cross section data were produced in detail and specified that an inadequate processing method of the thermal scattering law data in AMPX-6 caused the unusual cross section data. I modified AMPX-6 and obtained adequate AMPX continuous energy files of the JENDL-5 thermal scattering law data.

1. Introduction

The US nuclear safety analysis code system SCALE6.2.4 [1] or SCALE6.3.1 [2] is also widely used in Japan, but the bundled libraries are produced mainly from the US nuclear data library ENDF/B [3]. An AMPX continuous energy (AMPX CE) library for various codes in SCALE6.2 produced from JEFF-3.3 [4] was released in 2022 [5]. Thus I have prepared SCALE libraries from JENDL-5 [6] to disseminate JENDL-5. First I produced an activation cross section library for the ORIGEN code in SCALE6.2 or later and released it as ActLib-J5 [7, 8] in 2023. Next decay and fission yield libraries for ORIGEN were also prepared with a simple program and are under testing. Then I started to produce an AMPX CE library from JENDL-5 with the AMPX-6 code [9] bundled in SCALE6.3.1. This nuclear data processing revealed that several produced AMPX continuous energy files of the thermal scattering law (TSL) data in JENDL-5 had unusual cross section data. Here I examine reasons of the unusual cross section data in detail.

2. Production of JENDL-5 AMPX CE library

JENDL-5 has several sub-libraries. Here JENDL-5 u20 data, which are neutron data below 20 MeV, in the neutron sub-library were adopted because AMPX-6 caused infinite loop in processing MT=5 data above 20 MeV. The JENDL-5 TSL sub-library was also processed. Figure 1 shows the processing flow with AMPX-6. Input data for AMPX-6 were generated easily with a graphical user interface called ExSite

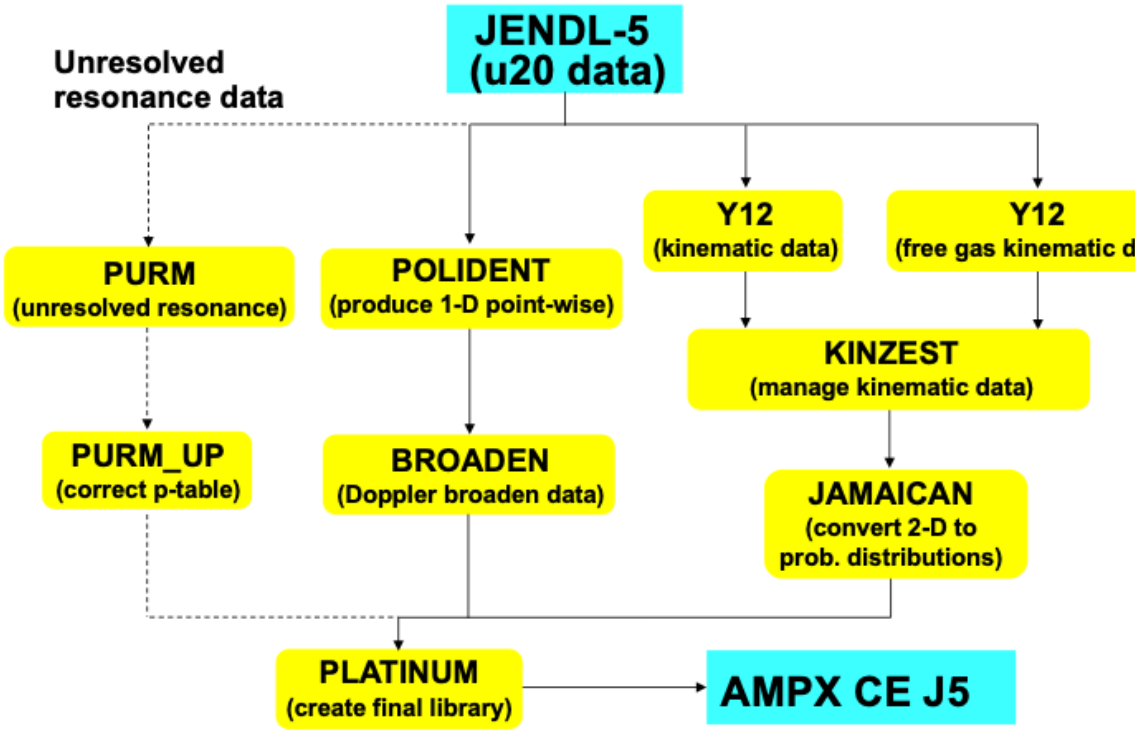

Fig. 1 AMPX processing flow.

[9] bundled in SCALE6.3.1. The same processing condition as the bundled AMPX CE libraries was selected as below.

- Temperature : 293, 565, 900, 1200, 2400 K
- Background cross section for unresolved resonance
  - ✓ 10^8, 10^6, 10^5, 10^4, 10^3, 10^2, 10, 1, 10^{-6} b for nuclei ≤ ^{90}Y
  - ✓ 10^8, 10^6, 10^5, 2x10^4, 1x10^4, 5x10^3, 2x10^3, 10^3, 6400, 320, 160, 120, 80, 60, 40, 30, 20, 15, 10, 8, 6, 4, 2, 1, 0.01, 10^{-6} b for nuclei ≤^{90}Zr
- Upper energy limit of TSL or free gas : 10 eV

AMPX CE files of JENDL-5 u20 data were produced without problems. Note that ^{156m2}Tb and ^{191m2}Ir in JENDL-5 u20 data were omitted because SCALE cannot treat m2 nuclei. Fig. 2 shows the total cross section in the produced JENDL-5 ^{235}U AMPX CE file with that in the official JENDL-5 ^{235}U ACE file [10]. Both the cross section data are almost the same, which demonstrates that the produced AMPX CE files have no problem.

On the contrary, several problems occurred in the processing of the JENDL-5 TSL sub-library. The ^{1}H file in light water has data in many temperatures and AMPX-6 could not process them. Then the temperature data of the ^{1}H file in light water were reduced to 293.6, 560, 570 and 600 K data. The reduced ^{1}H file in light water was processed with AMPX-6 but it was found that the produced AMPX CE file of ^{1}H in light water had unusual cross section data as shown in Fig. 3, which also appeared in other produced AMPX CE files from the JENDL-5 TSL sub-library. Fig. 3 also plots the total cross section of ^{1}H in light water in the bundled ENDF/B-VII.1 AMPX CE library for comparison. It is found that the total cross section of ^{1}H in light water in the produced JENDL-5 AMPX CE library is abnormally large from 1 to 10 eV compared with that in the bundled ENDF/B-VII.1 AMPX CE library. This issue is investigated in the next section.

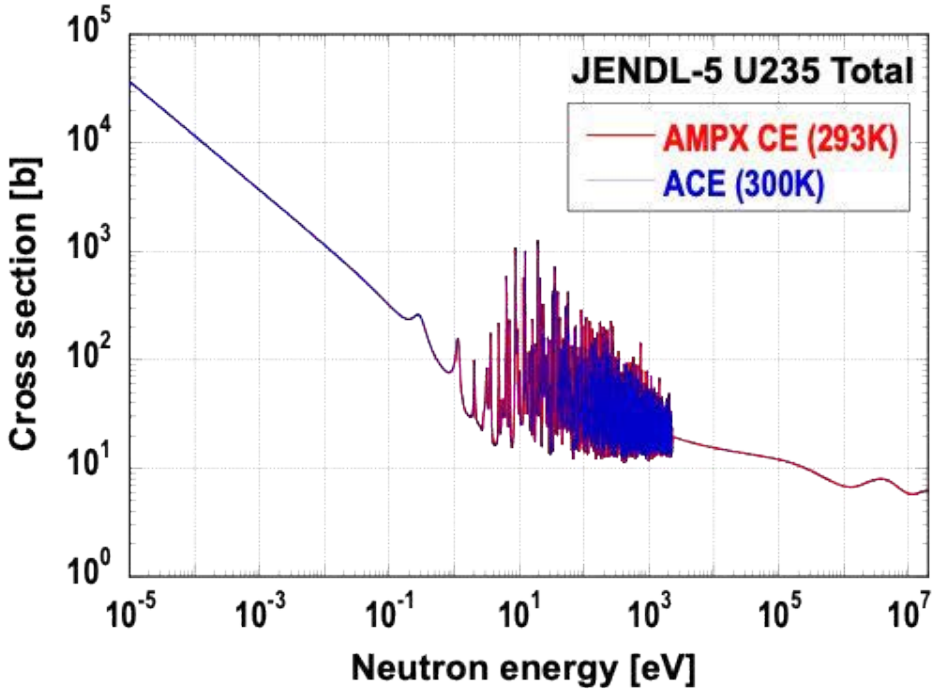

Fig. 2 Total cross section of ^{235}U in JENDL-5.

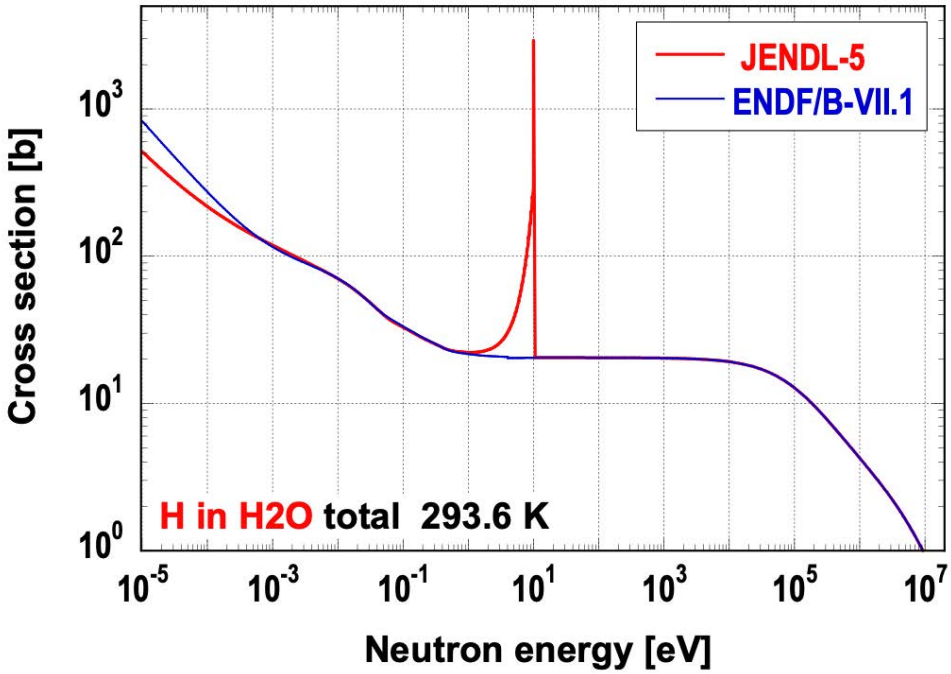

Fig. 3 Total cross section of ^{1}H in light water.

3. Problems of AMPX-6

To investigate the issue of ^{1}H in light water, the source code of AMPX-6 in SCALE6.2.4 was checked in detail because that in SCALE6.3.1 was not available. I compared the processing of AMPX-6 with that of NJOY2016.77 [11] which produced no unusual TSL cross section data. Note that the “H in

H2O" TSL data of JENDL-5 are not $S(\alpha,\beta)$ but $\log(S(\alpha,\beta))$ with the interpolation law of linear-linear, while those of ENDF/B-VII.1 are $S(\alpha,\beta)$ with the interpolation law of log-linear. AMPX-6 converts $\log(S(\alpha,\beta))$ in JENDL-5 to $S(\alpha,\beta)$ but does not change the interpolation law of linear-linear to that of linear-log.

The processing procedure of incoherent inelastic scattering double differential cross section data as shown in Eq. (1) is different between AMPX-6 and NJOY2016.77.

$$\frac{d^2\sigma}{d\Omega dE'}(E \to E', \mu, T) = \frac{M\sigma_b}{4\pi kT}\sqrt{\frac{E'}{E}}e^{-\beta/2}S(\alpha,\beta,T) \quad , \tag{1}$$

where E is the initial neutron energy, E' is the energy of the scattered neutron, μ is the scattering cosine in the laboratory system, T is the Kelvin temperature, k is Boltzmann's constant, M is the number of atoms, σ_b is the characteristic bound incoherent cross section for the nuclide, β is the dimensionless energy transfer (β=(E'−E)/kT), α is the dimensionless momentum transfer (α =E'+E−2$\mu EE'$/AkT) and A is the ratio of the scatter mass to the neutron mass. AMPX-6 calculates $e^{-\beta/2}S(\alpha,\beta,T)$ directly, while NJOY2016.77 calculates $e^{-\beta/2}S(\alpha,\beta,T)$ as $\exp(\log(e^{-\beta/2}S(\alpha,\beta,T)))$=$\exp(-\beta/2 + \log(S(\alpha,\beta,T))$. The NJOY method is better than the AMPX-6 one because $e^{-\beta/2}$ and $S(\alpha,\beta,T)$ may be too huge or too minute. AMPX-6 also has more minor bugs.

I modified AMPX-6 to use the correct interpolation law and the NJOY method for the $e^{-\beta/2}S(\alpha,\beta,T)$ calculation and fixed some bugs. Figs. 4 - 6 show the total cross sections in several AMPX CE files produced from JENDL-5 TSL sub-library with the modified AMPX-6 code, which indicates that the issue is solved.

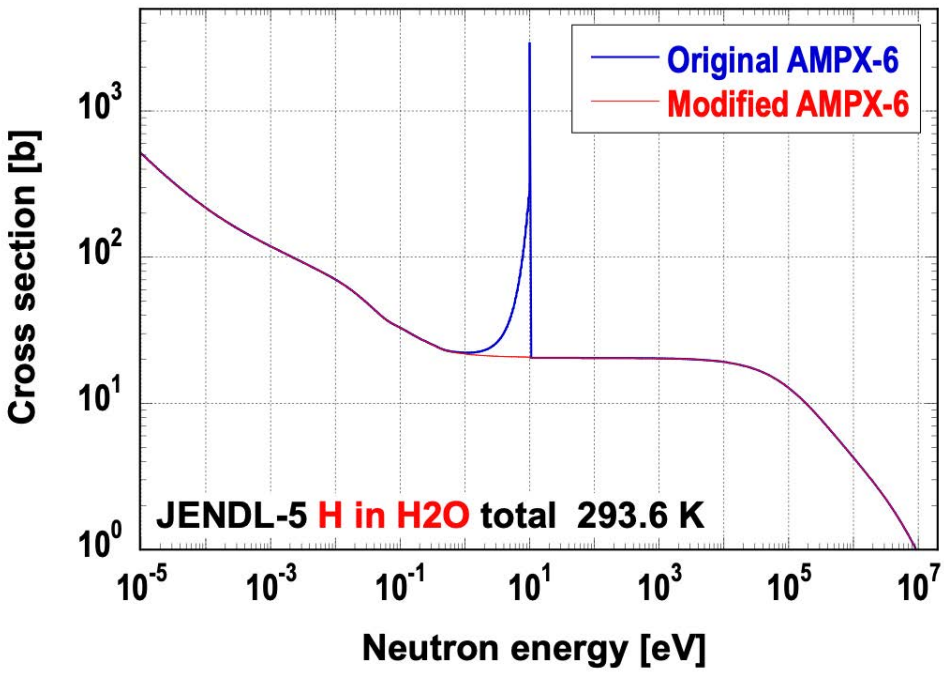

Fig. 4 Total cross section of ^{1}H in light water in JENDL-5.

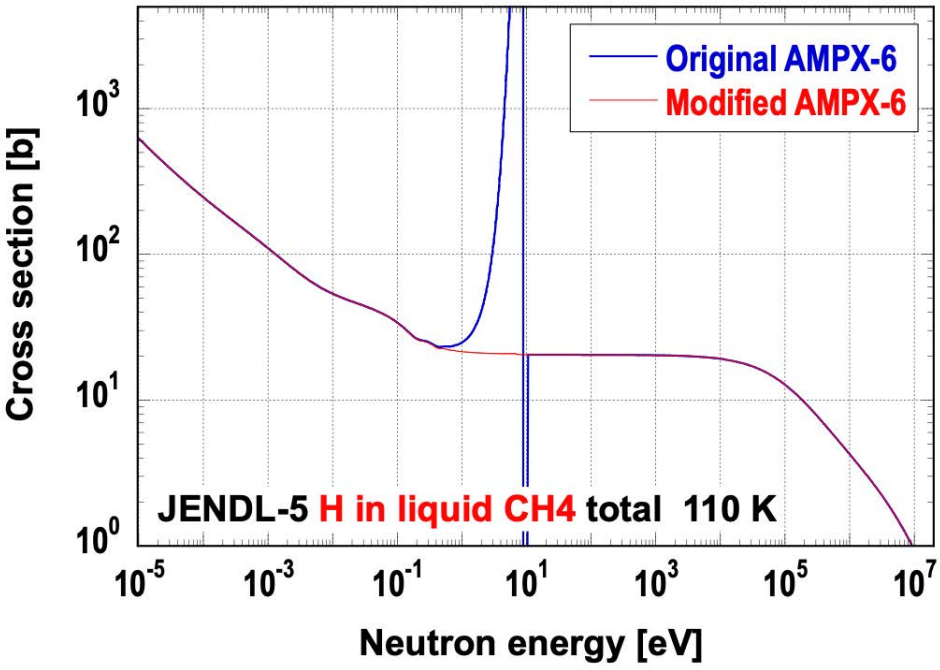

Fig. 5 Total cross section of ^{1}H in liquid CH_4 in JENDL-5.

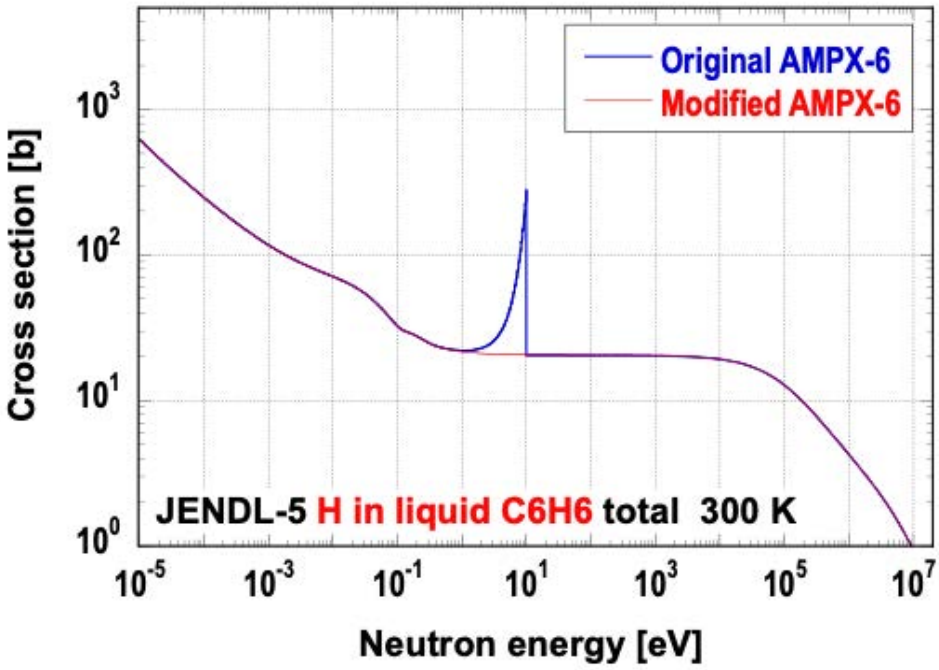

Fig. 6 Total cross section of ^{1}H in liquid C_6H_6 in JENDL-5.

4. Conclusion

The JENDL-5 AMPX CE library has been produced with AMPX-6 to disseminate JENDL-5. The JENDL-5 neutron sub-library up to 20 MeV was processed well, but the several AMPX-6 files produced from the JENDL-5 TSL sub-library had unusual cross section data. This issue was investigated in detail, which specified that an inadequate processing method of TSL data in AMPX-6 caused the issue. AMPX-6 was modified for the issue and it was confirmed that the issue was solved.

References

[1] (Ed.) Wieselquist, W.A., Lefebvre, R.A., Jessee, M.A., SCALE Code System, ORNL/TM-2005/39 Version 6.2.4, 2020.

[2] (Ed.) Wieselquist, W.A., Lefebvre, R.A., SCALE6.3.1 User Manual, ORNL/TM-SCALE6.3.1, 2023.

[3] Brown, D.A. et al., ENDF/B-VIII.0: The 8th Major Release of the Nuclear Reaction Data Library with CIELO-project Cross Sections, New Standards and Thermal Scattering Data, Nuclear Data Sheets, vol.148, 2018, pp.1-142.

[4] Jiménez-Carrascosa, A., Cabellos, O. Díez, C.J., García-Herranz, N., Processing of JEFF nuclear data libraries for the SCALE Code System and testing with criticality benchmark experiments, EPJ Web of Conferences, Vol.284, 2023, 14009.

[5] Plompen, A.J.M, et al., The joint evaluated fission and fusion nuclear data library, JEFF-3.3, The European Physics J. A, Vol.56, 2020, 181.

[6] Iwamoto, O., Iwamoto, N., Kunieda, S., et al., Japanese Evaluated Nuclear Data Library version 5 : JENDL-5, J. Nucl. Sci. Technol. vol.60, 2023, pp.1-60.

[7] Konno, C., Kochiyama, M., Hayashi, H., Generation and verification of ORIGEN and ORIGEN-S activation cross-section libraries of JENDL-5 and JENDL/AD-2017, Mechanical Engineering Journal, Vol.11, 2024, 23-00386.

[8] Japan Atomic Energy Agency, Nuclear Science and Engineering Center, Research Group for Reactor Physics and Thermal Hydraulics, https://rpg.jaea.go.jp/main/en/act-lib, (accessed 2025-03-07).

[9] Wiarda, D., Dunn, M.E., Greene, N.M., Williams, M.L., Celik, C., Petrie, L.M., AMPX-6: A Modular Code System for Processing ENDF/B, ORNL/TM-2016/43, 2016.

[10] Japan Atomic Energy Agency, Nuclear Science and Engineering Center, Research Group for Reactor Physics and Thermal Hydraulics, https://rpg.jaea.go.jp/main/en/ACE-J50, (accessed 2025-03-07).

[11] MacFarlane, R.E., Muir, D.W., Boicourt, R.M., Kahler, A.C., Conlin, J.L., The NJOY Nuclear Data Processing System, Version 2016, LA-UR-17-20093, 2016.

21. Study of INC model for alpha inelastic scattering at 230 MeV/u

Toshimasa FURUTA[1]*, Yusuke UOZUMI[1], and Yuji YAMAGUCHI[2]
1.Department of Applied Quantum Physics and Nuclear Engineering, Kyushu University
744 Motooka, Nishi-ku, Fukuoka-shi, Fukuoka-ken, Japan
2.Japan Atomic Energy Agency
*Email: furuta.toshimasa.451@s.kyushu-u.ac.jp

The Intranuclear Cascade model has been improved for calculating α-particle-induced reactions. The α-particle inelastic scattering is dominant for the α-particle-induced reaction, so that its cross section must be calculated accurately. However, it is difficult to optimize the inelastic reaction and the fragmentation reaction for all fragment channels in parallel. Therefore, in this study, we focus on the inelastic reaction only and calculate the cross section for alpha particles using the break-up model having dependence of target mass density. The calculation results were compared with experimental data of double differential cross sections for the alpha particle at incident energy of 230 MeV/u on ^{27}Al. As a result, good agreements are obtained.

1. INTRODUCTION

There are some simulation models for nuclear reactions caused by various particles, for example, JQMD model, INCL model and so on, which are assembled into Particle and Heavy Ion Transport code System (PHITS) [1]. However, there is no calculation models that are capable of simulating α-particle-induced reaction at few hundred MeV.

Intra-Nuclear Cascade (INC) model is one of simulation models for nuclear reactions. Generally, this model has good compatibility for calculations for proton-induced reactions above 200 MeV. However, experimental result for double differential cross sections (DDXs) for α-particle-induced reactions for all lighter charged particles than $Z < 4$ was only measured by J. R. Wu [2] at 35 MeV/u and that is out of energy range for INC model. Therefore, there was a problem to develop INC model for α-particle-induced reactions that experimental results are lack.

Under this circumstances, experimental result for DDXs for α-particle-induced reaction for emission charged particles at 230 MeV/u was measured by our group [3]. In them, there is characteristic broad peak in α particle spectrum in high energy region at front angle. It was analyzed that it was caused by the emission of α particles in case of peripheral incidence and their non-destructive of nature in collisions with nucleons in target nucleus.

We attempt to improve the INC model using the experimental results and their analytical results. However, it is difficult to optimize the yield of all fragment channel in parallel. Therefore, in this study, we focus only on the emission of the α particle at incident energies of a few MeV/u, i.e., inelastic scattering, which

is dominant for the α particle induced reaction. For that, the treatment of α-nucleon collisions and non-fragmentation probability, which have a large impact on the inelastic scattering, are modified.

2. INC MODEL

The INC model for α-particle-induced reaction is broadly divided into two processes; the cascade process and the fragmentation reaction. Schematic diagram about INC model is shown in Figure 1. The fragmentation reaction occurs at the phase when the α particle incident on the target. When no fragmentation reaction occurs, the α particles enter cascade process and are emitted through collisions with nucleons in the target nucleus. In addition, the "knock out process" is introduced same as (p,α) reaction in the INC-ELF model [4] to reflect the reaction that incident α particles eject the composite particles in target nucleus, which has a probability of producing an α particle. And, the trajectory of the α particle is bent at incident and emission phase to take into account the effect of the potential of the target nucleus.

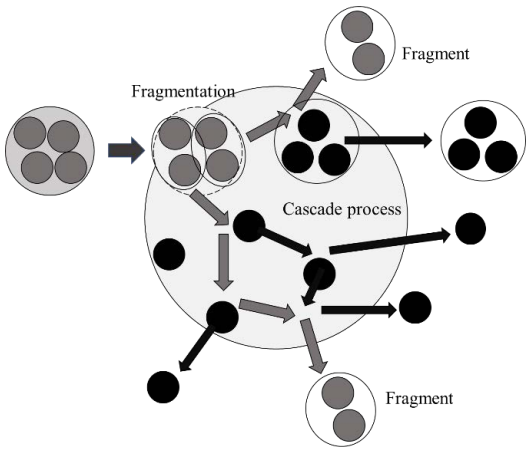

Fig.1 Schematic diagram for INC model

2.1. Fragmentation reaction

α particles are composed of overlaps of some cluster states according to wave function of an α particle which is showed as

$$\left|\alpha\right\rangle \rightarrow C_{\alpha}|\alpha\rangle + C_{\mathrm{pt}}|\mathrm{p},\mathrm{t}\rangle + C_{\mathrm{dd}}|\mathrm{d},\mathrm{d}\rangle + C_{^{3}\mathrm{Hen}}\left|\,^{3}\mathrm{He},\mathrm{n}\right\rangle + C_{\mathrm{ppnn}}|\mathrm{p},\mathrm{p},\mathrm{n},\mathrm{n}\rangle. \quad (1)$$

When an the α particle incident into a target nucleus, it can lose the binding as the α particle caused by temporarily forming a composite nucleus with the target nucleus. As a result, only one cluster state in α particles remains and that is equivalent to the splitting of the α particle. Viewed in this light, fragmentation reactions are regarded as reactions that incident α particles are broken up some fragments with a probability according to wave function of them by interaction with target nucleus.

On the other hands, the production probability of fragments generated from fragmentation reaction has the relationship to impact parameter according to experimental result; the production probabilities of proton,

deuteron and triton are large when impact parameter is small (conversely, the probabilities of ^{3}He and alpha are also large when b-parameter is large). Therefore, that probability is decided having impact parameter dependence. This results in the 33 % probability of α particle non-fragmentation for impact parameters below 3.6 fm and 1 % for all other cases.

2.2. Cluster-nucleon collision

Composite particles generated by fragmentation reactions travel in target nucleus and collide with nucleon. These cluster-nucleon collisions can be replaced by collision between nucleon in composite particles and nucleon in the target nucleus. As well as nucleon-nucleon collision, whether there is a cluster-nucleon collision or not is determined by

$$r_{ij} = \sqrt{\sigma/\pi}, \tag{2}$$

where r_{ij} is distance between nucleons inside and outside of the cluster, and σ is collision cross section of nucleon-nucleon collision. For σ, Cugnon's formula is adopted in this study [5]. After, momentum transfer of the nucleon in the cluster experimenting elastic collision is treated as one of the whole composite particles. However, the momentum transfer of the α particles is faced outward, because the α particle is heavy and has difficulty to enter into the region having high particle density such as center of target nucleus.

In addition, collisions such as below is prohibited; between nucleons in the same cluster, nucleons in separate particles generated fragmentation reaction, a nucleon in a cluster and a nucleon that have already collided another nucleon in that cluster once, and nucleons that have energies after the collision is under the Fermi energy.

3. RESULT AND DISCUSSION

The calculated DDX spectra for the α particle on aluminum at 230 MeV/u at laboratory angle of 15˚ and 40˚ by the previous INC model and the improved INC model are shown in Figures 2 and 3 with experimental data and calculation results by JQMD model [1] and INCL model [6]. Factors indicated in figures are multiplied to data to avoid overlaps of the each DDX spectrum between emission angles. The Generalized Evaporation Model (GEM) [7] is introduced to reproduce lower energy spectra than about 50 MeV/u and exciting energy calculated from the rest condition in the calculation models is used to calculate for it.

There are good agreements between DDX calculated by the improved INC model and the experimental DDX spectra for α particles at 15˚. There is a broad peak at 15˚ at 600 MeV, which is roughly equivalent to the energy of a 230 MeV/u α particle in one collision with a nucleon. Therefore, to form the peak, the incident α particle must be emitted without being broken up when it collides with a nucleon in the target nucleus. In the improved INC model, the incident α particles that did not undergo fragmentation reaction do not be broken up when colliding with a nucleon in target nucleus. As a result, the improved INC model is successful to reproduce the broad peak in the high-energy region. However, in the JQMD model and the INCL model, these results underestimate experimental result, especially the yields in the JQMD model and INCL the model are less than one tenth and one hundredth of the experimental result at the peak energy, respectively. On the

other hand, for the previous INC model, the peak is buried because of the too large yield in low energy region. In contrast, most of the incident α particles with low impact parameter are broken up, making it less likely that low-energy α particles resulting from multiple collisions are emitted in the improved INC model.

At 40˚, high-energy α particles generated in the improved INC model is more than these generated in other models. This is due to the inclusion of the effect of facing momentum transfer of α particle at α-nucleon collision in addition to the effects mentioned above. In low energy region, the improved INC model underestimate DDX, which is likely due to the insufficient contribution of the indirect pickup process.

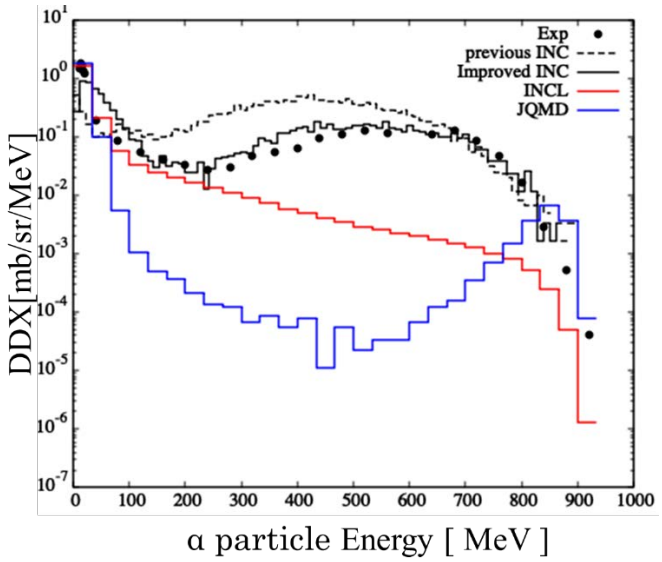

Fig.2 The previous INC model (dot line), the improved INC model (black line), the INCL model (red line), the JQMD model (blue line) and experimental (dots) DDXs for the Al(α,α'x) reaction at 230MeV/u at 15˚

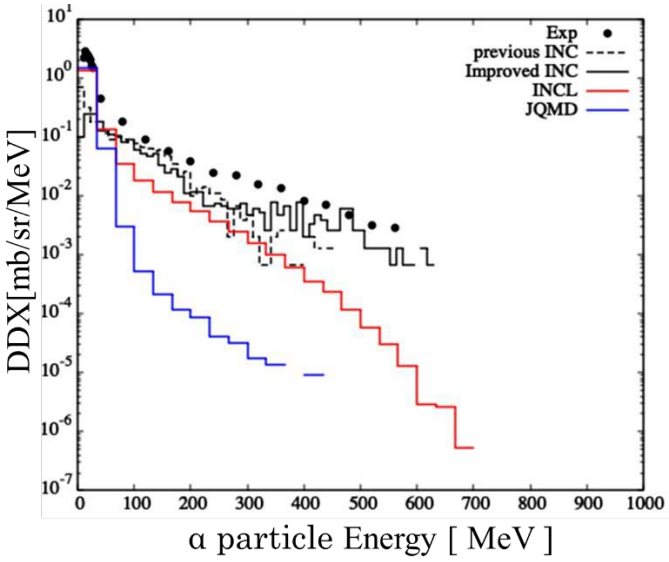

Fig.3 The previous INC model (dot line), the improved INC model (black line), the INCL model (red line), the JQMD model (blue line) and experimental (dots) DDXs for the Al(α,α'x) reaction at 230MeV/u at 40˚

4. CONCLUSION

In this study, the INC model was improved for α particle inelastic scattering with incident energy of a few hundred MeV/u, using the experimental results at incident energy of 230 MeV/u on aluminum measured by our group. We introduced the impact parameter dependence in fragmentation, and the outward momentum transfer of the α particles collided with nucleon. As a result, the α particle DDX spectrum at 15˚ reproduced the experimental result well whereas those calculated by the INCL model and the JQMD model significantly underestimated the experimental result. And the yield of α particles emitting at 40˚ was increased in the improved INC model too.

ACKNOWLEDGEMENTS

This work was conducted under the Research Project with Heavy Ions at QST-HIMAC.

This study was partially supported by JSPS KAKENHI Grant Numbers 22K04989 and 17H03522.

This work was supported by Neutron Source Section of J-PARC center, Japan Atomic Energy Agency under Contract R05K168.

REFERENCES

[1] T. Sato, Y. Iwamoto, S. Hashimoto, T. Ogawa, T. Furuta, S. Abe, T. Kai, P.-E. Tsai, N. Matsuda, H. Iwase, H. Shigyo, L. Sihver, and K. Niita, “Features of Particle and Heavy Ion Transport code System (PHITS) version3.02”, J. Nucl. Sci. Technol. 55, 2018, pp. 684-690.

[2] J. R. Wu, C. C. Chang, and H. D. Holmgran, “Charged particle spectra: 140 MeV α particle bombardment of ^{27}Al, ^{58}Ni, ^{90}Zr, ^{209}Bi, and ^{232}Th”, Phys. Rev. C 19, 1979, pp. 659-673.

[3] T. Furuta, Y. Uozumi, Y. Yamaguchi and et al.. “Double-differential cross sections for charged particle emissions from α particle impinging on Al at 230 MeV/u”, J. Nucl. Sci. Technol., https://doi.org/10.1080/00223131.2023. 2294192

[4] Y. Uozumi Y. Fukuda, Y. Yamaguchi and et al., “Direct pickup and knockout processes in inclusive (p,αx) reactions from 42 to 300 MeV”, Phys. Rev. C 97, 2018, 34630.

[5] J. R. Cugnon, and et al., “Simple parametrization of cross-sections for nuclear transport studies up to the GeV range”, Nucl. Instruments Methods Phys. Res. Sect. B Beam Interact. with Mater. Atoms 111, 1996, 21.

[6] A. Boudard, J. Cugnon, J. C. David, S. Leray, and D. Mancusi, “New potentialities of the Liège intranuclear cascade model for reactions induced by nucleons and light charged particles”, Phys. Rev C87, 2013, 014606.

[7] S. Furihata, “Statistical analysis of light fragment production from medium energy proton-induced reactions”, Nucl. Inst. Meth. in Phys. Res. B 171, 2000, 251.

22. Evaluation of nuclear decay data to revise ENSDF and verification of JENDL-5 Decay Data File for burnup calculation

Hideki IIMURA[1*], Tomoaki WATANABE[2] and Kenya SUYAMA[2]
[1]Nuclear Data Research Laboratory LLC
1-27-2 Futabadai, Mito-shi, Ibaraki-ken 311-4145, Japan
[2]Nuclear Safety Research Center, Japan Atomic Energy Agency
2-4 Shirane, Shirakata, Tokai-mura, Naka-gun, Ibaraki-ken 319-1195, Japan
[*]Email: iimura.hideki1@gmail.com

The updated nuclear decay data is necessary for the accurate burnup calculation. However, some decay data in the Evaluated Nuclear Structure Data File (ENSDF) are old. Therefore, we are performing new evaluations of these data by incorporating experimental data from recent publications. In this report, a few examples of our evaluation are presented. The half-life of ^{129}I, one of the long-lived fission products, has been newly evaluated to be 1.614 (12) $\times 10^7$ y. This value is approximately 3 % larger than those in the present ENSDF and JENDL-5 Decay Data File (DDF). The decay schemes of isomer states of ^{120}Ag, β-delayed neutron emission probabilities, and β-decay energies of some fission products have also been evaluated. Our recommended data have been compared to those in the present ENSDF and JENDL-5 DDF.

1. Introduction

To calculate reliably and accurately concentrations and activities for nuclides generated or depleted by fission and radioactive decay in nuclear fuel, it is necessary to use the updated nuclear decay data such as half-lives, branching ratios, and γ-ray spectra. ENSDF[a], maintained at the National Nuclear Data Center at Brookhaven National Laboratory, USA, is the only database of evaluated decay data for about 3500 nuclides. The data of ENSDF have been periodically revised by the evaluators, who constitute an international network under IAEA's auspices. However, for many nuclides, the latest revision of ENSDF was more than 10 years ago, and the evaluated data for them are old. Therefore, we are performing new evaluations of decay data for these nuclides. Examples presented in this report are the half-life of ^{129}I β decay, the decay schemes of isomer states of ^{120}Ag, β-delayed neutron emission probabilities and β-decay energies of some fission products. Our recommended values are compared with those in the present ENSDF. JENDL-5 DDF[b], one of the sub-libraries of JENDL-5, was publicized in 2021 and updated in 2022. Most of decay data for about 4000 nuclides in JENDL-5 DDF were taken from ENSDF. We verified

[a] https://www.nndc.bnl.gov/ensdf/
[b] https://wwwndc.jaea.go.jp/ftpnd/jendl/jendl-5-dec.html

JENDL-5 DDF data by using our newly evaluated data.

2. Half-life of ^{129}I β decay

The half-life of ^{129}I β decay is crucial nuclear data for managing nuclear waste because this nuclide is one of the long-lived fission products (LLFP). The present version of ENSDF for the mass number A=129, which includes the half-life of ^{129}I, was published in 2014 [1]. The references published before 2014 regarding the half-life measurements of ^{129}I were considered in that version. In 2018, the half-life of ^{129}I was measured by a collaboration of major metrological laboratories in Europe, including Joint Research Centre at Geel, Laboratoire National Henri Becquerel (LNE-LNHB), and Physikalisch-Technische Bundesanstalt (PTB) [2]. Because it is impossible to determine the half-lives longer than 1000 y by measuring the decay of radioactivity, they are deduced by

$$T_{1/2} = \ln(2) \times \mathrm{N}/\mathrm{A} \ , \qquad (1)$$

where A is the radioactivity, and N is the number of atoms in a sample. In Ref [2], A was measured using a liquid scintillator, a well-type Na(I) scintillator and a 4πβ-γ coincidence counter, while N using an ICP mass-spectrometer. From these measurements, the half-life of ^{129}I was determined to be 1.614 (12) ×10^7 y [2]. The uncertainty of radiation measurement was estimated by considering the statistical uncertainty of counts and the systematic uncertainties coming from the background counts, the impurities in a sample, and the decay data [2]. The uncertainty of mass measurement, which came mostly from the number of atoms in standard samples, was also included [2].

Except this measurement in 2018 the half-life of ^{129}I has been measured for 4 times so far: 1.72 (9)×10^7 y in 1951 [3], 1.56 (6) ×10^7 y in 1957 [4], 1.57 (4) ×10^7 y in 1972 [5], and 1.97 (14) ×10^7 y in 1973 [6], which are shown in Fig. 1. The weighted average of these 5 data is 1.613 (18) ×10^7 y, which is also indicated in Fig. 1 by a red line and shaded region. The reduced Chi-Square, $\frac{\chi^2}{n-1}$, is 2.46, where n is the number of data: n=5. When the reduced Chi-Square exceeds the critical value of 2.37, one may reject the hypothesis of the weighted average with a confidence level of 95 %. Therefore, it is

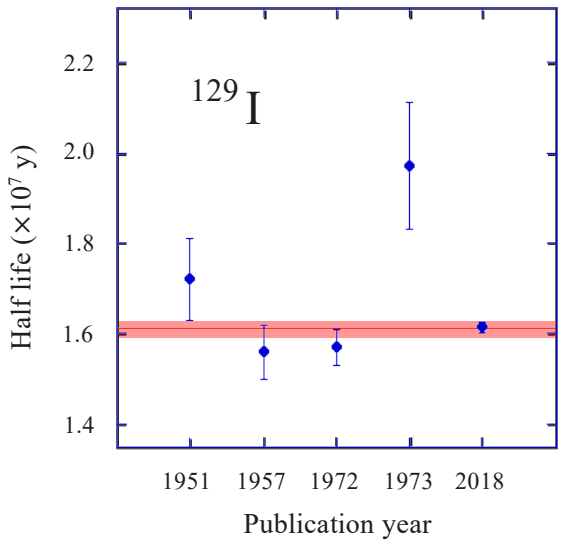

Fig. 1 The experimental values of the half-life of ^{129}I. The average of them is indicated by a red line and shaded region.

inappropriate to average all of these 5 data, and we removed old data measured in the 1950s. The data in 1973 should also not be adopted because its uncertainty is large. The weighted average of the remaining data in 1972 and 2018 is 1.610 (12) $\times 10^7$ y. Because its reduced Chi-Square of 1.11 is smaller than the critical value of 3.84, the weighted average of these two data is appropriate. However, the uncertainty of the data in 2018 is much smaller than that in 1972. Therefore, we have determined that the data in 2018, 1.614 (12) $\times 10^7$ y, should be the recommended value rather than the weighted average. The value in the present ENSDF is the same as the one in 1972. Our recommended value is approximately 3 % larger than this value. The value in JENDL-5 DDF is 1.5711×10^7 y $\pm$ 4.0027×10^5 y. This value was taken from the present ENSDF. A small difference between the present ENSDF and JENDL-5 DDF values seems to be a mistake in inputting data from the former to the latter.

3. Decay schemes of isomer states of ^{120}Ag

The decay scheme of ^{120}Ag in the present ENSDF [7], revised in 2002, was adopted from the experimental data by Forgerberg et al. [8]. In their experiment, ^{120}Ag was produced by the U(*n*, fission) reaction in a reactor, and then mass-separated online for subsequent γ-ray measurements. They found that there exists an isomer of ^{120}Ag having a half-life of 0.32 s and the excitation energy of 203 keV [8], as shown in the left part in Fig. 2. In 2018 Batchelder et al. [9] measured γ rays emitted from a ^{120}Ag sample by using a high-sensitive array of Compton-suppressed Ge detectors surrounding the sample, and found approximately 300 new γ-rays. Moreover, by carefully measuring the decay of these γ-rays they found another isomer state [9]. We adopt their results in our new evaluation, as shown in the right part in Fig. 2. Regarding the half-lives, the value in Ref. [8], 1.23(4) s, may be attributed to a mixture of two β decays. Therefore, we adopt the values in Ref. [9], 0.94(10) s and 1.52(7) s. Because it is unknown which half-life corresponds to the ground state, the excitation energies of these states are depicted as 0.0+x keV and 0.0+y keV in Fig. 2. As for the half-life of the isomer state at 203.2+y keV, three experimental values have been reported so far: 0.32 (4) s [8], 0.44 (5) s [9], and 0.40 (3) s [10]. Because the data in Ref. [8] is old, we determined the recommended value to be the weighted average, 0.41(3) s, of the data in Refs. [9] and [10]. Although the branching ratio of the isomer transition (IT) from the 203.2-keV state was

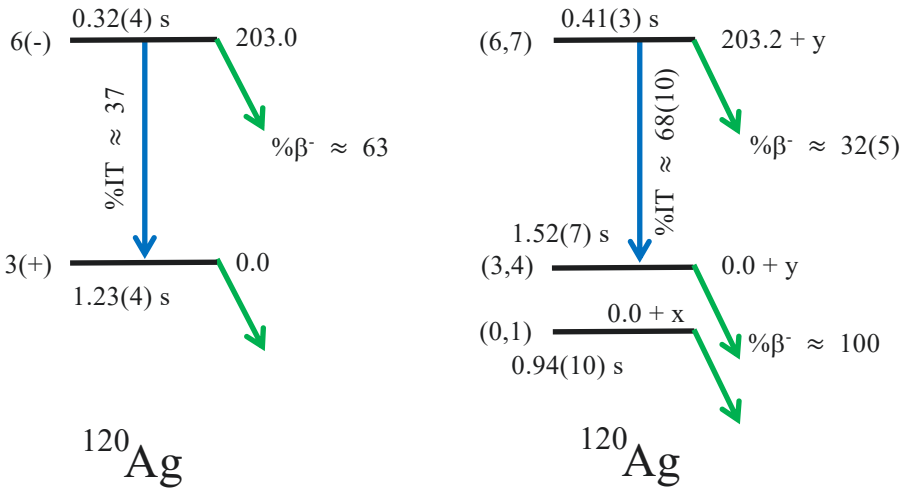

Fig. 2 A part of the decay scheme of ^{120}Ag adopted in the present ENSDF (left) and our new evaluation (right).

approximately 37% in Ref. [8], a much different value of 68(10) % was reported by Batchelder et al. [9]. We adopt the value in Ref. [9], because the uncertainty was not given for the value in Ref. [8]. We evaluated the spins and parities, as shown in the right part in Fig. 2, based on the β-decay branching ratios to the states of ^{120}Cd and the *E*3 multipolarity of IT [9]. Here, we calculated the β-decay branching ratios from the γ-ray intensities in Ref. [9]. As a result, we found a large negative intensity balance at the 1203.7-keV state of ^{120}Cd, which means there is an inconsistency in the data in Ref. [9].

The decay scheme of ^{120}Ag in JENDL-5 DDF is the same as in the present ENSDF, except for the half-lives and branching ratio. In JENDL-5 DDF, the half-lives of the ground state and the 203-keV state are 0.94 (10) s and 1.52 (7) s, respectively, and the branching ratio of IT is 27 %. These values are mistakes.

4. Delayed neutron emission probabilities in β decays

The updated data on delayed neutron is necessary to enhance calculational capabilities in nuclear energy, safeguards, and used fuel management. Recently, new measurements of β-delayed neutrons have been undertaken at various laboratories such as GSI, TRIUMF, ORNL and RIKEN. However the status of ENSDF is not satisfactory. For example, Table 1 lists some fission products for which there has no delayed neutron emission data in ENSDF. Our recommended values of one-and two-neutron emission probabilities (P_{1n} and P_{2n}) for these nuclides are adopted from recent measurements [11-14]. The P_{1n} value for ^{120}Rh$_{75}$ was reported as <5.4 [11], <8.9(4) [12], and 7.2(16) [13], and we adopt the most recent value in Ref. [13]. Similarly, we adopt the P_{1n} values for ^{129}Ag$_{82}$ from Ref. [14], rather than the same group's older value of 17.9(14) [13]. It should be noted that our evaluated P_{1n} and P_{2n} values possibly correspond to a mixture of β decays from ground and isomeric states. JENDL-5 DDF has data for ^{120}Rh$_{75}$, ^{120}Ag$_{73}$ and ^{129}Ag$_{82}$ as listed in Table 1. These values are different from our recommended values, and how these values were deduced is unknown.

The updated β-decay energies (*Q*) of fission products are necessary to estimate the decay heat accurately. The *Q* values can be calculated from the atomic masses of precursor and daughter nuclei: $Q=M(A,Z)-M(A,Z+1)$ for the β^- decay, where *M* is atomic mass, *A* mass number, and *Z* proton number. Wang et al. evaluate the atomic masses of all nuclides and revise their atomic mass database approximately every 4 years. We adopt masses in their latest version of the database, AME2020 [15]. The *Q* values in AME2020 for some fission products are listed in Table 2. The *Q* values in the present ENSDF and JENDL-5 DDF were taken from former versions of the atomic mass database,

Table 1. β-delayed one- and two-neutron emission probabilities (P_{1n} and P_{2n}) of some fission products

Element	*Z*	*N*	Our new evaluation		JENDL-5 DDF
			P_{1n} (%)	P_{2n} (%)	
Ru	44	76	6 (3)		
Rh	45	75	7.2 (16)		2.7
Pd	46	74	<0.7		
Ag	47	73	<0.003		0.0005
Ag	47	82	18.2 *+1.0-0.7*	<1.2	10
Cd	48	81	1.84 (15)		

Table 2. β-decay *Q* values of some fission products. The present ENSDF and JENDL-5 DDF values were taken from former atomic mass database versions, (a) AME2016 and (b) AME2012.

Element	*Z*	*N*	*Q* (keV)		
			AME2020	ENSDF	JENDL-5 DDF
Tc	43	77	14720	14490[a]	14490[a]
Ru	44	76	8900	8800[a]	8800[a]
Rh	45	75	11660	11470[a]	11470[a]
Pd	46	74	5372 (5)	5371 (5)[a]	5371 (5)[a]
Ag	47	73	8306 (6)	8306 (6)[a]	8306 (6)[a]
Cd	48	81	9713 (6)		9780 (17)[a]
In	49	80	7756 (17)	7769 (19)[b]	7753 (17)[a]
Sn	50	79	4039 (27)	4022 (29)[b]	4037 (27)[a]
Sb	51	78	2375 (71)	2376 (21)[b]	2375 (21)[a]

AME2016 [16], and AME2012 [17]. These *Q* values differ slightly between versions of the atomic mass database especially for short-lived nuclides.

5. Summary

The half-life of long-lived ^{129}I has been newly evaluated. Our recommended value is approximately 3 % larger than that of ENSDF and JENDL-5 DDF. Because the decay schemes of many isomer states are ambiguous, those in ENSDF and JENDL-5 DDF must be updated using newly available experimental data. For example, we evaluated the decay schemes of isomer states of ^{120}Ag and found significant changes from the present recommended data. Recently, much experimental data on the β-delayed neutron emission probabilities and the atomic masses have been reported because of the development of new techniques. However, as shown for some fission products, many of those data are not included in ENSDF and JENDL-5 DDF.

References

1) Timar, J., Elekes, Z., Singh, B., Nuclear Data Sheets for A=129, Nucl. Data Sheets, vol.121, 2014, pp.143-394.
2) Garcia-Torano, E. et al., The half-life of ^{129}I, Appl. Radiation and Isotopes, vol.140, 2018, pp.157-162.
3) Katcoff, S., Schaeffer, O.A., Hastings, J.M., Half-life of ^{129}I and the age of the elements, Phys. Rev., vol. 82, 1951, pp.688-690.
4) Russell, H.T., Recovery and half-life determination of ^{129}I, ORNL-2293, 1957.
5) Emery, J.F., Reynolds, S.A., Wyatt, E.I., Gleason, G.I., Half-lives of radionuclides-IV, Nucl. Sci. Eng., vol.48, 1972, pp.319-323.
6) Kuhry, J.G., Bontems, G., Periode de ^{129}I et section efficace de la reaction ^{129}I(n, 2n)^{128}I pour des neutrons de 14.5 MeV, Radiochem. Radioanal. Lett., vol.15, 1973, pp.29.

7) Kitao, K., Tendow, Y., Hashizume, A., Nuclear Data Sheets for A=129, Nucl. Data Sheets, vol.96, 2002, pp.241-390.
8) Fogelberg, B., Bäcklin, A., Nagarajan, T., Energy levels in $^{114, 116, 118, 120, 112}$Cd as observed in the beta decay of Ag isotopes, Phys. Lett. B, vol.36, 1971, pp.334-336.
9) Batchelder, J.C. et al., Low-lying collective states in ^{120}Cd populated by β decay of ^{120}Ag: Breakdown of the anharmonic vibrator model at the three-phonon level, Phys. Rev. C, vol.86, 064311, 2012, pp.1-15.
10) Wang, Y. et al., Decay of neutron-rich ^{118}Ag and ^{120}Ag isotopes, Phys. Rev. C, vol.67, 064303, 2012, pp.1-12.
11) Monters, F. et al., β-decay half-lives and β-delayed neutron emission probabilities for neutron rich nuclei close to the N = 82 r-process path, Phys. Rev. C, vol.73, 035801, 2006, pp.1-9.
12) Shearman, R. et al., Determination of β-delayed neutron emission probability limits of rhodium isotopes by γ-ray spectroscopy, J. Phys.: Conf. Ser., vol.1643, 012208, 2020, pp.1-9.
13) Hall, O. et al., β-delayed neutron emission of r-process nuclei at the N=82 shell closure, Phys. Lett. B, vol.816, 136266, 2021, pp.1-7.
14) Phong, V.H. et al., β-delayed one and two neutron emission probabilities southeast of ^{132}Sn and the odd-even systematics in r-process nuclide abundances, Phys. Rev. Lett., vol.129, 172701, 2022, pp.1-7..
15) Wang, M. et al., The AME2020 atomic mass evaluation (II). Tables, graphs and references, Chin. Phys. C, vol.45, 030003, 2021, pp.1-512.
16) Wang, M. et al., The AME2016 atomic mass evaluation (II). Tables, graphs and references, Chin. Phys. C, vol.41, 030003, 2017, pp.1-442.
17) Wang, M. *et al*., The AME2012 atomic mass evaluation (II). Tables, graphs and references, Chin. Phys. C, vol.36, 2012, pp.1603-2014.

23. Generation of JENDL-5 Covariance Libraries and their Application on the keff Uncertainties of the Indonesian RSG GAS Multipurpose Research Reactor Criticality Benchmark

Peng Hong LIEM[1,2*] and Donny HARTANTO[3]
[1]Scientific Computational Division, Nippon Advanced Information Service (NAIS Co., Inc.), 416 Muramatsu, Tokaimura, Ibaraki, Japan
[2]Cooperative Major in Nuclear Energy, Graduate School of Engineering, Tokyo City University (TCU),1-28-1 Tamazutsumi, Setagaya, Tokyo, Japan
[3]Oak Ridge National Laboratory (ORNL), One Bethel Valley Road, Oak Ridge, TN 37830, United States of America
[*]Email: liemph@nais.ne.jp

The criticality, sensitivity, and uncertainty analysis of the clean, first core of the Indonesian G. A. Siwabessy Multipurpose Reactor (RSG GAS, previously called MPR-30), using the newly released Japanese Nuclear Data Library version 5 (JENDL-5), was conducted to contribute to the validation effort of the JENDL-5, especially for its application on beryllium-reflected, light-water-moderated, low-enriched uranium (19.75 wt. %) fueled material testing reactors. The JENDL-5 sensitivity coefficients and covariance matrices were prepared by MCNP6 and AMPX-6, respectively. A special JENDL-5 covariance matrices was also prepared by adding ENDF/B-VIII.0 covariance matrices for JENDL-5 nuclides lack of covariance data. The neutron multiplication factor (keff) uncertainty was then evaluated using the TSUNAMI-IP module of SCALE-6. The criticality (keff) analysis results ([C/E-1]) showed maximum overestimations of 801 pcm, 477 pcm, and 547 pcm for JENDL-5, JENDL-4.0, and ENDF/B-VIII.0, respectively. The keff uncertainty originating from the nuclear data was estimated to be 620 pcm, 644 pcm, and 637 pcm for JENDL-5 only, JENDL-5 & ENDF/B-VIII.0, and ENDF/B-VIII.0 covariance data, respectively, which are comparable with the keff ([C/E-1]) values.

1. Introduction

Almost twelve years after the Japanese Evaluated Nuclear Data version 4 (JENDL-4.0) was released in 2012 [1], the new version, JENDL-5, was released in December 2021 [2] with the aim of addressing significant issues in nuclear energy development in Japan [3]. Notably, JENDL-5 provides more nuclides as well as covariance data than its predecessor, JENDL-4.0.

In our previous studies, criticality experiments on the clean, first core of the Indonesian G. A. Siwabessy Multipurpose Reactor (RSG-GAS) were used to validate JENDL and other widely used nuclear data libraries such as ENDF/B and JEFF. The RSG GAS is a light water-moderated and cooled material testing reactor, using low-enriched uranium (LEU, 19.75 wt. % enrichment) as fuel and

beryllium as a neutron reflector. It is designed with a maximum thermal power of 30 MW, achieving its first criticality in July 1987.

In continuation of our previous work, this study conducted a similar sensitivity and uncertainty (S/U) analysis for the newly released JENDL-5 [4]. For the S/U analysis, a JENDL-5 covariance library was generated utilizing all available JENDL-5.0 covariance data. Additionally, a specialized JENDL-5 covariance library was created, incorporating ENDF/B-VIII.0 covariance data for JENDL-5 nuclides that lacked their own covariance data.

2. RSG GAS First Core Criticality Experiments

The main specifications of the RSG GAS reactor, as well as the details of the criticality experiments, can be found elsewhere [5]. Figure 1 illustrates the full core configuration of the first core, including its standard (FE) and control (CE) elements. Two groups of criticality experiments were conducted for the first core of RSG GAS: (1) the criticality approach experiment for achieving the first criticality and the criticality experiment for core excess reactivity loading, and (2) control rod calibrations under critical full core conditions. In this study, the combinations of control rod positions that occurred during control rod calibration with the bank compensation method were selected for the benchmark calculations. As shown later in Table 1, Case 2-1 of the second group was selected for the S/U analysis.

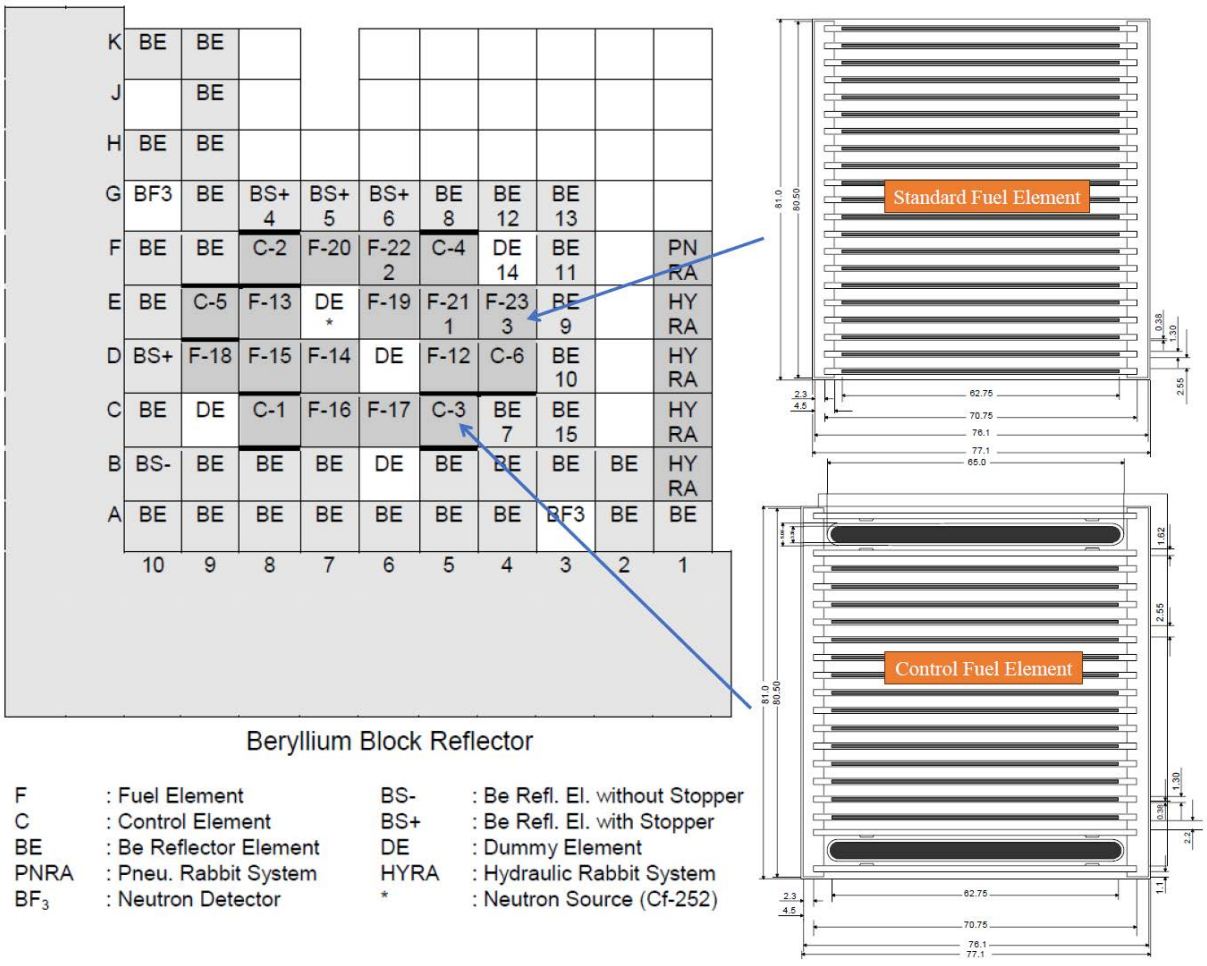

Figure 1. Full core configuration of the RSG GAS clean first core (plain numbers show the loading step of fuel, Be reflector and dummy elements after the first criticality; empty lattices contain water).

3. Methodology

3.1. Sensitivity and Uncertainty Analysis

The calculation procedure for the S/U analysis is illustrated in Figure 2. Sensitivity coefficients in a 252 energy-group were prepared using the MCNP-6.2 code [6] with the KSEN option. Covariance libraries in the COVERX 56 energy-group format were generated by employing the AMPX-6 code [7], utilizing the PUFF-IV module [8]. The 56 energy-group structure matches the one used in SCALE-6.2 [9]. Among the 795 nuclides in JENDL-5, only 105 have covariance data, whereas ENDF/B-VIII.0 contains 251 nuclides with covariance data. Given that JENDL-5 has significantly fewer nuclides with covariance data than ENDF/B-VIII.0, we also compiled a special JENDL-5 covariance library with additional ENDF/B-VIII.0 covariance data for JENDL-5 nuclides lacking their own covariance data. Using this specialized JENDL-5 covariance library, the uncertainty of JENDL-5 can be compared to that of ENDF/B-VIII.0. The TSUNAMI-IP module [10] was employed for the keff uncertainty calculations.

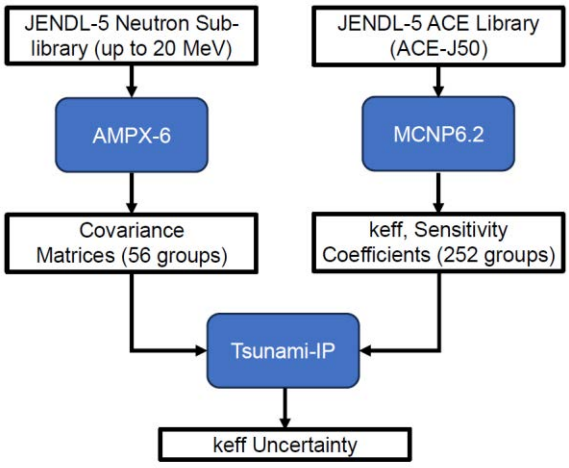

Figure 2. Analysis procedure of keff uncertainty due to nuclear data.

3.2. Monte Carlo Modelling

The active sections (7.71 x 8.1 x 60 cm^3) of both FE and CE were modeled according to their exact geometries and dimensions. However, the top and end-fittings, due to their complex geometry, were approximated by homogenizing the structure materials with water using volume weighting. All calculations in this benchmark were conducted at a room temperature of 300 K. Adjustments were made to the measured critical effective multiplication factors to correct for instances where the core isothermal temperature differed from 300 K. The analysis included a total of 10,000 batches (generations), each consisting of 10,000 histories, resulting in a total of 100 million effective histories. The first 100 batches were omitted to ensure the fundamental mode was reached before conducting the statistical evaluation of keff and other tallies. Under these calculation conditions, the fractional standard deviation (FSD) for keff was maintained below 0.01% for all cases.

4. Analysis Results and Discussion

The MCNP criticality analysis results for JENDL-5, JENDL-4.0, and ENDF/B-VIII.0 are presented

in Table 1, divided into two groups according to Ref. [5]. The experiment/measured keff is 1.0, enabling straightforward estimation of the calculated to experiment (C/E) values from the table (excluding non-critical cases, 1-2 and 1-3). Overall, the JENDL-4.0 results exhibit the closest agreement with the experimental results, followed by ENDF/B-VIII.0 and JENDL-5. In Group 1, the first criticality (Case 1-1) comprised 9 FEs and 6 CEs, with the core showing a slight excess reactivity equivalent to the insertion of the regulation rod (RR, position 475 mm). For this initial criticality condition, the keff values from JENDL-5, JENDL-4.0, and ENDF/B-VIII.0 indicated overestimations of 801 pcm, 477 pcm, and 547 pcm, respectively. In Group 2, the six cases of critical full core during control rod calibration (Case 2-1 to 2-6) included 12 FEs and 6 CEs, with all control rods partially inserted except the measured control rod. Here, the maximum overestimation of keff values for JENDL-5, JENDL-4.0, and ENDF/B-VIII.0 were 650 pcm, 431 pcm, and 452 pcm, respectively.

Table 1. Criticality analysis results [4].

Case	First criticality and excess reactivity loading (First Group)	JENDL-5	JENDL-4.0	ENDF/B-VIII.0
1-1	First criticality (9 FEs, 6 CEs, RR=475 mm)	1.00801 ± 0.00008	1.00477 ± 0.00008	1.00547 ± 0.00008
1-2	Full core (12 FEs, 6 CEs, CRs all up)	1.10167 ± 0.00008	1.09949 ± 0.00008	1.09912 ± 0.00007
1-3	Full core (12 FEs, 6 CEs, CRs all down)	0.92088 ± 0.00008	0.91957 ± 0.00008	0.91974 ± 0.00008
Case	Calibrated rod/grid position (calibrated rod position/other rod bank position) (Second Group, 12 FEs, 6 CEs)	JENDL-5	JENDL-4.0	ENDF/B-VIII.0
2-1	JDA06 / C-8 (600 mm / 290 mm)	1.00465 ± 0.00008	1.00282 ± 0.00008	1.00302 ± 0.00008
2-2	JDA01 / E-9 (600 mm / 284 mm)	1.00478 ± 0.00008	1.00257 ± 0.00008	1.00301 ± 0.00008
2-3	JDA03 / F-8 (600 mm / 293 mm)	1.00599 ± 0.00008	1.00379 ± 0.00008	1.00406 ± 0.00008
2-4	JDA05 / C-5 (600 mm / 288 mm)	1.00584 ± 0.00008	1.00400 ± 0.00008	1.00415 ± 0.00008
2-5	JDA04 / F-5 (600 mm / 290 mm)	1.00650 ± 0.00008	1.00431 ± 0.00008	1.00452 ± 0.00008
2-6	JDA07 / D-4 (600 mm / 282 mm)	1.00614 ± 0.00008	1.00422 ± 0.00008	1.00426 ± 0.00008

The sensitivity analysis has been conducted using JENDL-5, JENDL-4.0, and ENDF/B-VIII.0 libraries for Case 2-1 (Second group, 12 FEs, 6 CEs), where the full core was critical during C-8 regulation rod calibration. The keff sensitivities in the decreasing direction were primarily influenced by (n, gamma) reactions of H-1, U-235, Al-27, U-238, Be-9, Mn-55, Ag-109, In-115, Ag-107, Cd-113, and Fe-56. The sensitivities in the increasing direction were predominantly influenced by U-235 (total nu) & (fission), H-1 (free gas, elastic) & (S(α,β), inelastic), Be-9 (elastic) & (n, 2n), O-16 (elastic), and Al-27 (elastic). The sensitivity analysis results for JENDL-5 exhibited similar trends to those observed in previous work with JENDL-4.0 [11].

The uncertainty analysis was conducted using TSUNAMI-IP with JENDL-5 and ENDF/B-VIII.0 libraries for Case 2-1. The uncertainty analysis results are presented in Table 2, while the primary contributors to uncertainty for JENDL-5 are shown in Table 3. According to Table 2, the keff uncertainties due to nuclear data are presented for three combinations of sensitivity coefficients and covariance libraries: JENDL-5 only, JENDL-5 & ENDF/B-VIII.0, and ENDF/B-VIII.0. When using only the 105 covariance matrices of JENDL-5, the uncertainty was approximately 620 pcm. When additional

covariance matrices from ENDF/B-VIII.0 were used, the uncertainty increased to 644 pcm, indicating a small difference of around 24 pcm for the present system. The uncertainty for ENDF/B-VIII.0 was evaluated at 637 pcm, comparable to that of JENDL-5. Thus, the nuclear data uncertainties for JENDL-5 and ENDF/B-VIII.0 are of the same order for this system.

Table 2. Uncertainties analysis results [4] (pcm=10^{-5}).

Sensitivity Coefficients	Covariance Matrices	Uncertainty (pcm)
JENDL-5 (MCNP6.2, KSEN option)	JENDL-5 only (AMPX-6)	620
JENDL-5 (MCNP6.2, KSEN option)	JENDL-5 & ENDF/B-VIII.0 * (AMPX-6)	644
ENDF/B-VIII.0 (MCNP6.2, KSEN option)	ENDF/B-VIII.0 (SCALE 6.3.0)	637

*: For JENDL-5 nuclides which have no covariance data.

Table 3. Uncertainty main contributors (> 0.001%) [4]

Nuclide	Reaction	with	Nuclide	Reaction	% dR/R due to this matrix		
U-235	chi	with	U-235	chi	3.76E-01	+/-	1.78E-04
H-freegas	n,gamma	with	H-freegas	n,gamma	3.48E-01	+/-	9.93E-06
U-235	nubar	with	U-235	nubar	3.00E-01	+/-	1.19E-05
H-1	n,n'	with	H-1	n,n'	2.41E-01	+/-	6.47E-04
U-235	fission	with	U-235	fission	1.62E-01	+/-	1.08E-05
H-freegas	elastic	with	H-freegas	elastic	1.27E-01	+/-	2.85E-05
H-freegas	elastic	with	H-freegas	n,gamma	-1.14E-01	+/-	1.92E-05
Al-27	n,gamma	with	Al-27	n,gamma	1.07E-01	+/-	8.73E-07
Al-27	elastic	with	Al-27	elastic	8.63E-02	+/-	7.24E-05
Al-27	n,n'	with	Al-27	n,n'	7.15E-02	+/-	2.28E-05
Be-9	elastic	with	Be-9	elastic	6.29E-02	+/-	1.17E-05
Be-9	n,2n	with	Be-9	n,2n	3.56E-02	+/-	8.63E-06
U-238	n,gamma	with	U-238	n,gamma	3.46E-02	+/-	5.28E-07
U-235	n,gamma	with	U-235	n,gamma	3.19E-02	+/-	1.48E-07
U-235	fission	with	U-235	n,gamma	-2.80E-02	+/-	4.38E-07
Be-9	n,gamma	with	Be-9	n,gamma	2.37E-02	+/-	2.01E-07
U-238	n,n'	with	U-238	n,n'	2.03E-02	+/-	6.28E-06
Be S(α,β)	n,n'	with	Be S(α,β)	n,n'	1.86E-02	+/-	1.27E-05
Be-9	n,2n	with	Be-9	elastic	-1.71E-02	+/-	1.82E-06
Be-9	n,alpha	with	Be-9	n,alpha	1.43E-02	+/-	1.77E-07
Fe-56	n,gamma	with	Fe-56	n,gamma	1.37E-02	+/-	1.17E-07
O-16	elastic	with	O-16	elastic	1.28E-02	+/-	7.51E-07
U-238	elastic	with	U-238	elastic	1.26E-02	+/-	2.76E-06
Ag-109	n,gamma	with	Ag-109	n,gamma	1.20E-02	+/-	1.81E-07
U-238	elastic	with	U-238	n,gamma	1.16E-02	+/-	2.00E-06

In Table 3, the JENDL-5 uncertainty contributors are sorted and listed using the JENDL-5 & ENDF/B-VIII.0 covariance matrices. The dominant contributors (i.e., > 0.1 %) include U-235 (chi), (nu-bar) & (fission), H-1 (n, gamma), (elastic) & (S(α,β), inelastic), O-16 (elastic), and Al-27 (n, gamma). In the RSG GAS, LEU (19.75 wt. % U-235 enrichment) is used, thus U-235 fission-related parameters significantly contribute to keff uncertainty. Water, used as a moderator and coolant, is present in large quantities in the core, reflector, and other structural regions. Consequently, the H-1 component of water significantly contributes both as free gas (elastic) and when bound by O-16 (S(α,β), inelastic).

Referring to the JENDL-5 [C/E-1] of Case 2-1 shown in Table 1 (~465 pcm), the evaluated keff uncertainty of JENDL-5 at 644 pcm is comparable. However, it is premature to conclude that the deviation of [C/E] from 1.0 originated solely from the nuclear data, as other uncertainties, such as compositions, dimensions, and criticality measurements, were not accounted for.

References

[1] Shibata, K. et al., JENDL-4.0: A New Library for Nuclear Science and Engineering, J. Nucl. Sci. Technol., 48(1), 2011.

[2] Iwamoto, O. et al., Japanese Evaluated Nuclear Data Library version 5: JENDL-5, J. Nucl. Sci. Technol., 60(1), 2023, pp. 1-60.

[3] Iwamoto, O. et al., Status of JENDL, 2019 International Conference on Nuclear Data for Science and Technology (ND2019), Beijing, China.

[4] Liem, P. H. and Hartanto, D., JENDL-5.0 Nuclear Data Sensitivity, Uncertainty, and Similarity Analyses on the Criticality of RSG GAS Multipurpose Research Reactor, Nucl. Eng. Design 418, 2024, pp. 112899.

[5] Liem, P. H. and Sembiring, T. M., Benchmarking the new JENDL-4.0 library on criticality experiments of a research reactor with oxide LEU (20 w/o) fuel, light water moderator and beryllium reflectors, Ann. Nucl. Energy 44, 2012, pp. 58-64.

[6] Werner, C. J. et al. (Ed.), MCNP User's Manual; Code Version 6.2, LA-UR-1729981, 2017.

[7] Wiarda, D. et al., AMPX-6: A Modular Code System for Processing ENDF/B, ORNL/TM-2016/43, 2016.

[8] Wiarda, D. and Dunn, M. E., PUFF-IV: A Code for Processing ENDF Uncertainty Data into Multigroup Covariance Matrices, ORNL/TM-2006/147/R1 (October 2006, Revised 2008), 2008.

[9] Rearden, B. T. and Jessee, M. A. (Ed.), SCALE Code System, ORNL/TM-2005/39 Version 6.2.1, 2016.

[10] Rearden, B. T. and Jessee, M. A. (Ed.), Tsunami Utility Modules, ORNL/TM-2005/39 Version 6, Vol. III, Sect M18, 2009.

[11] Liem, P. H. et al., Sensitivity and uncertainty analysis on the first core criticality of the RSG GAS multipurpose research reactor, Prog. in Nucl. Energy 114, 2019, pp. 46-60.

Acknowledgements

We extend our gratitude to all members of the RSG GAS commissioning group for their efforts in compiling the criticality experiment data. We also express our appreciation to Mrs. Suzuko Ikegami for her preparation of the tables and graphs.

24. Decay branching ratios of ^{197m}Hg and ^{195m}Hg determined by decay curve analysis

Naohiko OTUKA[†1,2], Masayuki AIKAWA[2,4,5,6], Sándor TAKÁCS[3], Shuichiro EBATA[7], and Hiromitsu HABA[2]

[1]Nuclear Data Section, Division of Physical and Chemical Sciences, Department of Nuclear Sciences and Applications, International Atomic Energy Agency, 1400 Wien, Austria
[2]Nishina Center for Accelerator-Based Science, RIKEN, Wako 351-0198, Japan
[3]HUN-REN Institute for Nuclear Research (ATOMKI), 4026 Debrecen, Hungary
[4]Faculty of Science, Hokkaido University, Sapporo 060-0810, Japan
[5]Graduate School of Biomedical Science and Engineering, Hokkaido University, Sapporo 060-8638, Japan
[6]Global Center for Biomedical Science and Engineering, Faculty of Medicine, Hokkaido University, Sapporo 060-8648, Japan
[7]Graduate School of Science and Engineering, Saitama University, Saitama 338-8570, Japan
[†]Email: n.otsuka@iaea.org

Abstract

The decay branching ratios of ^{197m}Hg (24 h) and ^{195m}Hg (42 h) were studied by offline γ-ray spectroscopy of a natural platinum foil irradiated by α particles at 29 MeV. We observed strong cooling time dependence of the isomeric ratios of ^{197}Hg and ^{195}Hg determined with the decay branching ratios of these metastable states in the ENSDF library. To eliminate the cooling time dependence, we performed decay curve analysis with the decay branching ratios of these metastable states as adjustable parameters assuming that the isomeric ratios do not depend on the cooling time. We resolved the time dependence by adjusting the isomeric transition branching ratios to 94.5$\pm$0.7% and 48.9$\pm$1.8% for ^{197m}Hg and ^{195m}Hg, respectively. The ^{197m}Hg decay branching ratio obtained by us is very close to 94.68$\pm$0.09% published by Lebeda et al. in 2020.

1 Introduction

A metastable state of a nuclide may have several decay modes such as isomeric transition and β decay. The decay branching ratio, the probability to undergo a decay mode, is a basic property of the nuclide. It is routinely evaluated and compiled in data libraries such as the ENSDF library maintained by the International Network of Nuclear Structure and Decay Data Evaluators (NSDD) [1] and the Nubase table maintained by the Atomic Mass Data Center [2]. The decay branching ratio is an overall normalization factor of the emission probabilities of the decay γ lines belonging to the decay branch, and its accuracy has a large impact on the activation cross sections determined with the offline γ-ray spectroscopy. We have recently encountered unphysical cooling time dependence of the isomeric ratios of ^{197}Hg and ^{195}Hg produced by irradiation of a natural platinum foil by α particles at 29 MeV. We concluded that the cooling time dependence is caused by errors in the branching ratios of their metastable states, and adjusted the decay branching ratios and decay γ-ray emission probabilities to eliminate the cooling time dependence. This article reports the adjusted decay branching ratios and decay γ-ray emission probabilities along with

a brief introduction to the experiment. This adjustment was done as a part of experimental determination of the activation cross sections for natural platinum interacting with α particles, and the readers are referred to [3] for more details about the experiment and results.

2 Experimental

Pure metallic foils of natural platinum (12.433 mg/cm^2), natural titanium (2.344 mg/cm^2) and aluminium (1.500 mg/cm^2) were cut into 8×8 mm and assembled as a stack of nine sets of Pt-Al-Ti-Al. The stacked target was irradiated for 1 h by an α-particle beam provided by the RIKEN AVF cyclotron. After irradiation and cooling for 1 h, we started measurement of the activities of the irradiated foils by a HPGe detector calibrated with a multiple point-like source. The activities of the Pt and Al foils placed at the most upstream position were measured more than 50 times to see their time profile. We identified 27 γ-lines originating from production of 16 radionuclide products, and expressed the 1039 measured peak areas of these γ lines as linear combinations of the independent production cross sections of the 16 radionuclides. From these linear combinations, we determined the 16 independent production cross sections by the least-squares analysis. In addition to the production cross sections, we also treated the branching ratios of ^{197m}Hg and ^{195m}Hg as fitting parameters.

3 Results

Table 1 shows the branching ratios and decay γ-ray emission probabilities in the ENSDF library and those corrected through the least-squares analysis of the peak areas measured in this work. Our decay curve analysis suggests 3.4% increase and 10% decrease of the ^{197m}Hg and ^{195m}Hg isomeric transition branching ratio, respectively. We derived the corrected decay γ-ray emission probabilities and their uncertainties based on these correction factors. For ^{197m}Hg, Lebeda et al. [7] have recently performed a measurement to determine the decay branching ratio and decay γ-ray emission probabilities. The table shows the revised decay data determined by us and Lebeda et al. for ^{197m}Hg are very close to each other.

Table 1: Decay branching ratios p and decay γ-ray emission probabilities I_γ in the ENSDF library [4, 5], those corrected through the least-squares analysis of the peak areas measured in this work, and those reported by Lebeda et al. [7]. The decay γ-ray emission probabilities and their uncertainties in the ENSDF library were extracted from the IAEA LiveChart of Nuclides [6]. ϵ denotes electron capture and/or β^+ decay.

	C_{IT}		p (%)			E_γ (keV)	I_γ (%)		
			ENSDF	Corrected	Lebeda		ENSDF	Corrected	Lebeda
^{197m}Hg	1.0336 (2)	IT	91.4 (7)	94.5 (7)	94.68 (9)	134	33.5 (3)	34.6 (3)	34.8 (3)
		ϵ	8.6 (7)	5.5 (7)	5.32 (9)	279	6.1 (5)	3.9 (7)	3.79 (4)
^{195m}Hg	0.902 (6)	IT	54.2 (20)	48.9 (18)					
		ϵ	45.8 (20)	51.1 (18)		261	31 (3)	35 (4)	
						560	7.1 (5)	7.9 (7)	

Figure 1 shows the cooling time dependence of the isomeric ratios of the $^{\mathrm{nat}}$Pt(α,x)^{197,195}Hg reactions at 29 MeV. The isomeric ratios determined with the ENSDF isomeric transition branching ratios

show strong cooling time dependence except for the ^{197}Hg isomeric ratio determined with the 134 keV and 191 keV γ lines characterizing the metastable and ground states. However, the strong cooling time dependence is eliminated by adoption of the branching ratios determined by the decay curve analysis performed in the present work.

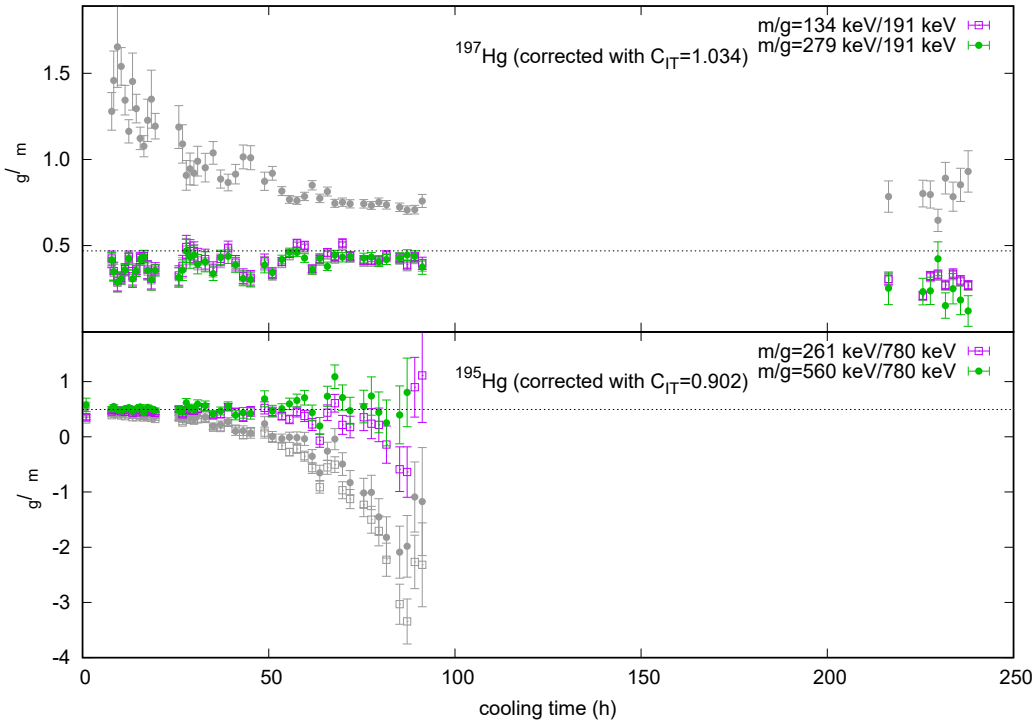

Figure 1: Cooling time dependence of the isomeric ratios of the $^{\mathrm{nat}}$Pt(α,x)^{197,195}Hg reactions at 29 MeV. The energies following m/g= in the legend are the γ-lines used for quantification of the metastable and ground states. The open square and solid circle are for two different pairs of the γ-lines characterizing the metastable and ground states. The grey symbols are for the isomeric ratios determined with the branching ratios taken from the ENSDF library [4, 5], while the purple and green symbols are for those determined with the ENSDF isomeric transition ratios corrected by the factor C_{IT}.

4 Summary

We determined the decay branching ratios of ^{197m}Hg (24 h) and ^{195m}Hg (42 h) by offline γ-ray spectroscopy of a natural platinum foil irradiated by α-particles at 29 MeV. The strong cooling time dependence of the ^{197}Hg and ^{195}Hg isomeric ratios determined with the decay data in the ENSDF library was resolved by the decay data determined by our decay curve analysis. The newly determined isomeric transition branching ratios are 94.5$\pm$0.7% for ^{197m}Hg and 48.9$\pm$1.8% for ^{195m}Hg. The ^{197m}Hg decay branching ratio obtained by us is very close to the branching ratio recently determined by Lebeda et al.

References

[1] Pronyaev, V.G., Nichols, A.L., Tuli, J. Nuclear Structure and Decay Data (NSDD) Evaluators' Network, International Atomic Energy Agency; 2004. INDC(NDS)-421 Rev. 1.

[2] Kondev, F.G., Wang, M., Huang, W.J., Naimi, S., Audi, G. The NUBASE2020 evaluation of nuclear physics properties, Chinese Phys. C . 2021; 45: 030001.

[3] Otuka, N., Takács, S., Aikawa, M., Ebata, S., Haba, H. Isomer production studied with simultaneous decay curve analysis for alpha-particle induced reactions on natural platinum up to 29 MeV, Eur. Phys. J. A 2024; 60: 195.

[4] Huang, X.L., Zhou, C.M. Nuclear data sheets for A=197, Nucl. Data Sheets 2005; 104: 283 – 426.

[5] Huang, X.L., Kang, M.X. Nuclear data sheets for A=195, Nucl. Data Sheets 2014; 121: 395 – 560.

[6] Verpelli, M., Abriola, D. Information management tools for evaluated nuclear structure data file (ENSDF) interrogation and dissemination, J. Kor. Phys. Soc. 2011; 59: 1322 – 1324.

[7] Lebeda, O., Kondev, F.G., Červenák, J. Branching ratio and γ-ray emission probabilities in the decay of the $J^{\pi}=13/2^{+}$ isomer in ^{196}Hg, Nucl. Instrum. Methods Phys. Res. Sect. A 2020; 959: 163481.

Acknowledgments

This experiment was performed at the RI Beam Factory operated by RIKEN Nishina Center and Center of Nuclear Science, University of Tokyo. The authors would like to thank Akihiro Nambu, Yudai Shigekawa and Sachiko Usuda for technical assistance with the experiment.

25. Proton beam irradiation for space use at 3NBT and proton beam irradiation facility plan in J-PARC

Shin-ichiro MEIGO[†1]

[1]J-PARC Center, Japan Atomic Energy Agency, Shirakata 2-4, Tokai, Ibaraki, 319-1195, Japan
[†]Email: meigo.shinichiro@jaea.go.jp

Abstract

The need for protons for space use has drastically increased, as the need to test the semiconductor devices mounted on the satellites in space environments against failures due to single-event effects (SEEs). Therefore, the needs are expected to increase drastically worldwide. To study material damage under the beam irradiation circumstance of accelerator-driven systems (ADS), the JAEA planned to construct a Transmutation Experimental Facility Target Facility (TEF-T) using J-PARC Linac 400-MeV negative hydrogen ion beam. The task force for evaluating partitioning and transmutation technology in the MEXT concluded that the facility should be considered to maximize the advantages of using Linac to meet users' various needs. The proton irradiation facility, a successor of TEF-T, will be constructed to supply the proton beam applications for space use as one of the purposes as the proton beam irradiation facility. Also, space agencies are required to use protons already to test their charged particle spectrometers. We have conducted the test using the proton scattered at the 3NBT beam dump window.

1 Introduction

As the increase of the need to test the semiconductor devices mounted on satellites in space environments against failures due to single-event effects, the need for protons for space use has drastically increased. Therefore, the needs are expected to increase drastically worldwide. To study material damage under the beam irradiation circumstance, especially for accelerator-driven systems (ADS), the JAEA planned to construct a Transmutation Experimental Facility Target Facility (TEF-T) [1] using J-PARC Linac 400-MeV negative hydrogen beam. The task force (TF) for evaluating partitioning and transmutation technology in the MEXT [2] concluded that the facility should be considered to maximize the advantages of using Linac to meet users' various needs. The proton irradiation facility, a successor of TEF-T, will be constructed to supply the proton beam applications for space use as one of the purposes of the Proton Beam Irradiation Facility.

Meanwhile, the Japan Aerospace Exploration Agency (JAXA) plans to develop the charged particle spectrum in space to observe astronauts' radiation dose for Artemis [3] programs. Also, the National Institute of Information and Communications Technology (NICT) plans to develop a spectrum to observe solar flares precisely. Both spectrometers aim to observe charged particles up to about 1 GeV. Those institutions want to examine the spectrometers using J-PARC accelerators. To match their requirements and fulfill the safety without disturbing the accelerator operation, a method using beam scattering at the window was developed in J-PARC, which gives us quasi-monoenergetic protons by placing the device at a small angle regarding the incident

proton directions. We have conducted the test using the proton scattered at the 3NBT beam dump window. In this paper, the proton usage in the PBIF and at the existing facility of 3NBT with beam scattering at the window are described.

2 Proton beam irradiation facility

JAEA has been researching and developing transmutation technology using the Accelerator Driven System (ADS) to reduce the volume and hazardousness of high-level radioactive waste generated by nuclear reactors. To solve technical issues related to the ADS, the Transmutation Experimental Facility (TEF) was planned in J-PARC, which consists of the ADS Target Test Facility (TEF-T) [1] and the Transmutation Physics Experimental Facility (TEF-P) [4]. TEF-T uses a 400 MeV, 250 kW intense negative hydrogen ion beam accelerated at the J-PARC Linac to irradiate a sample of liquid Lead-Bismuth Eutectic LBE (LBE), which is a candidate structural material for ADS under LBE flow as in the case of ADS.

In 2021, the TF for the evaluation of TEF [2], which discussed the future of the J-PARC TEF program, recommended that the experiments planned be replaced by more advanced computer simulations and the use of existing facilities. However, the experiments planned for TEF-T were thought to be limited by irradiation damage simulations and irradiation tests at existing facilities. The TF recommended selecting the experimental items and rationalizing the facilities through the above efforts. Therefore, the task force recommended that it would be appropriate to consider a test facility that prioritizes the functions of the TEF-T.

Following TF's recommendation, JAEA reconsidered the plans for the TEF. Also, the TF recommended that the rational approach to research and development, including narrowing down experimental items and sharing roles through international cooperation, should be considered and that the required roles of the facility should be reconfirmed before proceeding with the study. The TF also suggested that it is desirable to study the facility's specifications to maximize the advantages of the existing J-PARC proton accelerator, including the possibility of responding to various needs and solving the engineering issues of the ADS. Therefore, JAEA has decided to proceed with studying a new proton beam irradiation facility, prioritizing the functions of the TEF-T and including the possibility of responding to various needs.

Based on the TF recommendations, a survey of accelerator applications in other countries was first conducted. Based on the results of this survey, it was decided that the proton beam irradiation facility should mainly proceed as follows : 1) Material irradiation examinations from fission reactors to fusion, 2) Semiconductor soft-error research using spallation neutrons, 3) Proton beam applications for space use, 4) Medical RI production, In the utilization plan of the proton beam irradiation facility, the proton beam utilization for space equipment was considered in addition to the utilization methods planned for TEF-T. In order to further advance the utilization of the facility, a study group on the utilization of the facility has been held since 2022. A user community was created to reflect users' requests in the facility's design. Based on the requests of the user community, we reflected the specifications of the facility as desired by the users.

3 Proton Beam Irradiation Facility (PBIF)

A bird's-eye view of the PBIF is shown in Figure 1. The target station is located in the center of the facility, and the activation equipment handling room (hot cell) is used to maintain the target station equipment. Neutrons produced from the target are transported to the neutronics laboratory to test semiconductor soft errors. A low-intensity proton beam extracted from the

primary line will be transported to the proton beam application room, which will perform proton-based tests necessary for developing space equipment.

The postponement of the TEF-P project has made it possible to create a vacant space adjacent to the proton beam irradiation facility. In order to make effective use of this space and to promote materials research by Post Irradiation Examination (PIE), construction of a Post Irradiation Examination (PIE) facility [6] is being considered at the adjacent site. In the PIE facility, not only the proton beam irradiation facility but also the PIE of the targets and beam windows used in other facilities in J-PARC, such as the Materials and Life Science Experimental Facility (MLF). The present Linac operates at 25 Hz and will be ramped up to 50 Hz for this facility. The Linac tunnel has already been expanded with an additional tunnel in the form of an appendage, the end of which is block-shielded. The expansion of the Linac tunnel can be easily accomplished by dismantling the blocks at the end of the tunnel. The proton beam injected into the facility is a 400 MeV, 0.625 mA average current, 250 kW negative hydrogen beam from the J-PARC Linac. This beam is operated in long pulse mode with a frequency of 25 Hz, 50 mA peak current, and 0.5 ms pulse width. Therefore, the pitting damage problem caused by the short pulse beam does not occur, as in the case of the mercury target at the J-PARC MLF. Based on the stress analysis results of the target window, a Gaussian distribution with a full width at half maximum of about 4 cm and a peak current density of 30 μA/cm^2 will be used for the beam shape and the peak current density, respectively.

The LBE target is supported by a horizontal pull-out cart, as in the case of the mercury target in the MLF. A vacuum vessel with a built-in target container is installed at the end of the cart, and the LBE circulation system of the primary cooling system is installed behind the shielding. During beam irradiation, the cart is inserted to the center of the target station, and the target is surrounded by a concrete shield. In the activation equipment handling room behind the cart, the target vessel is exchanged, and the primary cooling system is maintained by remote control. The activation equipment handling room is equipped with a crane, manipulators, a shielded window, and jigs. A sample preparation room and a small cell are located adjacent to the activation equipment handling room, where post-irradiation examinations of the beam injection window and irradiation test plates are performed, and specimens will be cut.

Since uncontrollable conditions caused by single-event effects (SEEs) are a severe problem for spacecraft, tests using proton and heavy ion irradiation have been carried out domestically and internationally. Since the largest flux particles in space are protons, testing semiconductor devices onboard satellites using protons is crucial. Since it is difficult to obtain proton irradiation opportunities to test them in Japan, the user community [5] has been clamoring to construct a proton irradiation facility. Therefore, the establishment of a proton utilization room is planned in this facility, where tests from 20 MeV to 400 MeV can be performed.

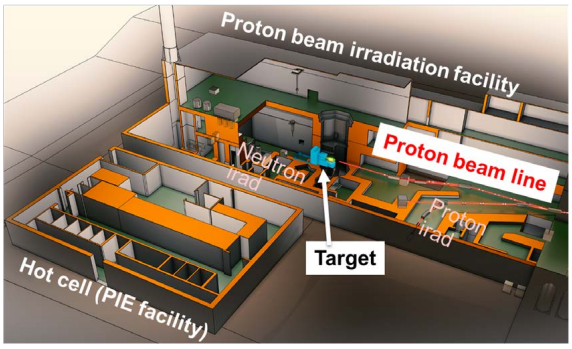

Figure 1: Birds-eye's view of the PBIF and post-irradiation examination facility at J-PARC.

The proton beam irradiation facility uses a high-intensity beam of 250 kW, but such beam is not suitable for testing space equipment. Therefore, we plan to use a 250 kW negative hydrogen ion beam by irradiating it with a laser and extracting a proton beam through charge exchange by photons of the laser. The J-PARC Transmutation Division has been developing a laser charge exchange method [7] to provide a weak beam of less than 10 W to the TEF-P. We have tested this

beam extraction method using a 3 MeV H^- ion beam at the Linac RFQ test stand. Although the kinetic energy of the H^- ions differs from that used in the present facility, it was confirmed that the beam intensity and time structure are as expected.

3.1 Proton delivery in broad range energies

Tests for spacecraft devices use protons ranging in energy from tens of MeV to 200 MeV. Because the test uses protons of various energies and evaluates the SEE generation rate as a function of energy, a rapid energy change is desirable in the test. The facility plans to provide protons of various energies by reducing the energy of the 400 MeV protons with a degrator, such as a metal plate. Degrators are commonly used for medical particle irradiation, and once the parameters of the magnets used for transport are determined, it will be possible to change the energy quickly. Since the beam stability of the Linac is excellent, this method is expected to enable a very short time of the energy changes. However, quantitative evaluation of the proton energy spread due to energy straggling in the degrator during the energy deceleration process is required. In addition, the intensity of the proton beam due to the interaction with the nuclei in the degrator must also be evaluated, which was calculated using the PHITS code.

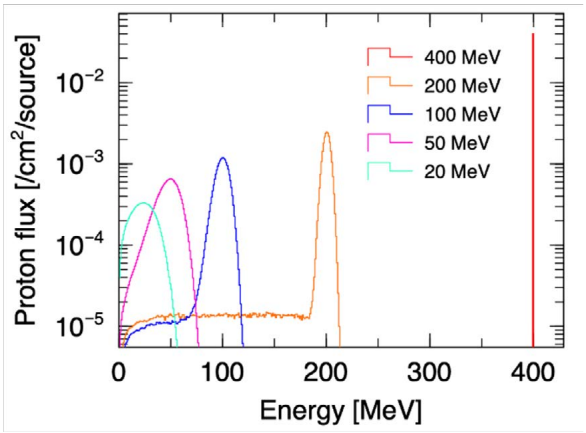

Figure 2: Energy spectrum of protons after degrader deceleration. The vertical axis shows the proton yield per proton incident on the degrator.

This study used tungsten as the degrator material to evaluate the proton behavior. To simplify the calculations, the proton deceleration process was investigated for a uniformly distributed 400 MeV proton beam with a diameter of 10 mm injected into a tungsten degrator with a cross section of 50 × 50 mm having various thicknesses. Figure 2 shows the proton energy distribution, which shows the spectra after deceleration using a degrator for certain cases of spectra having the peak energy of 20∼400 MeV. In the case of 400 MeV protons, the distribution is a δfunction, but the peak energy broadens as the beam decelerates, and the tail is drawn to the low-energy region.

3.2 Monoenergetic proton delivery

Since single-event rates are measured as a function of proton energy, users prefer monoenergetic protons. To enable the use of monoenergetic protons, it will not only change the thickness of the degrader but also install a bending magnet and slits downstream of the degrader to selectively supply protons with the desired energy, thereby making it possible to use monoenergetic protons. A calculation was made using PHITS to understand the characteristics of the proton yield.

Figure 3 shows the relationship between the mean proton energy and the relative yield (red line) and energy spread (blue line), which was derived from fitting a Gaussian function. It was found that a relative intensity larger than 10% of the primary protons can be achieved for the case of decelerated protons in the energy range above 20 MeV. Ideally, the proton energy spread supplied to the user should be as narrow as possible, but in this study, it was set to be less than 10%. The orange solid line in Fig. 3 shows the relative yield of protons for which the energy spread is less than 10%. The yield of 20 MeV protons with an energy

spread of less than 10% was about 0.1% of the 400 MeV protons. In the case of a 10 W beam produced by laser charge exchange, the beam current for 400 MeV protons is 25 nA, and the beam current for 20 MeV protons is about 25 pA with an energy spread of less than 10%. Assuming a uniform beam diameter of ϕ 2 cm for the irradiation test, the proton flux is 5×10^7 /cm^2/s, and the beam current is about 25 pA, which may satisfy the user community's request.

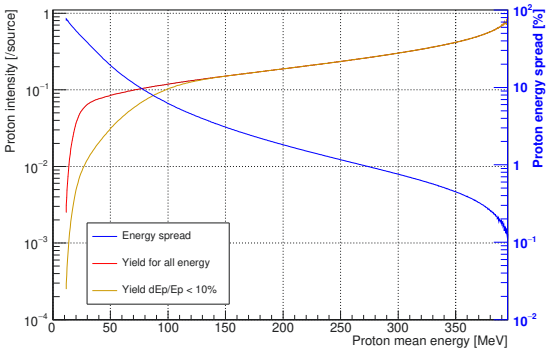

Figure 3: Relative yield and energy spread of protons as a function of extracted proton energies for the tungsten degrader.

A low flux beam is generally sufficient for tests using protons to prevent activation of the irradiated specimens. If the beam is too intense for the user, it may be possible to reduce it by 10^{-7} times by adjusting the laser power used for charge conversion. Increasing the beam diameter by about 30 cm without adjusting the laser power and reducing the flux by 10^{-3} times is also possible. In this study, the effect of downstream proton transport, such as beam loss, was not considered. The beam loss due to the increased emittance of the beam caused by the degrator will be evaluated. Also, the facility's radiation safety requires an evaluation of radiation effects due to the activation of the degrator and beam scattering. These subjects will be conducted in the future study. The user community has requested the use of spatially flat beams. This could be done using nonlinear beam optics [8] or rastering. Beam flattening is also essential for irradiation tests of targets and ADS and will be developed in the future at J-PARC.

4 Proton beam irradiation for space use at 3NBT

JAXA and NICT plan to develop a charged particle spectrometer to be applied to several GeV regions. Both spectrometers based on Cherenkov radiation are aimed to observe the charged particles up to about 1 GeV. Those institutions want to examine the spectrometers using J-PARC accelerators. To match their requirements and fulfill the safety without disturbing the accelerator operation, a method using beam scattering at the window located at the 3NBT beam dump in J-PARC was developed, which gives us quasi-monoenergetic protons by placing the device at a small angle regarding the incident proton directions.

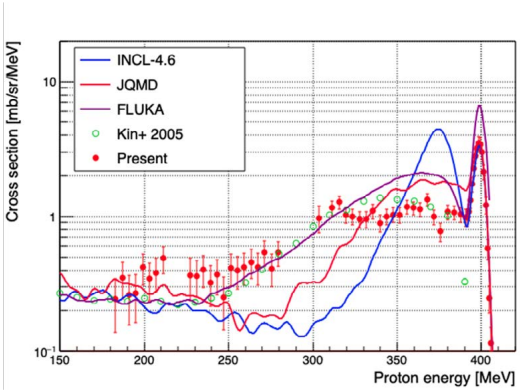

Figure 4: Al(p,xp) DDX for 0.4 GeV obtained by the present study compared with calculations of FLUKA and PHITS using INCL-4.6 and JQMD. Also, compared with the other experimental data [9].

To observe the scattered proton spectrum, as a calorimetric counter telescope, plastic scintillators (EJ200) with a cross section of 50 $\times$ 50 mm using various thicknesses from 50 to 400 mm were placed at the angle of 13° for the projectile protons. This technique lets us obtain the double differential cross sections (DDXs) in several GeV regions. To obtain DDX, unfolding was applied with the response functions of the

detectors, which were obtained with the calculations of PHITS. A tentative result of this study for 400 MeV projectile protons is shown in Figure 4. This result showed a good agreement with the calculation with FLUKA and PHITS with JQMD. Also, it was found that there was a significant overestimation at a quasi-elastic peak of around 350 MeV for PHITS with the INCL-4.6 model, which is recommended for use. The present data shows that quasi-monoenergetic protons are provided to users. JAXA and NICT started testing the spectrometers using this technique.

5 Summary

To fulfill the requirement of tests for spacecraft devices, a technique to provide quasi-monoenergetic protons was developed using a beam scattering at the window located in front of the 3NBT dump. JAXA and NICT started testing their devices using this technique. Also, a conceptual study was made to deliver the monoenergetic proton to users at the Proton Beam Irradiation Facility (PBIF) with Linac 400 MeV protons. A conceptual study of the PBIF was conducted, followed by the recommendation of the Task Force. A user community was established, and needs were surveyed and reflected in the design. Further studies will be conducted based on the expansion of needs in the future.

References

[1] Nuclear Transmutation Division J-PARC Center, Technical design report on J-PARC Transmutation Experimental Facility; ADS Target Test Facility (TEF-T), JAEA-Tech. 2017-003, (2017), 539p., in Japanese. https://doi.org/10.11484/jaea-technology-2017-003

[2] Ministry of Education, Culture, Sports, Science and Technology, Task Force on Evaluation of Partitioning and Transmutation Technology, “Evaluation of Partitioning and Transmu-tation Technology (Task Force Summary)” (2021), in Japanese. https://www.mext.go. jp/content/20211104-mxt_genshi-000018772_4.pdf , (accessed 2025-03-07).

[3] NASA,“Artemis”, https://www.nasa.gov/humans-in-space/artemis/ , (accessed 2025-03-07).

[4] Partitioning and Transmutation Technology Division, Nuclear Science and Engineering Center, Safety design report on J-PARC Transmutation Physics Experimental Facility (TEF-P), JAEA-Tech. 2017-033, (2018), 383 p., in Japanese. https://doi.org/10.11484/jaea-technology-2017-033

[5] “Study Group on the J-PARC Proton Beam Irradiation Facility Project and the Establish-ment of a User Community”, July 28, 2022, J-PARC Research Building Main Conference Room, in Japanese. https://kds.kek.jp/event/44002/ , (accessed 2025-03-07).

[6] S. Saito, et al., Conceptual study of Post Irradiation Examination (PIE) Facility at J-PARC, JAEA-Tech. 2023–025, (2024), 48p., in Japanese. https://doi.org/10.11484/jaea-technology-2023-025

[7] H. Takei, K. Tsutsumi, S. Meigo, J. Nucl. Sci. and Technol., 58(5):588–603 (2021). https: //doi.org/10.1080/00223131.2020.1848654

[8] S. Meigo, M. Ooi, H. Fujimori, Phys. Rev. Accel. Beams, 23:062802 (2020). https://link.aps.org/doi/10.1103/PhysRevAccelBeams.23.062802

[9] T. Kin, et al., Phys. Rev. C 72:014606 (2005). https://doi.org/10.1103/PhysRevC.72. 014606

26. Cross section measurement of the ^{nat}W(p,X) reactions by an activation method

Kenta SUGIHARA[†1,2], Shin-ichiro MEIGO[3],
Hiroki IWAMOTO[4], and Fujio MAEKAWA[3]

[1]High Energy Accelerator Research Organization (KEK), Oho, Tsukuba, Ibaraki 305-0801, Japan
[2]The Graduate University for Advanced Studies (SOKENDAI), Hayama, Kanagawa 240-0193, Japan
[3]J-PARC Center, Japan Atomic Energy Agency, 2-4 Shirakata, Tokai-mura, Naka-gun, Ibaraki 319-1195, Japan
[4]Nuclear Science and Engineering Center, Japan Atomic Energy Agency, 2-4 Shirakata, Tokai-mura, Naka-gun, Ibaraki 319-1195, Japan
[†]Email: kenta.sugihara@kek.jp

Abstract

Tungsten is applied to a particle-production target and shielding at accelerator facilities. Also, tungsten is a substance used in plugs of semiconductors. From the viewpoint of the radiation safety and soft error induced by galactic cosmic ray, nuclide distribution generated by proton incidence receives attention. This paper presents the measurement of the cross sections of the ^{nat}W(p,X) reactions. Comparisons among our present data, the results of previous studies, calculated results, and evaluated nuclear data library are also reported.

1 Introduction

Tungsten is applied to a particle-production target at accelerator facilities, e.g., ISIS [1] and European Spallation Source [2], owing to its high melting point and high strength in compression. Additionally, properties of tungsten, such as large atomic number and high density, are preferable to shielding of secondary particles. In fact, tungsten shielding is considered at the Accelerator-Driven System (ADS) [3] by JAEA. Thus, activation of tungsten by high-energy protons receives attention because residual γ-ray dose rate, which is derived from the nuclide production cross sections, impacts on a maintenance schedule.

In addition, tungsten is a substance used in plugs of semiconductor [4]. It is possible that high-LET nuclides are generated due to the galactic cosmic ray (including high-energy protons) incidence on tungsten. Subsequently, electron-hole pairs are created by the recoil high-LET nuclides, which degrade performance of semiconductors [4]. Thus, the contribution of the reactions between high-energy protons and tungsten to soft errors in semiconductors, i.e., the distribution of produced nuclides, should be investigated.

Although large-scale parallel calculations enabled us to predict the distribution of produced nuclides with nuclear reaction models, the prediction accuracy of the models should be studied more prior to practical use. There are previous studies of the ^{nat}W(p,X) reactions [5–10]. However, there remain nuclides which have not measured yet. Hence, further measurement of the reactions of interest should be carried out.

Then, we performed the cross section measurement of the ^{nat}W(p,X) reaction with GeV protons incidence at J-PARC [11] as a part of the systematic measurements [12–19]. This paper outlines the experiment of the nuclide production cross sections via the ^{nat}W(p,X) reaction. In addition, our present data are compared with the results of previous studies, nuclear reaction models, and JENDL/HE-2007 [20] to confirm the prediction accuracy. Moreover, the comparison between the ^{nat}W(p,X) and ^{nat}Pb(p,X) reactions are also presented.

2 Experiment

This experiment was carried out at the beam dump line [21] near the extraction port from the 3-GeV Rapid Cycling Synchrotron (RCS) [21] at J-PARC. Because this experiment was conducted in the same way already reported in previous studies [12,13], a brief explanation of this experiment is given here.

The energies of the proton beam from RCS were adjusted to be 0.4, 1.3, 2.2, and 3.0 GeV. The irradiation time and the total number of incident protons for all energies were 100 seconds and 2.2 × 10^{14}, respectively.

The ^{nat}W targets (99.95% purity) were placed at the target chamber installed on the beam line. The stacked targets of Al, W, and Al in order from upstream were prepared in this experiment. The size and weight of the target was 25 mm × 25 mm × 0.10 mm and 1.1 g, respectively.

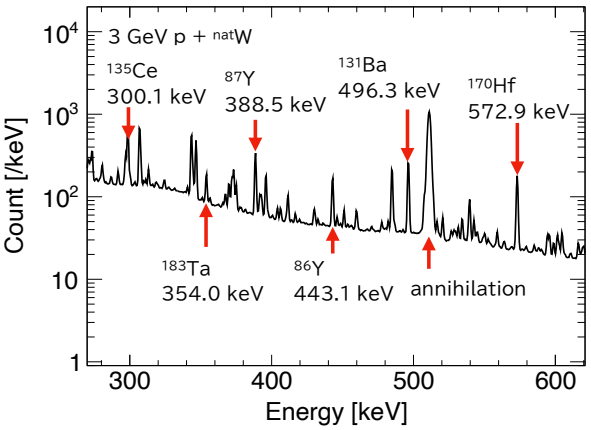

Figure 1: γ-ray spectrum by the HPGe detector. The horizontal and vertical axes are γ-ray energy [keV] and pulse height of each γ-ray energy [/keV], respectively.

By setting targets on the sample holder of High-Purity Ge (HPGe) detectors, the decay γ-ray spectrum were measured as shown in Figure 1.

3 Results and Discussion

We let references [12, 13] explain the analysis due to the limited space. Nuclide production cross sections obtained in this work are tabulated in Table 1. As the total uncertainty, the uncertainties of fitting parameter, incident proton intensity, branching ratio of the γ-ray energy, and intensity of the standard γ-ray sources were included. In this study, we successfully acquired 13 nuclides and 41 data points of the cross sections with four proton energies. The cross-section data for the ^{180}Ta were measured for the first time.

Figure 2 shows the excitation functions of ^{184}Re, ^{183}Re, ^{177}W, ^{180}Ta, ^{176}Ta, and ^{173}Ta with the results of nuclear reaction models in PHITS [22] (INCL/GEM [23,24] and JAM/GEM [25]), JENDL/HE-2007 [20], and preceding studies [5–10]. Our present data are consistent with the results of previous studies. The excitation functions generally have the functional type that is inversely proportional to the incident proton energy for the nuclides successfully measured in this study. This is because high incident energy opens the reaction channels for lighter nuclides even though the total cross section is rather constant in this energy region. It is demonstrated that the nuclear reaction models can describe the reactions of the target-like nuclides production.

Figure 3 shows the ratios of Calc. to Exp. (C/E) for the ^{nat}W(p,X) and ^{nat}Pb(p,X) [19] reactions. Calcs. agree with Exp. within 30% according to average values for the ^{nat}W(p,X)

Table 1: Nuclide production cross sections of the ^{nat}W(p,X) reactions with 0.4-, 1.3-, 2.2-, and 3.0-GeV proton incidence. Type "i" and "c" represent independent and cumulative cross sections, respectively. The branching ratio of used γ-ray energy (E_γ) is denoted in the parentheses below each E_γ. The total uncertainty (1σ) is written in the parentheses below each cross section.

Nuclide	E_γ [keV]	Type	$T_{1/2}$	Cross section (1σ Uncertainty) [mb]			
				0.4 GeV	1.3 GeV	2.2 GeV	3.0 GeV
$^{184(g+0.745m)}$Re	792.07	i	35.4 d	2.57	1.41	1.22	1.25
	(37.7%)			(0.12)	(0.06)	(0.06)	(0.06)
$^{183(g+m)}$Re	291.72	i	70.0 d	5.45	2.32	2.40	2.06
	(3.4%)			(0.55)	(0.23)	(0.40)	(0.21)
^{182}Re	229.32	i	64.2 h	7.91	-	-	-
	(25.8%)			(0.44)	-	-	-
^{181}Re	365.5	i	19.9 h	12.6	4.60	3.63	3.61
	(56%)			(1.6)	(0.59)	(0.47)	(0.47)
^{177}W	186.2, 115.65	c	132.4 m	37.3	21.9	16.6	15.5
	(15.2%, 47.3%)			(2.1)	(1.2)	(0.9)	(0.9)
^{184}Ta	414.01	c	8.7 h	-	4.95	4.10	3.94
	(72%)			-	(0.26)	(0.22)	(0.21)
^{183}Ta	353.99	c	5.1 d	17.6	13.2	10.8	11.0
	(11.6%)			(2.5)	(0.9)	(0.8)	(0.8)
$^{182(g+m1+m2)}$Ta	1189.04	c	114.74 d	13.6	13.9	-	12.0
	(16.49%)			(0.4)	(0.4)	-	(0.4)
^{180}Ta	93.32	c	8.154 h	-	28.0	22.6	-
	(4.51%)			-	(1.4)	(1.8)	-
^{178}Ta	426.36	i	2.36 h	11.8	-	11.6	11.4
	(97%)			(0.6)	-	(0.5)	(0.5)
^{176}Ta	1159.3	c	8.09 h	82.9	48.3	35.4	31.0
	(24.7%)			(7.0)	(4.0)	(3.0)	(2.8)
^{175}Ta	207.4	c	10.5 h	72.3	-	-	-
	(14.0%)			(7.3)	-	-	-
^{173}Ta	172.2	c	3.14 h	71.9	58.3	25.8	26.3
	(17.5%)			(7.8)	(3.4)	(2.8)	(2.8)

reactions. The comparison for both reactions suggests that Calcs. can describe the target-like nuclides production because the average values stay around 1.0 except for the ^{nat}Pb(p,2pxn) reaction. Although the average values are represented here, it should be noted that C/E has deviation.

4 Conclusion

Nuclide production cross sections via the ^{nat}W(p,X) reaction were measured for 0.4-, 1.3-, 2.2-, and 3.0-GeV proton incidence at J-PARC. In this work, we succeeded to obtain the 41 cross-section data. Additionally, our present data were compared with nuclear reaction models to confirm the prediction accuracy. It is demonstrated that Calcs. agree with Exp. for the (p,xpyn) reactions ($x = 0, 1, 2$).

In the future, we will analyze the data for lighter nuclides. Furthermore, we will compare

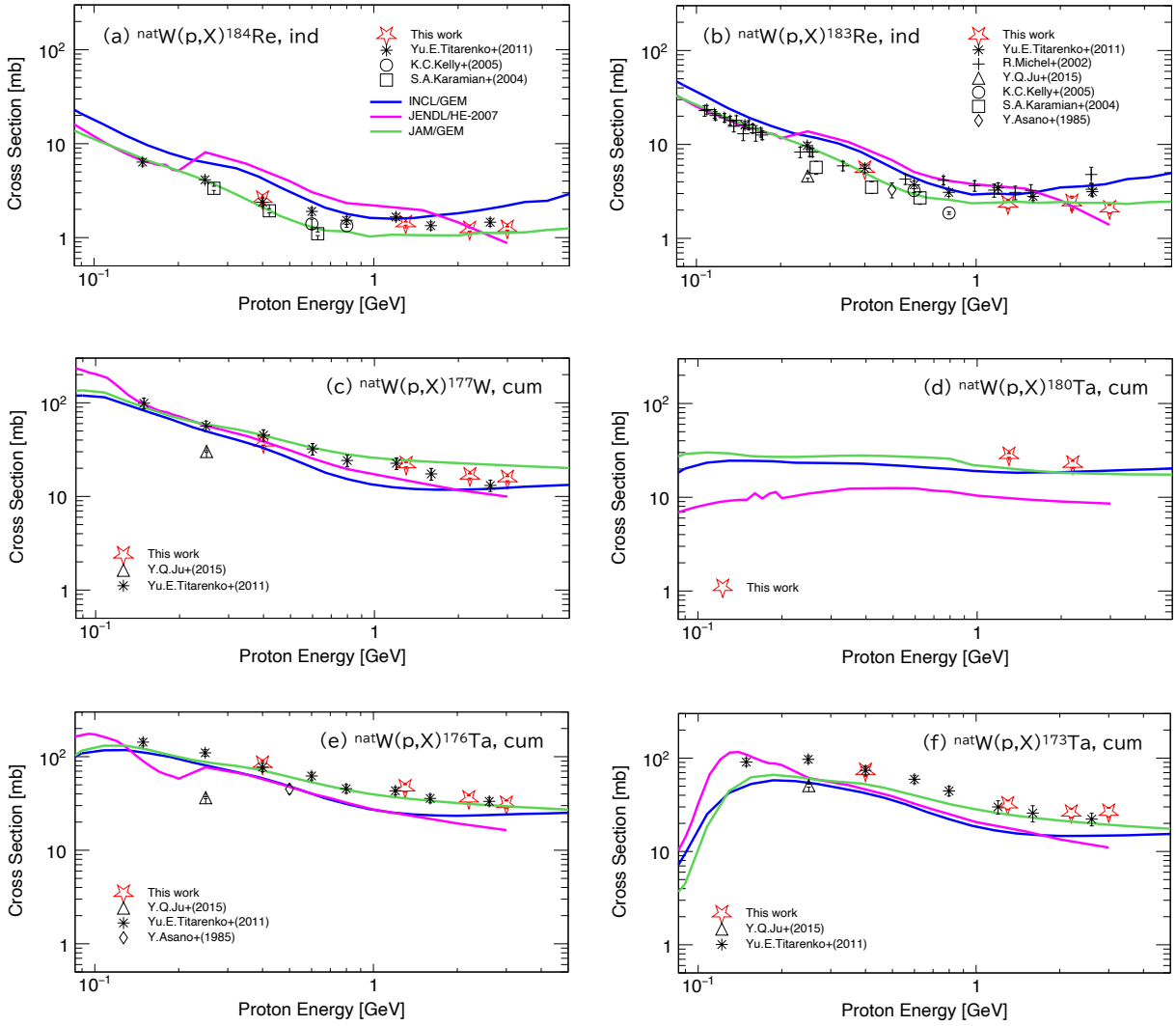

Figure 2: Excitation functions of ^{184}Re, ^{183}Re, ^{177}W, ^{180}Ta, ^{176}Ta, and ^{173}Ta. The horizontal and vertical axes represent the proton energy [GeV] and the nuclide production cross section [mb], respectively. The red and black markers stand for our present data and preceding results, respectively. The blue, pink, and green lines are the results of INCL/GEM, JENDL/HE-2007, and JAM/GEM, respectively.

the ^{nat}W(p,X) cross sections with other Exp. data conducted at J-PARC to confirm the target mass dependence of nuclide production cross sections.

Acknowledgments

This paper includes results obtained with the Subsidy for Research and Development on Nuclear Transmutation Technology. Calculations presented in the paper are performed by KEK Central Computing System (KEKCC).

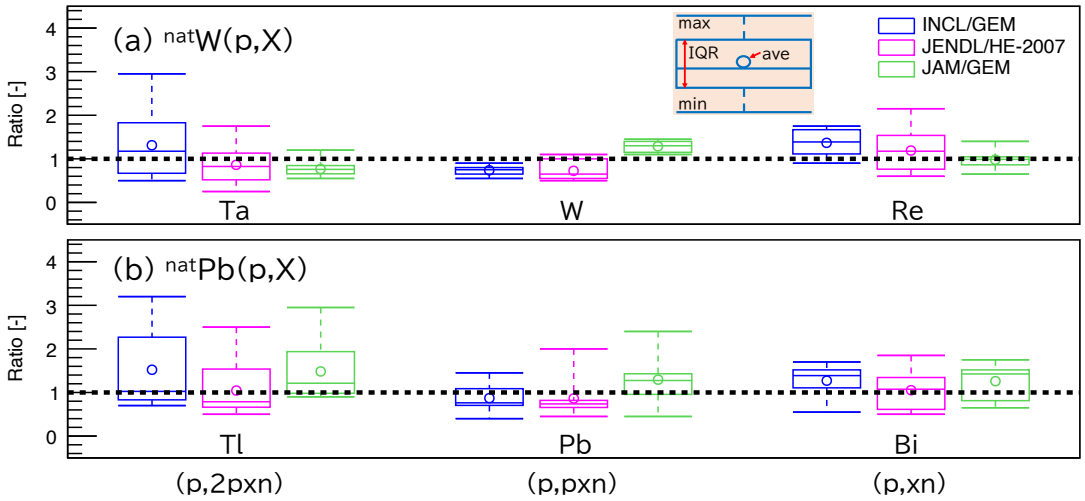

Figure 3: Boxplots of Calc./Exp. (C/E) for the (a) ^{nat}W(p,X) and (b) ^{nat}Pb(p,X) reactions.

[1] Findlay D.J.S., Škoro G.P., Allen G.M., *et al.*, Measurement and calculation of decay heat in ISIS spallation neutron target: Nucl. Instrum. Methods A, 908, (2018) pp. 91-96.

[2] Habainy J., Lee Y., Surreddi K.B., *et al.*, Study of heavy ion beam induced damage in tungsten for high power target applications: Nucl. Instrum. Methods B, 439, (2019) pp. 7-16.

[3] Iwamoto H., Meigo S., Nakano K., *et al.*, Radiation Shielding Analysis of the Upper Structure of an Accelerator-driven System: JAEA-Research 2021-012, (2022), 58p., Japanese.

[4] Schwank J.R., Shaneyfelt M.R., Baggio J., *et al.*, Effects of Particle Energy on Proton-Induced Single Event Latchup: IEEE Trans. Nucl. Sci., 52 (6), (2005), pp. 2622-2629.

[5] Asano Y., Mori S., Noguchi M., *et al.*, Spallation and Fission Yields in the Interactions of Tantalum, Tungsten, and Gold with 50-MeV Protons: J. Phys. Soc. Jpn., 54 (10), (1985), pp. 3734-3741.

[6] Karamian S.A., Adam J., Chaloun P., *et al.*, Yield of radionuclides and isomers produced in the fragmentataion of ^{nat}W and ^{186}W (97%) targets with protons at 630, 420, and 270 MeV: Nucl. Instrum. Methods A, 527, (2004), pp. 609-623.

[7] Kelly K.C., Hertel N.E., Pitcher E.J., *et al.*, ^{148}Gd production cross section measurements for 600- and 800-MeV protons on tantalum, tungsten, and gold: Nucl. Phys. A, 760, (2005), pp. 225-233.

[8] Michel R., Gloris M., Protoschill J., *et al.*, Cross Sections for the Production of Radionuclides by Proton-Induced Reactions on W, Ta, Pb, and Bi from Thresholds up to 2.6 GeV: J. Nucl. Sci. Technol., 39 (2), (2002), pp. 242-245.

[9] Titarenko Yu.E., Batyaev V.F., Titarenko A.Yu., *et al.*, Measurement and Simulation of the Cross Sections for Nuclide Production in ^{nat}W and ^{181}Ta Targets Irradiated with 0.04- to 2.6-GeV Protons: Phys. At. Nucl., 74 (4), (2011), pp. 551-572.

[10] Ju Y.Q., Zhang X.Y., Ma F., *et al.*, The production of residual radionuclides by a 250MeV proton beam: J. Phys. G: Nucl. Part. Phys., 42, (2015), 125102.

[11] Hotchi H., Kinsho M., Hasegawa K., *et al.*, Beam commissioning of the 3-GeV rapid cycling synchrotron of the Japan proton accelerator research complex: Phys. Rev. ST Accel. Beams, 12, (2009), 040402.

[12] Matsuda H., Meigo S., and Iwamoto H., Proton-induced activation cross section measurement for aluminum with proton energy range from 0.4 to 3 GeV at J-PARC: J. Nucl. Sci. Technol., 55 (8), (2018), pp. 955-961.

[13] Takeshita H., Meigo S., Matsuda H., *et al.*, Measurement of nuclide production cross sections for proton-induced reactions on Mn and Co at 1.3, 2.2, and 3.0 GeV: Nucl. Instrum. Methods B, 511, (2022), pp. 30-41.

[14] Takeshita H., Meigo S., Matsuda H., *et al.*, Measurement of nuclide production cross sections for proton-induced reactions on ^{nat}Ni and ^{nat}Zr at 0.4, 1.3, 2.2, and 3.0 GeV: Nucl. Instrum. Methods B, 527, (2022), pp. 17-27.

[15] Matsuda H., Takeshita H., Meigo S., *et al.*, Measurement of Nuclide Production Cross-Sections of ^{nat}Fe for 0.4-3.0 GeV Protons in J-PARC: Proc. 3rd J-PARC Symposium (J-PARC2019), JPS Conf. Proc. 33, (2021), 011047.

[16] Iwamoto H., Nakano K., Meigo S., *et al.*, Nuclide production cross sections in proton-induced reactions on Bi at GeV energies: Proc. 15th International Conference on Nuclear Data for Science and Technology (ND2022), EPJ Web of Conf. 284, (2023), 01033.

[17] Sugihara K., Meigo S., Iwamoto H., *et al.*, Measurement of nuclide production cross sections for proton-induced reactions on ^{nat}Ti and ^{93}Nb at 0.8 and 3.0 GeV: Nucl. Instrum. Methods B, 545, (2023), 165153.

[18] Sugihara K., Meigo S., Iwamoto H., *et al.*, Measurement of Nuclide Production Cross Sections for GeV-region Proton-induced Reactions on ^{nat}Mg, ^{nat}Si, ^{nat}Fe, ^{nat}Cu, and ^{nat}Zn: Nucl. Instrum. Methods B, 549, (2024), 165299.

[19] Sugihara K., Meigo S., Iwamoto H., *et al.*, Measurement of heavy nuclide production cross-section for ^{nat}Pb irradiated with several GeV protons: JAEA-Conf 2023-001, INDC(JPN)-0209.

[20] Watanabe, Y., Kosako K., Kunieda S., *et al.*, Status of JENDL high energy file: J. Korean Phys. Soc., 59, (2011), pp. 1040-1045.

[21] Meigo S., Noda F., Ishikura S., *et al.*, Evaluation of the 3-GeV proton beam profile at the spallation target of the JSNS: Nucl. Instrum. Methods A, 562, (2006) pp. 569-572.

[22] Sato T., Iwamoto Y., Hashimoto S., *et al.*, Recent improvements of the particle and heavy ion transport code system - PHITS version 3.33: J. Nucl. Sci. Technol., 61 (1), (2024), pp. 127-135.

[23] Boudard A., Cugnon J., David J.-C., *et al.*, New potentialities of the Liège intranuclear cascade model for reactions induced by nucleons and light charged particles: Phys. Rev. C, 87, (2013), 014606.

[24] Furihata S., Statistical analysis of light fragment production from medium energy proton-induced reactions: Nucl. Instrum. Methods B, 171, (2000), pp. 251-258.

[25] Nara Y., Otuka N., Ohnishi A., *et al.*, Relativistic nuclear collisions at 10A GeV energies from p+Be to Au+Au with the hadronic cascade model: Phys. Rev. C, 61, (1999), 024901.

[26] Cugnon J., L'Hôte D., and Vandermeulen J., Simple parametrization of cross-sections for nuclear transport studies up to the GeV range: Nucl. Instrum. Methods B, 111, (1996), pp. 215-220.

27. Feedback on neutron capture cross-section of ^{133}Cs from analysis of measured inventories of ^{133}Cs and ^{134}Cs of UO_2 fuel irradiated in TMI Unit 1

Toru YAMAMOTO[a]

1-16-22, Higashi-asahina, Kananzawa-ku, Yokohama, 236-0033, Japan
*Email: yamamototoru12345@gmail.com

Nuclide inventory calculations with MVP-BURN and JENDL-4.0 were performed for the twelve fuel samples taken from the two 15×15 PWR fuel assemblies irradiated in Three Mile Island (TMI) Unit 1. The calculated results of ^{133}Cs for the two-cycle-irradiation fuel samples and those of ^{134}Cs for the one-cycle-irradiation fuel samples were compared with the measured data. The averaged C/E-1s of ^{133}Cs and ^{134}Cs were 2.9% and −11.2%, respectively. They were similar to those in the previous studies. The C/E-1s were also compared with those with SCALE 6.1.2 (ENDF/B-VII.0) for ^{133}Cs and those with SCALE 5.1 (ENDF/B-V) for ^{134}Cs. The differences in the C/E-1s were mainly attributed to the differences in the neutron capture resonance integrals (RIγs) of ^{133}Cs in the nuclear data libraries. The C/E-1s of ^{133}Cs and ^{134}Cs in the present study indicated that a larger RIγ of ^{133}Cs than that in JENDL-4.0 would improve the C/Es.

1. Introduction

The inventory of ^{133}Cs in the irradiated UO_2 fuel is produced by the fission of the heavy nuclides and that of ^{134}Cs ($T_{1/2}$: 2.0652 y) is mainly produced by the neutron capture of ^{133}Cs. Their inventories are sensitive to the fission yield and the neutron capture cross-section of ^{133}Cs. The neutron capture cross-section of ^{133}Cs is characterized by a prominent resonance at 5.9 eV which causes dominant neutron capture reaction in typical light water reactor fuels. **Figure 1** illustrates the examples of the energy dependency of the calculated pellet-average neutron flux and neutron capture reaction rate in 108 neutron energy group for one of the fuel samples taken from the 15×15 fuel assembly irradiated in Three Mile Island (TMI) Unit 1 [1-3].

The neutron capture resonance integrals (RIγ) of ^{133}Cs differ among the evaluated nuclear data libraries. **Table 1** lists those in the JENDL and ENDF/B libraries [4-9] as examples. The RIγ in JENDL-5 [6] is higher by 13% than that in ENDF/B-VII.1 [9].

[a] Former affiliation: Regulatory Standard and Research Department, Secretariat of Nuclear Regulation Authority (S/NRA/R), Tokyo, Japan.

The authors have performed burnup calculations using the continuous-energy Monte Carlo burnup code with JENDL-3.3 and JENDL-4.0 and reported the comparison results with the measured inventories of ^{133}Cs and ^{134}Cs. [12-14]. **Figure 2** illustrates the C/E-1(%) for the BWR 9 × 9 UO_2 fuel samples with the initial fuel enrichments of 2.1 to 4.9 wt% and the fuel burnups of 28 to 68 GWd/t [12], the PWR 15 × 15 UO_2 fuel sample with the initial enrichment of 4.3 wt% and the fuel burnups of 46.3 GWd/t and 71.6 GWd/t [13], and the PWR 18 × 18 UO_2 fuel sample with the initial fuel enrichments of 3.8 wt% and the fuel burnup of 54.7 GWd/t [14]. The differences in the C/E-1s of ^{133}Cs between the results with JENDL-3.3 and JENDL-4.0 were relatively small and both were close to zero, while the C/E-1s of ^{134}Cs with JENDL-4.0 were larger than those with JENDL-3.3, and both were negative with one exception. The differences in the C/E-1s of ^{133}Cs and ^{134}Cs between JENDL-3.3 and JENDL-4.0 were attributed to the differences in the RIγs of ^{133}Cs in the libraries. However, the number of fuel samples indicating the trend was limited, and further analysis study was necessary.

Following the previous studies [12-14], the author performed the analysis study of the measured nuclide inventories of the UO_2 fuel samples taken from the PWR UO_2 fuel assemblies irradiated in TMI Unit 1 [1,2] using MVP-BURN [15] with JENDL-4.0 [5] and utilized for the validation of the neutron

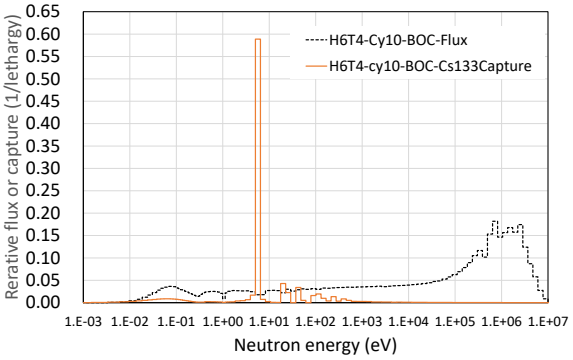

Figure 1. The energy dependency of the calculated pellet-average neutron flux and neutron capture reaction rate in 108 neutron energy group for one of the fuel samples taken from the 15 × 15 fuel assembly irradiated in TMI Unit 1 [1-3].

Table 1. RIγs of ^{133}Cs in some nuclear data libraries (293K, neutron energy: 0.5 eV-10^7 eV).

Library	JENDL-3.3 [4]	JENDL-4.0 [5]	JENDL-5 [6]	ENDF/B-V [7]	ENDF/B-VII.0 [8]	ENDF/B-VII.1 [a][9]
RIγ (b) (Ratio to JENDL-4.0)	396.2 (0.888)	446.2 (1.000)	458.7 (1.028)	382.9 (0.858)	421.0 (0.943)	405.5 (0.909)

[a] The RIγs in ENDF/B-VIII.0 [10] and JEFF-3.3 [11] are the same as that in ENDF/B-VII.1.

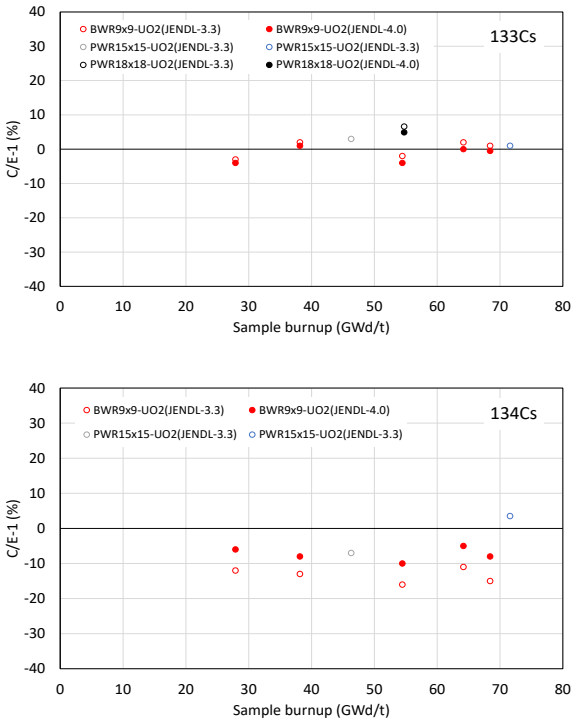

Figure 2. The C/E-1s of the calculated inventories of ^{133}Cs and ^{134}Cs with JENDL-4.0 [12-14].

capture cross-section of ^{234}U in JENDL-4.0 [3]. The present study aims to examine the analysis results of the measured inventories of ^{133}Cs and ^{134}Cs in the same fuel samples to validate the RIγ of ^{133}Cs in JENDL-4.0, which was smaller by 2.7 % than that in JENDL-5 [6]. They were also compared with those calculated with ENDF/B-VII.0 and ENDF/B-V reported by Gauld et al. [2] and Radulescu et al. [1], respectively; since the RIγs of ^{133}Cs in these nuclear data libraries are different from that in JENDL-4.0 as mentioned in the previous paragraph so that their results were useful to know the sensitivity of the inventories of ^{133}Cs and ^{134}Cs to the RIγ of ^{133}Cs. With the obtained information, possible directions for improving the accuracy of the RIγ of ^{133}Cs in JENDL-4.0 were discussed.

2. Nuclide inventory measurements of ^{133}Cs and ^{134}Cs for fuel samples from TMI Unit 1

References [1,2] reported the nuclide inventory measurements of the fuel samples from TMI Unit 1. The fuel samples for the nuclide inventory measurements were taken from the two fuel assemblies, one of which was the NJ05YU fuel assembly irradiated in the 9th cycle operated from 1991/11/14 to 1993/9/10, and the 10th cycle operated from 1993/10/16 to 1995/9/8 in TMI Unit 1. The other was the NJ070G fuel assembly irradiated in the 10th cycle. Both were the B&W 15×15 fuel assemblies. **Table 2** shows the summary of the fuel samples. The inventory measurements for the fuel samples from the fuel rods D5 and H6 were performed at Oak Ridge National Laboratory (ORNL) in 2013 for 12 actinides and 34 fission product nuclides which included ^{133}Cs. Those from the fuel rods O1, O12, and O13 were performed at General Electric Vallecitos Nuclear Center (GE-VNC) in 1999 for 16 actinide nuclides and 15 fission product nuclides which included ^{134}Cs.

The measurement data were given in the unit of g/g U-238 for the fuel samples from the NJ070G fuel assembly [16]. Those for the fuel samples from the NJ05YU fuel assembly were given in the unit of mg/g U [2]. They were converted to the unit of g/g U-238 in the present study.

Table 2. Summary of fuel samples and C/E-1 (%) of ^{133}Cs and ^{134}Cs.

Fuel assembly (fuel enrichment (wt%)	Fuel rod and sample ID	Axial height (cm) [a]	Measured/calculated burnup (GWd/t)	Measured nuclide	C/E－1 (%) of ^{134}Cs and ^{133}Cs in present study	C/E－1 (%) of ^{133}Cs for SCALE 6.1.2 and ^{134}Cs for SCALE 5.1
NJ05YU (4.013)	D5 T1	342.1	45.9/45.8	^{133}Cs	4.215	5.343
	D5 T2	267.0	55.0/54.6		2.234	4.449
	H6 T3	197.2	53.5/52.4		2.234	4.069
	H6 T4	233.2	52.7/53.2		2.999	5.172
		Av.	51.8/51.5	Av.	2.921	4.758
NJ070G (4.657)	O1 S1	39.37	25.8/25.8	^{134}Cs	-9.205	-18.219
	O1 S2	197.104	29.9/30.2		-7.819	-19.534
	O1 S3	278.13	26.7/28.1		-12.130	-22.780
	O12 S4	37.37	23.7/23.7		-12.087	-20.807
	O12 S5	197.104	26.5/26.6		-11.215	-21.919
	O12 S6	278.13	24.0/24.3		-13.776	-24.887
	O13 S7	39.37	22.8/23.6		-10.220	-25.150
	O13 S8	197.104	26.3/26.4		-12.832	-23.000
		Av.	25.7/26.1	Av.	-11.161	-22.037

[a] Distance between the sample axial location and the tip of the bottom end plug.

3. Analysis with MVP-BURN and JENDL-4.0

The reference [3] described the details of the burn-up calculations of the fuel samples performed using MVP-BURN [15] with JENDL-4.0u1 [4]. A general burnup chain model ChainJ40 (u4cm6fp119bp14T) developed by Okumura et al. [17] based on JENDL-4.0 [5] was used.

The fuel rods for the fuel samples in the NJ0YU fuel assembly were located away from the sides of the fuel assembly. The calculation model was a single fuel assembly with a mirror reflector. Those for the fuel samples in the NJ070G fuel assembly were located at the corner (O1) or the side (O12 and O13) of the fuel assembly. Therefore, the calculation models were designed to consider the other fuel rods adjoining them [3].

In each burnup step, the effective neutron histories of 400,000 with 10,000 neutron histories per batch and 10 skip batches were calculated for the fuel samples from the NJ0YU fuel assembly, and those of 4,000,000 with 10,000 neutron histories per batch and 40 skip batches were calculated for the fuel samples from the NJ070G assembly. With these calculation conditions, the statistical uncertainty in the obtained inventories of ^{133}Cs was 0.1% for the fuel samples from the NJ0YU fuel assembly, that of ^{134}Cs was 0.4% for the fuel samples from the NJ070G assembly, and that of ^{148}Nd was 0.1% for the fuel samples from both fuel assemblies. The burnup calculations were performed to reproduce the measured inventories of ^{148}Nd so that the difference between the calculation and the measurement was smaller than 0.5%.

4. Comparison of calculated results with measurements

The calculated results with JENDL-4.0 were compared with the measurements and the C/E-1s were obtained. They are shown in **Table 2** and **Figure 3**. The error bars in Figure 3 show the uncertainties (1σ) in the C/E-1s which consisted of the measurement errors and the statistical uncertainties in the calculations. Those in the present study are 1.0% for ^{133}Cs and 1.7% for ^{134}Cs. The averaged C/E-1 for ^{133}Cs was 2.9%. The C/E-1s for ^{133}Cs in the present study were slightly larger than those with JENDL-3.3 and JENDL-4.0 for the BWR 9×9 UO_2 fuel samples [12] and slightly smaller than those with JENDL-3.3 and JENDL-4.0 for the PWR 18×18 UO_2 fuel sample [14]. The average C/E-1 for ^{134}Cs was −11.2%. The C/E-1s for ^{134}Cs in the present study were close to those with JENDL-3.3 and JENDL-4.0 for the BWR 9×9 UO_2 fuel samples [12].

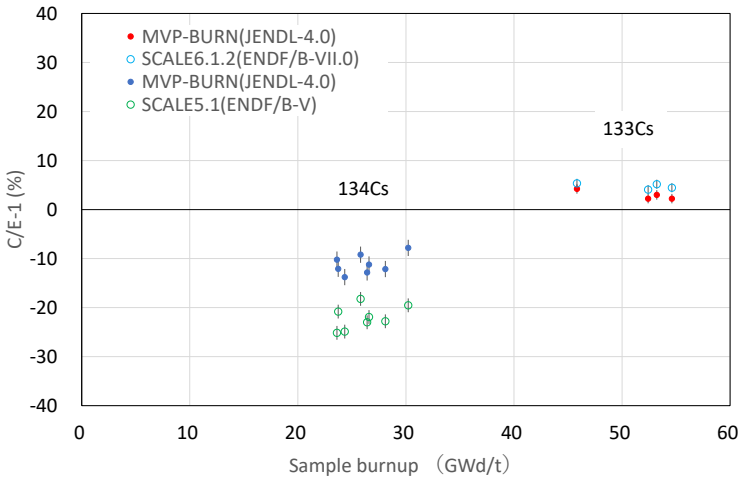

Figure 3. C/E-1s of the inventories of ^{133}Cs and ^{134}Cs in the present study and SCAL 6.1.2 and SCALE 5.1 for the fuel samples from

Table 2 and Figure 3 also show the C/E-1s with SCALE 6.1.2 (ENDF/B-VII.0) for ^{133}Cs [2] and those with SCALE 5.1 (ENDF/B-V) for ^{134}Cs [1]. The C/E-1s with SCALE 6.1.2 for ^{133}Cs were larger than those

in the present study and the average C/E-1 was 4.8%. The C/E-1s with SCALE 5.1 for ^{134}Cs were smaller than those in the present study and the average C/E-1 was −22.0%.

According to the study on the nuclear data sensitivity of the nuclide inventories reported by Oizumi et al. [18], the sensitivity of the neutron capture cross-section of ^{133}Cs to the inventory of ^{133}Cs was −0.192 and that to the inventory of ^{134}Cs was 0.843 at the cooling time of 10 years of a typical PWR fuel with the burnup of 50GWd/t. The differences in the C/E-1s of ^{133}Cs between the present study and SCALE 6.1.2 and those of ^{134}Cs between the present study and SCALE 5.1 were mainly attributed to the differences in the RIγs of ^{133}Cs in JENDL-4.0 and ENDF/B-VII.0 and JENDL-4.0 and ENDF/B-V, respectively.

The C/E-1s of ^{134}Cs and ^{133}Cs in the present study indicated that a larger RIγ of ^{133}Cs than that in JENDL-4.0 would bring the C/Es closer to 1. Applying the above-mentioned sensitivities to the C/E-1s of ^{133}Cs and ^{134}Cs in the present study, an increasing factor to the RIγ was estimated by dividing the negative values of the average C/E-1s of ^{133}Cs (−2.9%) by the sensitivity (−0.192) and obtained to be 15.1%. That was estimated by dividing the negative values of the average C/E-1s of ^{134}Cs (11.2%) by the sensitivity (0.843) and obtained to be 13.3%. The increasing factors in the present study based on the inventory measurements of ^{133}Cs and ^{134}Cs were considerably large. Recently, Block et al. [19] reported the measurement data of the RIγ as 460 ± 10 b which is larger by 3 ± 2% than that in JENDL-4.0 and close to that in JENDL-5.0. The resonance parameters in JENDL-5 adopted those of Block et al. [19]. Sims and Juhnke [20] reported the measurement data of the RIγ as 495 ± 17 b, which is listed in the reference [19] as one of the past measurements. While their data is isolated from the other data, and larger by 10.9% than that in JENDL-4.0, the estimated RIγs in the present study were close to their data.

The sensitivities to the fission yield of ^{133}Cs were 0.93 for the inventory of ^{133}Cs and 0.92 for that of ^{134}Cs [18]. Increasing the fission yield of ^{133}Cs to make the C/Es of ^{134}Cs closer to 1 brought the C/Es of ^{133}Cs away from 1 and therefore was not likely.

5. Conclusions

The inventory calculations of ^{133}Cs and ^{134}Cs with MVP-BURN and JENDL-4.0 for the twelve fuel samples taken from the two PWR fuel assemblies irradiated in Three Mile Island (TMI) Unit 1 presented that the averaged C/E-1s for ^{133}Cs and ^{134}Cs were similar to those in the previous study.

The C/E-1s of ^{133}Cs and ^{134}Cs in the present study indicated that a larger RIγ of ^{133}Cs than that in JENDL-4.0 would bring the C/Es closer to 1. The increasing factors for the RIγ of ^{133}Cs were estimated using the cross-section sensitivities and the C/Es of the inventories of ^{133}Cs and ^{134}Cs. They were 15.1% and 13.3%, respectively.

References

[1] Radulescu G, Gauld IC, Ilas G. SCALE 5.1predictions of PWR spent nuclear fuel isotopic compositions. Oak Ridge (Tennessee): Oak Ridge National Laboratory; 2010. (ORNL/TM-2010/44).

[2] Gauld IC, Giaquinto JM, Delashmitt JS. Re-evaluation of spent nuclear fuel assay data for the Three Mile Island unit 1 reactor and application to code validation. Annals of Nuclear Energy. 2016 Jan; 87(2): pp. 267-281.

[3] Yamamoto T. Feedback on neutron capture cross-section of ^{234}U from analysis of measured

inventories of UO_2 fuel irradiated in TMI Unit 1. J Nucl Sci Technol. 2024 Dec;61: pp.1621-1628.

[4] Shibata K, Kawano T, Nakagawa T, et al. Japanese evaluated nuclear data library version 3 revision-3: JENDL-3.3. J Nucl Sci Technol. 2002 Nov;39: pp. 1125-1136.

[5] Shibata K, Iwamoto O, Nakagawa T, et al. JENDL-4.0: a new library for nuclear science and engineering. J Nucl Sci Technol. 2011 Jan;48: pp. 1-30.

[6] Iwamoto O, Iwamoto N, Kunieda S, et al. Japanese evaluated nuclear data library version 5: JENDL-5. J Nucl Sci Technol. 2023 Jun;60: pp. 1-60.

[7] Data formats and procedures for the evaluated nuclear data file, ENDF/B-V. National Nuclear Data Center, Brookhaven National Laboratory; 1983. BNL-NCS-50496 (ENDF-102).

[8] Chadwick MB, Obložinsky P, Herman M, et al. ENDF/B-VII.0: next generation evaluated nuclear data library for nuclear science and technology. Nuclear Data Sheets. 2006 Dec;107(12): pp. 2931-3060.

[9] Chadwick MB, Herman MW, Obložinský P. et al. ENDF/B-VII.1 nuclear data for science and technology: cross sections, covariances, fission product yields and decay data. Data Sheets. 2011 Dec;112(12): pp. 2887-3152.

[10] Brown DA, Chadwick MB, Capote R, et al. ENDF/B-VIII.0: the 8th major release of the nuclear reaction data library with CIELO-project cross sections, new standards and thermal scattering data. Nuclear Data Sheets. 2018; pp. 148:1-142.

[11] Plompen AJM, Cabellos O, De Saint Jean C, et al. The joint evaluated fission and fusion nuclear data library, JEFF-3.3. Eur. Phys. J. A. 2020;56: pp. 1-181.

[12] Suzuki M, Yamamoto T, Fukaya H, et al. Lattice physics analysis of measured isotopic compositions of irradiated BWR 9×9 UO2 fuel. J Nucl Sci Technol. 2013 Dec;50: pp.1161-1176.

[13] Yamamoto T, Suzuki et al. Analysis of measured isotopic compositions of high-burnup PWR MOX and UO_2 fuels in the MALIBU program. J Nucl Sci Technol. 2012 Sep;49: pp. 910-925.

[14] Yamamoto T. Monte Carlo burnup analysis of measured nuclide inventories on high-burnup PWR - UO_2 and BWR-MOX fuels in the REBUS program. J Nucl Sci Technol. 2024 Jul: 61: pp. 1000-1017.

[15] Okumura K, Mori T, Nakagawa M, et al. Validation of a continuous-energy Monte Carlo burn-up code MVP-BURN and its application to analysis of post irradiation experiment. J Nucl Sci Technol. 2000 Feb;37: pp. 128-138.

[16] Michel-Sendis F, Gauld I, Martinez JS, et al. SFCOMPO-2.0: an OECD NEA database of spent nuclear fuel isotopic assays, reactor design specifications and operating data. Annals of Nuclear Energy. 2017;110: pp. 779-788.

[17] Okumura K, Kojima K, Okamoto T. Development of the burn-up chain data chainJ40 based on JENDL-4.0. Proc. Annual Meeting on the Atomic Energy Society of Japan; 2012 Mar 19-21; Fukui (Japan). E21. [in Japanese].

[18] Oizumi A, Jin T, Yokoyama K, et al., Database for nuclear data sensitivity of burnup composition in light water reactors. Tokai-mura (Japan): Japan Atomic Energy Agency; 2014. JAEA-Data/Code 2013-019, 278 p. [in Japanese].

[19] Block RC, Burke JA, Barry DP, et al. Neutron transmission and capture measurements of 133Cs from 0.01 to 600 eV. Nucl. Sci. Eng. 2019 Mar;193: pp. 269-282.

[20] Sims GHE, Juhnke DG. The thermal neutron cross-sections and resonance integrals of ^{50}Cr, ^{109}Ag, ^{123}Sb, ^{133}Cs. Journal of Inorganic and Nuclear Chemistry. 1968 Feb;30: pp. 349-353.

28 Analysis of angular momentum of produced nuclei and particle emission angles in multinucleon transfer reactions

Yusei MAEDA[1*], Kohta NAKAJIMA[1] and Yoshihiro ARITOMO[1]
[1] Graduate school of Science and Engineering, Kindai University
3-4-1 Kowakae, Higashiosaka city, Osaka 577-8502, Japan
[*]Email: y.maeda1312@kindai.ac.jp

The analysis of the properties of nuclei in the neutron-rich region, one of the challenges in nuclear reactions, is very important in the study of superheavy element synthesis. However, most nuclei in this region are not yet known. As a means of reaching this region, a method based on multinucleon transfer reactions has been proposed.

In this study, a theoretical dynamical model applying the Langevin equation was used to analyze multinucleon transfer reactions. Correlations between the particle emission angle and the number of transferred nucleons, and the angular momentum of the product nucleus were investigated. This is important for multinucleon transfer reactions because the survival probability depends on the angular momentum of the produced nuclei. We report on the correlation of each parameter since the calculations were performed in a reaction using an Xe beam and a target nucleus.

1. Introduction

To reach the Island of Stability and clarify the r-process, it is necessary to analyze the properties of nuclei in the neutron-rich region. In addition, reactions such as ^{238}U + ^{238}U and ^{238}U + ^{248}Cm are expected to produce superheavy elements as a counterpart of ^{208}Pb, which is a double magic nucleus, and neutron-rich nuclei can be produced. Therefore, the analysis of the properties of nuclei in the neutron-rich region, one of the challenges in nuclear reactions, is very important. However, most nuclei in this region are not yet known [1]. As a means of reaching this region, a method based on multinucleon transfer reactions has been proposed [2]. The creation of nuclei using multinucleon transfer reactions is beginning to take place worldwide, but the mechanism is complex and not fully understood [3]. In the reaction, when the product nuclei are heavy or superheavy nuclei, if the angular momentum of compound nucleus is low, it survives as an evaporation residue. However, if the angular momentum is high, it undergoes fission [4]. Hence, predicting angular momentum is important for finding optimal reaction systems and energies to produce neutron-rich nuclei by multi-nucleon transfer reactions. In this study, we analyze the relationship between the scattering angle and the number of transfer nucleons, which can be measured experimentally, and the angular momentum of producing nuclei, which cannot be measured experimentally. By analyzing this correlation, we are trying to elucidate the fusion process. In this study, we adopt a theoretical dynamical model applying the Langevin equation. This paper contains as follows Sec. 2 describes the details of the

model framework. Sec. 3 discusses the relation between number of transfer nucleons, scattering angle, and angular momentum of producing nuclei. The last section describes the conclusion.

2. Theory

We adopted the dynamical model which similar to unified model [5]. The model is used for theoretical calculations of nuclear fusion and fission, and it enables us to follow the time evolution of nuclear shapes. We perform a trajectory calculation on potential energy surfaces.

2.1. Two-center shell model

We adopted the two-center shell model to represent the shape of nucleus. The two-center shell model describes the nuclear shape using three parameters: the two center distribution z, the nuclear deformation δ, and the mass asymmetry α [6]. Here, R_{CN} is radius of the spherical compound nucleus.

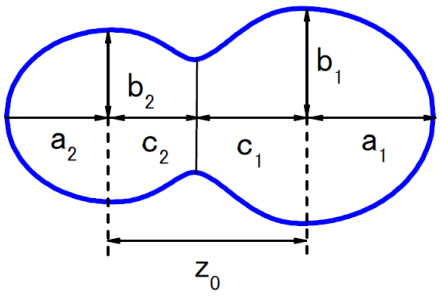

Figure 1. Nuclear shape by the two-center parametrization.

$$z = \frac{z_0}{R_{CN}B} \tag{1}$$

$$B = \frac{3+\delta}{3-2\delta} \tag{2}$$

$$z_0 = |c_1| + |c_2| \tag{3}$$

$$\delta = \frac{3(a-b)}{2a+b} \tag{4}$$

$$\alpha = \frac{A_1 - A_2}{A_1 + A_2} \tag{5}$$

2.2. Potential energy

We treated the entire process within a single framework by connecting the diabatic potential with the adiabatic potential, using a time-dependent weighting function.

We consider the time evolution of potential energy from the diabatic one $V_{\mathrm{dia}}(q)$ to adiabatic one $V_{\mathrm{adi}}(q)$ [7]. Here, q denotes a set of collective coordinates representing nuclear deformation. The diabatic potential is calculated by a folding procedure using effective nucleon-nucleon interaction. However, the adiabatic potential energy of the system is calculated using an extended two-center shell model. Then, we connect the diabatic and the adiabatic potentials with a time-dependent weighting function as follows:

$$V(q,t) = V_{\mathrm{dia}} f_\varepsilon(t) + V_{\mathrm{adi}}[1 - f_\varepsilon(t)] \tag{6}$$

$$f_{\varepsilon}(t) = \frac{1}{1 + \exp\left(-\frac{t}{\tau_{\mathrm{relax}}}\right)} \tag{7}$$

$$\tau_{\mathrm{relax}} = 1.0 \times 10^{-22}[\mathrm{s}] \tag{8}$$

2.2.1. Diabatic potential

The potential energy between two nuclei at infinity that crosses the Coulomb barrier and encounters each other is called the diabatic potential. The diabatic potential is calculated by a folding procedure using effective nucleon-nucleon interaction [5,8,9].

$$V_{\mathrm{dia}} = M(A_1, Z_1, \delta_1) + M(A_2, Z_2, \delta_2) - M\left(A_T, Z_T, \delta_T^{g.s}\right) - M\left(A_P, Z_P, \delta_P^{g.s}\right) \tag{9}$$

$$V_{12} = \int_{V_1} \rho_1(r_1) \int_{V_2} \rho_2(r_2) v_{NN}(r_{12})\, d^3r_1 d^3r_2 \tag{10}$$

Here r is the distance between the oscillator centers, r_i indicate radius of nucleus, and $r_{12} = r + r_2 - r_1$. v_{NN} is effective nucleon-nucleon interaction and $\rho_i(r_i)$ is density distributions of nuclear matter in the nuclei.

2.2.2. Adiabatic potential

The adiabatic potential energy of the system is calculated using an extended two-center shell model [9]. The potential energy is defined as a sum of the liquid-drop part, a microscopic part and centrifugal part:

$$\mathrm{V_{adi}} = V_{\mathrm{LDM}}(q) + V_{\mathrm{SHE}}(q, T) + V_{\mathrm{CEN}}(q, L) \tag{11}$$

$$V_{\mathrm{LDM}}(q) = E_{\mathrm{S}}(q) + E_{\mathrm{C}}(q) \tag{12}$$

$$V_{\mathrm{SHE}}(q, T) = E_{\mathrm{shell}}(q)\Phi(T) \tag{13}$$

$$V_{\mathrm{CEN}}(q, L) = \frac{\hbar^2 L(L+1)}{2\mathcal{I}(q_{\mathrm{i}})} \tag{14}$$

$$\Phi(T) = \exp\left(-\frac{E^*}{E_{\mathrm{d}}}\right) \tag{15}$$

Here, $\mathcal{I}(q_{\mathrm{i}})$ is the moment of inertia of the rigid body with deformation q. The centrifugal energy (V_{CEN}) generated from the angular momentum L of the rigid body is also taken into account. V_{LDM} and V_{SHE} are the potential energy of the finite range liquid drop model and the shell correction energy that takes into account temperature dependence, respectively. The symbol E_{shell} indicate the shell correction energy at T=0. The temperature dependence factor $\Phi(T)$ is explained in Ref. [10], where E^* indicates the excitation energy of the compound nucleus. E^* is given $E^* = aT^2$, where a is the level density _ij parameter. The shell damping energy E_d is selected as 20 MeV. This value is given by Ignatyuk et al. [11]. The symbols E_{S} and E_{C} stand for generalized surface energy [12] and Coulomb energy, respectively.

2.3. Langevin equation

We use the multidimensional Langevin equation [8,10,13] unified following:

$$\frac{dq_i}{dt} = (m^{-1})_{ij} p_j \tag{16}$$

$$\frac{d\theta}{dt} = -\frac{l}{\mu_R R^2} \tag{17}$$

$$\frac{d\varphi_1}{dt} = \frac{L_1}{\xi_1} \tag{18}$$

$$\frac{d\varphi_2}{dt} = \frac{L_2}{\xi_2} \tag{19}$$

$$\frac{dp_i}{dt} = -\frac{\partial V}{\partial q_i} - \frac{1}{2}\frac{\partial}{\partial q_i}(m^{-1})_{jk}p_j p_k - \gamma_{ij}(m^{-1})_{jk}p_k + g_{ij}R_j(t) \tag{20}$$

$$\frac{dl}{dt} = -\frac{\partial V}{\partial \theta} - \gamma_{tang}\left(\frac{l}{\mu_R R} - \frac{L_1}{\xi_1}a_1 - \frac{L_2}{\xi_2}a_2\right)R + Rg_{tang}R_{tang}(t) \tag{21}$$

$$\frac{dL_1}{dt} = -\frac{\partial V}{\partial \varphi_1} + \gamma_{tang}\left(\frac{l}{\mu_R R} - \frac{L_1}{\xi_1}a_1 - \frac{L_2}{\xi_2}a_2\right)a_1 - a_1 g_{tang}R_{tang}(t) \tag{22}$$

$$\frac{dL_2}{dt} = -\frac{\partial V}{\partial \varphi_2} + \gamma_{tang}\left(\frac{l}{\mu_R R} - \frac{L_1}{\xi_1}a_1 - \frac{L_2}{\xi_2}a_2\right)a_2 - a_2 g_{tang}R_{tang}(t) \tag{23}$$

The collective coordinates q_i represents z, δ, and α, the symbol p_i denotes momentum conjugated to q_i, and V is the multidimensional potential energy. Here θ and l are the relative orientation of nuclei and relative angular momentum. φ_1 and φ_1 are the angles of rotation of the nuclei in the reaction plane (their moment of inertia and angular momentum are $\xi_{1,2}$ and $L_{1,2}$), $R_{1,2}$ is radius of nucleus, and R is distance between the nuclear centers. The total angular momentum $L = l + L_1 + L_2$. The symbol μ_R is reduced mass, and γ_{tang} is tangential friction. m_{ij} and γ_{ij} stand for the shape-dependent collective inertia and friction tensors elements, respectively. We adopted the hydrodynamic inertia tensor m_{ij} in Werner-Wheeler approximation for the velocity field [14]. The normalized random force $R_i(t)$ is assumed to be white noise: $\langle R_i(t_1)R_j(t_2)\rangle = 2\delta_{ij}\delta(t_1 - t_2)$. According to Einstein relation, the strength of the random force g_{ij} is given $\sum_k g_{ik}g_{jk} = T\gamma_{ij}$, where T is the temperature of the compound nucleus calculated from the intrinsic energy of the composite system.

3. Results and Discussion

In this study, we analyzed the reaction ^{136}Xe + ^{209}Bi at an incident energy of 684 MeV. The parameters used in our calculations were fitted to experimental angle-dependent differential cross-section data [15, 16]. Figure 2 shows the relationship between the number of transfer nucleons, the scattering angle, and the angular momentum of producing nuclei. Here, the number of transferred nucleons represents the nucleon transfer from the projectile nucleus to the target nucleus.

Figure 2(a) shows the relationship between the number of transfer nucleons and the scattering angle. From this figure, it can be observed that as the number of transferred nucleons increases, the scattering angle tends to shift toward forward scattering. This indicates that a longer contact time results in a greater number of transferred nucleons, accompanied by a shift to forward scattering angles.

Figure 2(b) shows the relationship between the scattering angle and the angular momentum of the produced nuclei. The data suggest that as the scattering angle shifts toward forward angles, the angular momentum of the produced nuclei increases. In the high-scattering-angle region, the angular momentum also increases due to contributions from backward scattering, which involves trajectories where the projectile nucleus moves around the target nucleus. In such cases, prolonged contact times facilitate nucleon transfer, thereby increasing the angular momentum of the system.

Figure 2(c) shows the relationship between the number of transfer nucleons and the angular momentum of producing nuclei. From this figure, as the number of transfer nucleons increases, the

angular momentum of producing nuclei also increases. Therefore, it is considered that angular momentum is transferred along with the nucleons during the transfer process.

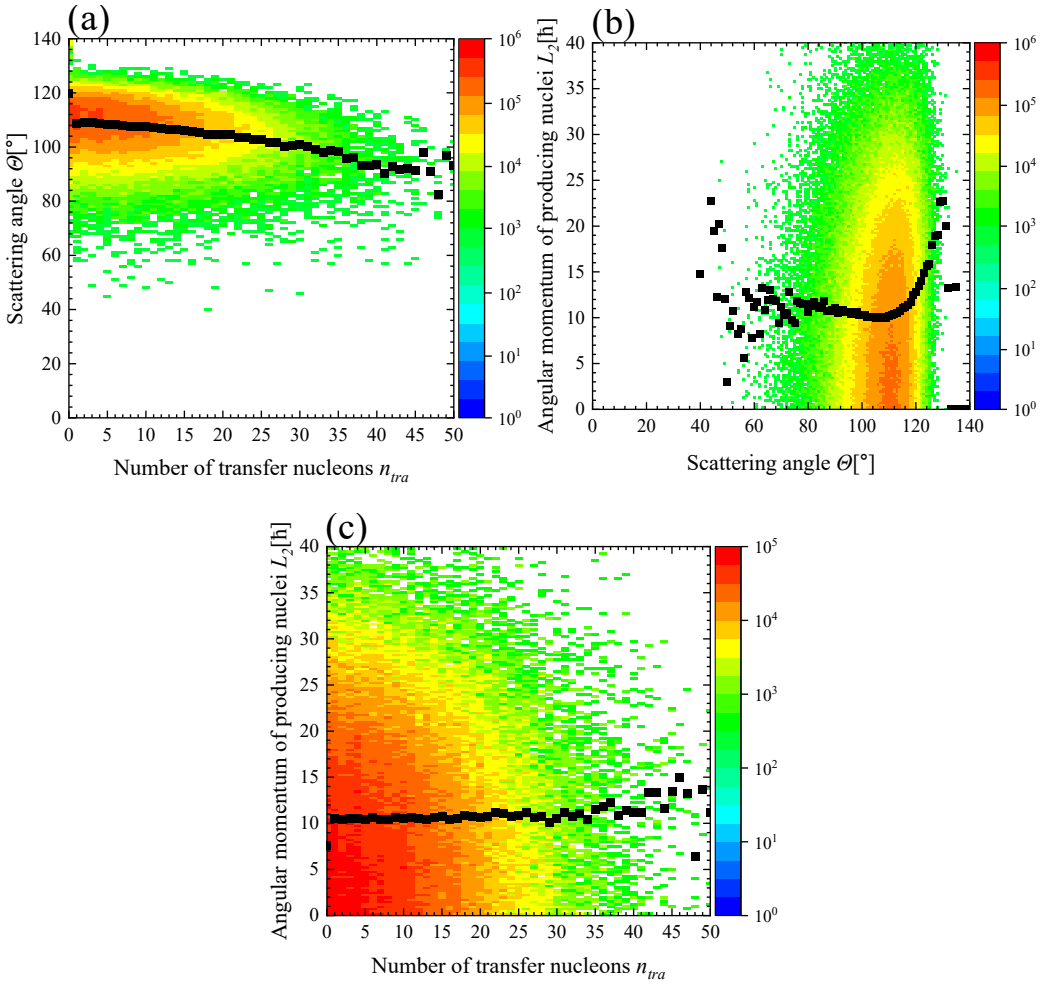

Figure 2. Calculated number of transfer nucleons, scattering angle, and angular momentum of producing nuclei at ^{136}Xe + ^{209}Bi. The dots in the figure indicate the average value of the parameter at each value.

4. Summary

In this study, we show the relation between number of transfer nucleons, scattering angle, and angular momentum of producing nuclei in ^{136}Xe + ^{209}Bi. The results show that contact time is related to each parameter, with the angular momentum of producing nuclei increasing as contact time increases.

As future work, we aim to perform calculations with ^{238}U + ^{238}U, ^{238}U + ^{248}Cm and other combinations to reach the Islands of Stability and explore the synthesis of new elements. In this study, we use spherical nucleus as target but ^{238}U and ^{248}Cm are deformed nucleus. So, we want to calculate with deformed nucleus as a target. Additionally, we would like to clarify the reaction mechanism to produce neutron-rich nuclei in the super heavy element region in the future.

References

[1] V. Zagrebaev, A. Karpov and W. Greiner, J. Phys: Conf. Ser. 420, 012001 (2013).
[2] V. Zagrebaev, W. Greiner, Phys. Rev. Lett. 101, 122701 (2008).
[3] Y. X. Watanabe et al., Phys. Rev. Lett. 115, 172503 (2015).
[4] S. Tanaka, *et al.,* Phys. Rev. C 105, L021602 (2022).
[5] V. Zagrebaev and W. Greiner, J. Phys. G 34, 11, 2265 (2007).
[6] Maruhn and W. Greiner, Z. Phys 251, 431 (1972).
[7] V. Karpov et al. Phys. Rev. C 96, 024618 (2017).
[8] V. Zagrebaev and W. Greiner, J. Phys. G 31, 7, 825 (2005).
[9] V.I. Zagrebaev, *et al*., Phys. Part. Nuclei 38, 469 (2007).
[10] Y. Aritomo and M. Ohta, Nucl. Phys. A 744, 4 (2004).
[11] A.N. Ignatyuk, G.N. Smirenkin and A.S. Tishin, Sov. J. Nucl. Phys 21, 255 (1975).
[12] H.J. Krappe, J.R. Nix and A.J. Sierk, Phys. Rev. C 20, 992 (1979).
[13] Y. Aritomo, Phys. Rev. C 80, 064604 (2009).
[14] K.T.R Davies, A.J. Sierk and J.R. Nix, Phys. Rev. C 13, 2385 (1976).
[15] W. W. Wilcke, J. R. Birkelund, *et al.* Phys. Rev. C 22, 128 (1980).
[16] W.Schroder, J. R. Birkelund, *et al.* Phys. Rep. 45, 301 (1978).

This is a blank page.